1221

Refractive Index and Thermo-Optical Detectors for Capillary Electrophoresis

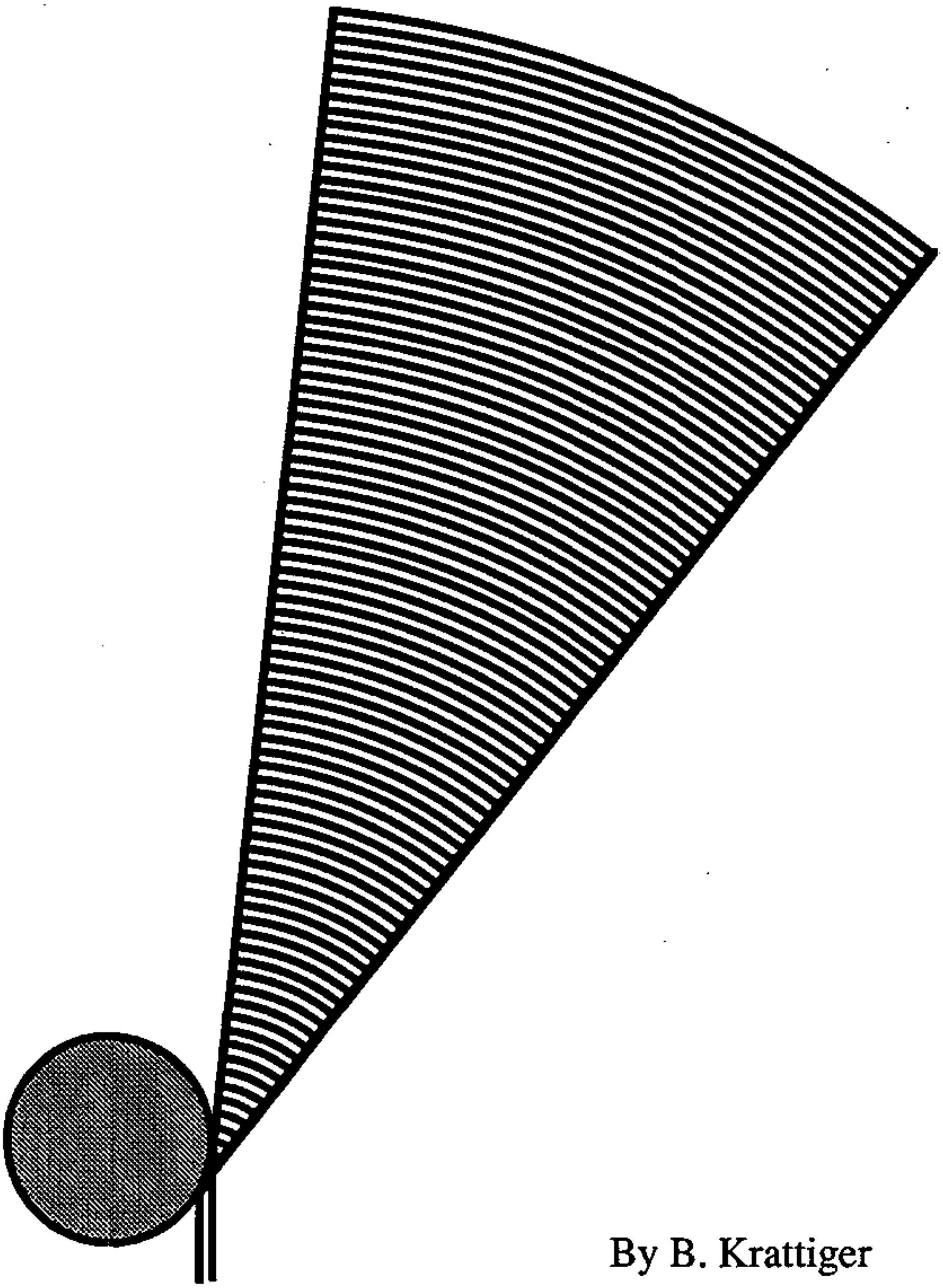

By B. Krattiger

Ciba-Geigy Basle
Corporate Analytical Research

University of Neuchâtel
Institute of Microtechnology

Refractive Index and Thermo-Optical Detectors for Capillary Electrophoresis

Ph. D. Thesis
by
Beat Krattiger

Dissertation Director:
Prof. Dr. R. Dändliker, Institute of Microtechnology, University of Neuchâtel

Examination Committee:
Prof. Dr. H. M. Widmer, Corporate Analytical Research, Ciba-Geigy
Prof. Dr. E. S. Yeung, Dept. of Chemistry, Iowa State University, USA
Prof. Dr. N. de Rooij, Institute of Microtechnology, University of Neuchâtel
Dr. A. E. Bruno, Corporate Analytical Research, Ciba-Geigy

Ciba-Geigy Ltd., Corporate Analytical Research, 4002 Basle, Switzerland

PREFACE

Chemical analysis is a key step in chemical product development, process control and research. Legal regulations require chemical analysis for registration, product safety etc. Growing fields for chemical analysis are e.g. the environment sciences, biochemistry, or food science.

Most chemical analysis systems consist of at least two stages, the separation stage, where the sample components are spatially or temporally separated according to intrinsic qualities of the sample components and, the detection stage, where the quantity of the separated species is measured. The separation is obtained by means of optimized interaction between the sample and a stationary phase or a liquid where also fields can be applied to influence the separation.

The detection stage can be designed to meet different needs of which high sensitivity is probably the most encountered. Detectors can also be designed to be universal (i.e. not selective at all) or, on the contrary, to selectively detect only desired species (i.e. high selectivity) or, to capture more than one information simultaneously in order to enhance information of an incomplete separation.

Separation and detection form a pair of interdependent items (like the hen and the egg). An improvement in one stage immediately asks for a revision of the other stage[1], and hence their developments have to be considered in parallel.

An outstanding example of chemical analysis is capillary electrophoresis (CE) which was found in 1967 by Hjertén[2]. However, the most prominent example of chemical analysis systems is high performance liquid chromatography (HPLC), which is applied in a vast majority of separations and therefore is almost a synonym to chemical analysis. The virtues offered by CE stem from the low sample and solvent consumption, the high separation efficiencies, the short separation times, the simple and inexpensive operation and the high potential for automation. Due to these advantages CE is now "the trend" in analytical chemistry, replacing HPLC in various applications and opening completely new fields. CE has experienced a tremendous growth in the past ten years[3]. Although the first instrument was introduced on the market only six years ago, CE is already applied in about 10 % of all separations and one is about to speculate whether CE could reach the same importance as HPLC. The efforts in CE research are now mainly method development. As many commercially available instruments are working close to the physical limits, fewer instrumental and more application developments are reported now. The instrumental research in CE comprises application of additional external fields, miniaturization, hyphenation of different capillary segments and alternative detection methods.

Among various detection schemes used in CE, optical detection is mainly preferred because it allows simple, remote and contactless measurement. Due to its chemical properties fused silica is the preferred construction material for the separation capillaries and, as fused silica is transparent in the UV/vis spectral range, optical detection seems obvious. Other (than optical) detection methods are well described in the literature and are reproduced in many laboratories but until now they are not part of commercially available CE instruments.

As a majority of samples of analytical interest absorb in the UV/vis spectral range, all available CE systems are equipped with on-column absorbance detection. As only alternative now, laser induced fluorescence (LIF) detection has just become commercially available to CE instruments.

However, for a minority of transparent samples, such as carbohydrates, hydrocarbons, and single ions, various experimental refractive index (RI) detectors are devised for CE, but less than a dozen applications are reported. Although RI detectors belong to routine equipment (number two or three after absorbance) for HPLC, no comparable device is on the market yet for CE. The straightforward miniaturization of existing HPLC detectors was successful for CE absorbance detection but this approach did not work for RI detection. Alternative methods such as indirect absorbance detection or chemical derivatizations were established for CE separation of transparent samples, and RI detection was left aside.

The first aim of this work is therefore to develop capillary RI detectors for CE. As these detectors are the key elements in thermo-optical absorbance (TOA) detection, the second aim is the application of these RI detectors to design TOA detectors.

The thesis comprises 8 chapters. Most of them are publications, three are already published, two are accepted and one is being prepared for publication. The list of names of authors below the titles of the publications express the fact that its content is not the work of one single person but rather represents the efforts of a whole group.

Chapter 1 Introduction

A short summary of the capillary electrophoresis (CE) separation principle is presented. Detection problems related to CE are discussed. The problem associated to the miniaturization of HPLC detectors adapted for CE is discussed.

Chapter 2 "On-Column Laser-Based Refractive Index Detector for Capillary Electrophoresis"

Bruno, A. E.; Krattiger, B.; Maystre, F.; Widmer, H. M. *Anal. Chem.* 1991, *63*, 2689-2697.

This paper demonstrates the first application of a refractive index (RI) detector in CE. The detector was demonstrated with a CE separation of underivatized sugars. Thermal and electronical noise aspects are discussed in detail.

Chapter 3 "Laser-based refractive index detection for capillary electrophoresis: ray-tracing interference theory"

Krattiger, B.; Bruno, A. E.; Widmer, H. M.; Geiser, M.; Dändliker, R. *Appl. Opt.* 1993, *32*, 956-965.

This publication presents a theoretical model which explains the fringe patterns associated witb side illuminated capillaries. The model is applied to propose optimizations of capillary RI detectors.

Chapter 4 "Enhanced Refractive Index Detection for Capillary Electrophoresis Using Flared Capillaries"

Saz, J. M.; Krattiger, B.; Bruno, A. E. *Anal. Methods Instrum.* (in press 1994).

This publication describes a novel optical arrangement for a RI detector based on a Wollaston prism. The detector is used with flared and normal capillaries to detect sugars separated by CE.

Chapter 5 "Hologram-Based Refractive Index Detector for Capillary Electrophoresis: Separation of Metal Ions"

Krattiger, B.; Bruin, G. J. M.; Bruno, A. E. *Anal. Chem.* 1994, *66*, 1.

A detector is constructed using holographic optics and laser diodes (LDs). A model is presented which predicts the instrumental behavior. The detector is used in the CE separation of small cations. Its performance is compared with that of indirect UV absorbance detection.

Chapter 6 "Hologram Based Thermo-Optical Absorbance Detection in Capillary Electrophoresis; Separation of Nucleosides and Nucleotides"

Krattiger, B.; Bruno, A. E.; Widmer, H. M.; Dändliker, R. *Anal. Chem.* (submitted)

A TOA detector based on the hologram RI detector is constructed. A model is presented to predict the detector signal. A CE separation of a TOA detected mixture of underivatized samples is demonstrated.

Chapter 7 "The Pigtailing Approach to Optical Detection in Capillary Electrophoresis"

Bruno, A. E.; Maystre, F.; Krattiger, B.; Nussbaum, P.; Gassmann, E. *Trends in Anal. Chem.* 1994, *13*, 190.

In this publication it is argued that detection noise can sometimes be reduced by reduction of the number of optical interfaces. A capillary RI detector is realized by gluing an optical fiber directly onto the capillary. Pigtail absorbance and fluorescence detectors based on light emitting diodes (LEDs) are demonstrated in CE separations.

Chapter 8 Conclusion of the Thesis

This chapter contains a summary of the work, suggestions for instrumental improvements, remarks on the acceptance of capillary RI detection as well as suggestions for further studies.

This work was partially supported by the CERS (Commission pour l'Encuoragement de la Recherche Scientifique), Project 2156.1.

Parallel to this work, which was mainly done at Ciba-Geigy in Basle, profound theoretical calculations of the fringe patterns ("Scattering of an off-axis Gaussian beam by a dielectric cylinder using a rigorous electromagnetic approach")[4] were performed at the IMT in Neuchâtel completing the work of Chapter 3.

References

(1) Scott, R. P. W.; In *Liquid Chromatography Detectors*; Elsevier: New York, 1986

(2) Hjertén, S. *Chromatogr. Rev.* 1967, 9, 122.

(3) Braun, T.; Nagydiósi-Rózsa, S. *Trends Anal. Chem.* 1991, *10*, 266.

(4) Zimmermann, E.; Souli, N.; Dändliker, R.; Krattiger, B. *Appl. Opt.*, submitted (1994).

Refractive Index and Thermo-Optical Detectors for Capillary Electrophoresis

Contents

Chapter 1	Introduction	(pages I 1 - I 3)
Chapter 2	On-Column Laser-Based Refractive Index Detector for Capillary Electrophoresis	
Chapter 3	Laser-Based Refractive Index Detection for Capillary Electrophoresis: Ray-Tracing Analysis	
Chapter 4	Enhanced Refractive Index Detection for Capillary Electrophoresis Using Flared Capillaries.	
Chapter 5	Hologram-Based Refractive Index Detector for Capillary Electrophoresis: Separation of Metal Ions	
Chapter 6	Hologram Based Thermo-Optical Absorbance Detection in Capillary Electrophoresis; Separation of Nucleosides and Nucleotides.	
Chapter 7	The Pigtailing Approach to Optical Detection in Capillary Electrophoresis.	
Chapter 8	Conclusions	(pages C 1 - C 2)

Chapter 1 Introduction

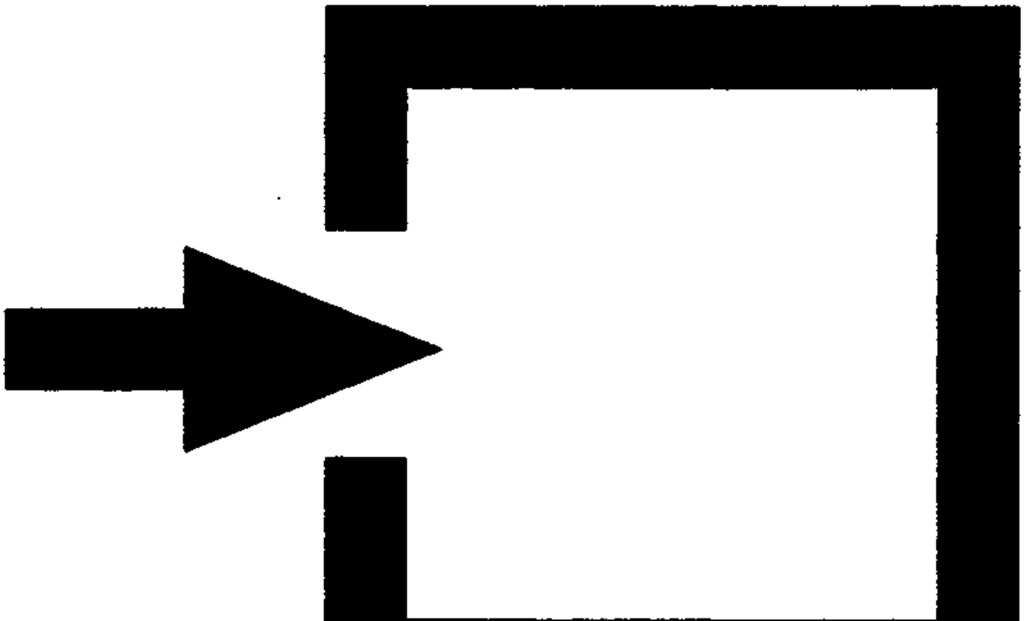

Chapter 1. INTRODUCTION

Capillary Electrophoresis: Capillary electrophoresis (CE) is a separation technique for chemical analysis which is based on the migration of electrically charged sample (i.e. ions) in a electrolyte filled capillary which is subjected to an electrical field. Detailed information is given by Li[1]; a schematic view of a CE system is shown in Fig. 1.

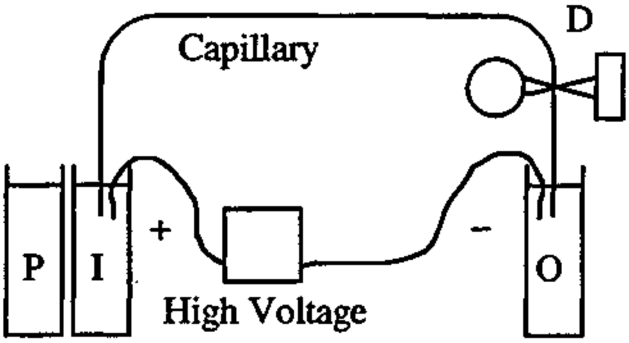

Figure 1. CE system. D: on-column detector (absorbance, fluorescence, RI), I: inlet viel with buffer, O: outlet vial with buffer, P: probe vial with sample.

Unlike a metallic solid, where the electric current is governed by electrons, the current in liquids is due to the migration of ions. The principle of ionic migration in an electrolyte is sketched in Fig. 2.

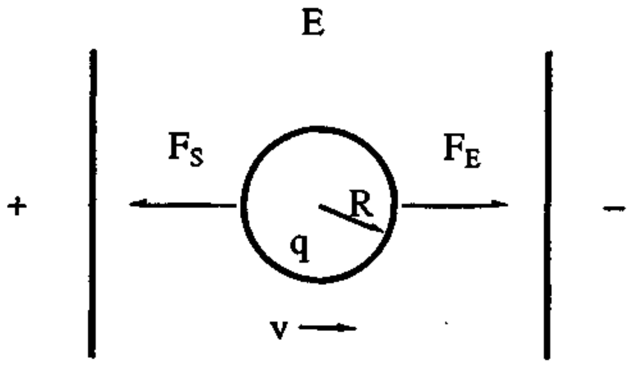

Figure 2. Forces acting on a charged particle migrating through a liquid. The electrical field, E, is symbolized by capacitor plates and the polarity sign. The particle has a positive charge, q.

In an electrical field E, a particle which carries the charge q is subjected to the force

$$F_E = q\,E \ . \qquad (1)$$

The particle is not accelerated permanently (as one could guess) because a second opposite force, the Stoke's drag, immediately builds up. The Stoke's drag, F_S, for laminar flow is given by

$$F_S = 6\pi\eta R v \ , \qquad (2)$$

where v is the velocity of the charged particle with respect to the buffer, η is the viscosity and R is the Stoke's radius. R represents the interaction between sample and buffer and can be related to the geometrical radius of the sample ion. After reaching the steady state, the two forces are equal and one obtains from combination of Eqs. (1) and (2) the electrophoretic mobility

$$\mu_{ep} = \frac{v}{E} = \frac{q}{6\pi\eta R} \ , \qquad (3)$$

which is the basic parameter of electrophoretic separations. The average charge of the sample is depending on the buffer pH. Sample ions tend to be more negatively charged for increasing pH and more positively for decreasing pH, respectively. The electrophoretic migration velocity, v_{ep}, is given by

$$v_{ep} = \mu_{ep}\,E \ . \qquad (4)$$

As the different species carry different charges and/or display different Stoke's radii, they have different electrophoretic mobilities. Due to their individual propagation velocities they appear, after some time, spatially separated.

This is not the only effect which governs CE. A pumping effect, electroosmosis, is observed as an electric field is applied along the buffer filled capillary. This electroosmotic flow is superposed to the electrophoretic motion of the sample and is the second driving effect (in open tube) CE. This phenomenon is a consequence of the usually negative surface charges on the capillary wall. The uppermost silica atoms tend to bind OH^- from the buffer solution. As the net charge in the capillary cross-section has to be zero, the buffer solution delivers thus positive charges which concentrate up towards the negatively charged capillary wall. The positive charges closer to the wall are attracted and immobilized, but a distant, more diffuse positive layer is mobile and pushed forward to the negative pole by the electric field. As the diffuse layer surrounds the bulk buffer solution like a jacket, it transports, coupled by shear force, the entire buffer solution to the cathode end.

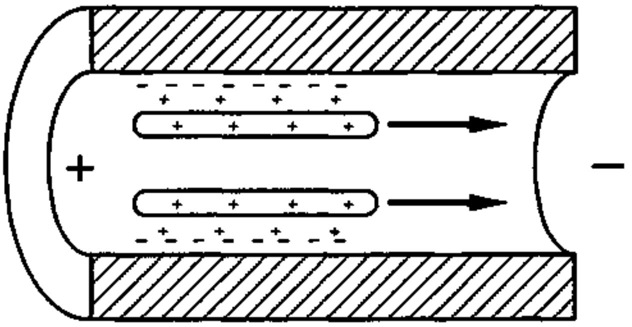

Figure 3. Charge distribution inside a capillary. The arrows indicate the electroosmotic flow.

The velocity of the electroosmotic flow (EOF) is given by

$$v_{eo} = \frac{\varepsilon\zeta}{4\pi\eta}E \quad , \qquad (5)$$

where ε is the dielectric constant of the buffer and ζ the zeta potential. The EOF can be controlled by the buffer pH. At high pH the OH^- concentration at the wall increases and thus also the negative surface charges are enhanced. The increased charge density translates into higher electroosmotic flows. On the other hand it is possible to reduce the EOF by using low pH buffers. The electroosmotic flow can also be controlled (e.g. eliminated) by coatings and even positive surface charges have been reported.

The two velocities add up to render the effective velocity

$$v_{eff} = v_{ep} + v_{eo} \quad . \qquad (6)$$

As the buffer pH influences both, the electrophoretic and the electroosmotic mobility, respectively, it is the most important chemical parameter for optimizing a separation.

A detector is installed near the capillary end to indicate the arrival of the species, which are identified according to their migration times (Fig. 1).

The capillary inner diameter, the electric field, the capillary length and the choice of the buffer solution affect the separation efficiency, i.e. the relative sharpness of the peaks. The best electropherogram results from the optimization of these parameters.

CE can be performed either by simple self made equipment as well as by using different commercially available systems (in the 40 – 80 000 $ range) featuring auto samplers and powerful analysis software.

Detection: The basic detection methods in CE are discussed by Li[1]. However some arguments concerning the miniaturization of optical detectors are given below. In a standard HPLC separation system (Fig. 4) a pump/valve unit pumps solvent through the column and the detector cell, which is at the end of the line.

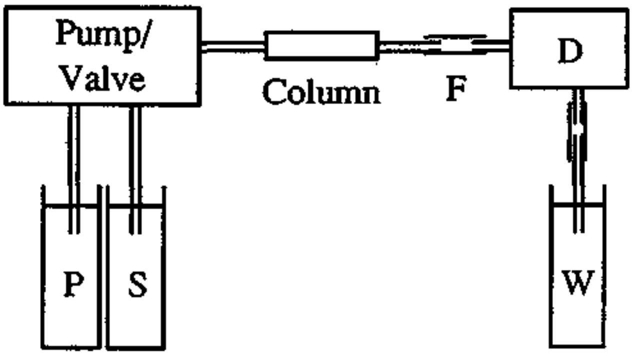

Figure 4. HPLC system with hyphenated detector. D: detector, F: fittings, P: probe vial, S: solvent vial, W: waste vial.

To begin a separation, a minute amount of the probe solution is injected by switching the injection valve. The injected plug is thus pressed through the column where it is separated into its compounds which are detected after the column. As the flow is quite high, the elements of the separation system are connected by tubes and fittings with inner dimensions in the sub millimeter range. Their dead volumes, which cause mixing effects, are small if compared to the volumes of the eluting peaks and therefore the hyphenation of the column to the detector does not lead to severe peak broadening.

HPLC absorbance detectors (Fig. 5a) are optimized to return with a minimum of analyte a maximum in S/N. The required volume for UV/vis detection is in the 1-10 µl range. This volume can not further be reduced without decreasing drastically the S/N.

As in CE the inner cross sections and flow rates are at least 2-3 orders of magnitude smaller than in HPLC, the established HPLC detectors can not be applied because the detection volumes are rather large. The entire capillary volume (e.g. i.d = 75 µm, length = 1 m) is of the same order than just the detection volume of a HPLC absorbance cell. An application of such a detector to CE would therefore lead to mixed, indistinguishable peaks. Therefore, and also to avoid peak broadening due to hyphenation, "on-column" detection (Fig. 5b) is the straightforward evolution step, imperative for CE.

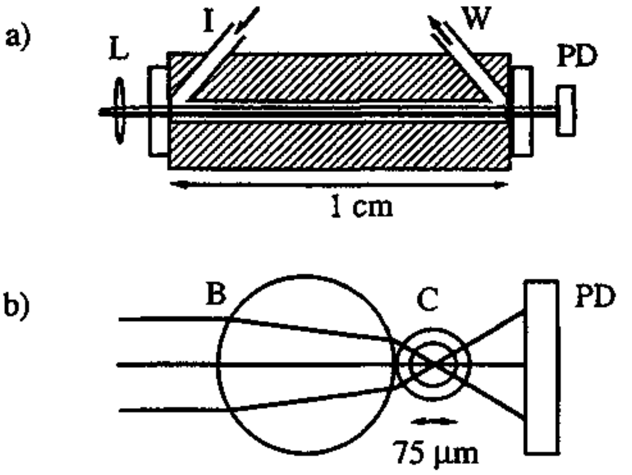

Figure 5. Typical absorbance detection arrangements. a) flow cell for HPLC and b) on-column detection for CE. L: lens, I: input to flow cell from column, W: output to waste, PD: photo detector, B: ball lens, C: capillary.

CE separations are performed in capillaries having i.d.s in the order of 5–100 µm, but mostly CE is performed in 50–100 µm capillaries, corresponding to 1-2 orders of magnitude shorter detection paths than in HPLC. The reduced probing paths translate in a deterioration of the concentration detection sensitivity, which is one of the major problems in CE.

Another problem of on-column absorbance detection, also caused by the small capillary i.d., is the focusing of the light sources onto the capillary. Conventional light sources, i.e. not lasers, can only be very inefficiently focused to the small spots, and are not suited to properly illuminate capillaries below 75 µm i.d.. For smaller capillaries, much light passes outside the fluid string without gathering information from the analyte and the amount which does is so small that its detection is limited by shot noise leading to a reduction of the S/N ratio[2,3]. As the illuminating spot is larger than the capillary i.d., the light is also scattered at the interfaces and adds noise to the detection[3].

Many efforts were undertaken to improve the detection stage in CE for the various schemes. Geometric conformations of the detection cell, without intersecting the capillary, were devised. On the other hand the shape of the light was modified. The use of lasers gives well defined small detection beams with intense irradiation for absorbance or fluorescence detection. Absorbance detection, however, relies frequently on the tunability of the light source, but in the most important UV range no adequate tunable lasers exist. Therefore, the application of lasers is limited to special cases.

In Fig. 6 a HPLC RI detector is displayed. The flow cell consists of two (hollow) prisms. One prism is flushed with eluent from the separation column where the other contains, as a reference, the solvent. As the peaks elute from the column, the RI difference refracts the beam according to Snell's law. The deflection, α, constitutes, upon calibration, the RI signal. The cell volumes are in the 1-10 µl range.

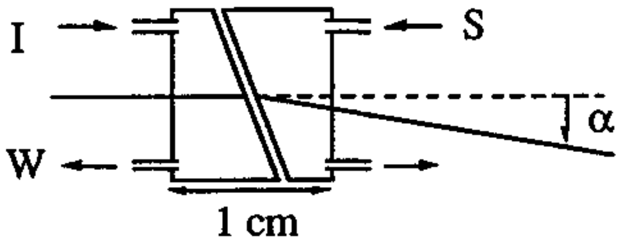

Figure 6. Flow cell of an RI detector for HPLC. I: input from column, W: output to waste, S: solvent for reference, α: deflection.

Although successful for absorbance, the straightforward miniaturization of an HPLC RI detector, while conserving the principle, is not possible. The double prism arrangement of a conventional HPLC RI detector is not feasible for on-column detection within a 75 µm capillary. To resolve this dilemma new principles were developed for on-column RI detection for CE.

References

(1) Li, S. F. Y. In *Capillary Electrophoresis*, Elsevier: New York, 1992.

(2) Bruin, G. J. M.; Stegeman, G.; Asten, van A. C.; Xu, X.; Kraak, J. C.; Poppe, H. *J. Chromatogr.* **1991**, *559*, 163-181.

(3) Bruno, A. E.; Krattiger, B.; Maystre, F.; Widmer, H. M. *Anal. Chem.* **1991**, *63*, 2689-2697.

Chapter 2 On-Column Laser-Based Refractive Index Detector for Capillary Electrophoresis

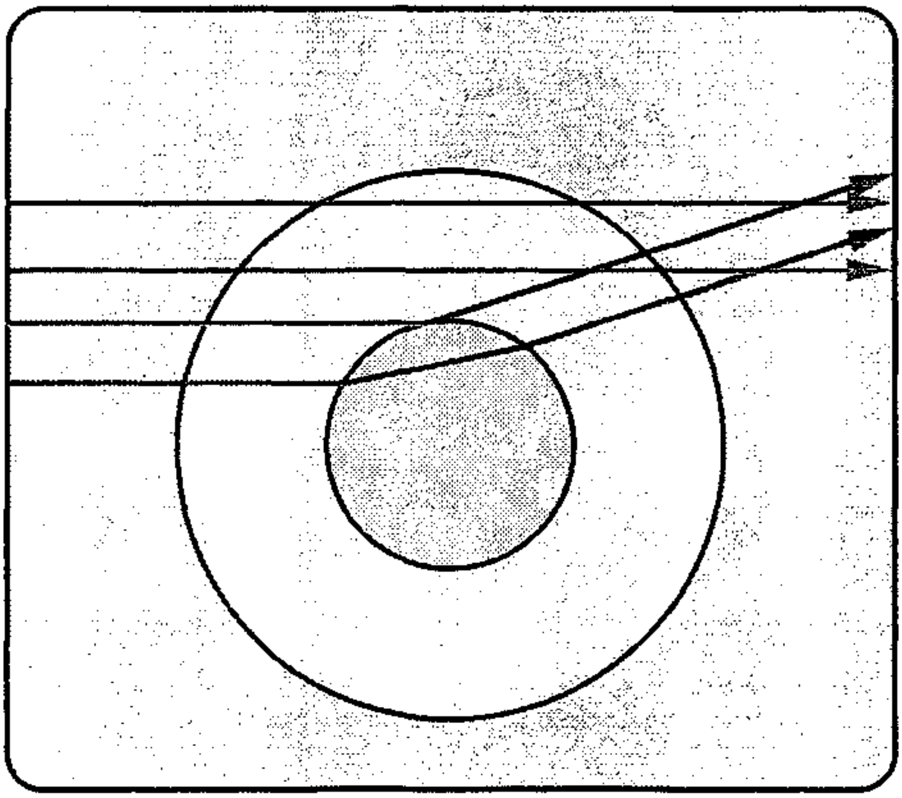

Anal. Chem. 1991, 63, 2689–2697

On-Column Laser-Based Refractive Index Detector for Capillary Electrophoresis

Alfredo E. Bruno,* Beat Krattiger, François Maystre, and H. Michael Widmer

CIBA-GEIGY Ltd., Analytical Research, CH-4002 Basel, Switzerland

The interference pattern from side-illuminated capillary tubes has been exploited to develop a sensitive universal refractive index (RI) detector suitable for nanoliter on-column capillary separation techniques. A 2-fold benefit is obtained by surrounding the capillary tube with a RI-matching fluid: the fringe pattern is simplified, and thermal noise is reduced. The key to RI detection in CE, provided that the instrument delivers sufficient sensitivity, has been found to be thermal stability. A thermal stability of $\Delta T = 2.0 \times 10^{-4}$ °C is achieved in a Peltier cooled RI cell having a highly symmetric design aimed to ensure fast thermal response from the thermoelectric system. The linear dynamic range extends to more than 3 orders of magnitude with a typical RMS noise level of 3×10^{-8} RIU and baseline drifts of 2×10^{-6} RIU h^{-1} at 1 Hz. This is about 1 order of magnitude above the calculated shot noise limit for these tube dimensions. These noise levels correspond to an angular deflection of the selected fringe of 100 nrad, which has been obtained by using a large position-sensitive photodiode. The optical geometric arrangement of the photodiode, with respect to the fringe width, has been optimized theoretically. A detailed description of the instrument and its noise sources is presented, and the technique is demonstrated in CE in the analysis of underivatized carbohydrates using a 50-μm tube.

INTRODUCTION

Capillary electrophoresis (CE) is undoubtedly *the trend* in liquid-phase chemical analysis. Several features including speed of analysis, high resolution, and efficiency account for the present acceleration in the acceptance of this technique. High electric fields are used in CE to force ionic solutes to migrate through a buffer- or gel-filled capillary. The species, injected in minute amounts, are separated along the tube on the basis of charge, size, or both (*1, 2*) and are subsequently detected near the capillary end. The various forms of this technique, capillary zone electrophoresis (CZE), isothachophoresis (ITP), micellar electroosmotic chromatography (MECC), and capillary gel electrophoresis (CGE), have been successfully demonstrated in the analysis of pharmaceuticals, peptides, proteins, carbohydrates, oligonucleotides, subcellular structures, and even whole cells (*3–10*).

Various instrumental aspects contribute to the overall performance in CE. Detection, being perhaps the most important one, is most conveniently carried out using optical methods. The benefits observed when the inner diameter of the capillary is reduced are compromised in the detection stage when path length dependent optical schemes are used (*11, 12*). There is therefore a growing demand to improve the sensitivity of known detection systems or to develop alternative ones. Primarily because of their spatial coherence, lasers have led to the development of a series of novel capillary detectors featuring impressive detection limits (*13*).

In order to preserve the spatial profile of the eluting substances achieved in high-performance separations, only on-column detection (*11*) is meaningful in CE. The most popular detection scheme used in CE is UV/vis absorption (*14–16*). It is accomplished by modifying a conventional absorbance photometer using optical fibers or masking the optical path with a pair of slits (*11*). However, nonlinear responses for absorbance vs concentration curves are not uncommon (*11*). These are due to stray light and/or changes in the refractive index (RI) of the mobile phase due to solute concentration, pressure gradients, etc., which alter the optical path and lead to unwanted dynamic effects. For absorption measurements in narrow-bore capillaries, crossed-beam thermooptical (CBTO) absorption techniques (*17*) offer definite advantages. An interesting feature of CBTO is that as the capillary's diameter is reduced, the pumped heat is more efficiently quenched at the walls and high electric fields can be applied along the tube for faster separations (*12*).

Laser-induced fluorescence (*15*) (LIF) is the most sensitive detection method devised to date. However, because only a few molecules of interest fluoresce at available laser lines, rather complicated precolumn derivatizations (*16*) are required.

Much stricter conditions than those required for example in liquid chromatography (HPLC), are to be met when designing a detector for CE. Therefore, not all detection schemes of standard use have been made available to CE. Bulk RI detection, unavoidable when the substances of interest neither absorb nor fluoresce, is a typical example. Joule heat poses the major challenge in the development of a RI detector suitable for CE. Since most applications require a sensitivity below $\Delta n = 10^{-6}$ RIU (RI units, n is the RI of the mobile phase) and the change in RI with the temperature (dn/dT) for most solvents is of the order of 10^{-4} RIU/K at room temperature, thermal stability becomes the limiting factor in the quest for lower detection limits.

A RI detector, whose operational principle is based on the interference pattern arising from side-illuminated fused-silica capillaries, demonstrated in HPLC by Bornhop and Dovichi (*18–20*), has shown promising results. An insightful theoretical analysis was later given by Synovec (*21*), and various refinements, aimed to adapt the technique to CE, was subsequently published (*22–24*).

The approach given by Chen et al. (*22*), to overcome thermal fluctuations inside the capillary in CE, was to partially modulate the electric fields in a so-called analyte velocity modulation method. The sensitivity of this detector appears to be comparable to those attained with other methods (*23, 24*), but much instrumental work and applications are awaited to fully appreciate the benefits of this technique.

Pawliszyn (*23, 24*) proposed a concentration gradient differential detector based on Schlieren optics which is rather insensitive to thermal fluctuations inside the capillary suitable for ITP. However, as, in this method, one obtains the first derivative of the signal, it is necessary to integrate the output signal to reconstruct the electropherogram, and the optical arrangement needs to be optimized for each separation system.

---

* To whom correspondence should be addressed.

0003-2700/91/0363-2689$02.50/0

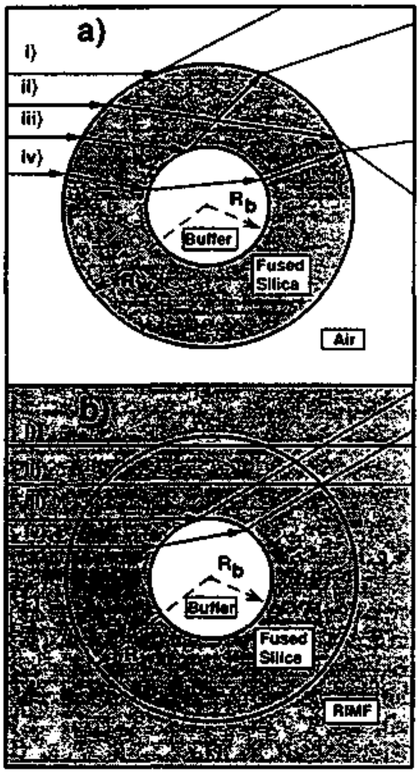

Figure 1. Capillary tube cross section and corresponding ray-tracing diagram for four significant rays: (a) capillary surrounded with air. (b) capillary surrounded with RIMF. Reflections and refractions at the different interfaces are indicated as arrows. The different n values of the propagating media are represented by the density of the pattern; e.g. air [n = 1.00] has no associated pattern, water (n = 1.333) has a lighter dotted pattern, and fused silica (n = 1.467) and RIMF (n = 1.467) are represented by identical darker patterns.

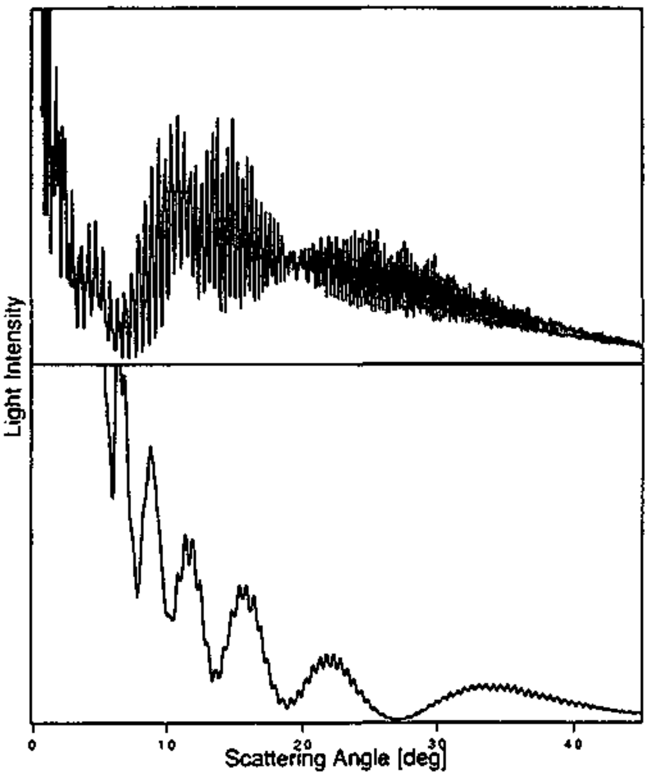

Figure 2. (Top) forward scattering fringe pattern of a water-filled silica capillary having i.d. = 50 μm and o.d. = 365 μm side-illuminated with a He–Ne laser beam. (Bottom) fringe pattern for the same capillary immersed in RIMF. The scattering angle ϕ = 0° corresponds to the optical axis. The residual high-frequency intensity modulation in the bottom figure is most likely due to a slight mismatch of the RIMF caused by temperature differences.

In this contribution we describe a RI detector based on the design originally proposed by Bornhop et al. (*18–20*). In the present instrument we introduce the use of index-matching fluids (RIMFs) and position-sensitive photodiodes (PSDs), in conjuction with thermoelectric stabilization, integrated into a compact, highly symmetric RI cell design. A detailed analysis of the noise sources, with emphasis in the shot noise and the noise due to thermal fluctuations, is made and used to improve the detector. In addition, we present a model to study the interference pattern produced by the capillary. The improvements obtained in the overall detector performance are demonstrated in the CE separation of synthetic underivatized saccharide mixtures. Considering their importance in biochemistry, food science, etc., sugar mixtures were chosen to demonstrate the new technique. Also, it has been recently shown (*16, 25–28*) that CE represents an alternative to other traditional (*29*) and electrophoretic methods (*30–32*) used in the analysis of sugars.

THEORY

Index-Matched Capillary Walls. The present detection method takes advantage of the light interferences, typical of side-illumination of liquid-filled capillary tubes by laser light (*18–20*), to measure changes in the RI (Δn) of the effluents. As in the case of optical fibers (*33*), when coherent light strikes a capillary transversaly, the light is scattered over 360° in the plane perpendicular to the capillary axis. The resulting fringe pattern is characteristic of the capillary dimensions, RI of the propagating media (i.e. capillary wall and orifice), focusing properties of the beam, and light polarization. As shown in Figure 1, depending on their incident position and angle, the light rays either (i) are reflected at the outer capillary surface, (ii) enter the capillary, propagate through its wall, and emerge without intercepting the inner bore, (iii) are reflected at the inner capillary wall/liquid interface, or (iv) propagate through both the capillary wall and bore. Hence, the interference pattern is produced by four types of scattered rays, and therefore is rather complex, as shown in Figure 2 (top). Some of the fringes change their position as a consequence of changes in the RI of the effluent. The angular shift of the fringes, due to refractions and changes in the optical path of the rays (*34*), are used to measure the effluent's Δn. Without index-matching fluid around the capillary, it is difficult to select a sensitive fringe which also has a high contrast. In addition, only a very small fraction of the total optical power is available in every fringe and sharp fringes led to a narrow dynamic range of the detector in question. It is thus desirable to simplify the fring pattern in order to select the fringe which shifts the most for a given Δn and to direct the optical power into these fringes.

Simplification of the fringe pattern is achieved here by immersing the fused-silica (FS) capillary in a transparent liquid (RIMF) having the same index of refraction as the capillary wall (i.e n = 1.4587 at T = 25 °C for λ = 632.8 nm). This technique is routinely used to measure the core dimensions of optical fibers (*33*). In this way, the reflections and refractions at the external capillary wall (i.e. type i rays) are eliminated according to basic optical principles (*34*). The overall pattern is dominated by interferences between the rays of type iii and iv, as illustrated in Figure 1b. The total number of refractions and reflections, indicated by arrows in the figure, is dramatically reduced from 10 to 3, resulting in a much simpler interference pattern, as shown in Figure 2 (bottom).

Modeling of the Interference Pattern. Computer simulations have been used to predict the fringe shifts per Δn and thus to maximize the sensitivity of the instrument. The profile of the whole interference pattern, for the simplified case in which the capillary is immersed in RIMF and has an i.d. greater than 30 μm, can be quantitatively described by

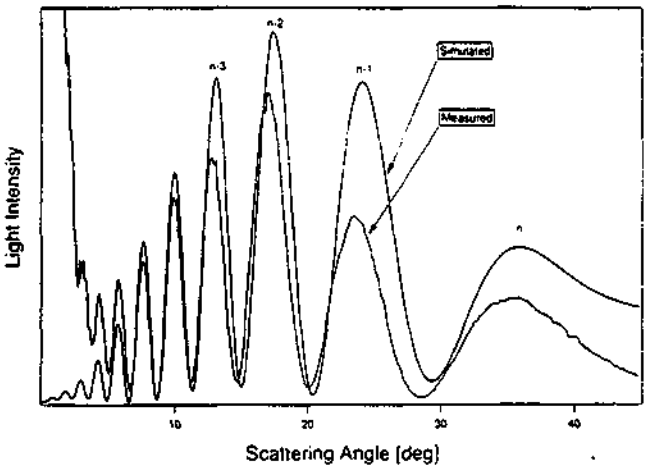

Figure 3. Measured and simulated interference fringes for an i.d. = 50 μm capillary immersed in RIMF. Fringes are arbitrarily labeled starting with n, which is the last well-defined and easily identified fringe from the optical axis.

Table I. Shot Noise Limits for Different Fringes of the Scattering Pattern[a]

fringe no.	$n - 1$	$n - 2$	$n - 3$	
position	24	16	12	deg
ang shift	−223	−200	−172	deg/Δn
4σ	7.7	5.3	3.2	deg
P_{opt}	25*	25*	10*	μW
δ_{sn}	3.4×10^{-8}	2.3×10^{-8}	2.2×10^{-8}	rad
Δn_{sn}	8.7×10^{-9}	6.6×10^{-9}	7.3×10^{-9}	

[a] These values are typical for an i.d. = 50 μm i.d. capillary filled with water and illuminated by a 2-mW He–Ne laser (λ = 633 nm). The detection bandwith is assumed to be B = 1 Hz. The values quoted with an asterisk are measured data.

a ray-tracing model which does not take into account diffraction effects.

In the present optical configuration the capillary behaves as a pseudo Mach–Zehnder interferometer and the fringes are thus the result of interactions between two rays. The *reference* beam (ray iii in Figure 1b) strikes the wall/buffer interface at an angle greater than critical (α_{crit} = 66°) and is totally reflected. The *sampling* beam (ray iv in Figure 1b) propagates through the capillary bore where it is refracted twice at the wall/buffer interfaces (Figure 1). Both rays propagate through different optical paths, and as they recombine in the far field, they form the observed interferences. Depending on whether the optical path difference between the reference and sampling ray is an integer multiple or an integer multiple plus one half of the wavelength, constructive and destructive interferences occur (*33, 34*).

A computer program based on classical optics (*34*) has been developed and was used to select a priori the most sensitive fringe to Δn, for a given capillary diameter, known polarization, and intensity distribution of the incoming beam, for each ray. For each scattering direction the algorithm computes the associated trajectories of both rays and therefore their intensities and relative phase differences. The far-field distribution is computed by making use of coherent superposition of rays, assuming that the incident beam is a bundle of parallel rays with a Gaussian intensity profile. A typical result of the measured and computed interference patterns for a 50-μm capillary is shown in Figure 3, and significant results are summarized in the upper part of Table I.

Thermal Analysis. Once the problems associated with the selection of a monitoring fringe have been solved, the thermal instability in the capillary is the limiting factor in the quest for maximum detection sensitivity, at least in CE. In this regard, an additional benefit is observed when surrounding the capillary with RIMFs, i.e. the possibility to further stabilize the temperature inside the capillary in the detection region. Because the thermal conductivity coefficients of liquids are about 20 times larger than that of air, the surrounding RIMF acts as an efficient heat sink.

Table II. Definitions (Reproduced from Reference 38) and Values of Dimensionless Variables for a Fused-Silica Capillary (i.d. = 50 μm and o.d. = 365 μm) Cooled by Naturally Convecting Air and by a Surrounded Liquid (RIMF) in Contact with a Thermoelectric Cooling System

		convecting air	RIMF
$\theta = (T - T_0)/\Delta T_{ref}$	dimensionless temp	1.102[a] 0.843[b]	40.20[a] 39.66[b]
$\eta = r/R_B$	dimensionless radial coordinate	r/25	r/25
$\Delta T_{ref} = \kappa_0 E^2 R^2{}_B/k$	characteristic temp rise	0.64[c]	0.64[c]
$\lambda = \sqrt{\kappa_1 \Delta T_{ref}}$	autothermal param	0.172[d]	0.172[d]
$Bi_{0A} = h_{0A}R_B/k$	overall biot no.	0.055[e]	1.22[f]
$f(\lambda)$		0.457[g]	0.968[g]

[a] Computed with eq A-1, at r = 0 μm. [b] Computed with eq A-1, at $r = R_b$ = 25 μm. [c] κ_0 = 1 S/m, $k_{[H_2O]}$ = 0.61 W m^{-1} K^{-1}, E = 250 V cm^{-1}. [d] κ_1 = 0.046 K^{-1}, from ref 38. [e] Typical value, taken from ref 38. [g] Computed using eq A-2.

The support buffer in the capillary, which has an associated electrical resistance of $R = U/I$ dissipates a considerable amount of heat, up to P = 1.3 W in the present case, resulting in various negative side effects in CE. The thermal Joule effect associated with CE and its consequences to column efficiency have been thoroughly studied (*35–40*). Of relevance to this study are a detailed knowledge of the temperature profile in the capillary bore as a function of radial position and the total difference in temperature between the center of the capillary (hottest region) and its surrounding at the detection part of the tube.

In the absence of the polyimide coating, which was removed in the detection region and under the assumption that the only heat source is the electrical current circulating in the buffer (e.g. there is no absorption of the laser light in the detection volume), the total temperature change from the center of the capillary to the surrounding thermal bath ΔT_{total} can be subdivided into

$$\Delta T_{total} = \Delta T_b + \Delta T_w + \Delta T_{sur} \qquad (1)$$

where ΔT_b is the temperature drop in the bore, ΔT_w in the wall, and ΔT_{sur} in the surrounding bath.

The temperature distribution $T(r)$ is known (*35*) to be approximately parabolic across the bore and logarithmic across the silica wall and in the immersion bath. According to the theory of Grushka et al. (*36, 37*), the temperature profile $T(r)$ within the capillary satisfies

$$k \frac{1}{r} \frac{d}{dr} r \frac{dT}{dr} = -E^2 \kappa \qquad (2)$$

where E is the applied electric field, k is the thermal conductivity of the buffer, and κ is its electrical conductivity.

Exact solutions to eq 2 in the capillary bore have most recently been proposed in terms of the dimensionless variables θ, ΔT_{ref}, λ, η, Bi_{0A}, and ΔT_b, defined and computed in Table II, by Gobie and Ivory (*38*). In this formalism, ΔT_b can be obtained by integrating eq 2 with the appropriate boundary conditions in the capillary bore (i.e. from r = 0 to $r = R_b$, in Figure 1) and reads

$$\Delta T_b = \theta \Delta T_{ref} \qquad (3)$$

Details on the evaluation of the dimensionless temperature θ and on the characteristic temperature raise, ΔT_{ref}, are given

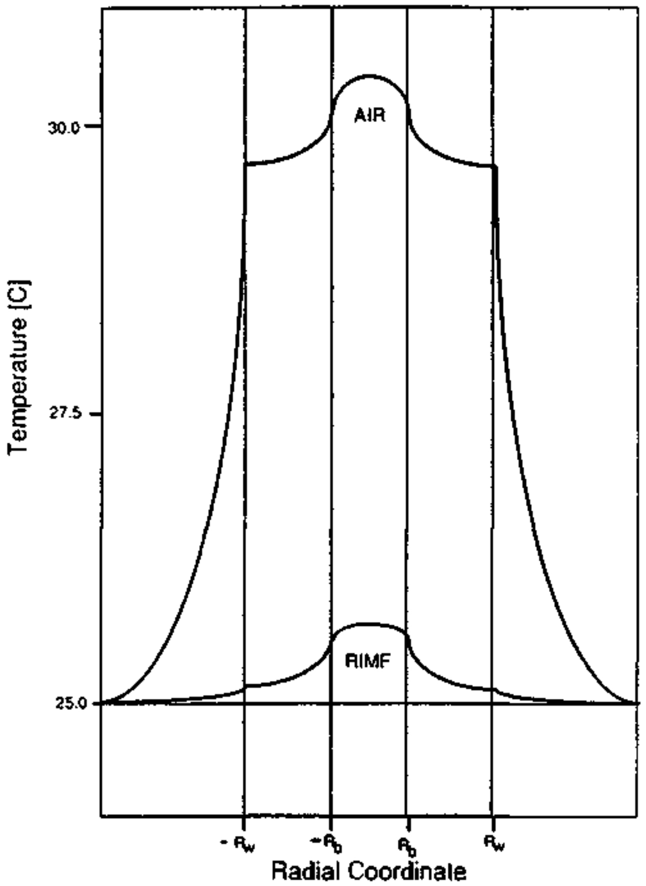

Figure 4. Temperature profile as a function of the radial coordinate in the capillary bore and fused-silica wall (i.d. = 50 μm, o.d. = 365 μm) and surrounding media for a capillary filled with an aqueous solution and immersed in RIMF (lower trace) and cooled by naturally convecting air (upper trace). Both profiles have been computed as explained in the text.

in the Appendix, and the results are reported in Table II. It is found that $\Delta T_b = 0.350$ °C when the capillary is surrounded by air and $\Delta T_b = 0.165$ °C when the capillary is surrounded by RIMF.

The temperature drop in the capillary wall ΔT_w can be computed with

$$\Delta T_w = \frac{EI}{2\pi}\left[\frac{1}{k_w}\ln\frac{R_w}{R_b}\right] \tag{4}$$

where I is the electrical current and k_w is the thermal conductivity of the capillary wall. Equation 4 has been derived from eq 3 in ref 37, by ommiting the term representing the temperature drop in the polyimide coating. Setting $R_w/R_b = 7.5$ as well as the other experimental values (see Experimental Section) in eq 4, it is found that $\Delta T_w = 0.305$ °C for both cases considered—air- and RIMF-cooled capillaries.

Finally, to compute the temperature drop in the RIMF bath, we follow the approach used by Nelson et al. (*40*) to tackle a similar problem. Accordingly (*40*), ΔT_{sur} is given by

$$\Delta T_{sur} = EI/2\pi hR_{sur} \tag{5}$$

where R_{sur} is the radius of the surrounding bath. Using the values (*40*) of $h = 2600$ W m^{-2} K^{-1} for RIMF, $h = 70$ W m^{-2} K^{-1} for air and taking $R_{sur} = 1$ mm, one obtains $\Delta T_{sur} = 0.125$ °C in the RIMF and $\Delta T_{sur} = 4.63$ °C in air.

ΔT_{total} (eq 2) is computed using the values above for ΔT_b, ΔT_w, and ΔT_{sur}. Finally, the total temperature drop from the center of the capillary to the surrounding media is, for the RIMF-thermocooled case, $\Delta T_{total} = 0.60$ °C and, for the naturally convecting air case, is $\Delta T_{total} = 5.29$ °C. Adding to these values the temperature at which the thermocooler operates (i.e. typically 25 °C), one obtains the value of the temperature at the center of the bore. For the RIMF-cooling case it is found that at the center of the bore $T(r = 0) = 25.60$ °C and for the naturally convecting air-cooled case $T(r = 0) = 30.28$ °C. A summary of the temperature calculations is presented in Table III. Temperature gradients and thus thermal noise are localized in the neighborhood of the inner and outer capillary wall interfaces (Figure 4).

Table III. Temperature Variations (°C) across a Capillary Tube Cooled by Naturally Convecting Air and by a Surrounded Liquid (RIMF) in Contact with a Thermoelectric Cooling System[a]

	ΔT_b	ΔT_w	ΔT_{sur}	ΔT_{total}	$T(r = 0)$
air	0.350	0.305	4.631	5.286	30.28
RIMF	0.165	0.305	0.125	0.595	25.60

[a] Capillary dimensions i.d. = 50 μm and o.d. = 365 μm, applied electric field E = 25- V cm^{-1}, current = 57 μA.

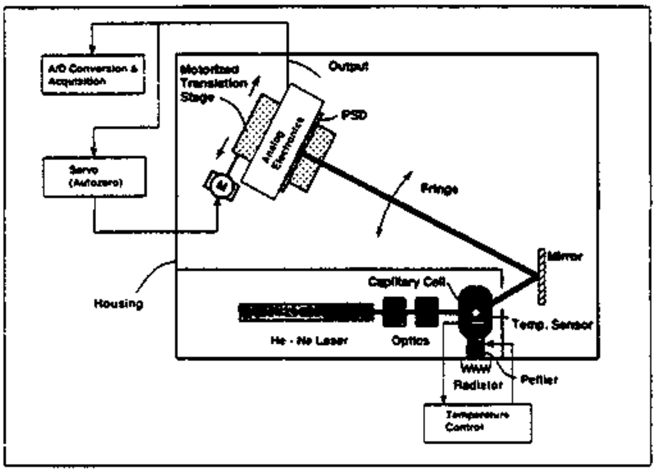

Figure 5. Instrumental optomechanical arrangement of the capillary refractive index detector.

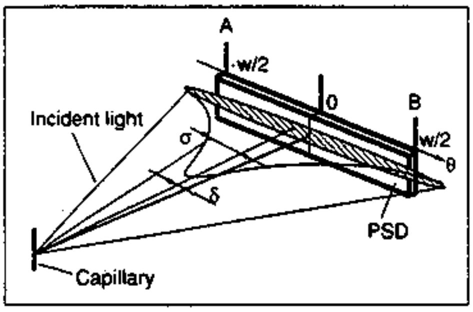

Figure 6. PSD geometric arrangement used to measure the fringe deflection angle δ. The width of the PSD is *w* and the fringe angular spread (spot size) is σ. A null signal is produced when the center of gravity of the fringe is centered on the PSD.

Position-Sensitive Diode (PSD). A Δ*n* in the capillary bore results in an angular displacement of the scattering fringes. The shift of a selected fringe is measured with a PSD which, upon calibration, gives an electrical signal proportional to Δ*n*. Although most high-resolution position sensors are built with dual photodiodes (*23, 24*), for this experiment, PSDs were found to be quieter, especially at frequencies below 1 Hz; most certainly due to the fact that PSDs are made of a single silicon chip and therefore their characteristics are constant over the whole device (*41–43*). Moreover, state of the art PSDs are known to have good linearity and low dark current properties which make them attractive for applications requiring very high resolution (*44*).

The optical arrangement which has been used to measure fringe shifts is shown in Figure 5. The light from one fringe is directed to the detector and forms an elliptical spot whose center of gravity is centered on the detector (Figure 6). As the spot moves across the active area, output currents I_A and I_B are generated which are proportional to the distance between the location of the center of the spot and the end contacts of the detector (*44*). To produce a signal with zero output for a centered spot, which in addition cancels the intensity fluctuations of the light (e.g. due to laser noise), the complementary outputs currents of the detector are wired to yield

$$V(\delta) = \frac{I_A - I_B}{I_A + I_B} \tag{6}$$

The angular resolution of the detection scheme depends on the width of the selected fringe as well as on the ratio of the PSD width to the spot size. This ratio is given by the distance from the capillary to the actual PSD location. In order to determine the geometric configuration which would render the highest sensitivity and to calculate the value of the shot noise limited angular shift, the following analysis is made.

For a narrow light spot at a distance δ away from the center of the detector (Figure 6), the difference between the two photocurrents, as obtained after the substraction in the PSD circuit, is (*43, 44*)

$$I_A - I_B = I(\delta) = sP_{opt}\frac{2}{w}\delta \tag{7}$$

where w is the PSD width, P_{opt} is the total optical power within the spot, and s is the spectral sensitivity of the detector (i.e. $s = 0.35$ A W^{-1} at $\lambda = 633$ nm for the Hamamatsu S1352 employed (*41*)). If the light intensity is distributed over the whole surface of the detector rather than on a point (Figure 6), the detector response can be calculated by adding the contributions of each point (*44*). For a normalized Gaussian distribution having a width σ and with the center of gravity at position δ, it can be shown that

$$I(\delta) = sP_{opt}\int_{-w/2}^{w/2}\frac{2\theta}{w}\frac{1}{\sigma\sqrt{2\pi}}\exp\left[-\frac{1}{2}\left(\frac{\theta-\delta}{\sigma}\right)^2\right]\mathrm{d}\theta \tag{8}$$

Furthermore, it can be verified that for small angular displacements (i.e. $\delta \ll w$) around $\delta = 0$, the sensitivity can be expressed as

$$\frac{\mathrm{d}I}{\mathrm{d}\delta} \cong G(a,\sigma) = sP_{opt}\frac{1}{\sigma\sqrt{2\pi}}\left[\int_{-2\sigma/a}^{2\sigma/a}\frac{a}{2\sigma}\exp\left[-\frac{1}{2}\left(\frac{\theta}{\sigma}\right)^2\right]\mathrm{d}\theta - \exp\left[-\frac{1}{2}\left(\frac{2}{a}\right)^2\right]\right] \tag{9}$$

where $a = 4\sigma/w$ is the *aspect ratio* of the spot size to the detector width. Figure 7 shows that the behavior of the sensitivity G and of the relative sensitivity σG vary according to eq 9. The curve for the relative sensitivity displays an almost linear increase near zero followed by an exponential decay for large values of the *aspect ratio*. These results indicate that in order to obtain the best performance, the PSD must be operated at a distance from the capillary where the selected fringe and the detector width leads to an aspect ratio of $a \cong 0.9$.

Shot Noise. Among all the phenomena which limit the smallest measurable angular shift, shot noise sets an ultimate limit which is given by the nature of light itself. The shot noise limit therefore constitutes a valuable benchmark and allows the determination of the margin left for the improvement of the optical detector.

To calculate the shot noise limit for the present optical configuration, it is assumed that the angular position of the selected fringe moves sinusoidally about the center position with an amplitude δ and at a frequency Ω. The expression for the output detector signal can be derived from eq 9 as

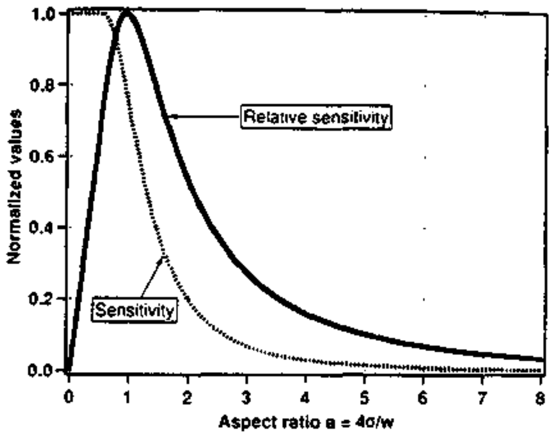

Figure 7. Theoretical sensitivity of a PSD detector for a Gaussian spot as a function of finite width.

$$I(t) = sP_{opt}0.37\frac{1}{\sigma}\delta\sin(\Omega t) \tag{10}$$

where the factor 0.37 arises from the evaluation of the maximum sensitivity (in eq 9). The corresponding signal power is therefore

$$\langle I^2(t)\rangle = \frac{1}{2}\left(0.37sP_{opt}\frac{1}{\sigma}\right)^2\delta^2 \tag{11}$$

The power spectrum of the shot noise is known to be white (i.e. flat) and its density $\langle I_{sn}^2\rangle$ is proportional to the optical power reaching the detector (*45*). To take into account that both the $(I_A - I_B)$ and $(I_A + I_B)$ outputs generate independent noise contributions to the useful signal (eq 10), the total shot noise power becomes

$$\langle I_{sn}^2\rangle = 4BesP_{opt} \tag{12}$$

where B is the detection bandwidth and e is the elementary charge. Shot noise limited detection is reached when the signal power (eq 11) equals the shot noise power (eq 12), i.e.

$$\left(\frac{\delta}{\sigma}\right)_{sn} = 2\sqrt{Be2\frac{1}{s}\frac{1}{P_{opt}}7.11} \tag{13}$$

Substituting in eq 13 typical values for this experiment (e.g. $B = 1$ Hz, $s = 0.35$, and $P_{opt} = 25$ μW), one obtains $(\delta/\sigma)_{sn} = 1 \times 10^{-6}$. Furthermore, eq 13 is used to compute the shot noise limits associated with various fringes employed in the present measurements (Table I). It is found that shot noise limits are very similar for the last three fringes ($n - 1$, $n - 2$, and $n - 3$) with associated values which are only 1 order of magnitude smaller than the measured noise value of $\Delta n = 2.5 \times 10^{-8}$ (see Results). For optical powers below about 10 μW, the thermal noise level of the electronics becomes comparable to the shot noise, and therefore would set new detection limits.

EXPERIMENTAL SECTION

RI Cell. The best thermal stability in the cell is achieved when the thermocooler system is set at a temperature slightly higher than ambient. The resulting ca. 1 °C temperature gradient is localized near the cell windows and is directly correlated to a n gradient in the RIMF and fused silica according to their dn/dT thermal coefficients. Small fluctuations in the temperature around the exit air/window/RIMF interface, in contact with the environment, introduce an additional source of noise if a flat exit window is employed.

In a cell constructed with two plane parallel windows, the incoming laser beam crosses the entrance air/window/RIMF interface at 90°, and the n gradient does not alter the light-propagating path (i.e. no refraction). However, at the exit window,

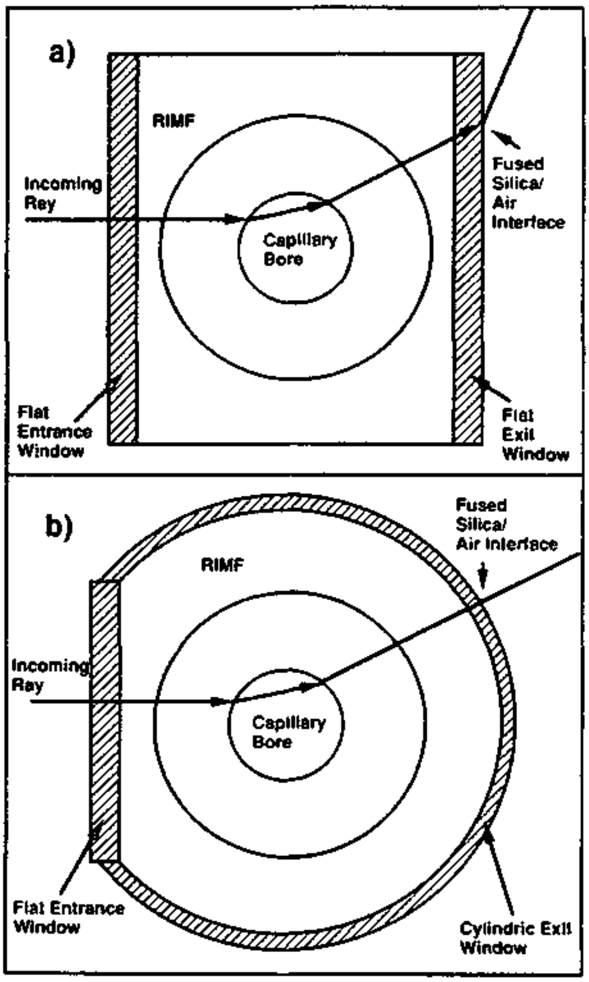

Figure 8. Ray path of a significant ray crossing a RI cell fitted with two flat windows (a) and crossing a cell having a flat entrance window but a cylindric exit window coaxially placed to the capillary axis (b). Refractions are indicated as arrows.

the rays are scattered at all angles and the propagating ray is refracted as it crosses this last interface, as illustrated in Figure 8a. Small fluctuations in the temperature around this interface, which is in contact with the environment, cause the rays to change their paths and introduce additional noise.

This source of noise was eliminated by replacing the flat exit window with a cylindrical one, placed coaxially with respect to the capillary tube, as indicated in Figure 8b. In this optical arrangement the scattered rays cross the exit window perpendicularly, independent of their scattering angles, thus avoiding refraction.

The design of the cell takes into account the effects discussed above. The capillary tube and the flat entrance window are mounted and sealed with a pair of "O" rings and screws whereas the cylindrical exit window is epoxied to the cell body. The capillary is coiled into a groove around the external part of the aluminum block before it enters the chamber filled with RIMF after crossing a region in contact with the Peltier element. The Peltier element (Melcor, FC 06.6605L) is in contact with the capillary tube 5 mm before it enters the chamber filled with RIMF. A calibrated thermistor (ILX Lightwave DL 890884) is placed on the opposite side of the thermocooler, in close contact with the capillary tube in a small hole in the aluminum block. Both elements are driven by a thermoelectric system (ILX Lightwave Model LDT-5412). When no electrical current flows through the buffer, the short-term thermal stability ($\tau = 1$ s) of the system is better than 2×10^{-4} °C and has a typical drift of less than 1×10^{-2} °C h^{-1}.

A good RIMF should have a refractive index as close as possible to the value of the FS, have a small dn/dT coefficient, not be photodegrade, and have a good transmittance. We employed a commercial RIMF oil (Nos. 19569 and 19571, R. P. Cargille Laboratories Inc., Cedar Grove, NJ) having $n = 1.4571$ and $dn/dT = 3.86 \times 10^{-4}$ RIU K^{-1} at 25 °C.

RI Detector. A diagram of the experimental setup is shown in Figure 5 and has been constructed using commercial parts (Spindler & Hoyer, Germany).

A very important aspect to be considered in the overall design of the instrument is that the RI detector measures Δn originated not only at the capillary bore but at any point of the optical path from the laser output coupler to the PSD. The laser (Uniphase No. 1103P), optical isolator (constructed with a polarizing filter and a $\lambda/4$ plate, Dr. Steeg & Reuter, Germany, Nos. 011110 and 042005, respectively), focusing optics, and cell are therefore mounted on four sliding stainless steel rods (S & H No. 061216) in contact with each other to prevent air flows in the beam path. The laser beam has a diameter of 600 μm and is focused into the capillary bore with a $f = 40$ cylindrical lens producing a beam waist of ca. 23×600 μm in the capillary bore. The cell volume, defined by the capillary i.d. and the beam waist, for a 50 μm i.d. tube is 1.2 nL. The fringe selected for the measurement is directed onto the PSD (S1352, 2.5×34 mm, Hamamatsu, Japan) using a mirror. An autozero for the instrument is constructed by feeding the output of the PSD into a servo system (No. MMC-QR-030024-02LD-00A, Maxon Motor, Switzerland) which drives the PSD to the desired position by means of a DC motor (No. 2230F0112S, Faulhaber, Germany).

Capillary Electrophoresis. The Ce results reported here have been performed in an i.d. = 50 μm, o.d. = 365 μm fused-silica capillary (Polymicro Technologies, Phoenix, AZ) where 5 mm of the polyimide coating were removed for detection. The home-built CE apparatus has been previously described (*10, 12*). Data acquisition was performed with the Nelson software package (Perkin-Elmer, Switzerland) on an IBM AT computer.

The chemicals needed for the preparation of the electrolyte solutions were purchased from Merck (Darmstadt, Germany) and the carbohydrates from Fluka (Buchs, Switzerland).

RESULTS

The overall sensitivity of the RI detector depends mainly on the size of the capillary tube employed and to a less extent on the fringe selected for the measurement. For the 50-μm capillaries and a time constant of $\tau = 1$ s ($B = 1$ Hz) the short-term RMS noise (i.e. "grass") is 2.5×10^{-8} RIU corresponding to a thermal stability of 2.5×10^{-4} °C computed with the Nelson software (Figure 9). With only the inherent time constant of the PSD amplifiers (i.e. $\tau < 1$ ms), the noise level rises to 1.8×10^{-7} RIU. In both cases, the baseline drifts are about 2×10^{-6} RIU h^{-1}. These performances were obtained using the RI detector in a flow injection analysis mode (FIA) under constant, pressure-induced flow conditions using the fringes labeled ($n - 1$) and ($n - 2$) in Figure 3 appearing at 24 and 16° from the optical axis. These fringes shift 210 ± 10°/RIU (Table I). Combining this information with the noise levels, it is found that the fringe deflection stability of the apparatus is 100 n-radians (6 μ-deg).

For the typical widths of the selected fringes, the optimum working distance from the capillary for the PSD is approximately 28 cm (see Position-Sensitive Diode subsection). In this position the minimum measured angular deflection of 100 nrad corresponds to a position resolution capability of 3×10^{-2} μm or 1 order of magnitude better than the manufactured specification (*41, 42*), which is 1 μm.

Unfortunately, in CE one cannot make full use of the above reported sensitivities because of the heat produced by Joule effect. The degrading effect that voltage and current have in terms of baseline drift can be seen in Figure 10. Although the short-term noise does not significantly degrade with increasing E and I, the baseline medium term drift (i.e. $\tau = 1$ min) degrades at a rapid pace and, at currents higher than 60 μA, the noise reaches a level unacceptable for CE experiments.

The linear dynamic range of the apparatus extends from the achieved sensitivity up to 10^{-3} RIU, which corresponds to 4 orders of magnitude in the present case. This has been

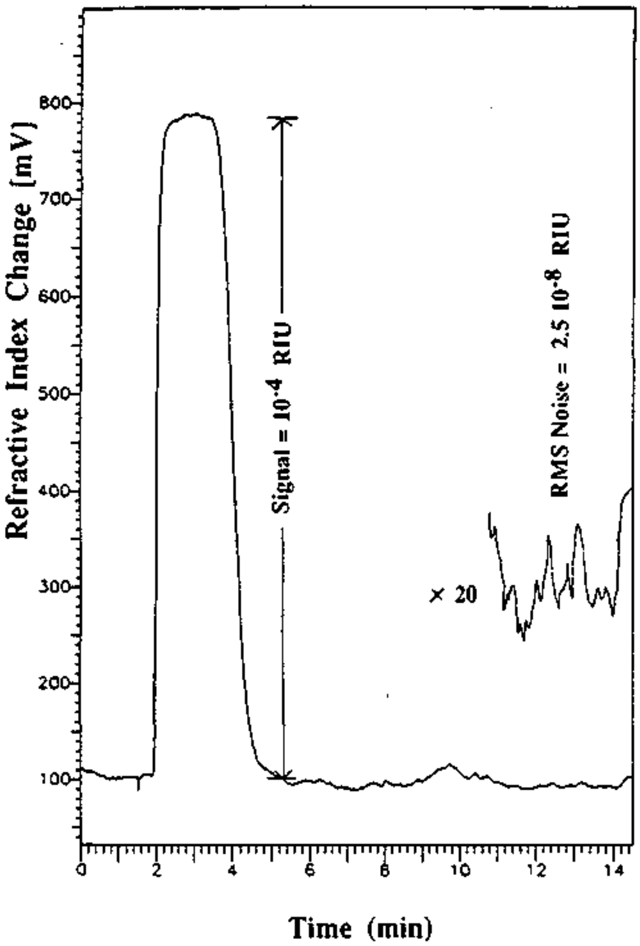

Figure 9. Sensitivity performance of the RI detector operator in the FIA mode with an i.d. = 50 μm capillary. The peak corrasponds to an injection of 0.5 μL of saccharose aqueous solution calibrated to produce a $\Delta n = 1.0 \times 10^{-4}$ RIU.

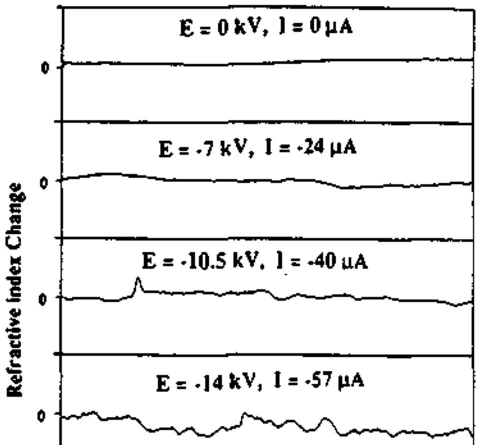

Figure 10. Degradation of the baseline of the RI detector in the CE mode with increasing voltage (E) and current (I).

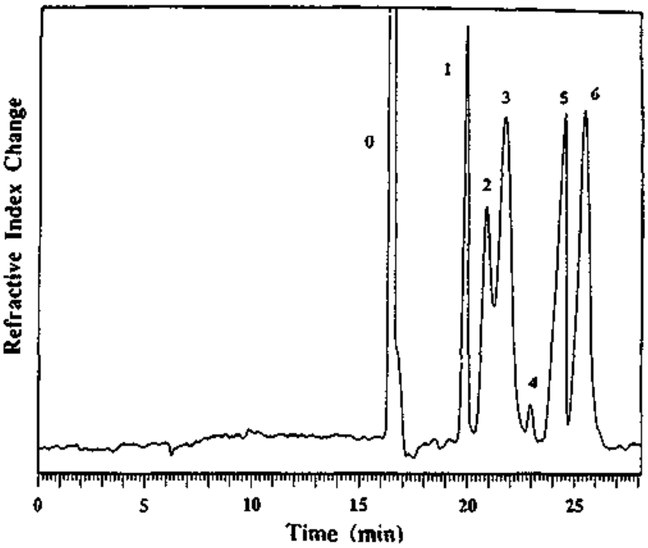

Figure 11. Electropherogram of a mixture of five underivatized saccharides. The peaks are identified as buffer (0), saccharose (1), *N*-acetylglucosamine (2), cellubiose (3), impurity (4), *N*-acatylgalactosamine (5), and lactose (6). Conditions: each 1% except for saccharose, 0.5%; buffer 100 mM tetraborate, pH 9.; capillary length 70 cm, 55 to detector; i.d. = 50 μm; CE voltage, 14 kV; current, 50 μA; injection time 7 s at 12 kV; thermocooler temperature 27 °C; interference fringe, $n - 2$.

determined from a double logarithmic plot of output signal vs RI constructed using saccharose solutions having concentrations ranging from 58 μM to 150 mM (2×10^{-3}% to 5% w/v) operating the instrument in the FIA mode ($R = 1.000$). The lowest measured detection limit for saccharose at $S/N = 2$ is 10 μM. At $\Delta n > 10^{-3}$ RIU, the fringe selected for the measurement "walk away" from the PSD and strong deviations from linearity are observed.

An electropherogram of a mixture of five underivatized saccharides is shown in Figure 11. The first peak (0), appearing at $t = 16$ min, results from the difference in the n values of the buffer and the sample and serves as an electroosmotic flow rate marker. The remaining peaks correspond to saccharose (1), *N*-acetylglucosamine (2), cellobiose (3), *N*-acetylgalactosamine (5), and lactose (6); peak (4) is an impurity. The injected volume is 6.6 nL corresponding to 33 ng of saccharose and similar amounts for the other species.

Most sugars are neutral species and therefore not eligible for CE. This difficulty can be overcome in borate buffers (*25*). Borate complexes sugars (*44*, *48*) into two types of single negatively charged species. The magnitude of the charge and thus their electroosmotic mobility depend mainly on the concentration of borate—higher concentrations leading to more stable complexes (*25*). Borate solutions (100 mM) were employed as support buffers to ensure stable complexations resulting in electrophoretic currents atypically high for an i.d. = 50 μm tube.

Six forms of sugar coexist in aqueous solutions, α- and β-pyranoses and -furanoses, as well as the open-chain and hydrated forms (see Figure 1 of ref 25), multiplying the complexation possibilities. Only saccharose does not form complexes and therefore appears as the sharpest peak in the electropherogram (Figure 11). The broadening observed in the remaining peaks is due to the complexation effects rather than to column overloading. For this reason saccharose was chosen to determine the separation efficiency of the system (*47*). The best theoretical plate number, N, was obtained by electrokinetically injecting 6 mM saccharose solutions for $t = 2$ s at $E = -11$ kV (saccharose has an electrophoretic mobility (*25*) of $\mu_{\text{total}} = 3.3 \times 10^{-4}$ cm² V⁻¹ s⁻¹), resulting in $N = 1.6 \times 10^5$.

Under identical FIA experimental conditions, a higher RI sensitivity is obtained with a 100-μm capillary than with the 50-μm capillary employed here. However, in CE the electric current is proportional to the area of the capillary cross section and therefore to the square of its radius (i.e. area = πR_b^2 and $I \propto R_b^2$). The current is expected to increase 4 times for a capillary twice the diameter, for identical voltages across the capillary and under stable CE conditions. In the electropherogram shown in Figure 11 the current derived with a 50-μm tube is 57 μA. For an i.d. = 100 μm tube under identical electric field the current would be 228 μA, a value at which the buffer would have already boiled even before this current value was reached (*40*). The choice of the capillary diameter for the present experiments was thus the result of a compromise between these two opposite factors.

DISCUSSION

A smooth temperature gradient inside the capillary bore leads to a smaller temperature fluctuations in the buffer (see Thermal Analysis subsection). This, in turn, corresponds to small ΔT_{total} and ΔT_b values as desired, and vice versa. Thermal fluctuations are responsible for the observed noise in the baseline, thus precluding the instrument to operate at the expected shot noise limit. Larger turbulences in the optical path, associated with large temperature gradients, are located near the buffer/capillary wall and capillary wall/RIMF or air interfaces as shown in Figure 4. In order to retain sufficient sensitivity to be able to perform CE using RI detection, the use of a very efficient and stabilized thermal bath at the measuring region is imperative. Furthermore, it is apparent from inspection of eq 4 that ΔT_w decreases with smaller R_w/R_b ratios for both cases studied, indicating that faster heat dissipation is obtained when thick-wall capillaries are employed (*40*).

Angular deflections slightly better than the here obtained 100 nrad have been achieved (*24*) through the use of quiet electronics and using a very stable LED light source in a test bench with a bicell as PSD. However it will be very difficult to realize these 2-fold improvements in a real system subject to matarial expansions and mechanical vibrations and employing much noisier laser light.

A comparison between the present results (Figure 11), obtained without the use of RIMF, PSD, and thermocooling (e.g. with an instrument as that proposed by Dovichi et al. (*18–20*), would have been interesting. However, no such information exists in the literature and, from our experience, the *S/N* ratios obtained under CE conditions witb such an experimental setup were much worse than those shown in the bottom trace of Figure 10 as a consequence of inefficient heat dissipation, precluding the experiment to succeed. This most likely explains the absence of this information in the literature.

The approach to achieve higher stability of the sugar complexes given by Hoffstetter-Kuhn et al. (*25*) was to increase column temperature using moderate concentrations of borate (as compared to those here used, e.g. 60 mM) obtaining similar separation efficiencies. Absorption detection at 190 nm was possible in this case because borate was found to induce a red shift in the quartz UV absorption profile of the studied saccharides. To increase the temperature while retaining high buffer concentration and thus to profit from both complexation mechanisms, our experimental setup would have to be modified. Separation and detection, with the present integrated cell design, can only be carried out at identical temperatures. To realize different temperatures the separation part of the capillary should be separated from detection as usually done in other separation techniques.

Admittedly, the chemical system selected to demonstrate the instrumental capability was not the most suitable if one considers that high buffer concentrations were required. For a chemical system such as peptides or small ions, requiring lower buffer concentrations in the separations or for hyphenation of this RI instrument to conventional and micro HPLC (i.e. small or no Joule effects, respectively), the use of larger i.d. capillaries (e.g. 75 or 100 μm) would be more appropriate.

CONCLUSIONS

The present work extends the scope of RI detection to the CE domain. The performance delivered by the described instrument is comparable to or better than, in terms of sensitivity and linearity, that offered by alternative universal methods such as electric field modulation (*22*), differential methods (*24*), or indirect absorption or fluorescence techniques (*49*) which were the goals of the present investigation.

The ultimate detection limits for this instrument, given by the shot noise, have not been reached. Instrumental improvements and intensive application work aiming to approach the theoretical limits are now being undertaken.

It must be noted that the use of RIMFs to improve instrumental performance is not restricted to RI detection. It has been proposed (*50*) that the use of RIMFs should also benefit absorbance and fluorescence detectors employing capillaries. Indeed, it has been just demonstrated that RIMF is a very effective means to improve the sensitivity of fluorescence detection in CE (*51*).

ACKNOWLEDGMENT

We thank S. Hoffstetter-Kuhn for her advice in the CE results and E. Gassmann, M. Moriseau, and T. Olefirowicz for the critical reading of this manuscript as well as the corrections they proposed. We thank P. E. Jordi for the CAD design and mechanical work and A. Wüthrich for his advice in the electronics.

APPENDIX

Dimensionless Parameters. In terms of J_i (for $i = 0, 1$), the Bessel functions of the first kind, θ is given by (*38*)

$$\theta = \frac{1}{\lambda^2} \frac{J_0(\lambda\eta) - J_0(\lambda) + \dfrac{2\lambda}{\mathrm{Bi}_{\mathrm{oA}}} J_1(\lambda)}{\mathrm{f}(\lambda)} \qquad \text{(A-1)}$$

where the function f(λ), representing the *autothermal* effect (*38*), is given by

$$\mathrm{f}(\lambda) = J_0(\lambda) - \frac{2\lambda}{\mathrm{Bi}_{\mathrm{oA}}} J_1(\lambda) \qquad \text{(A-2)}$$

The $\mathrm{Bi}_{\mathrm{oA}}$ parameter appearing in the denominator of eq A-2 is the overall biot number defined in Table II where, in addition, the computed values of θ, f(λ), and $\mathrm{Bi}_{\mathrm{oA}}$ are reported.

The *heat-transfer* coefficient, h_{oA}, for a bare capillary (i.e. without the polyimide coating) can be evaluated using (*35*)

$$h_{\mathrm{oA}} = \frac{1}{R_{\mathrm{L}}} \left\{ \left[\frac{\ln\left(\dfrac{R_w}{R_b}\right)}{k_w} \right] + \left[\frac{1}{R_{\mathrm{P}} h_s} \right] \right\}^{-1} \qquad \text{(A-3)}$$

where k_w is the thermal conductivity of the wall and h_s is the *surface heat transfer* coefficient (h) and k_w = 1.5 W m^{-1} K^{-1}. For liquid-cooled capillaries h_s is so large that the last term in the denominator can be neglected (*35*) and $h_{\mathrm{oA}} = 3.0 \times 10^4$ W m^{-2} K.

LITERATURE CITED

(1) Jorgenson, J. W.; DeArman Lukacs, K. D. *Science* **1983**, *222*, 266.
(2) Mikkers, R. E. P.; Evaeraerts, F. M.; Verhaeegaen, Th. P. *J. Chromatogr.* **1978**, *169*, 11.
(3) Gordon, M. J.; Huang, X.; Pentoney, S. L.; Zare, R. N. *Science* **1988**, *242*, 224.
(4) Grossman, P. D.; Colburn, J. C.; Lauer, H. H.; Nielson, R. M.; Riggin, R. G.; Sittapalmam, G. S.; Rickard, E. C. *Anal. Chem.* **1988**, *61*, 1186.
(5) Ewing, A. G.; Wallingford, R. A.; Olefirowicz, T. M. *Anal. Chem.* **1989**, *61*, 292A.
(6) Lauer, H. H.; McManigill, D. *Anal. Chem.* **1986**, *58*, 166.
(7) Nielsen, R. G.; Sittampalam, G. S.; Rickard, E. C. *Anal. Biochem.* **1989**, *177*, 20.
(8) Tsuda, T.; Takagi, K.; Watanabe, T.; Satake, T. *HRC & CC, J. High Resolut. Chromatogr. Chromatogr.* **1988**, *11*, 72.

(9) Cohen, A. S.; Paulus, A.; Karger, B. L. *Chromatographia* **1987**, *24*, 15.
(10) Paulus, A.; Gassmann, E.; Field, M. J. *Electrophoresis* **1990**, *11*, 702.
(11) Yang, F. *HRC & CC, Commun.* **1981**, *4*, 83.
(12) Bruno, A. E.; Paulus, A.; Bornhop, D. *J. Appl. Spectrosc.* **1991**, *45*, 462.
(13) Dovichi, N. J. *Rev. Sci. Instrum.* **1990**, *61* (12), 653.
(14) Bruno, A. E.; Gassmann, E.; Pericles, N.; Anton, K. *Anal. Chem.* **1989**, *61*, 876.
(15) Gassmann, E.; Kuo, J. E.; Zare, R. N. *Science* **1985**, *230*, 813.
(16) Liu, J.; Shirota, D.; Novotny, M. *Anal. Chem.* **1991**, *63*, 413.
(17) Dovichi, N. *CRC Crit. Rev. Anal. Chem.* **1987**, *17*, 357.
(18) Bornhop, D. J.; Dovichi, N. J. *Anal. Chem.* **1986**, *58*, 504.
(19) Bornhop, D. J.; Dovichi, N. J. *Anal. Chem.* **1987**, *59*, 1632.
(20) Bornhop, D. J.; Nolan, T. G. Dovichi, N. J. *J. Chromatogr.* **1987**, *384*, 181.
(21) Synovec, R. E. *Anal. Chem.* **1987**, *59*, 2877.
(22) Chen, C. Y.; Demana, T.; Huang, S. D.; Morris, M. D. *Anal. Chem.* **1989**, *61*, 1590.
(23) Pawliszyn, J. *Anal. Chem.* **1988**, *60*, 2796.
(24) Pawliszyn, J. *Spectrochim. Acta Rev.* **1990**, *13*, 354.
(25) Hoffstetter-Kuhn, S.; Paulus, A.; Gassmann, E.; Widmer, H. M. *Anal. Chem.* **1991**, *63*, 1541.
(26) Honda, S.; Iwasa, S.; Makino, A.; Fujiwara, S. *Anal. Biochem.* **1989**, *176*, 72.
(27) Garner, T. W.; Yeung, E. S. *J. Chromatogr.* **1990**, *515*, 639.
(28) Nardi, A.; Fanali, S.; Foret, F. *Electrophoresis* **1990**, *11*, 774.
(29) Churms, S. C. *J. Chromatogr.* **1990**, *500*, 555.
(30) Bettler, B.; Amado, R.; Neukom, H. *J. Chromatogr.* **1990**, *498*, 213.
(31) Scher, H. *Electrophoresis* **1990**, *11*, 18.
(32) Al-Hakim, A.; Linhardt, R. *Electrophoresis* **1990**, *11*, 23.
(33) Marcuse, D. In *Principles of Optical Fiber Measurements*; Academic Press: New York, 1981.
(34) Born, M.; Wolf, E. In *Principles of Optics*; Pergamon Press: New York, 1989.
(35) Knox, J. H. *Chromatographia* **1988**, *26*, 329.
(36) Jones, E. J.; Grushka, E. *J. Chromatogr.* **1989**, *466*, 219.
(37) Grushka, E.; McCormick, R. M.; Kirkland, J. J. *Anal. Chem.* **1989**, *61*, 241.
(38) Gobie, W. A.; Ivory, C. F. *J. Chromatogr.* **1990**, *516*, 191.
(39) Vinther, A.; Sieberg, H. *J. Chromatogr.* **1991**, *559*, 27–42.
(40) Nelson, R. J.; Paulus, A.; Cohen, A. S.; Guttman, A.; Karger, B. L. *J. Chromatogr.* **1989**, *480*, 111.
(41) Hamamatsu. Technical note TN-102, 1982.
(42) United Detector Technology. Technical note The guide to position sensing. 1986.
(43) Siebert, H. P. *Sensoren 1; Elektronik* **1986**; *241*, 34.
(44) Renn, C. N.; Synovec, R. E. *Anal. Chem.* **1988**, *60*, 1188.
(45) Yariv, A. In *Optical Electronics*, 3rd ed.; CDS College Publishing: New York, 1985.
(46) Demtröder, W. In *Laser Spectroscopy*, Springer-Verlag: Berlin, 1982.
(47) Huang, X.; Gordon, M. J.; Zare, R. M. *Anal. Chem.* **1988**, *60*, 375.
(48) Consden, T. W.; Stanier, W. M. *Nature* **1952**, *169*, 783.
(49) Garner, T. W.; Yeung, E. S. *J. Chromatogr.* **1990**, *515*, 639.
(50) Bruno, A. E. Eur. Pat. Appl. No. 87-17928, 1990.
(51) Kurosu, Y.; Sasaki, T.; Saito, M. *J. High Resolut. Chromatogr.* **1991**, *14*, 86.

RECEIVED for review July 1, 1991. Accepted September 12, 1991.

Chapter 3 Laser-Based Refractive Index Detection for Capillary Electrophoresis: Ray-Tracing Analysis

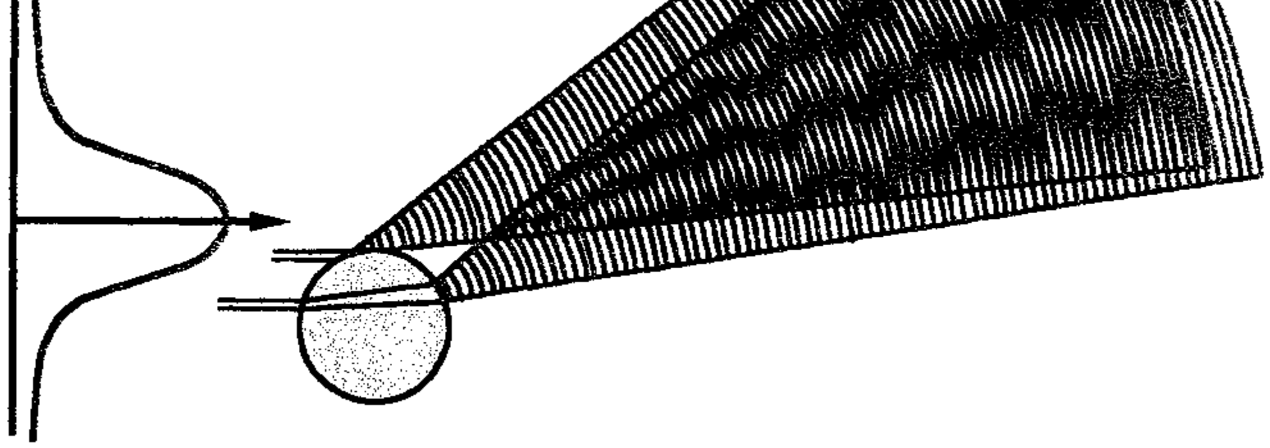

a reprint from Applied Optics

Laser-based refractive-index detection for capillary electrophoresis: ray-tracing interference theory

Beat Krattiger, Alfredo E. Bruno, H. Michael Widmer, Martial Geiser, and René Dändliker

The fringe pattern observed in a far field after a laser beam illuminates a fused silica capillary immersed in a refractive-index matching material and filled with an analyte fluid is exploited to develop a sensitive optical detector for capillary chemical analysis. The inner capillary interface splits the laser beam into a reflected beam fan and a refracted beam fan, which, on overlapping in the far field, lead to interferences. The intensity and the position of the fringes for capillaries with 250 μm ≥ i.d. (inner diameter) ≥ 25 μm are well reproduced by the presented model. The calculation predicts the fringe pattern for various beam/i.d. geometric configurations and is used to optimize the performance of the nanoliter–picoliter refractive-index on-column detection studied. It is found that the best contrast corresponds to a capillary that is illuminated with a beam waist of $w_0 \sim$ i.d./12, which is off-center focused with an offset of $s \sim$ i.d./2. For a given interference pattern, the fringes that are found to be more sensitive to Δn are those that appear near the optical axis but still retain high intensity and contrast. The sensitivity increases approximately linearly with the fringe number, and the maximal fringe number increases proportionally with the i.d.

1. Introduction

The development of nanoliter–picoliter optical detectors for capillary separation techniques, such as capillary electrophoresis (CE), is gaining considerable importance in chemical analysis. Indeed, CE represents the trend in fluid-phase chemical separation sciences.[1] Several aspects, including speed of analysis, high resolution, and efficiency account for the acceptance of this technique.[2] High electrical fields across the capillary ends force the ionic species to migrate through a buffer-filled capillary. The different species travel at different speeds according to their charge, size, or both. However, the high resolution delivered by CE is often lost at the detection stage, which is most conveniently done by optical methods,[3] as a result of hyphenation with relatively insensitive detectors.

Because the separation performance increases with a reduction of the inner diameter (i.d.) of the capillary tube employed in CE separations, there is a growing demand to upgrade low-volume detectors used in high-performance liquid chromatography[4] (HPLC) or to develop new detectors that are specifically suitable for CE.[3] Refractive-index universal detection (i.e., detection that responds to virtually all compounds), which is the third most important detection choice in HPLC after absorbance and fluorescence, has not been made available to CE until recently and then only in research laboratories (i.e., no commercial refractive-index detector exists to date for CE).

An issue in the quest to develop nanoliter or picoliter detectors for capillary techniques is that sensitivity is compromised when the i.d. of the tube is reduced. Primarily because of their spatial coherence, lasers have led to the development of a series of novel optical detectors that feature impressive detection limits. Dovichi[5] and Bruno *et al.*[6] have succeeded in developing an on-column laser-based refractive-index detector as well as various related thermooptical detectors that display sensitivities that are not linear with respect to path length, as is the case in absorption or fluorescence.

Further instrumental developments in the original design[7,8] of the refractive-index detector of Dovichi *et al.* demonstrated in HPLC and flow injection analysis (FIA) were made in our laboratory.[9] We demonstrated the use of refractive-index capillary detection

---

B. Krattiger, A. E. Bruno, and H. M. Widmer are with Analytical Research, Ciba-Geigy, 4002 Basel, Switzerland. M. Geiser and R. Dändliker are with the Institut de Microtechnique, Université de Neuchâtel, 2000 Neuchâtel, Switzerland.

Received 14 May 1992.
0003-6935/93/060956-10$05.00/0.

in CE for the analysis of underivatized saccharides in i.d. = 50-μm tubes. This instrument featured refractive-index matching fluids (RIMF's) and position-sensitive photodiodes.

A far-field interference pattern is observed[9-11] whenever a coherent light beam strikes a transparent cylindrical object such as an optical fiber[10] or a capillary tube. The angular fringe displacement that is due to changes in the refractive index in the core of the capillary, Δn_i, corresponds to phase shifts between the two recombining rays, the TIR (total internally reflected) ray and the TP (transmitted probing) ray (Fig. 1) and constitutes the output signal of the refractive-index detector. In a previous paper[9] we demonstrated that, as in the case of step-index fibers,[10] the complex light-scattering pattern of freestanding capillaries is greatly simplified after their immersion in a matching material, which results in a geometric configuration such as that shown in Fig. 1. This translates into manifold benefits for the performance of the CE detector. The number of fringes is reduced and the light intensity in the remaining fringes is larger than it would be otherwise. In addition, the RIMF acts as a heat sink that reduces the thermal noise associated with Joule heat in CE.

Here we present a theoretical model based on geometric optics (ray tracing) that accurately reproduces recorded fringe patterns of capillaries with 250 μm $\geq$ i.d. $\geq$ 25 μm. (Although CE is performed with capillaries with i.d. < 100 μm we extended the analysis to larger i.d.'s for those interested in using the refractive-index detector for HPLC.) The model is used to calculate the fringe shift as a function of the refractive-index change Δn_i for a given capillary i.d. and beam waist. The path-length dependence of the fringe sensitivity as a function of i.d. and fringe number is investigated to find geometric configurations that should render higher instrumental performance.

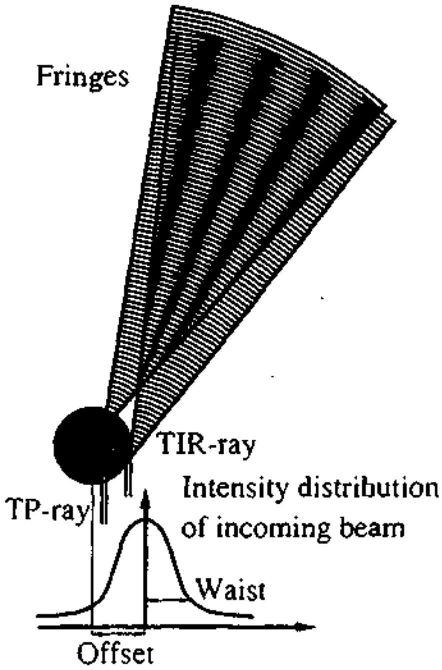

Fig. 1. Illustration of the optical arrangement of the refractive-index detector for CE, which resembles a Young double-slit interferometric arrangement. The fringes, which are formed by the coherent addition of the exiting TP and TIR rays, are represented as moiré structures in the figure.

2. Theoretical Model

A. Introduction to Theory

As indicated by Watkins,[11] because the capillary dimensions considered here are much larger than the illuminating wavelength, ray-tracing methods are adequate to describe the optical problems encountered. These ray-tracing methods are simpler and easier to implement than those based on wave theory. Because the capillary is immersed in an RIMF the outer capillary wall is optically dissolved, as illustrated in Fig. 1 of Ref. 9; the total number of reflections and refractions is thus reduced from 10 to 3 as the number of interfering fans is reduced from 4 to 2. The optical device under investigation consists of only a cylindrical string represented by the fluid-filled capillary bore embedded in a large surrounding media with the refractive index of fused silica. The illumination consists of a set of parallel rays that interact with the fluid string in the capillary bore, in which the following effects are considered (Figs. 1 and 2):

(1) Snell's refraction law is used to relate the ray impact height x_{TP} to the ray output angle α.

(2) Reflection law determines the dependency between the ray impact height x_{TIR} and emerging angle α.

(3) Depending on the impact height x_{TP}, the TP ray undergoes a phase change that is due to the refractive index in the fluid string.

(4) The TIR ray undergoes a phase shift at the reflection, depending on its angle of incidence, its polarization, and on the refractive indices n_i and n_c.

(5) Because of the divergence lens and the mirror effect of the capillary, both rays suffer an intensity decrease, depending on their impact height and distance to the detector.

(6) The intensity of the TP ray is further decreased because of reflections of parts of the ray at the

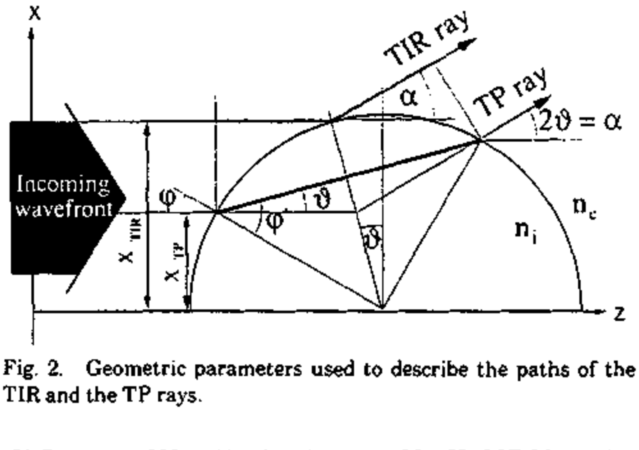

Fig. 2. Geometric parameters used to describe the paths of the TIR and the TP rays.

two fluid string–fused silica interfaces. This intensity decrease also depends on the polarization, the angle of incidence, and on the refractive indices n_i and n_e.

(7) The illuminating beam has an intensity profile (i.e., Gaussian) that defines the initial impact intensities for both rays.

The final aim is to calculate the interference pattern in the far field $I(\alpha)$ as a function of the scattering angle α while taking into account effects (1)–(7). To simplify the formalism, we derive all equations as functions of $H_{\mathrm{TP}} = x_{\mathrm{TP}}/R$, which is the reduced height with respect to the capillary radius R. It should be noted that, unlike that of Watkins,[11] the present model now includes effects (4)–(7).

B. Ray Tracing and Phases

Only the realistic case in which the refractive index n_i in the core is smaller than n_e of the capillary wall and the surrounding propagation media is considered here (e.g., the use of aqueous buffers with $n_i = 1.332$ and fused silica capillaries with $n_e = 1.457$). The laser beam, propagating in the z direction, strikes the capillary from one side perpendicularly to the capillary (the y axis); i.e. the discussion is restricted to a two-dimensional system.

Depending on the entrance height, the capillary core splits the incoming beam into a TP ray and a TIR ray. As their original phases are altered, both rays interfere subsequently in the far field. In other words, the capillary acts (1) as a beam splitter, (2) as a dephaser for the incoming rays, (3) as a diverging mirror for the TIR ray, and (4) as a diverging lens for the TP ray (see Figs. 1 and 5). The overall system thus performs like a Young double-slit arrangement.

To simplify the analysis it is convenient to introduce three reduced variables:

$$N = \frac{n_i}{n_e} \leq 1, \tag{1a}$$

$$H_{\mathrm{TP}} = \frac{x_{\mathrm{TP}}}{R}, \qquad 0 \leq H_{\mathrm{TP}} \leq H_{\max}, \tag{1b}$$

$$H_{\mathrm{TIR}} = \frac{x_{\mathrm{TIR}}}{R}, \qquad H_{\max} \leq H_{\mathrm{TIR}} \leq 1, \tag{1c}$$

where R is the capillary internal radius (i.e., $R = \mathrm{i.d.}/2$), N is the reduced refractive index, H_{TP} is the reduced impact height of the TP ray, and x_{TP} is the impact for the incoming TP ray (see Fig. 2).

The necessary condition for the two beams TP and TIR to interfere in the far field is that they be parallel, i.e., that they emerge in the same direction α (Fig. 2.). In this case the entrance height H_{TIR} of the TIR ray is related to the entrance height H_{TP} of the TP ray by

$$H_{\mathrm{TIR}} = \frac{1}{N}\left[(N^2 - H_{\mathrm{TP}}^2)^{1/2}(1 - H_{\mathrm{TP}}^2)^{1/2} + H_{\mathrm{TP}}^2\right]. \tag{2}$$

Using definitions (1a), (1b), and Snell's law, we find that the refraction angle $\alpha = 2\vartheta$ (Fig. 2) is given by

$$\alpha(H_{\mathrm{TP}}) = 2[\arcsin(H_{\mathrm{TP}}/N) - \arcsin(H_{\mathrm{TP}})]. \tag{3}$$

From geometric considerations (Fig. 2) it can be shown that the optical path lengths OP (i.e., the geometric path multiplied by the refractive index of the propagating media) for the TIR and TP rays are given by

$$\mathrm{OP}_{\mathrm{TIR}}(N, H_{\mathrm{TP}}) = \frac{2Rn_e}{N}\left[(N - H_{\mathrm{TP}})(1 - H_{\mathrm{TP}}^2)^{1/2} + H_{\mathrm{TP}}(N^2 - H_{\mathrm{TP}}^2)^{1/2}\right], \tag{4a}$$

$$\mathrm{OP}_{\mathrm{TP}}(N, H_{\mathrm{TP}}) = 2Rn_e(N^2 - H_{\mathrm{TP}}^2)^{1/2}. \tag{4b}$$

According to the Fresnel equations for TIR,[12] the TIR ray undergoes a phase shift $\Phi_{p,s}$ as a function of the angle of incidence, namely,

$$\Phi_p = -2\arctan\left(\frac{1}{N^2}\left\{\frac{N^2(1-N^2)}{H_{\mathrm{TP}}^2[(1-N^2)^{1/2} - (N^2 - H_{\mathrm{TP}}^2)^{1/2}]^2} - 1\right\}^{1/2}\right), \tag{5a}$$

$$\Phi_s = -2\arctan\left(\left\{\frac{N^2(1-N^2)}{H_{\mathrm{TP}}^2[(1-N^2)^{1/2} - (N^2 - H_{\mathrm{TP}}^2)^{1/2}]^2} - 1\right\}^{1/2}\right), \tag{5b}$$

where the subscripts p and s refer to parallel and perpendicular polarizations, respectively.

Introducing these additional phase shifts $\Phi_{p,s}$ that are due to the TIR, we find that the total phase difference between the interfering rays is given by

$$\Psi(H_{\mathrm{TP}}, N) = \frac{2\pi}{\lambda}(\mathrm{OP}_{\mathrm{TP}} - \mathrm{OP}_{\mathrm{TIR}}) - \Phi_{p,s}, \tag{6a}$$

which, by using Eqs. (4), becomes

$$\Psi(H_{\mathrm{TP}}, N) = \frac{4\pi R n_e}{\lambda}\,\frac{H_{\mathrm{TP}} - N}{N} \times \left[(1 - H_{\mathrm{TP}}^2)^{1/2} - (N^2 - H_{\mathrm{TP}}^2)^{1/2}\right] - \Phi_{p,s}. \tag{6b}$$

C. Fringes and Sensitivity

Assuming that the amplitudes of the two emerging rays are the same (constant for all scattering angles), the far-field light intensity is simply proportional to $1 + \cos(\Psi)$ (Fig. 3). The fringes are conveniently labeled by the fringe order

$$m = \frac{\Psi}{2\pi}, \tag{7}$$

where $m = 0$ corresponds to the outermost fringe ($\alpha = \alpha_{\max}$) for which the phase difference is 0. The magnitude of m increases toward the optical axis ($H_{\mathrm{TP}} = 0$) where the fringe labeled $m_{\max}$ appears (note that m is negative and the subscript max refers to its magnitude only).

The phase difference [Eq. (6b)] reaches its maximum value for emerging rays propagating along the optical axis (i.e., $H_{\mathrm{TP}} = 0$, $\alpha = 0$) and its minimum for rays striking at the critical angles where reflection and refraction coincide (i.e., $H_{\mathrm{TP}} = H_{\max}$), which, from Snell's law and Eq. (1b) (Fig. 2) occurs at

$$H_{\max} = N. \tag{8}$$

At $m = 0$, the TIR and TP rays overlap at the capillary interface and the distinction between the TIR and the TP ray is no longer meaningful. The geometric path difference and also the phase shift Φ [Eqs. (5) and (6b)] vanish at this point.

The maximum fringe number $m_{\max}$ occurs at $\Psi_{\max}$. Taking into account that the phase shift $\Phi = -\pi$ [Eqs. (5)] and using Eq. (6a), we find that

$$m_{\max} = \frac{\Psi_{\max}}{2\pi} = \frac{2R(n_i - n_e) + 0.5\lambda}{\lambda}. \tag{9}$$

For illumination with $\lambda = 0.633\ \mu\text{m}$ (He–Ne laser) and for a 25-μm-i.d. capillary with $\Delta n = n_e - n_i = 0.125$ (water-filled fused silica capillary), one gets $m_{\max} = -4$, which indicates that a total of 5 fringes are expected to occur, with $m = 0, -1, -2, -3$, and -4.

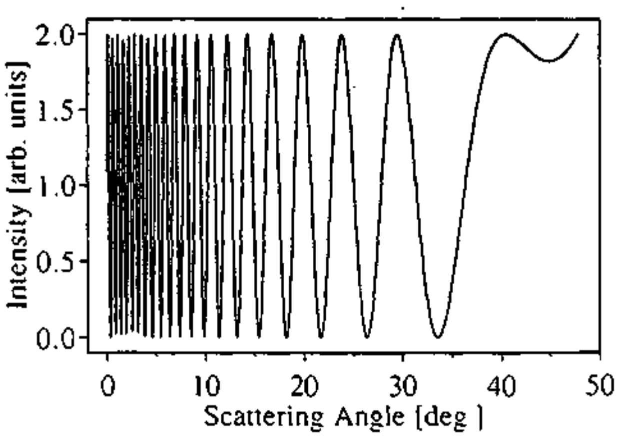

Fig. 3. Ideal fringe pattern (equal intensities of interfering rays) versus scattering angle α for a water-filled capillary with i.d. = 100 μm and $N = 0.914$.

As the current interferometric setup corresponds to a device that is used for the measurement of refractive-index changes, it is convenient to define an instrumental sensitivity S, which is considered as the differential change of the phase with refractive index and normalized to the fringe width ($\Delta\Psi = \pi$), that is,

$$S = \frac{1}{\pi}\frac{\partial\Psi}{\partial n_i} = \frac{1}{\pi n_e}\frac{\partial\Psi}{\partial N}. \tag{10}$$

Neglecting the phase shift $\Phi_{s,p}$ that is due to the TIR, we derive the sensitivity S from Eq. (6b) as

$$S = \frac{4R}{\lambda}\left\{\frac{H_{\mathrm{TP}}}{N^2}\left[(N^2 - H_{\mathrm{TP}}^2)^{1/2} - (1 - H_{\mathrm{TP}}^2)^{1/2}\right] + \frac{(N - H_{\mathrm{TP}})}{(N^2 - H_{\mathrm{TP}}^2)^{1/2}}\right\}. \tag{11a}$$

Equation (11a) indicates that as H_{TP} increases $\partial\Psi/\partial N$ decreases. The largest phase change for a given ΔN (or Δn_i) would then be observed for the fringe appearing on the optical axis, as seen in Fig. 4, which shows the dependence of S on the scattering angle α. In Fig. 4 the maximum value of S is then

$$S_{\max} = \frac{4R}{\lambda}, \tag{11b}$$

which indicates that, in the absence of a phase shift that is due to the total reflection, the maximal sensitivity to the capillary size increases linearly with the capillary dimensions.

D. Ray Amplitudes

If the intensities of all interfering rays were the same, the best monitoring fringe (the one used to track the fringe shifts) for refractive-index detection would be the one appearing near the optical axis. However, fringe patterns reveal low fringe contrast in this

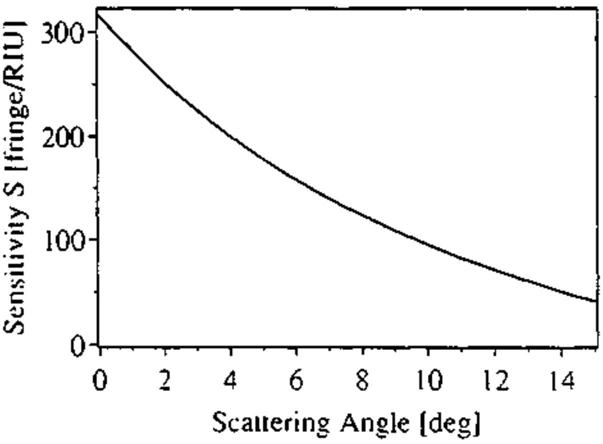

Fig. 4. Sensitivity S as a function of scattering angle α for a 100-μm-i.d. water-filled capillary. S is maximum for axial rays, where the longest possible optical path through the sample occurs. RIU, refractive-index unit.

region because the TIR ray carries low intensity compared with the TP ray.

The TIR ray does not suffer amplitude losses because of Fresnel's formulas[12] at the capillary interface, but the TP ray is partially reflected at both interfaces as it twice crosses the fused silica–fluid string interface [effect 6]. The total amplitude transmissions for both polarizations T_p and T_s can be computed by multiplication of the individual amplitude transmission coefficients given by the Fresnel formulas[12] as

$$T_p(H_{\mathrm{TP}}) = \frac{4N^2(N^2 - H_{\mathrm{TP}}^2)^{1/2}(1 - H_{\mathrm{TP}}^2)^{1/2}}{[(N^2 - H_{\mathrm{TP}}^2)^{1/2} + N^2(1 - H_{\mathrm{TP}}^2)^{1/2}]^2}, \qquad (12a)$$

$$T_s(H_{\mathrm{TP}}) = \frac{4(N^2 - H_{\mathrm{TP}}^2)^{1/2}(1 - H_{\mathrm{TP}}^2)^{1/2}}{[(N^2 - H_{\mathrm{TP}}^2)^{1/2} + (1 - H_{\mathrm{TP}}^2)^{1/2}]^2}. \qquad (12b)$$

In addition, the radius of curvature of the capillary wall introduces a divergence effect in the (x, z) plane, which also contributes to the attenuation of the intensities for both rays. This effect can be accounted for by invoking power conservation in the beam before and after the capillary, i.e., $P_{\mathrm{out}} = P_{\mathrm{in}}$, where P is the total optical power over the whole cross section. The geometric beam cross sections before and after the capillary (see Fig. 5) are $\Delta x \Delta y$ and $(\Delta\alpha u)\Delta y$, respectively, and power conservation thus yields

$$I_{\mathrm{in}}\Delta x \Delta y = I_{\mathrm{out}}(\Delta\alpha u)\Delta y. \qquad (13)$$

The intensity attenuation D^2 for the rays in the far field at a distance u from the capillary axis, if we take into account the spreading of the rays, is given by

$$D_{\mathrm{TP}}^2(H_{\mathrm{TP}}) = \frac{I_{\mathrm{out}}}{I_{\mathrm{in}}} = \left|\frac{1}{u}\frac{\partial x_{\mathrm{TP}}}{\partial\alpha}\right|, \qquad (14a)$$

$$D_{\mathrm{TIR}}^2(H_{\mathrm{TP}}) = \frac{I_{\mathrm{out}}}{I_{\mathrm{in}}} = \left|\frac{1}{u}\frac{\partial x_{\mathrm{TIR}}}{\partial\alpha}\right|. \qquad (14b)$$

The corresponding factor for the amplitude attenuation is D. Because D_{TIR}^2 can be only positive and $\partial x_{\mathrm{TIR}}/\partial\alpha$ is negative, only the absolute values are to be considered. It can be shown that they can be written as

$$D_{\mathrm{TP}}^2(H_{\mathrm{TP}}) = \frac{R}{2u}\frac{(1 - H_{\mathrm{TP}}^2)^{1/2}(N^2 - H_{\mathrm{TP}}^2)^{1/2}}{(1 - H_{\mathrm{TP}}^2)^{1/2} - (N^2 - H_{\mathrm{TP}}^2)^{1/2}}, \qquad (15a)$$

$$D_{\mathrm{TIR}}^2(H_{\mathrm{TP}}) = \frac{(1 - H_{\mathrm{TP}}^2)^{1/2}}{u}. \qquad (15b)$$

Finally, the complex amplitudes A associated with both rays, in terms of H_{TP}, OP, T, and D, are given by

$$A_{\mathrm{TP}} = T(H_{\mathrm{TP}})D_{\mathrm{TP}}(H_{\mathrm{TP}})\exp[i\mathrm{OP}_{\mathrm{TP}}(H_{\mathrm{TP}})], \qquad (16a)$$

$$A_{\mathrm{TIR}} = D_{\mathrm{TIR}}(H_{\mathrm{TP}})\exp[i\mathrm{OP}_{\mathrm{TIR}}(H_{\mathrm{TP}})]. \qquad (16b)$$

The far-field light intensity I that is obtained by the superposition of the two rays is given by[12]

$$I(N, H_{\mathrm{TP}}) = |A_{\mathrm{TP}} + A_{\mathrm{TIR}}|^2 = (A_{\mathrm{TP}})^2 + (A_{\mathrm{TIR}})^2 + 2A_{\mathrm{TP}}A_{\mathrm{TIR}}\cos\Psi(N, H_{\mathrm{TP}}), \qquad (17)$$

where the relative phase Ψ of the two rays is given by Eq. (6b).

The weight of the two attenuation factors D and T is different. D_{TP} and D_{TIR} strongly dominate over the whole fringe pattern, whereas the influence of T is small and visible only for scattering angles greater than $\alpha = 40°$. For this reason T can be omitted in the calculation unless the zero-order fringe ($m = 0$) is investigated.

Typical fringe patterns, as the one shown in Fig. 6 for a 100-μm-i.d. capillary, have been calculated as a function of the scattered angle α [Eq. (3)] by using Eq. (17). In the figure, the intensities associated with both individual rays [the square of Eqs. (16)] are also

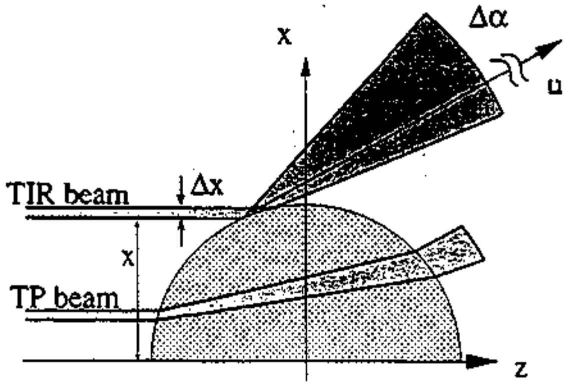

Fig. 5. Intensity attenuation that is due to the curvature of the inner capillary wall.

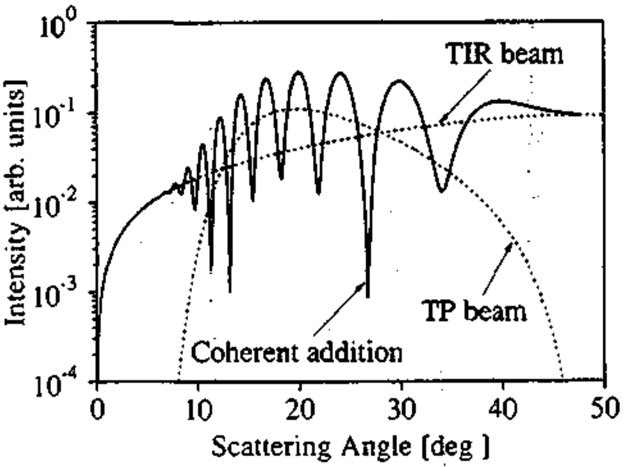

Fig. 6. Fringe pattern simulation for a 100-μm-i.d. fused silica capillary filled with water, illuminated by a beam with a waist of $w_0 = 8.4$ μm and an offset of $s = 48$ μm. The individual intensity contributions of the TIR and TP rays are given as dotted curves. Maximum fringe contrast is observed for equal intensities at $\alpha = 12°$ and $\alpha = 28°$.

displayed. Highest contrast is observed when the individual intensities are identical, i.e., $|A_{TP}|^2 = |A_{TIR}|^2$, which occurs, in this case, at approximately $\alpha = 12°$ and $\alpha = 28°$.

E. Gaussian Beams

Until now, the incoming rays were considered to have uniform intensity. If the illumination is provided by a laser, the intensity distribution in the beam cross section is essentially Gaussian. For a Gaussian incoming beam the initial ray amplitude A_G of the ray is given by[13]

$$A_G(H) = A_0 \exp\left[-\left(\frac{HR - s}{w_0}\right)^2\right], \qquad (18)$$

where s is an incoming offset parameter in the x direction (see Fig. 1) and w_0 is the waist of the incoming beam.

It is interesting to observe how the interference pattern changes as the incoming beam waist w_0 or the offset s varies ($s = 0$ corresponds to on-center illumination and $s \neq 0$ corresponds to off-axis illumination). In this way it is possible to make an *a priori* prediction regarding which geometric configuration would render the highest fringe contrast. This is shown in Fig. 7, where the fringe pattern for a 100-μm-i.d. capillary and a beam waist of $w_0 = 8.4$ μm for seven different configurations, with offsets ranging from $s = 0$ μm to $s = 60$ μm, are simulated. For $s \leq 30$ μm the whole beam cross section transverses the capillary without suffering reflection losses. The lens effect of the fluid string translates the beam offsets into an angular deflection of the spot, whose Gaussian beam profile is, although distorted, conserved. If the beam offsets are further increased, a substantial part of the light is also reflected and interference fringes are visible, as shown for $s = 40$ μm. An additional increase in the offset increases the fringe contrast, because balance in the intensities of the two outgoing rays is approached. In this case it is apparent that an off-axis illumination of $s = \text{i.d.}/2 = 50$ μm gives the best illumination condition (i.e., the highest fringe contrast) for the current purpose. If the beam offset is further increased, the contrast fades because only the faint intensity of the slope of the Gaussian beam profile now transverses the center of the fluid string, which reduces the TP intensity with respect to the TIR intensity. Furthermore, the overall intensity decreases rapidly because the mirror effect at the fluid string surface disperses the beam strongly. The Gaussian beam profile is reproduced again, this time by the mirror effect, as shown in the curved base line for s = 60 μm in Fig. 7.

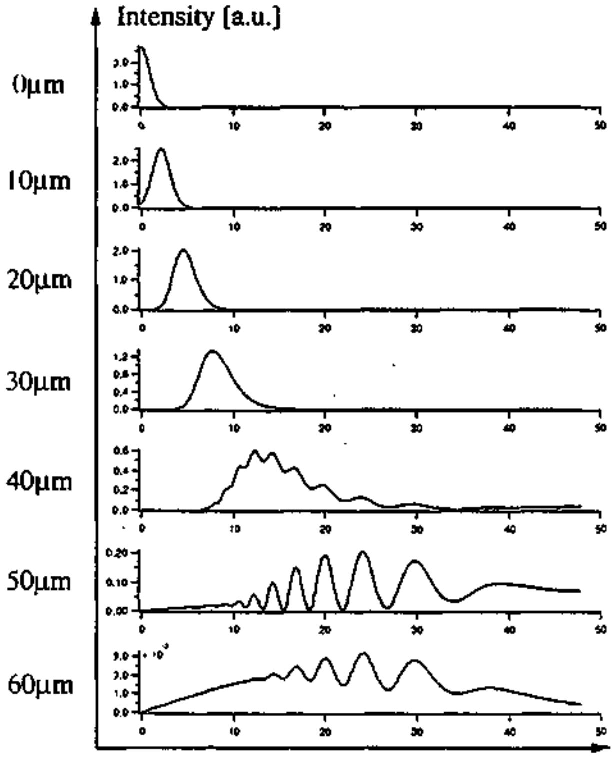

Fig. 7. Fringe pattern simulations for 100-μm-i.d. capillary illuminated by a beam with a waist $w_0 = 8.4$ μm for various beam offsets ranging from $s = 0$ μm to $s = 60$ μm.

3. Experimental Results

A. Experimental Setup

The experimental setup consists basically of a goniometer with a photodetector attached to the rotating arm (see Fig. 8) driven by a computer (a Macintosh IIfx with the LabView package for data acquisition and Igor software for calculations). The light source is a linearly polarized He–Ne laser with 2-mW output power (Uniphase 1103P). An optical isolator, placed immediately after the output coupler, is used to decouple the laser resonator from retroreflections. Spatial filtering was not necessary. The incoming laser beam is focused by a 5× microscope objective onto the capillary, resulting in a spot size of $2w_0 = 16.8$ μm. The fused silica capillaries investigated ($n_e = 1.457$ at $T = 25°C$ for $\lambda = 632.8$ nm) had an outer diameter of ~330 μm and inner diameters ranging from 5 to 250 μm (Polymicro Technologies).

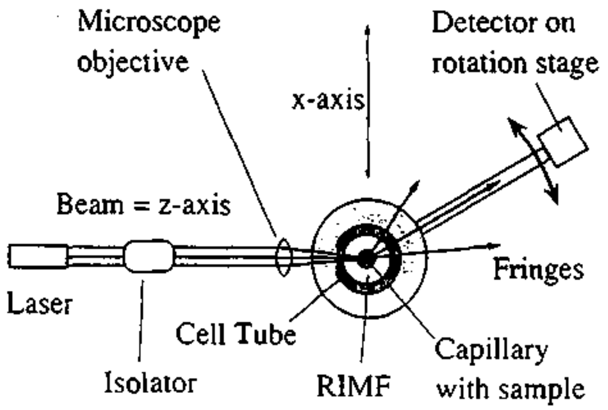

Fig. 8. Experimental setup used to record the fringe patterns. The capillary, which is immersed in RIMF, is concentric to the cell tube and the x-axis translation corresponds to the beam offset s.

In all cases the protective polyimide coatings were removed. The capillary is immersed in a cell filled with RIMF[9] (e.g., Ciba-Geigy transparent index matching epoxy V.P. XW 396/397) and is mounted on a two-dimensional translation stage. To allow a 360° observing angle we made the cell from a glass tube (9-mm diameter) with a flat polished entrance window (4.4 mm × whole tube length) to prevent cylindrical aberrations on the beam waist (see Fig. 8 of Ref. 9). The concentric arrangement of the capillary within the cell tube permits all rays originating from the capillary to cross the cell tube perpendicularly, which, in turn, preserves the original direction of the rays when returning to the air, where the detection is performed. To guarantee perfect centering of the capillary with respect to the cell tube, the fringe patterns corresponding to two on-axis illuminations from two perpendicular directions were recorded. If both patterns are symmetric around the zero deflection angle, the capillary is assumed to be centered.

The angular distribution of the light intensity is measured by a standard Si p-i-n photodiode (BPW 34) at a distance of 10 cm away from the capillary (far field). A set of slits is located in front of the photodiode, so as to produce a view field of 1.1° and to prevent perturbations that are due to background light from the environment.

B. Results

The measured fringe patterns are the same as those employed in the refractive-index detector described in Ref. 9. A comparison between the calculated and the measured fringe patterns is provided in Fig. 9, in which the fringe pattern of a 100-μm-i.d. capillary as well as the corresponding simulation are plotted as functions of the scattering angle. For the calculations we employed values given in the literature for the refractive indices and measured values for the beam waists. The beam offsets and i.d.'s were varied (e.g., to account for the tolerance in the i.d. dimensions) in order to obtain their best fit. The calculated and the recorded fringe patterns for capillaries with i.d. = 50 μm down to 5 μm are shown in Fig. 10. Although the recording has not been done with the same accuracy as the one displayed in Fig. 9, it is apparent that the quality of the fit degrades with smaller i.d.'s (see discussion Section 4).

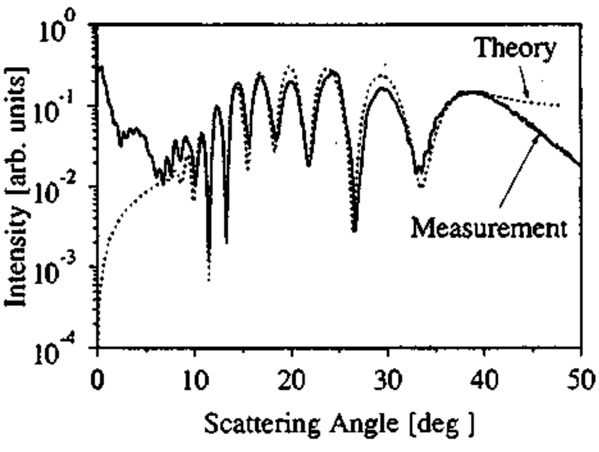

Fig. 9. Experimental (solid curve) and simulated (dotted curve) fringe patterns. Best fit is achieved for a simulation with i.d. = 105 μm, which is slightly outside production tolerance of the capillary (error probably caused by imperfection of the cell window).

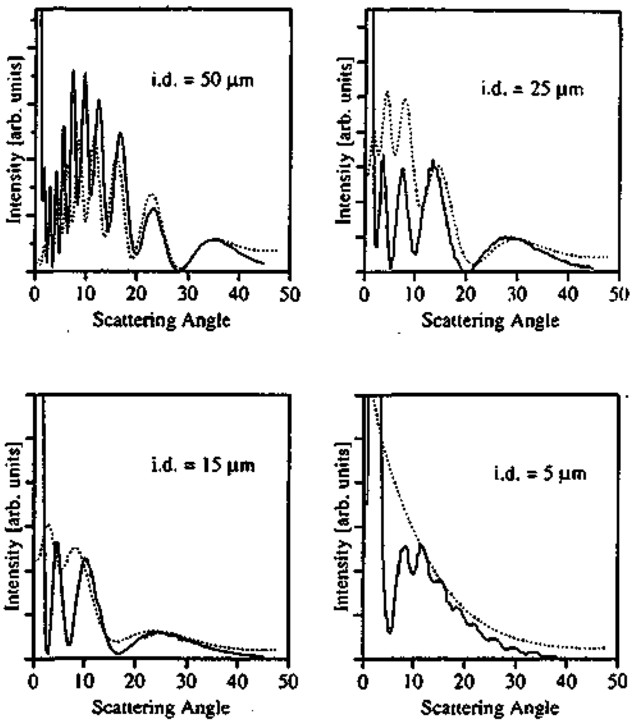

Fig. 10. Recorded and simulated fringe patterns for capillaries with i.d. = 50, 25, 15, and 5 μm illuminated by a beam with a waist of w_0 = 22 μm and beam offsets of s = 36, 21, 19, and 0 μm, respectively.

4. Discussion

Ignoring interference effects, Synovec[14] developed a pure deflection ray-tracing model to predict the sensitivity associated with a (TP) ray [see Eqs. (28)–(32) in Ref. 14]. The presented model and the experimental results indicate, at least for capillaries with i.d. ≤ 250 μm, that the dominant effect is interference, not deflection as previously proposed.[3,6,14]

The simulated fringe pattern shown in Fig. 9 for a 100-μm-i.d. tube mimics the recorded fringes over the scattering region of interest ($5° < \alpha < 40°$) within experimental accuracy. As mentioned by Watkins,[11] for angles $\alpha < 5°$ the detector (shown in Fig. 8) is too close to the optical axis, and interference configurations other than those shown in Fig. 1 arise and lead to discrepancies between theory and measurement (e.g., diffraction of incoming rays grazing to the capillary bore). The intensity behavior on the opposite side of the fringe pattern is dominated by the intensity of TIR rays (Fig. 6). In this region, the discrepancy between measurement and calculation observed in the fringe with $m = 0$ (Fig. 9) could be related to deviations from the ideal TIR that is due to

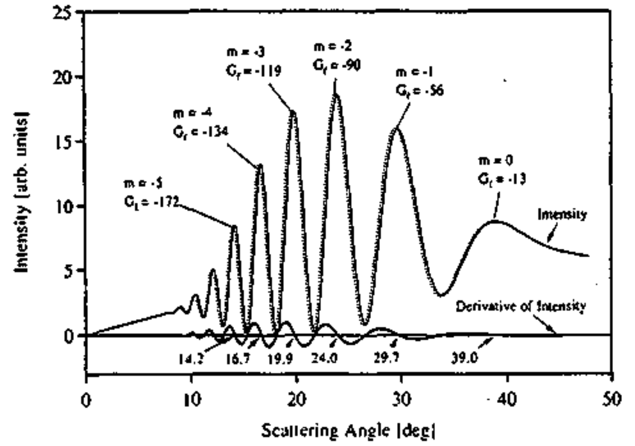

Fig. 11. Sensitivity calculation performed with two fringe patterns for a 100-μm-i.d. tube illuminated by a beam with $w_0 = 8.4$ μm for $\Delta n_i = 1.0 \times 10^{-3}$ refractive-index units. The first derivative of the fringe pattern simulation is used to determine the points of maximum intensity, and is shown in the lower trace.

surface effects (surface roughness leads to reflection loss) or to diffraction effects (the TP ray crosses the bore close to the interface and the optical path differences have dimensions that are comparable to those of λ).

As predicted in Section 2 it is observed that the best fringe contrast corresponds to off-center illumination with a beam offset of $s \sim$ i.d./2 = R. The beam waist should be smaller than the bore radius of the capillary, or more precisely, it should be in the range of $(x_{\mathrm{TIR}} - x_{\mathrm{TP}})$, e.g., $w_0 \sim$ i.d./12. This permits a greater degree of freedom when choosing the distribution of initial intensity for the two competitive rays by variation of the offset parameter s. The initial intensity distribution should be such that the exiting rays, after suffering all losses, have equal intensity. This is the condition that is required for enhancing the contrast and thus the instrumental sensitivity of capillary refractive-index detection.

The model fails to simulate the fringe pattern of capillaries with i.d.'s that are smaller than 25 μm, as shown in Fig. 10. This was expected, considering that the current model is based entirely in geometric optics and does not include diffraction effects. As the dimensions of the i.d. approach those of λ, it is imperative to account for these effects. This kind of correction to the current model would be necessary to study interference patterns for small i.d. capillaries used in thermo-optical absorption measurements.[6]

Taking into account that beam deflections are measured[9] with a position sensitive detector, the most significant parameter to judge instrumental performance is the fringe sensitivity G_f, which is conveniently defined as the fringe angular displacement $\Delta\alpha$ per refractive index change Δn_i normalized to the angular fringe width σ:

$$G_f = \frac{\Delta\alpha}{\Delta n_i \sigma}. \tag{19}$$

For the ideal situation in which paraxial fringes with maximum contrast are considered and the fringe width σ is taken at half-maximum intensity (FWHM), the fringe sensitivity reaches the theoretical value of

$$G_f = -S. \tag{20}$$

If the contrast is not maximum, the resulting fringe width σ is larger, which reduces the magnitude of G_f. The magnitude of G_f has been determined numerically from the angular shift between two fringe pattern simulations for two values of n_i that differ by a small amount, e.g., $\Delta n_i = 1.0 \times 10^{-3}$ refractive-index units, as shown in Fig. 11. For the most usual case, in which the solvent has a refractive index smaller than that of the fused silica (i.e., $n_i < n_e$), a positive change in Δn in the bore (which is due to a substance, to be detected, that is dissolved in the solvent) translates into an angular shift toward the optical axis and G_f is negative (dotted curve in Fig. 11). The fringe positions and their angular shifts $\Delta\alpha$ are more accurately determined from the zeros of the derivative of the fringe pattern (also displayed in Fig. 11), whereas their associated FWHM σ are obtained graphically by drawing tangents to the slopes and then measuring their separation. This procedure

Table 1. Computed Fringe Sensitivities G_f As Defined in Eq. (19) for the Most Important Fringes for Capillaries with 25 μm ≤ I.d. ≤ 250 μm

	25 μm[a]		50 μm		75 μm		100 μm		250 μm	
m	Angle	G_f	Angle	G_f	Angle	G_f	Angle	G_f	Angle	G_f
−0	29.7	−16 lc	35.5	−18 lc	37.8	−17 lc	39.0	−13 lc	42.0	−17 lc
−1	14.4	−31	22.8	−48	27.1	−55	29.7	−56	36.3	−61
−2	8.1	−34	16.0	−67	20.8	−81	24.0	−90	32.3	−108
−3	4.4	−34 lc	11.8	−81	16.5	−106	19.9	−119	29.3	−141
−4	1.8	? li, lc	8.7	−102	13.3	−122	16.7	−134	26.8	−186
−5	*b*	*b*	*c*	*c*	10.9	−155	14.2	−172	*c*	*c*

[a] lc, Low-contrast fringe; li, low-intensity fringe.
[b] Value does not exist.
[c] Not evaluated.

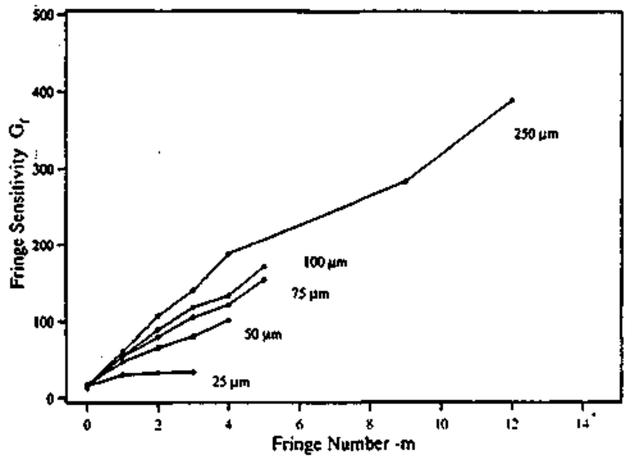

Fig. 12. Fringe sensitivity G_f as a function of fringe number m for various capillaries (data from Table 1). The larger capillaries display more fringes and, for equivalent fringes, higher sensitivities. The fringe number dependence can also be interpreted as the path-length dependence of G_f.

was repeated for all the capillaries studied and the results are summarized in Table 1.

The dependence of G_f on the fringe number and on the capillary i.d. is displayed in Fig. 12. It is noted that the sensitivity increases as a function of the fringe number. With an increasing fringe number the fringes approach the optical axis, which corresponds to longer TP paths through the fluid string and thus collects larger phase difference changes for a given variation of n_i. The fringe number dependence of G_f can, therefore, also be interpreted as its path-length dependence.

The relative insensitive behavior (e.g., constant G_f for a large angular region) for the 25-μm-i.d. capillary is due to the low contrast associated with higher-order fringes. Equivalent fringes for capillaries of different sizes are generated from rays that strike the wall interface at different angles, which explains the observed behavior in the fringe sensitivities G_f of the various capillaries studied.

In the described refractive-index detector, the fringe displacement Δn is measured with a position-sensitive photodiode whose resolving power is a function of G_f and the fringe intensity (see the shot noise and position-sensitive photodiode sections in Ref. 9). The selection of the most suitable fringe to be used in the refractive-index detector (which is called the monitoring fringe in Ref. 9) is not trivial. In addition to G_f, it requires the inspection of the power associated with each fringe. This is important to be able to determine the expected instrumental noise and thus predict the ultimate detection limit.

Furthermore, according to Eq. (11a), the maximum value of $\partial\Psi/\partial n_i$ corresponds to the fringe that appears closest to the optical axis. This fringe, however, is narrow for large capillaries and must be widened by a lens or by a long path through free air to reach the position-sensitive photodiode under optimal geometric conditions.[9] This widening introduces additional noise by temperature variations in air (e.g., schlieren effects) and refraction at the lens surfaces. However, paraxial fringes carry only a fraction of the light power compared with lower-order fringes. As a consequence of these counteracting effects a recipe for the choice of the monitoring (best) fringe cannot be easily formulated. As only a rule of thumb, one should try to use the fringes that appear as close as possible to the optical axis, provided they carry sufficient intensity and display high contrast.

Equation (19) is also useful to predict the instrumental angular resolution required in a refractive-index detector with detection limits (i.e., noise level) in the $\Delta n_i = 10^{-8}$ refractive-index unit range (which is the typical value of a good commercial refractive-index detector for HPLC with a cell path length of 1 cm and a cell volume of 10 μL). For a 100-μm-i.d. capillary the corresponding fringe width (data from Fig. 11) is $\sigma = 1.8°$ and $G_f = -119$ when the fringe order $m = -3$ is used, which indicates that the position-sensitive photodetector should be able to resolve angular spot shifts as small as $\Delta\alpha = 2 \times 10^{-6\circ}$. Commercial position-sensitive photodetectors are quoted as delivering a resolution of $10^{-6\circ}$ and, by using specific electronics, it is possible to improve the quoted spot detection by almost 1 order of magnitude,[9,15] which indicates that the construction of a refractive-index detector suitable for on-column detection with a noise level of Δn_i (noise) $= 10^{-9}$ refractive-index units is a realistic proposition, provided that one selects the proper monitoring fringe, a much higher illuminating power, such as the one used in Ref. 9 (to avoid operating at shot noise limit), and a thermal stability of $\Delta T \sim 10^{-4}$°C within a detection bandwidth of $B = 1$ Hz.

This work was supported by the CERS (Commission pour L'encouragement de la Recherche Scientifique), project 2156.1. We also thank P. Jordi for fruitful discussions and mechanical help from his workshop. Electronic help was provided by A. Wüthrich. For scientific discussion we thank F. Maystre and H. P. Herzig. This paper was presented at the OSA Laser Applications to Chemical Analysis Meeting, Salt Lake City, Utah, 1992.[16]

References

1. T. Braun and S. Nagydiosi-Rozsa, "Capillary electrophoresis: prospects for growth," Trends Anal. Chem. **10**, 266–268 (1991).
2. A. G. Ewing, R. A. Wallingford, and T. M. Olefirowicz, "Capillary electrophoresis," Anal. Chem. **61**, 292A–303A (1989).
3. N. J. Dovichi, "Laser-based microchemical analysis," Rev. Sci. Instrum. **61**, 3653–3666 (1990).
4. E. S. Yeung, *Detectors for Liquid Chromatography* (Wiley, New York, 1986), Chap. 1.
5. N. J. Dovichi, "Thermo-optical spectrometries in analytical chemistry," Crit. Rev. Anal. Chem. **17**, 357–423 (1987).
6. A. E. Bruno, A. Paulus, and D. J. Bornhop, "Thermo-optical absorption detection in 25-μm-i.d. capillaries: capillary electrophoresis of dansylamino acids mixtures," Appl. Spectrosc. **45**, 462–467 (1991).

7. D. J. Bornhop and N. J. Dovichi, "Simple nanoliter refractive index detector," Anal. Chem. 58, 504–505 (1986).
8. D. J. Bornhop and N. J. Dovichi, "Simultaneous laser-based refractive index and absorbance determinations within microliter diameter capillary tubes," Anal. Chem. 59, 1632–1636 (1987).
9. A. E. Bruno, B. Krattiger, F. Maystre, and H. M. Widmer, "On-column laser-based refractive index detector for capillary electrophoresis," Anal. Chem. 63, 2689–2697 (1991).
10. D. Marcuse, *Principles of Optical Fibre Measurements*, 1st ed. (Academic, New York, 1981), Chap. 4.5, p. 153.
11. L. S. Watkins, "Scattering from side-illuminated clad glass fibers for determinstion of fiber parameters," J. Opt. Soc. Am. 64, 767–772 (1974).
12. M. Born and E. Wolf, *Principles of Optics* (Pergamon, New York, 1980), Chap. 1.5, p. 36.
13. A. Yariv, *Optical Electronics* (Holt, Rinehart & Winston, New York, 1985), Chap. 2.5, p. 28.
14. R. E. Synovec, "Refractive index effects in cylindric detector cell designs for microbore high-performance liquid chromatography," Anal. Chem. 59, 2877–2884 (1987).
15. J. Pawliszin, M. F. Weber, and M. J. Dignam, "Dual-beam laser deflection sensor," Rev. Sci. Instrum. 56, 1740–1743 (1985).
16. A. E. Bruno, "Laser based refractive index detection in capillary tubes," in *Laser Applications to Chemical Analysis*, Vol. 2 of 1992 OSA Technical Digest Series (Optical Society of America, Washington, D.C., 1992), p. 165.

Chapter 4 Enhanced Refractive Index Detection for Capillary Electrophoresis Using Flared Capillaries.

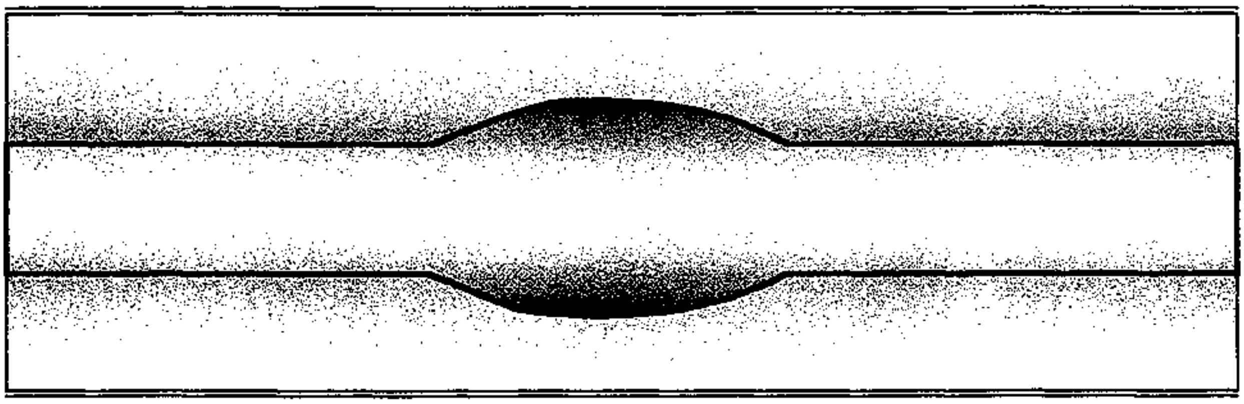

Enhanced Refractive Index Detection for Capillary Electrophoresis Using Flared Capillaries.

José María Saz[#], *Beat Krattiger*[†], *Alfredo E. Bruno*[†,*], *François Maystre*[†] *and H. Michael Widmer*[†]

[†]CIBA-GEIGY Ltd., Corporate Analytical Research, 4002 Basle, Switzerland,

[#] Department of Analytical Chemistry, Faculty of Science, University of Alcalá de Henares, 28871 Alcalá de Henares, Madrid, Spain.

ABSTRACT

A novel on-column refractive index detector suitable for capillary electrophoresis, whose optical arrangement is based on a known interferometric principle[1], is described. In the present version the holographic element is replaced by two conventional optical elements, a Wollaston prism and a microscope objective. When using RI detection in capillary electrophoresis the noise is dominated by Joule heat effects, therefore we introduce the use of flared capillaries to minimize its impact. Typical flared capillaries have a three times larger diameter at the bubble, where optical detection is performed, than at the separation section resulting in a large enhancement in the instrumental sensitivity. The usefulness detector has been demonstrated in the capillary electrophoretic separation of a mixture of underivatized sugars resulting in detection limits in the high μM range.

Key Words: Refractive Index, interferometry, capillary electrophoresis, flared capillary, Wollaston prism, underivatized sugars.

[*] To whom correspondence should be submitted.

INTRODUCTION.

Recent instrumental improvements[1-4] in refractive index (RI) detectors for capillary electrophoresis (CE) are bringing this rather insensitive technique closer to the useful realm. The most recent improvement was given by Krattiger et al.[1] who introduced the use of holographic optical elements in optical detection for CE in a compact and highly sensitive RI detector which was used with capillaries having inner diameters (i.d.s) as small as 5 µm. The holographic element, in this "on-axis" interferometric design[3], divides the initial beam into two focusing beams. One beam probes the capillary bore through the middle whereas the second beam, propagating through the capillary wall and refractive index matching (RIM) material, acts as the reference beam in this double-slit Young interferometer[5]. Because in this arrangement the probing beam propagates through the middle of the core the fully available optical path length is used, as compared to e.g. the "off-axis" designs[2, 7], larger shifts of equally spaced fringes detected by a photo-diode array (PDA) result in higher instrumental response.

Electrical currents produce Joule heat[8] which is known to degrade separation efficiency in CE due to band broadening and, when using RI detection, it is the dominant source of noise due to schlieren effects in the buffer[2]. Considering that these thermal effects are proportional to the cross section of the capillary and also, that small i.d. tubes offer a higher surface to volume ratio which facilitates heat dissipation through the capillary wall, the use of smaller i.d. capillaries is preferred from the separation point of view. However, as the decrease in optical path length is correlated with a reduction in the sensitivity, the optimum capillary diameter is the result of a compromise between detection and separation arguments.

The RI detector presented here uses an optical arrangement identical to that recently reported[1]. However, the core of the interferometer, given by the holographic element in the previous design[1], is realized here by means of a set of conventional optical elements. The main novelty in the present arrangement is the use of flared capillaries (Fig. 1) to enhance the instrumental sensitivity. Flared capillaries, presently in use in conjunction with UV/vis detectors, allow an increase in optical path lengths without compromising the benefits observed in the separation efficiency associated to thinner capillaries. The performance of this detector is evaluated using a synthetic mixture of underivatized sugars as test sample.

THEORY

Principle of operation.

The optical configuration of this detector is identical to that of the hologram-based RI detector described in Ref. 1. In the present version the holographic element is replaced by two conventional optical elements, a Wollaston prism[6] and a microscope objective (MO), arranged as shown in Fig. 2. The diverging beam of a laser diode (LD), which is first collimated by a lens within the laser module, is divided by the Wollaston into two orthogonally polarized beams diverging by an angle α. The MO, placed at its focal distance f from the Wollaston, makes both beams parallel and focuses them. The capillary is placed also at the distance f from the MO (i.e., the Wollaston and capillary are placed symmetrically with respect to the MO) in such a way that its bubble intercepts the probe beam. The remaining beam, the reference beam, propagates undisturbed by its side. Both beams, the probing and reference beam, can, after passing a polarizer, recombine and mix in the far field and, because they originate from the same coherent source, they build a regularly spaced interference pattern as shown in Fig. 2.

Changes in the refractive index (Δn) in the bubble part of the capillary modify the optical phase of the probing beam resulting in a lateral shift of the interference pattern. These shifts are monitored by a PDA wired to produce a position sensitive output signal[1, 2] which, upon calibration, becomes the output signal of the RI detector. The polarizer at 45°, placed before the PDA (Fig. 2), ensures maximum contrast of the fringes. The capillary bubble is surrounded with RIM material (n = 1,46) to eliminate unwanted reflection and refraction at the optical interfaces[2] as well as to allow an efficient removal of the Joule heat produced in CE which is known[2] to contribute to the overall noise due to schlieren effects in the buffer.

Beam diagnostic.

The beam waists (twice the spot size, i.e., 2 w_0) of both beams, at the focal point of the ten times MO employed (f = 17 mm), is estimated by

$$w_0 = \frac{2\lambda f}{\pi d}, \qquad (1)$$

where d are the original beam diameters. The spot size is fifty times smaller than the i.d. at the bubble (i.d. = 150 μm) implying that the entire probing beam propagates through the capillary flare.

The beams after the MO, are separated by a distance D which is approximately given by

$$D \approx f\,\alpha, \qquad (2)$$

where α is the diverging angle of the Wollaston prism employed. In the present case $\alpha = 0.5°$ and thus D = 150 μm which is about half the external diameter of the capillary (o.d. = 340 μm). The reference beam propagates thus through the capillary wall without intercepting the core.

Instrumental response

As in the hologram based RI detector[1], the instrumental response is given by

$$\frac{dU}{dn} = \frac{4\ C\ i.d.\ K}{\lambda}, \qquad (3)$$

where dU/dn is the change in the voltage output per RI unit (RIU) change, K the amplification of the electronic circuit (10 V in our case) and C the fringe contrast given by[5]

$$C = \frac{I_{max} - I_{min}}{I_{max} + I_{min}}. \qquad (4)$$

In Eq. 4, I_{max} and I_{min} refer to the maximum and minimum intensity observed in the fringe pattern. In practice C is most easily determined by noticing that

$$C = \frac{U_{max}\,\pi}{2\ K}, \qquad (5)$$

(derived from Eq. 13 of Ref. 1) and by measuring the highest signal voltage, U_{max}, as the PDA is scanned through the fringe pattern. The maximum signal measured in our instrument was 6 V leading to a contrast of C = 0.94 which is very close to the maximum ($C_{max} = 1$) to be observed when I_{min} is zero (Eq. 4). The instrumental response of our instrument is, as computed with Eq. 3, dU/dn = 8.4 mV/μRIU

EXPERIMENTAL SECTION

RI Detector

The RI detector (Fig. 2) was assembled almost entirely with commercially available components (Spindler & Hoyer, Germany). The multimode LD, the driving electronics and the collimating lens are contained in the laser module (LDM 135, Imatronic Inc., Batavia, IL). The LD lases at 672 nm and delivers 1 mW of output power. Precautions are taken to adjust the LD chip parallel with respect to the capillary to minimize the effects of aberration. The Wollaston prism (PWQ30.10, Bernhard Halle Nachfl. GmbH & Co., Berlin, Germany), MO (Spindler & Hoyer, Germany) and polarizer are adjusted to produce the best fringe contrast.

The flared part of the capillary is introduced in a heavy wall fused silica tube (i.d. ≈ 1 mm, o.d. ≈ 6 mm) and the empty space is filled with RIM material (# 19569 and 19571, R.P. Cargille Laboratories Inc., Cedar Grove, NJ, USA) to form the "detection cell". One side of the heavy wall tube was polished flat to form the "entrance window" and it was mounted in an aluminum body.

Only 14 of the 46 elements PDA (S4111 series, Hamamatsu) are used to detect 7 adjacent fringes. The odd and even numbered elements are wired together (as shown in Fig. 4 of Ref. 1) and both channels are fed into a position sensitive amplifier (Model 301-DIV, UDT, Hawthorne, CA) delivering a signal proportional to the fringe shift which is rather insensitive to light intensity fluctuations[2]. The LM and the detection cell are thermostatized by temperature controllers (Model LDT-5412, ILX Lightwave, Bozeman, MT) using Peltier elements (Melcor, Trenton, NJ). The LabVIEW (National Instruments, Austin, TX) and IGOR (WaveMetrics, Lake Oswego, OR) software packages, running on a Macintosh IIfx ,were used for data acquisition and analysis.

Capillary electrophoresis.

The flared capillary (Hewlett Packard, #G 1600-61-231) employed had an i.d. of 50 µm at the separation part and 150 µm at the bubble (Fig. 1) and a length of 60 cm (50 cm to the detector). The standard 50 µm-i.d. capillary (Polymicro, Phoenix, AZ, USA), used for comparison purposes, had a length of 75 cm (50 cm to detector). CE is performed at 8 kV and 10 kV with the flared and standard capillary, respectively. Injection, in both cases, was hydrodynamically performed with a Prince CE system (Lauer Labs, Emmen, The Netherlands). Chemicals were purchased from Merck (Darmstadt, Germany) and Fluka (Buchs, Switzerland).

RESULTS AND DISCUSSION

The present RI detector is demonstrated with both a flared and a standard capillary in the CE separation of a mixture of six underivatized sugars. The corresponding electropherograms are shown in Figs. 3a and 3b. Most sugars are neutral species and therefore not eligible for CE (see Ref. 9 for the pK and Ref. 10 for the mobilities of sugars). This difficulty is overcome using borate buffers[4, 9-11]. Borate complexes sugars into various types of negatively charged species. The magnitude of the charge, and thus their electroosmotic mobility, depends mainly on the concentration of borate. Six forms of sugars coexist in aqueous solutions, α- and β- pyranoses and furanose forms, as well as the open-chain and hydrated forms multiplying the complexation possibilities. Saccharose and raffinose complexes into a single species and therefore appear as the sharpest peaks in the electropherograms. The broadening observed in the other peaks is due to the various complexes associated with each type of sugar having similar mobilities (rather than to column overloading). Optimal results were obtained with a 33 mM borate/13.3 mM CAPS buffer (3-cyclohexylamino-1-propane sulfonic acid) at pH 9.4 where the current decreased by a factor of about four with respect to a 100 mM borate buffer previously used[2] while efficiency is maintained.

Table 1 summarizes the S/N and the limits of detection (LOD) obtained with the normal and flared capillary with the present RI detector from the raffinose peak in the electropherograms shown in Figs. 3a and 3b. The theoretical plate numbers, determined from the raffinose peak, are 60'000 and 130'000 for the standard and flared capillary, respectively. The electrophoretic mobilities of the investigated sugars in the buffer employed are reported in table 2.

Table 1: Signal, Noise and Limits of Detection obtained with the standard and flared capillary. Peak height data from the raffinose peak in Figs. 3a and 3b.

	Standard Capillary	**Flared Capillary**	$\frac{\textbf{Flared}}{\textbf{Standard}}$
Signal [mV]	221	706	3.2
Noise [mV]	11.5	6.75	1.7
S / N	19	105	5.4
LOD [µM]	860	160	0.19

Table 2: Electrophoretic mobilities obtained with the standard and flared capillaries obtained for various sugars in the borate/CAPS buffer employed.

	Standard $[10^{-5}\ \mathrm{cm^2/Vs}]$	**Flared** $[10^{-5}\ \mathrm{cm^2/Vs}]$
SAC	3.65	3.56
NAG	4.54	4.46
RAF	6.09	6.01
MAL	7.14	6.99
LAC	8.86	8.73
RIB	-	18.10

The increase in the capillary i.d. at the detection zone, offered by flared capillaries when using RI detection, results in a decrease in the overall noise and an increase in the signal, leading to a five fold enhancement in the S/N. Although the observed threefold increase in the signal is easily explained using

Eq. 3, dealing with the instrumental response, a quantitative analysis to explain the observed decrease in the noise is not straightforward.

There are various sources contributing to the overall noise. Schlieren effect in the detection path caused by Joule heat is, in the present case, the dominant source[2] while the electronics, particles or bubbles in the buffer and wavelength jitter contribute to a lesser extent to the overall noise. With regards to Joule heat there are a few factors that play a role in dissipating heat in the presence of flared capillaries. Considering that FS has good heat conducting property, and air a poor one, the rate of heat dissipation for naked capillaries is mainly determined by the o.d. and the inner volume-to-surface ratio which increases for smaller capillaries. In the case of capillaries having their outer wall in contact with RIM materials the o.d. can be considered as infinite and the volume-to-surface plays a smaller role in determining the rate of heat dissipation. It has to be noticed that the total electrical current (I) remains constant along the capillary including the bubble. However, at the bubble, the cross section is nine times higher, therefore the associated electrical resistance (R) is nine times smaller than in the rest of the capillary and, the electric field (E) should decrease also by the same amount (i.e. $E \approx R * I$). Because Joule heat, and its associated schlieren effects, are caused by the electrical field, they should also decrease explaining the observed reduction in the noise.

The separation efficiencies obtained from the electropherograms displayed in Figs. 3a and 3b are rather similar. Although the bubble introduces a small dead volume in the capillary, the smooth change in cross section (see Fig. 1) should not alter the laminar flow, and peak broadening is not expected. The small differences in the electrophoretic mobilities reported in Table 2 are within the experimental error.

CONCLUSION

The "on-axis" illumination configuration for the construction of capillary RI detectors, based on commercially available optical elements, here proposed provides more flexibility and is certainly easier to realize than the configuration based on holographic plates. One advantage offered by the present arrangement is that light losses are very small at the Wollaston as compared to those associated to a hologram given by the diffraction efficiencies which are in the 10 - 30 % range. However, using multi-element photo-detectors, light intensity is no longer an issue in the quest for higher sensitivity. The major issue in this regard is thermal and mechanical stability[3] which is better achieved using miniature optical components such as holographic plates. Therefore, we believe that the best capillary RI detector would be one based on "on-axis" illumination using a holographic element and featuring a flared capillary. The LODs reported in table 1 are better than those reported in Ref. 2 and comparable to what is obtained by other methods provided that the sugars are not derivatized[4, 10].

ACKNOWLEDGMENTS

The authors would like to thank P. Nussbaum and R. Dändliker (Institut de Microtechnique, Neuchâtel, Switzerland) for lending us the Wollaston prism and for providing us technical support. One of us (J. M. S) would like to thank J. C. Díez-Masa (Instituto de Química Orgánica del CSIC) for making the three month visit to the Ciba-Geigy laboratories possible and, to the Universidad de Alcalá de Henares and Comunidad Autonoma de Madrid, for the financial support.

BIBLIOGRAPHY

(1) Krattiger B.; Bruin, G. J. M.; Bruno, A. E. *Anal. Chem.*, 1994, *66*, 1.

(2) Bruno, A. E.; Maystre, F.; Krattiger, B.; Widmer, H. M. *Anal. Chem.*, **1991**, *63*, 2689.

(3) Bruno, A. E.; Krattiger, B.; Maystre, F.; Nussbaum, P.; Gassmann, E., *Trends in Anal. Chem.*, (in press).

(4) Bruno, A. E.; Krattiger, B. In *Carbohydrate Analysis*; Rassi, E., Ed.; Elsevier: New York; chapter 13. (in press).

(5) Born, M.; Wolf, E. In *Principles of Optics*; Pergammon Press: New York, 1989.

(6) Hecht, E.; Zajac, A. In *Optics*; Addison-Wesley Publishing, Inc.: Reading, Massachusetts, 1979.

(7) Krattiger, B.; Bruno, A. E.; Widmer, H. M.; Geiser, M.; Dändliker, R. *Appl. Opt.* **1993**, *32*, 956.

(8) Li, S. F. Y. In *Capillary Electrophoresis*, Elsevier: New York, 1992.

(9) Rendle, J. A. In *Carbohydrates in Solution*, Isbell, H. S. Ed.; ACS: Washington DC, 1973, p. 54.

(10) Hoffstetter-Kuhn, S.; Paulus, A.; Gassmann, E.; Widmer, H. M.; *Anal. Chem.*, **1991**, *63*, 1541.

(11) Honda, S.; Iwase, S.; Makino, A.; Fujiwara, S. *Anal. Biochem.*, **1989**, *176*, 72.

FIGURE CAPTIONS

Fig. 1: Picture of the bubble of the flared capillary employed. The i.d.s at separation part and bubble are 50 µm and 150 µm, and the o.d. are 310 µm and 340 µm, respectively.

Fig. 2: Diagram of the detector experimental set-up. **LM:** laser module, **WP:** Wollaston prism, **MO:** microscope objective, **C:** capillary cell, **P:** polarizer, **F:** fringe pattern, **PDA:** photo-detector array.

Fig. 3: Electropherograms of a mixture of sugars obtained with the RI detector operated in conjunction with **a)** the bubble and **b)** the standard capillaries. The peaks are identified as: **SAC:** saccharose, **NAG:** N-acetyl-D-glucosamine, **RAF:** raffinose, **MAL:** maltose, **LAC:** lactose, **RIB:** ribose. Electrical field of 10 kV and a current of 19 µA. The concentration of each sugar is 8,3 mM and the electrophoretic conditions and buffer employed are reported in experimental section.

Fig. 1

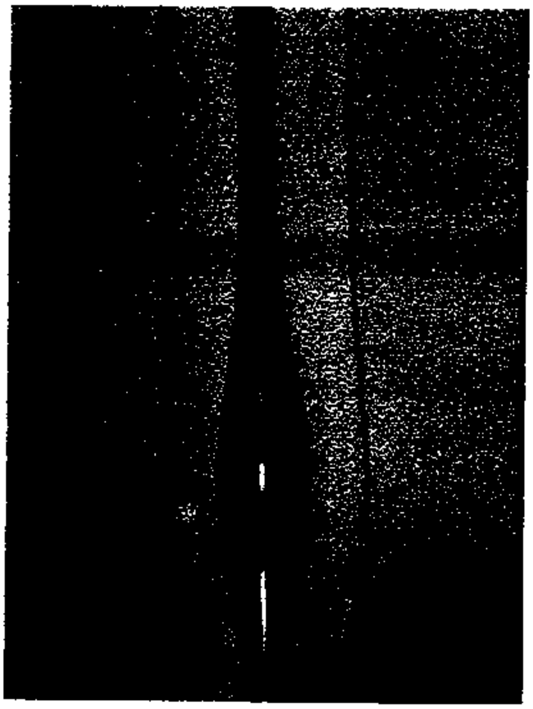

Fig. 1

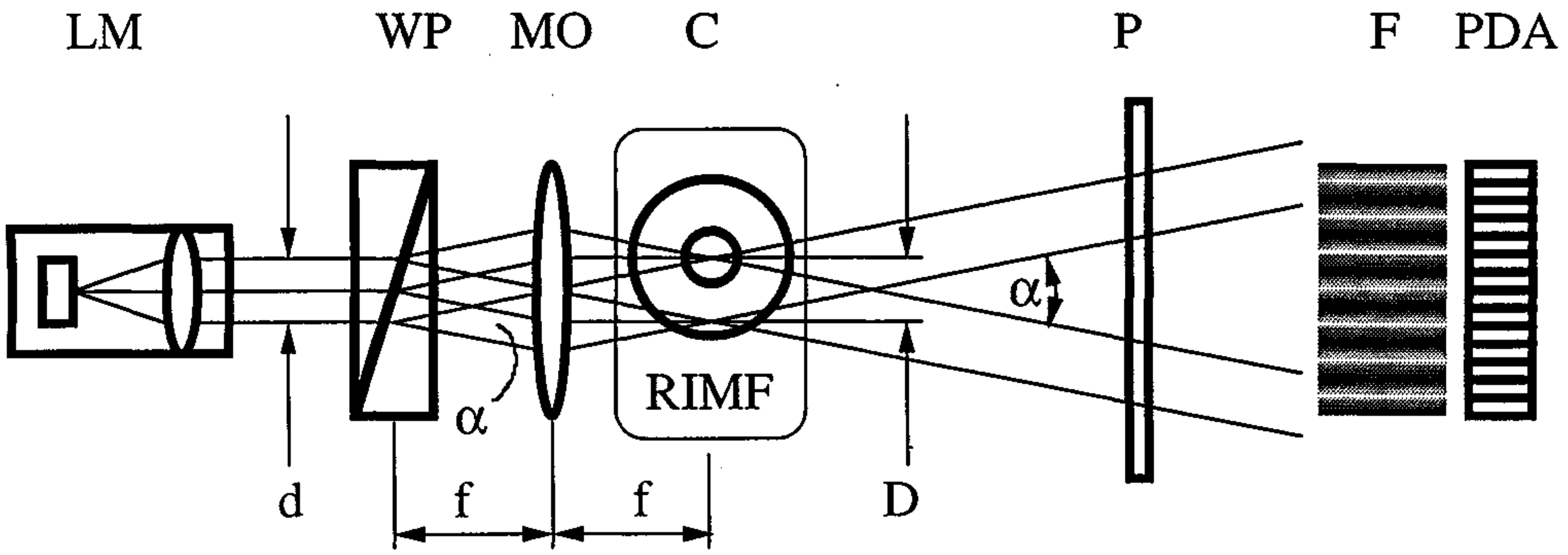

Fig. 2

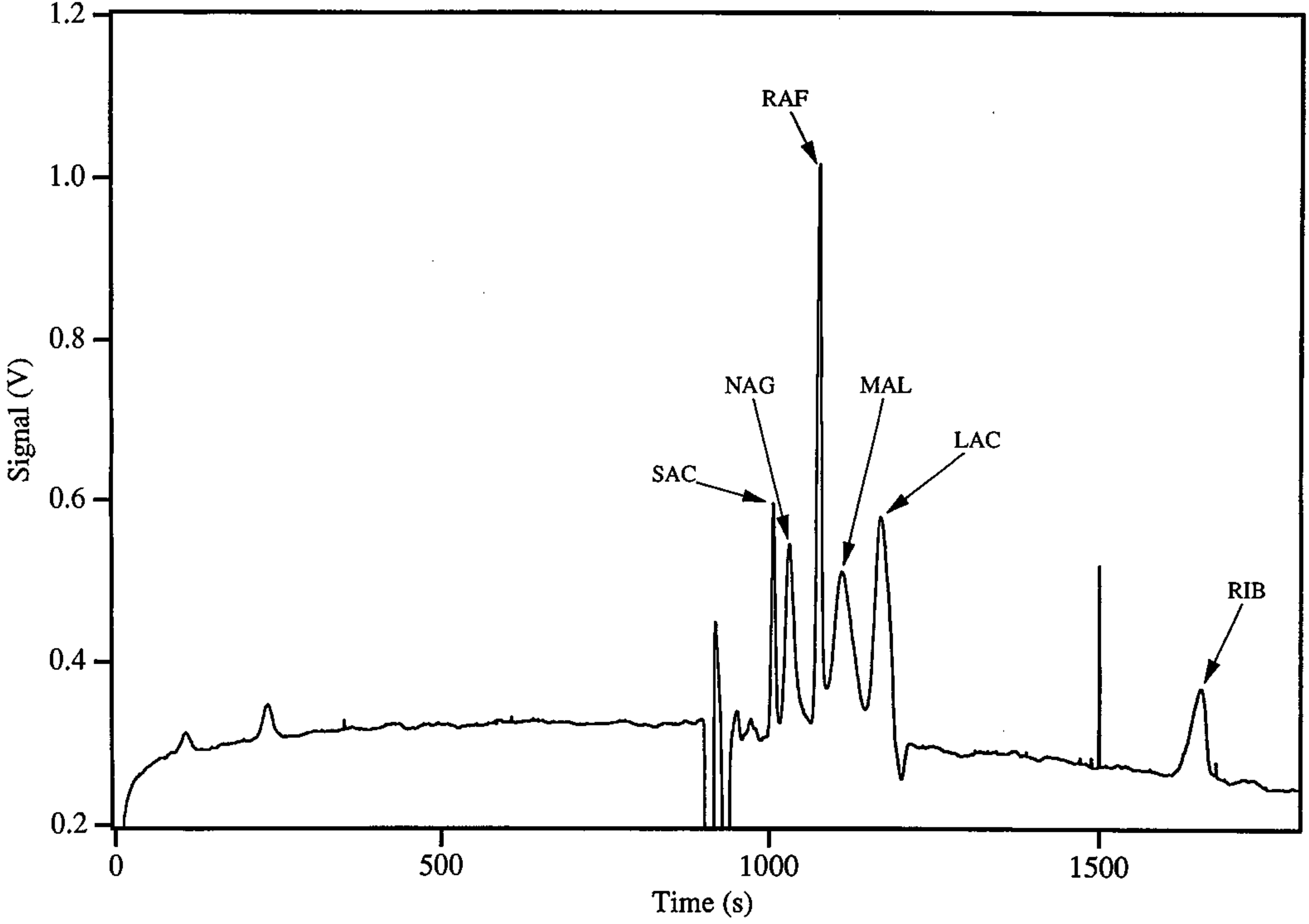
1.2
1.0
0.8
0.6
0.4
0.2
Signal (V)
0
500
1000
1500
Time (s)
RAF
NAG
MAL
LAC
SAC
RIB

Fig. 3a

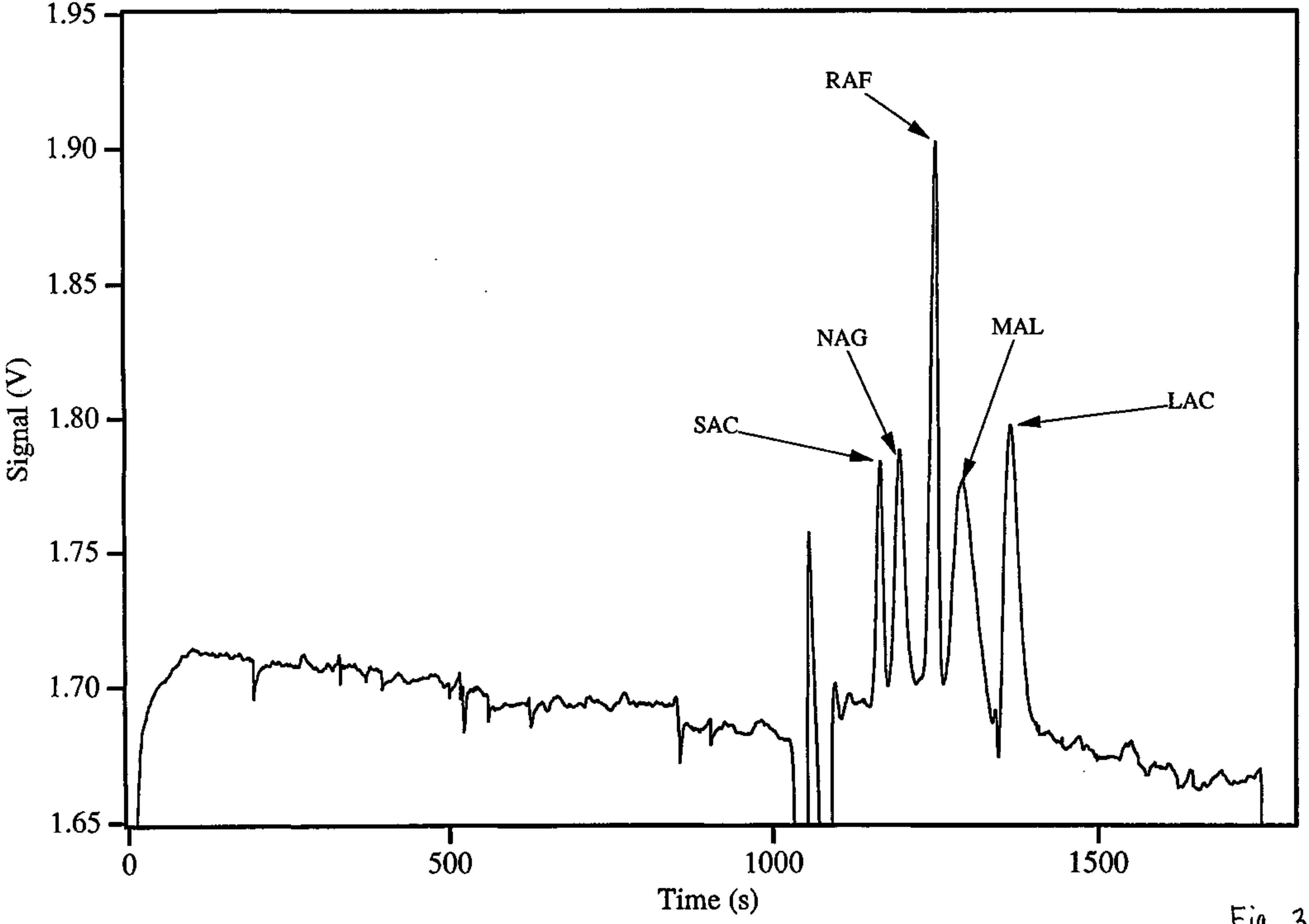
1.95
1.90
1.85
1.80
1.75
1.70
1.65
Signal (V)
0
500
1000
1500
Time (s)
RAF
NAG
SAC
MAL
LAC

Fig. 3 b

Chapter 5 Hologram-Based Refractive Index Detector for Capillary Electrophoresis: Separation of Metal Ions

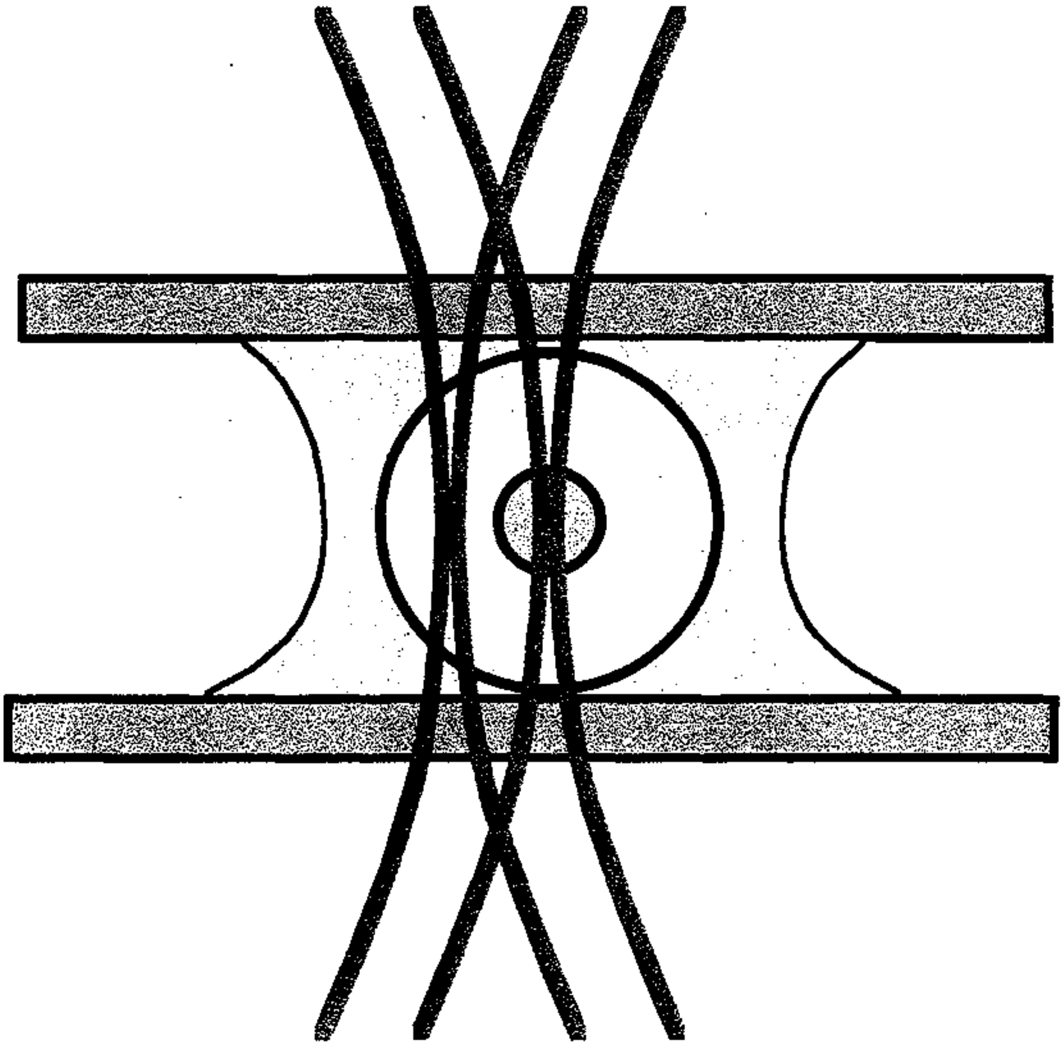

Reprinted from Analytical Chemistry, 1994, *66*.

Hologram-Based Refractive Index Detector for Capillary Electrophoresis: Separation of Metal Ions

Beat Krattiger, Garard J. M. Bruin, and Alfredo E. Bruno*
Ciba Geigy Ltd., Corporate Analytical Research, 4002 Basle, Switzerland

A novel refractive index detector suitable for capillary separations is presented and demonstrated in the capillary electrophoretic separation of metal cations in 10-μm-i.d. tubes. The principle of the detector is interferometric; it features a laser diode and, as the main optical element, a holographic optical element which performs several optical functions allowing the use of capillaries with inner diameters as small as 5 μm. In contrast to the "off-axis" method, the use of holographic plates permits probing of the capillary through its center, where the optical path is larger and diffraction effects are smaller. With an i.d. = 10 μm capillary the detector resolves 2 μRIU and covers a linear dynamic range of three to four decades. Joule heat effects preclude the detector to operate at its maximum sensitivity which is delivered in the absence of electrical fields. For this reason, the use of smaller inner diameter capillaries and buffers having low conductivities is recommended. Under field-amplified sample injection conditions, the detection limits for the studied cations are in the low nanomolar range. The performance of this detector is compared with indirect UV-absorption detection, which also helps to elucidate the mechanisms leading to refractive index changes in ionic solutions.

Considering that holographic optical elements (HOEs) could greatly simplify the construction of optical instruments without compromising performance, their use is gaining acceptance in analytical instrumentation such as spectrographs.[1,2] The present investigation represents the first application of HOEs to on-column refractive index (RI) detection for the analysis of transparent substances using capillary electrophoresis (CE).

Optically dense compounds are most commonly detected by absorbance methods, and when the substances of interest emit, sensitive fluorescence methods (e.g., laser-induced fluorescence, LIF) are recommended. For transparent substances, such as carbohydrates or small ions without chromophoric groups absorbing above 200 nm, other schemes have been devised which involve either pre- and postcolumn derivatization combined with LIF detection,[3] indirect UV absorbance (IUVA)[4] or indirect fluorescence detection (IF),[5] RI detection,[6,7] or amperometric detection methods.[8] RI detection, together with IUVA, IF, and amperometry, remain as interesting options for those cases where derivatizations are difficult or are not yet available for the substances of interest.

The interest in developing universal RI detectors for capillary separation techniques is twofold. First, it is a relatively simple technique, useful in the micro- to millimolar range, which can be used with a wide spectrum of buffers, and as shown in this study, it offers the possibility of miniaturization. A second interest stems from the fact that capillary RI detectors can be readily used to perform sensitive absorption detection in narrow-bore capillaries (i.d. ≤ 50 μm) using thermooptical (TO) methods[9a,10] as required, for example, in the pharmaceutical industry for in vivo studies where chemical derivatizations are not desired.

---

* Author to whom correspondence should be addressed.

(1) Tedesco, J. M.; Owen, H.; Pallister, D. M.; Morris, M. D. *Anal. Chem.* 1993, *65*, 441A.

(2) Bains, S. *Laser Focus World* 1993, *29* (4), 151.

(3) (a) Cheng, Y.-F.; Wu, S.; Chen, D.-Y.; Dovichi, N. J. *Anal. Chem.* 1990, *62*, 496. (b) Zhao, J. Y.; Waldron, K. C.; Miller, J.; Zhang, J. Z.; Harke, M.; Dovichi, N. J. *J. Cromatogr.* 1992, *608*, 239. (c) Albin, M.; Weinberger, R.; Sapp, E.; Moring, S. *Anal. Chem.* 1991, *63*, 417.

(4) Bruin, G. J. M.; Asten van, A. C.; Xu, X.; Poppe, H. *J. Cromatogr.* 1992, *608*, 97.

(5) (a) Kuhr, W. G.; Yeung, E. S. *Anal. Chem.* 1988, *60*, 2642. (b) Garner, T. W.; Yeung, E. S. *J. Cromatogr.* 1990, *515*, 639.

(6) Bruno, A. E.; Krattiger, B.; Maystre, F.; Widmer, H. M. *Anal. Chem.* 1991, *63*, 2689.

(7) Krattiger, B.; Bruno, A. E.; Widmer, H. M.; Geiser, M.; Dändliker, R. *Appl. Opt.* 1993, *32*, 956.

(8) Huang, X.; Pang, T.-K.; Gordon, M. J.; Zare, R. N. *Anal. Chem.* 1987, *59*, 2747.

(9) (a) Bornhop, D. J.; Dovichi, N. J. *Anal. Chem.* 1987, *59*, 1632. (b) Dovichi, N. J.; Zarrin, F.; Nolan, T. G.; Bornhop, D. J. *Spectrochim. Acta* 1988, *43B*, 639. (c) Bornhop, D. J.; Dovichi, N. J. *Anal. Chem.* 1986, *58*, 1986.

(10) Bruno, A. E.; Paulus, A.; Bornhop, D. J. *J. Appl. Spectrosc.* 1991, *45*, 462.

0003-2700/94/0366-0001$04.50/0

Earlier versions of capillary RI detectors exploited the interference fringe pattern characteristic of side "off-axis" laser illuminated capillaries. The optical interfaces of the capillary split the illuminating beam into a *reflected*, a *refracted*, and a *transmitted* beam fan which all overlap and interfere in the far field, yielding a characteristic fringe pattern. Changes in the RI of the streaming liquid in the capillary shift the position of the fringes which, upon processing, constitute the output signal. The off-axis method was demonstrated by Bornhop and Dovichi[9a] in flow injection analysis (FIA), in high-performance liquid chromatography (HPLC), and in CE using thermooptical detection in 50-μm tubes. Similar TO experiments were subsequently performed by Bruno et al.[10] with 25-μm tubes using frequency-doubled light from an Ar^+ laser.

The off-axis method was demonstrated in CE by Bruno et al.[6] in the analysis of underivatized sugars in a 50-μm-i.d. capillary. The experimental setup was conceived to simplify the fringe pattern, obtain a higher thermal stability in the capillary, and minimize the effect of laser noise in the output signal. Such improvements were achieved mainly by using refractive index matching (RIM) materials around the capillary and by using position-sensitive detectors (PSDs) to monitor fringe shifts. Under these experimental conditions, Joule heat was identified as the main source of noise. For this reason, and in order to maximize S/N ratios, it is recommended that small inner diameter capillaries be used as much as possible.

Support from the theoretical side was given by Synovec and Krattiger. Synovec[11] provided a ray tracing analysis for wide-bore capillaries (i.d. $\geq$ 475 μm) for the pure deflection situation (i.e., absence of interferences and diffractions). More recently, Krattiger et al.[7] provided the complete theoretical analysis for the interference case in the absence of diffraction effects for capillaries ranging from 25 to 250 μm. In this study[7] it was shown that in the off-axis method the laser beam does not probe the maximum optical path available, thus resulting in a loss of sensitivity, and for capillaries with i.d. $<$ 10 μm, diffraction effects dominate the resulting interference pattern.

Another method for detection of RI changes in capillaries was published by Pawliszyn.[12] In this method one detects the RI gradient along the capillary, which renders the derivative of the signal of interest and is thus more suitable for isotachophoresis (ITP) rather than for capillary zone electrophoresis (CZE). For proteins, in isoelectric focusing experiments, the detection limits are comparable to those obtained in UV absorbance.[12b]

In this paper we demonstrate a RI detector based, as in the off-axis method, on an interferometric operation principle. The optical functions leading to interferences, performed by the capillary in the off-axis model, are instead performed by a HOE in the present model. Here, the sampling arm of the interferometer crosses the capillary through its center where the optical path is longer and diffraction effects smaller. The performance of this detector is compared to IUVA detection in a CE separation of small cations. These experiments also help to elucidate the mechanisms leading to refractive index changes in ionic solutions.

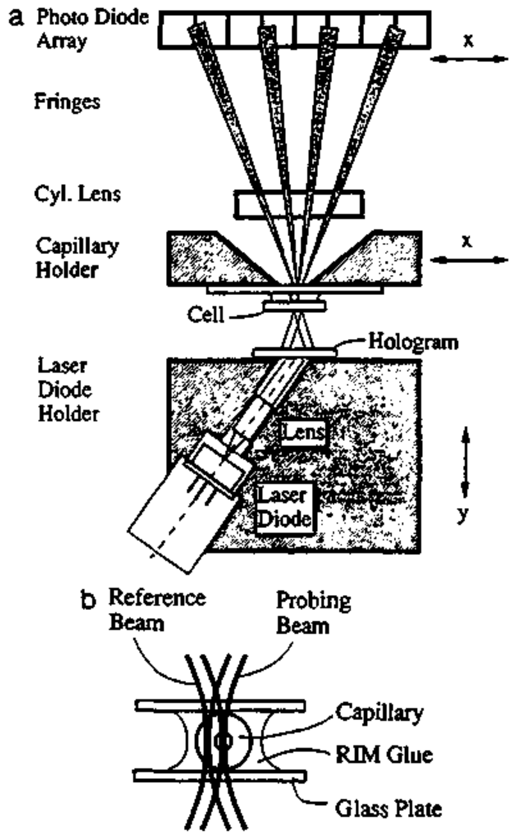

Figure 1. (a) Overview of the hologram RI detector showing all optical components and (b) details of the capillary cell. The capillary (z axis) and the eight-element photodiode array can be displaced along the x axis whereas the LD, collimating optics, and HOE can be adjusted along y.

THEORY

Principle of Operation. The principle of operation of the present RI detector is similar to that of a double-slit Young[13] interferometer where the two arms are realized by means of a HOE as indicated in Figure 1. Coherent light is provided by the collimated output of a laser diode (LD) which is partially deflected by the HOE placed at a given angle ($\approx$30°) with respect to the illumination beam. This HOE acts as a set of two nearly superimposed focusing lenses laterally displaced by a distance D which is slightly larger than the capillary bore radius plus the beam waist w_0 ($D >$ (i.d./2) + w_0) producing an output like the one shown in Figure 2.

The capillary, glued between two parallel glass plates with RIM glue, is placed at the focal point of the *probing* beam while the *reference* beam propagates beside the capillary bore through the RIM glue and capillary wall as indicated in Figure 1b. Both beam fans overlap in the far field, and as both originate from the same wave, they interfere, leading to regularly spaced fringes. RI changes (Δn_l) in the capillary bore induce phase changes in the probing beam which, in turn, translate into lateral shifts of the fringe pattern. Because the fringes are equally spaced, shifts are conveniently mon-

---

(11) Synovec, R. E. *Anal. Chem.* **1987**, *59*, 2877.
(12) (a) Pawliszyn, J. *Anal. Chem.* **1988**, *60*, 2796. (b) Wu, J.; Pawliszyn, J. *Anal. Chem.* **1992**, *64*, 219. (c) Wu, J.; Pawliszyn, J. *Anal. Chem.* **1992**, *64*, 224. (d) Wu, J.; Pawliszyn, J. *Anal. Chem.* **1992**, *64*, 2934.

(13) Born, M.; Wolf, E. In *Principles of Optics*; Pergammon Press: New York, 1989.

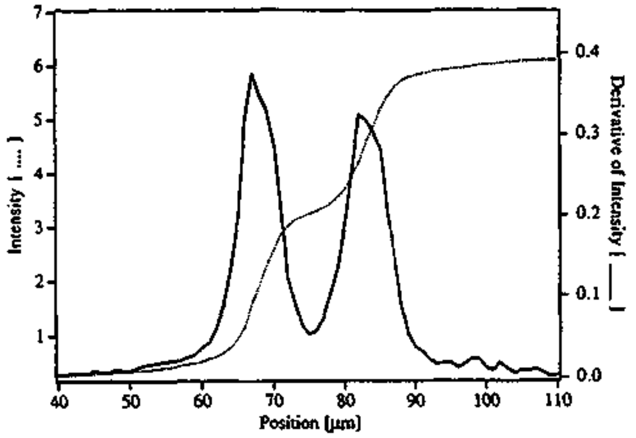

Figure 2. Typical output (solid line) of a HOE at its focal points as the first derivative of the cumulated intensity (dotted line) recorded using the knife edge method. The spot separation in this case is 14 μm.

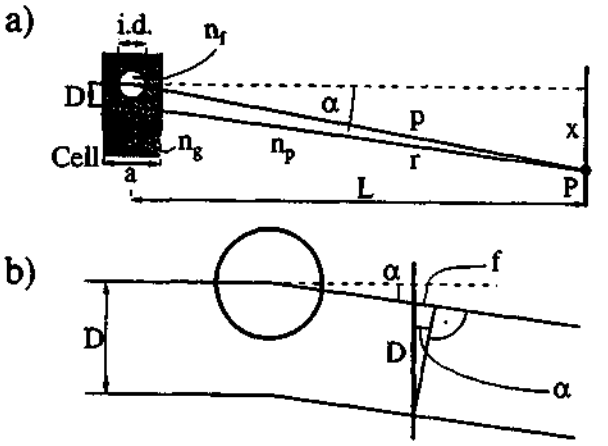

Figure 3. (a) Optical paths of the *probing* and *reference* rays. These rays have a spot separation *D* and travel from the capillary cell to the PDA where they recombine in *P*. (b) Geometric parameters used to derive the path difference f between two interfering rays defining an angle α with the optical axis (dotted line).

itored by a photodiode array (PDA) wired to produce position-sensitive detection[6] (PSD). To gather more light at the PDA, the fringe pattern is compressed along the z dimension by a cylindrical lens. As the fringes shift with Δn_f, the output of the PSD electronic circuit constitutes, upon calibration, the output signal of the RI detector.

Instrumental Response. The response delivered by the present instrument can be accurately predicted by a simple equation in terms of geometric parameters and fringe contrast. This equation is derived by computing the fringe shifts as a function of Δn_f combined with the mathematical description of the optoelectronic response.

(a) Fringe Shifts. The expressions describing the optical phases, φ_p and φ_r, of the *probing* and *reference* ray, respectively, in the meeting point *P* are derived with help of Figure 3, where their corresponding propagation lengths are displayed. Accordingly, the length difference f between the two rays is given by

$$f = D \sin \alpha \qquad (1)$$

where D is the spot separation and α the angle between the rays and the optical axis. Considering that for small angles $\sin \alpha \approx \tan \alpha \approx \alpha$ and $\cos \alpha \approx 1$ (paraxial approximation),

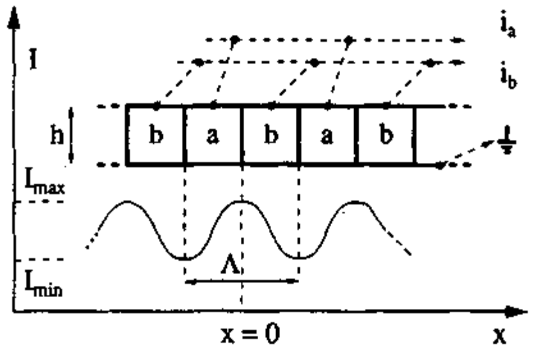

Figure 4. Diagram of the PDA (middle) showing its parallel wiring of the "a" and "b" PDA elements (top) and the periodic fringe pattern (bottom). The dotted arrows indicate electrical connections.

eq 1 can be rewritten as

$$f = xD/L \qquad (2)$$

where x and L are the position of the fringe and the distance from the capillary to the PDA, respectively. The PDA is positioned at a distance L such that each fringe matches a pair of PDA elements separated by a spacing Λ (Figure 4). For one wavelength difference between both rays $x = \Lambda$ and $f = \lambda_0/n_p$ and the spacing becomes

$$\Lambda = L\lambda_0/n_p D \qquad (3)$$

where n_p is the refractive index of air. The accumulated phases (number of wavelengths multiplied by 2π) of the reference and probing rays, φ_r and φ_p at P, (Figure 3) can be written as

$$\varphi_r = \frac{2\pi}{\lambda_0}[an_g + Ln_p] \qquad (4a)$$

$$\varphi_p = \frac{2\pi}{\lambda_0}[(a - \text{i.d.})n_g + \text{i.d.}n_f + (L + f)n_p] \qquad (4b)$$

where both phases are identical at the entrance surface of the cell ($\varphi_r = \varphi_r = 0$) and n_g, n_f, and n_p are the refractive indexes of the propagating media, i.e., glass, fluid in the capillary bore, and air, respectively.

Interferences (constructive superposition of rays) at P (Figure 3) are observed whenever the phases associated with the *probing* and *reference* rays differ exactly by $2\pi m$

$$\varphi_r = \varphi_p + 2\pi m \qquad (5)$$

where m is the fringe order. For $m = 0$ (zero-order fringe) and by substitution of eqs 4a and b into eq 5 it is found that f (eq 2) can also be written as

$$f = \frac{n_g - n_f}{n_p}\text{i.d.} \qquad (6)$$

This implies that the position x of the zero-order fringe, in terms of n_f and i.d., is given by

$$x = \frac{L\text{i.d.}}{n_p D}(n_g - n_f) \qquad (7a)$$

and the higher-order fringes are to be found at

$$x = \frac{L\text{i.d.}}{n_p D}(n_g - n_f) + \frac{Lm\lambda_0}{n_p D} \qquad (7b)$$

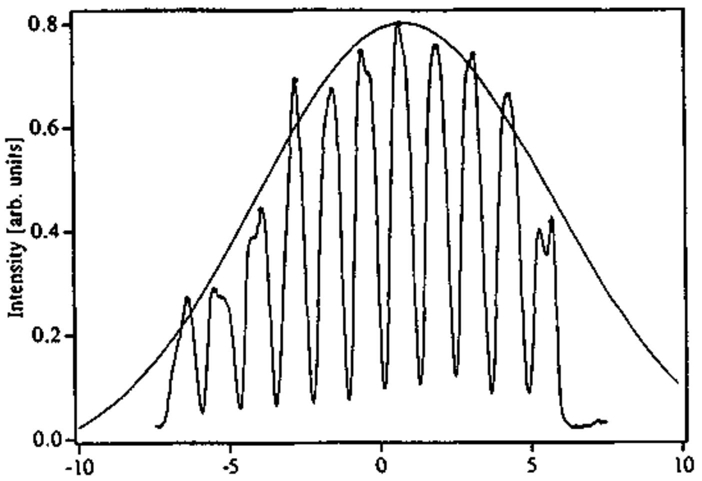

Figure 5. Recorded fringe pattern obtained with a HOE without capillary. The envelope is the fit of the fringe maxima.

Using eq 3, eq 7b transforms into

$$x = \frac{\Lambda \text{i.d.}}{\lambda_0}(n_g - n_f) + m\lambda \tag{7c}$$

Fringe shifts as a function of Δn_f, which are independent of the fringe order m and identical for all fringes, are readily obtained by differentiating eq 7b with respect to n_f

$$\frac{dx}{dn_f} = -\frac{L\text{i.d.}}{n_p D} \tag{8a}$$

or by using eq 7c

$$\frac{dx}{dn_f} = -\frac{\Lambda\text{i.d.}}{\lambda_0} \tag{8b}$$

(b) PDA Response. The PDA output generated by a given fringe shift x can be deduced from Figure 4. As can be seen in Figure 5, the intensity distribution $I(x')$ along the coordinate x' of the interference fringe pattern is well described by the sinusoidal function[13]

$$I(x') = I_{\text{mean}}\left(1 + C\cos\frac{2\pi}{\Lambda}x'\right) \tag{9}$$

where Λ is the period and I_{mean} is the average intensity illuminating the elements of the PDA and C is the intensity contrast[13] defined as

$$C = \frac{I_{\max} - I_{\min}}{I_{\max} + I_{\min}} \tag{10}$$

which takes the maximum value $C = 1$ if $I_{\min} = 0$.

The current i_b produced by each PDA element b (Figure 4) is simply

$$i_b = h\sigma\int_0^{\Lambda/2} I(x' - x)\,dx' \tag{11a}$$

where σ and h are the conversion efficiency and the height of a PDA element, respectively, and I is given by eq 9 which, upon integration, leads to

$$i_b = \frac{h\sigma I_{\text{mean}}\Lambda}{2}\left[1 + \frac{2C}{\pi}\sin\frac{2\pi}{\Lambda}x\right] \tag{11b}$$

The expression for i_a is identical to eq 11b except for the sign in the bracket, which is negative

$$i_a = \frac{h\sigma I_{\text{mean}}\Lambda}{2}\left[1 - \frac{2C}{\pi}\sin\frac{2\pi}{\Lambda}x\right] \tag{11c}$$

The electronic PSD circuit attached to the PDA produces

$$U = K\frac{i_a - i_b}{i_a + i_b} \tag{12}$$

as voltage output, where K is the amplification. The expression which relates the PDA output with position x is obtained by substitution of eqs 11b and c into eq 12 leading to

$$U = -K\frac{2C}{\pi}\sin\frac{2\pi}{\Lambda}x \tag{13}$$

However, as the instrument is zeroed (i.e., $U = 0$ V) before each measurement, the signal change dU in the electronics output with fringe shift dx is more important than U and is given as

$$\frac{dU}{dx} = -\frac{4CK}{\Lambda}\cos\frac{2\pi}{\Lambda}x \tag{14}$$

For small values of x the PDA response (eq 14) can, to a good approximation, be computed by

$$\frac{dU}{dx} = -\frac{4CK}{\Lambda} \tag{15}$$

which is independent of the total light intensity (I), conversion efficiency (σ), and PDA element height (h), indicating that the PDA response, for a given K and C, depends only on the element spacing Λ.

The absolute detector output as a function of n_f can be obtained by substitution of eq 7c into eq 13

$$U = -K\frac{2C}{\pi}\sin\frac{2\pi\text{i.d.}}{\lambda_0}(n_g - n_f) \tag{16}$$

The instrumental response (signal output per Δn_f), R, defined as

$$R = \frac{dU}{dn_f} = \frac{dx}{dn_f}\frac{dU}{dx} \tag{17}$$

can therefore be calculated, for small deflections, by performing this operation to eq 16 resulting in

$$R = \frac{4C\text{i.d.}K}{\lambda_0} \tag{18}$$

Equation 18 is used to predict the response of the present RI detector. The maximum achievable response corresponds to a fringe contrast $C = 1$ (eq 10). For a set of typical values such as $C = 0.5$, $d = 10\ \mu$m, $\lambda_0 = 672$ nm, and $K = 10$ V, the response of the instrument, as computed with eq 18, is $R = 300$ mV/mRIU. For an i.d. = 10 μm capillary we measured instrumental responses ranging from $R = 240$ to 420 mV/mRIU, depending on the illumination conditions (e.g., LD aberrations, HOE quality, etc.), and for a 5-μm-i.d. capillary, a response of 90 mV/mRIU was measured.

EXPERIMENTAL SECTION

RI Detector. The diagram of the RI detector is shown in Figure 1a. The LD (Told 9201, Toshiba) is driven by a precision current source (Model LDX 3412, ILX Lightwave, Bozeman, MT) and is mounted on a machined aluminum block which also contains the HOE and a collimating lens (from a CD player or a standard lens $f = 5$ mm, diameter, 5 mm, plano-convex Spindler & Hoyer). HOEs have been manufactured according to standard photographic procedures,[1] rendering deflection efficiencies ranging from 16% to 32%. To prevent drift caused by humidity variations, the HOE was sealed by a glass plate on the emulsion side using RIM glue.

The capillary cells (see Principle of Operation), having 10-μm capillaries fixed with UV-curing RIM glues (Norland Products Inc., New Brunswick, NJ) between two plates, are glued to an aluminum block as indicated in Figure 1. The LD and capillary aluminum blocks are spring loaded on a single ground aluminum plate by means of sliding guides for fine adjustment with micrometer screws along the dimensions indicated in Figure 1a. The sliding guides provide good thermal contact to the ground plate to ensure a high temperature stability of the LD and capillary by a single temperature controller (LDT 5901B, ILX Lightwave) set to room temperature using a Peltier element (Melcor, Trenton, NJ) and a thermistor sensor. The PDA (Model KOM 2045, Siemens, Fürth, Germany) is mounted on a translation stage (Microbench, Spindler + Hoyer, Göttingen, Germany) to zero the output of the instrument before each measurement. The PDA is wired in parallel to electronically combine the signals of four fringes, thus averaging over their fluctuations (Figure 4). Its terminals are connected to a PSD signal-conditioning amplifier (Model 301-DIV, UDT United Detector Technologies, Hawthorne, CA). This type of electronics delivers a signal which is zero when the intensity of each fringe is equally distributed on each pair of a–b PDA elements, and it is insensitive to light intensity fluctuations.[6]

CE Apparatus. Injection, hydrodynamically and electrokinetically, was performed at room temperature with a Prince programmable injector system (Lauer Labs, Emmen, The Netherlands). Electrokinetic injections were occasionally performed manually in some RI-detected separations using a high-voltage supply (Model HCN 14-20000, Fug Elektronik GmbH, Rosenheim, Germany). Data acquisition and processing in the RI measurements was performed on a Macintosh IIfx with the LabView (National Instruments) and Igor (WaveMetrics, Lake Oswego, OR) software packages, respectively. These separations were performed in a 10-μm-i.d., 80-cm-long (60 cm to detector) polyacrylamide-coated capillary under a separation voltage of 20 kV resulting in a recorded current of 1.3 μA (otherwise stated). A UV–visible detector (Model 206, Linear Instruments, Reno, NV) operated at a wavelength of 220 nm was used for the IUVA detection experiments, and the data were acquired on an IBM PS/2 using System Gold (Beckman Inc).

Chemicals. The RI calibration solution was 0.0690% sucrose in water, rendering $\Delta n = 10^{-4}$RIU. Sample stock solutions (10 mM) consisted of equally concentrated CsCl, KCl, $BaCl_2$, NaCl, $CaCl_2$, $MgCl_2$, $MnCl_2$, LiCl, $CoCl_2$, and $ZnCl_2$ salts dissolved in water or separation buffer. $MgCl_2$ was purchased from Aldrich (Steinheim, Germany) and $MnCl_2$ from Merck (Darmstadt, Germany), and all other chemicals were from Fluka (Buchs, Switzerland).

The buffer solution was similar to the one used by Foret et al. in the separation of lanthanides,[15a] and as for other inorganic ion separation,[15] IUVA detection was applied. For optimum results in RI detection, the originally proposed concentrations of 30 mM acetic acid, 30 mM creatinine, and 4 mM hydroxyisobutyric acid (HIBA) were increased to 100 mM acetic acid, 100 mM creatinine, and 4 mM HIBA having a pH 4.67.

RESULTS

Instrumental Results. *HOEs.* The deflecting efficiency of the HOEs ranged from 16% to 32% from batch to batch and it did not degrade with time, exposure to light, or humidity when sealed with a glass plate (see Experimental Section). The spot widths ($=2w_0$) and separations (D) were estimated by collecting the total amount of light that reaches a photodiode where the light is masked by a knife blade located at the focusing plane, which is scanned by means of a stepping motor (knife edge method). The recorded intensity appears as a step function (Figure 2) which, upon derivation, renders the deflected intensity profile. However, the spot widths thus obtained represent only an upper limit due to stray light and diffraction effects.

The actual width of the focal spots of the HOEs are better determined from the interference pattern (Figure 5). The envelope and fringe spacing define the spot widths and separation, respectively. The numerical aperture (NA) of the HOE is determined from the envelope as NA = tan θ, where θ is the emission angle of the envelope where its intensity drops to $1/e^2$. For the HOE shown in Figure 5, NA = 0.36 and the beam waists ($w_0 = \lambda/\pi\mathrm{NA}$) for this HOE are 0.63 μm, corresponding to a spot width of 1.26 μm, i.e., 8 times narrower than the i.d. of the capillary used with this HOE (i.d. = 10 μm). The distance between the spots in this method is calculated with the help of eq 2 as $D = (fL/x) = 14.1$ μm, where $L = 25$ mm, $f = \lambda_0 = 675$ nm and $x = \Lambda = 1.2$ mm, the measured fringe spacing. The spots retain the cylindrical aberrations of the LD and the contrast (eq 10) decreases from about $C = 0.75$ to $C = 0.5$ when the capillary intercepts one of the spots.

Linear Dynamic Range and Sensitivity. The deviation from linearity, used to compute the linear dynamic range (LDR) of this detector, is given by the difference between the sinusoidal response function (see eq 13) and its tangent at $x = 0$. The theoretical LDRs (=RI working range/3·RI noise) and corresponding working ranges for different linearities are reported in Table 1. Those values have been computed by assuming 0.3-mV long-term noise (see Figure 4 in Chapter 1 of ref 18), 1-s time constant, and a response of 420 mV/mRIU under no flow or electric current in the capillary. For a 5% deviation of linearity, the LDR covers close to four decades (i.e., LDR = 6700 and the working range is 14.4 mRIU). The maximal dynamic range, where a signal voltage can be related to a RI value, is larger than 15 000 for the capillary employed. The sensitivity of the RI detector, at 3 times the noise, for a 10-μm capillary, is ≈2 μRIU, depending on the fringe contrast (see Instrumental Response).

---

(14) Hjertén, S. *J. Cromatogr.* 1985, *347*, 191.

(15) (a) Foret, F.; Fanali, S.; Nardi, A.; Bocek, P. *Electrophoresis* 1990, *11*, 780. (b) Chen, M.; Cassidy, R. M. *J. Chromatogr.* 1993, *640*, 425. (c) Jackson, B. E.; Haddad, P. R. *Trends Anal. Chem.* 1993, *12*, 231.

Table 1. LDR and Working Ranges for Different Linearity Deviations

deviation from linearity (%)	working range (mRIU)	linear dynamic range
10	18.2	8500
5	14.4	6700
2	10.6	4900
1	8.4	3900
0.5	6.7	3100
0.2	4.9	2300
0.1	3.9	1800

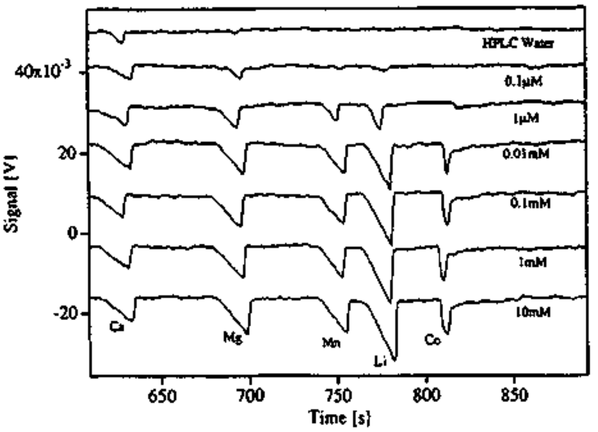

Figure 6. RI-detected electropherograms of different concentrations of metal ions (standard sample) injected under identical FASI conditions (2 kV/40 s) in a 10-μm-i.d. capillary.

Table 2. Detection Limits Obtained Using RI and IUVA Detection for Different Injecting Modes[a]

	ion concn (μM)				
	RI detection (10-μm capillary)			IUVA detection (50-μm capillary)	
	1	2	3	4	5
	electrokin samp		hydrodynamic	electrokin samp	
metal ion	in water inj 2 kV/ 40 s	in buffer inj 2 kV/ 60 s	samp in water inj 416 mb/ 15 s	in water inj 5 kV/ 5 s	in buffer inj 5 kV/ 5 s
Cs^+	0.1–1	1000	1600	0.3	20
K^+	< 0.01[b]	700	1000	0.3	20
Ba^{2+}	0.1–1	700	800	0.18	12
Na^+	<0.01[b]	300	200	0.13	12
Ca^{2+}	<0.01[b]	300	200	c	10
Mg^{2+}	0.01–0.1	130	200	0.18	9
Mn^{2+}	0.1–1	300	250	0.15	14
Li^+	0.1–1	200	130	0.22	14
Co^{2+}	0.1–1	300	1300	0.25	20
Zn^{2+}	0.1–1	1000	2000	0.44	18

[a] The order of the listed cations is according to the elution order. RI detection: buffer 100 mM acetic acid/creatinine + 4 mM HIBA, pH 4.67; capillary length 60 cm (80 cm total). IUVA detection: buffer 30 mM acetic acid/creatinine, pH 4.97; capillary length 59.9 cm (76.4 cm total). [b] The values correspond to the upper limits because the measurement interferes with the corresponding cation content in the HPLC grade water used, probably from the glass wall. [c] Because of a Ca^{2+} impurity in the water, probably from the glass wall, detection limits cannot be given for this cation.

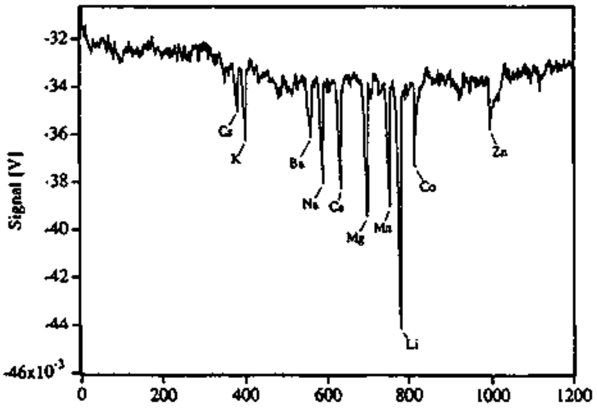

Figure 7. CE separation of a 10 mM standard sample dissolved in water detected with the hologram RI detector: injection, 2 kV/20 s; capillary, length 60 cm (80 cm total), i.d. = 10 μm; separation, U = 20 kV, I = 1.3 μA; RI detector response 420 mV/mRIU.

CE Separations of Metal Ions. Two modes of detection have been carried out in order to compare the performance of the RI detector in 10-μm capillaries with that obtained with standard IUVA detection in 50-μm capillaries.

RI Detection. The positively charged creatinine acts as background electrolyte (and as UV-absorbing compound in IUVA), and in combination with acetate, it delivers good buffering between pH 4 and 5. The separations were carried out in polyacrylamide-coated capillaries, prepared according to a method described by Hjertén,[14] in order to reduce the electroosmotic flow almost to zero for increased resolution as suggested by Foret et al.[15a] Most separations have been performed under field amplified sample injection (FASI) working condition.[16] Under these conditions, the electrokinetic injection is performed from sample ions dissolved in liquids having lower conductivity than that of the separation buffer. Even for low sample concentrations, mostly sample ions are attracted by the electric field emerging from the capillary orifice, resulting in a selective and efficient concentration of sample ions into the injection plug. The amount of a thus injected sample is proportional to its electrophoretic mobility, the injection current, and the injection time. The injected mass is therefore, within a wide range, rather insensitive to sample concentration as shown in Figure 6.

The FASI separations shown in Figure 6 are performed with the standard sample dissolved in water covering five concentration decades (10 mM to 0.1 μM) but keeping constant the injection parameters (2 kV during 40 s). The peak shapes are triangular, typical for column overload leading to field distortions. The electropherograms are nearly identical over 3 orders of magnitude of sample concentration until it approaches 10^{-6} M, corresponding to 10 times the H_3O^+ concentration in neutral water (pH 7). At this low concentration, a substantial amount of the injection current is taken by the highly mobile H_3O^+, which reduces the amplification efficiency of the injection. As reported in Table 2, the limits of detection for Mg^{2+}, Mn^{2+}, and Li^+ are lower than 0.1 μM and the FASI mechanism is so efficient that K^+, Na^+, and Ca^{2+} impurities can be detected even in the HPLC grade water employed. The electropherogram of a 10 mM standard sample dissolved in water, injected under FASI conditions similar to those used to record Figure 6 (injection time is 20 s instead of 40 s to increase separation efficiency), is displayed in Figure 7. The species are separated within 17 min, and the theoretical plate number determined from the Li^+ peak is ≈70 000.

IUVA Detection. In this detection mode it is important to choose the concentration of the UV-absorbing ion in the linear part of its calibration curve.[4] Otherwise, the IUVA signal

---

[16] (a) Chien, R.-L.; Burgi, D. S. *J. Cromatogr.* **1991**, *559*, 141. (b) Chien, R.-L.; Burgi, D. S. *Anal. Chem.* **1992**, *64*, 489A.

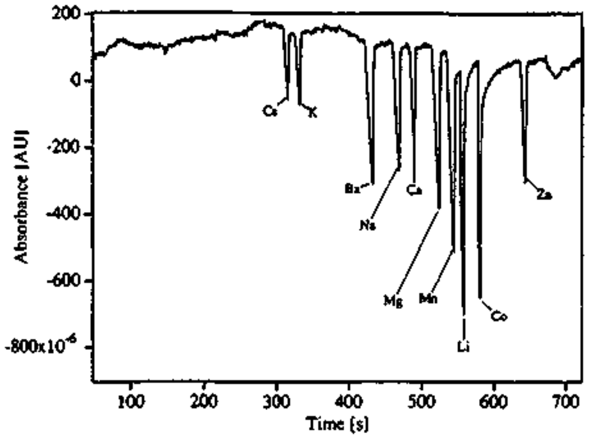

Figure 8. IUVA-detected separation of the standard sample, 1 mM dissolved in buffer. The coated 50-μm capillary had a length of 59.8 cm (76.4 cm total): separation buffer, 30 mM creatinine/acetic acid; injection, 5 kV/5 s; CE, 20 kV.

could decrease in spite of the fact that the replacement ratio (defined as the ratio of the displaced amount of the absorbing ion to the amount of sample in the sample zone) remains constant. Buffer (100 mM creatinine/100 mM acetate without HIBA) was first taken as background electrolyte without affecting the separation order in the IUVA-detected separations. However, for the abovementioned considerations the UV absorbance exceeded the upper limit of linearity ($\approx$0.18 AU), resulting in lower detection response. The optimal concentration consisted of 30 mM creatinine/30 mM acetate inducing an absorbance of $\approx$0.12 AU, which is close to the upper limit of the calibration curve for creatinine. The lower ionic strength of this buffer, as compared to that used in the RI-detected separations, leads to somewhat higher electrophoretic mobilities and shorter separation times.

A separation of the standard sample, using this buffer system, electrokinetically injected (5 kV/5 s), is shown in Figure 8. Because the electrophoretic mobilities of most of the metal ions are larger than the effective mobility of creatinine, their peaks display a fronting shape. The higher conductivity in the sample zones of these ions creates a lower electric field in this zone which results in peak shapes with a diffuse front and a sharp boundary at the edge.[17] For these reasons, the best-shaped peak corresponds to Zn^{2+}, which has an electrophoretic mobility and conductivity in its zone comparable to that of creatinine at pH 4.97.

The effect of concentration overload is the smallest for Zn^{2+} and the largest for the early-eluting peaks, as can be observed clearly in Figure 8. For the present injection parameters, the limit of detection for the various metal ions depends on the displacement response ratio and thus on the position in the electropherogram. For instance, doubly charged ions displace more creatinine than singly charged ones. The LODs range between 2×10^{-5} M for Cs^+ and 9×10^{-6} M for Mg^{2+}, as can be seen in Table 2. These values improve by more than 1 order of magnitude (70 times for most of the ions) under FASI conditions as reported in Table 2.

The concentration detection limits obtained with the same sample using RI detection are also summarized in Table 2,

Table 3. Absolute and Normalized Limits of Detection (= Abs LOD·i.d.) Obtained with RI and Thermooptical (TO) Detection

i.d. (μm)	absolute LOD (μRIU)	normalized LOD (μRIU·μm)	application
500	0.6	300	RI/LC[9c]
475	1.2	600	RI/LC[11]
50	4	200	RI/LC[9c]
50	~1	50	RI/CE[6]
25	2	50	TO/CE[10]
10	2	20	RI/CE[a]
5	10	50	static condn[a]

[a] This work.

where columns 1–3 refer to RI detected whereas columns 4 and 5 refer to IUVA-detected separations. Because of the different injection modes, injection amounts, and capillary inner diameters, the RI values cannot be compared directly to the IUVA values. The reason why FASI seems to be more efficient for the smaller capillary is most likely related to the different buffers employed.

DISCUSSION

The most obvious advantage of the present optical system based on holographic interferometry, as compared to the off-axis scheme,[6,7] is that the capillary is probed at its center where the optical path is as large as the inner diameter. Furthermore, the fringe patterns resulting from a HOE display regular spacing, allowing the use of multiple fringe detection with PDAs. Four times (using an eight-element PDA) more light at the PDA relieves the electronics and permits operation at less critical conditions. Multiple-fringe detection averages the pointing stability and schlieren effects (the reference and probing rays propagate from the capillary to the PDA through air) at the fringes. The lack of linearity due to fringe substructures (see Figure 5) is minimized. The improvements translated in lower noise, allowing for the first time on-column RI detection in 5- and 10-μm capillaries.

The smaller capillary used in conjunction with RI detection using the off-axis method[10] had an i.d. = 25 μm. The fringe sensitivity G_f ($G_f = \Delta x/\Delta n_{fs}$, where Δx and s are fringe shift and width, respectively) for such a fringe has been computed[7] to be $G_f = 34$. This fringe sensitivity corresponds to a response (eq 18) of R = 340 mV/mRIU in the present formalism. For the same capillary and contrast ($C = 0.5$), the present detector would render a response of R = 740 mV/mRIU, i.e., more than twice the response. To produce a fair comparison, and considering that the present RI detector has been used only with capillaries having i.d. $\leq$ 10 μm, we reproduce the sensitivities obtained with previous instruments in RI units "normalized" to the path length (μRIU·μm). The absolute RI LODs are also included in Table 3. It can be seen that the normalized LODs for 10-μm tubes are lower than those obtained with a 5-μm tube. Taking that into consideration, we performed most of the measurements with the i.d. = 10 μm capillary.

Although the RI and IUVA measurements are not identical (IUVA detection was not possible in an i.d. = 10 μm tube), in terms of capillary inner diameters and injection parameters

---

(17) Mikkers, F. E. P.; Everaerts, F. M.; Verheggen, Th. P. E. M. *J. Cromatogr.* **1979**, *169*, 1.

(18) Scott, R. P. W. In *Liquid Chromatography Detectors*; Elsevier: New York, 1986.

it is apparent that the concentration LODs reported in the second column of Table 2 and the electropherogram shown in Figure 7 obtained in 10-μm capillaries for RI detection are $\approx$1 order of magnitude worse than those obtained with IUVA detection in 50-μm capillaries reported in column 5 and the electropherogram shown in Figure 8. The similarities in the peak shapes and signs obtained with both methods (in both cases the peaks correspond to a decrease in the signal) suggest a similar mechanism in the generation of the ΔRI signals. In this context, the displacement of the creatinine cation, which is much larger than the metal cations, is believed to reduce the RI value in the sample zone leading to negative signal peaks as observed (see Figures 6 and 7). This observation is also supported by other RI-detected separations using a 100 mM borax buffer where negative and positive signal peaks were obtained with the same sample as well as by the fact that the intensities associated with each ion in the electropherograms shown in Figures 7 and 8 are indeed quite similar. To take full advantage of this observation and to increase sensitivity the selection of the buffer is crucial.

CONCLUSION

As anticipated[1] and here demonstrated, the use of HOEs in conjunction with LDs results in a substantial miniaturization and a simplification in the architecture of the instrument accompanied by improvements in its performance. Considering that the present RI detector performs at theroretical limits and its performance is limited by the noise generated in the capillary, further instrumental improvements aimed at gaining sensitivity seem no longer needed. In this regard, and as argued in the discussion section, the difference in molecular refractivity between the sample and the background electrolyte is the factor responsible for the RI signal in the case of ions. Only the proper choice of a buffer might result in higher sensitivities. A good buffer for RI detection should have low conductivity to minimize Joule heat effects, and the buffer ions should have a large difference in molar refractivity (including perhaps solvatization) with respect to that of the sample.

The improvements made in the instrumentation in on-column RI detectors, including the present one, have not helped much in lowering the concentration detection limits but have helped in the reduction of the mass detection limits (i.e., injected amounts) and in the inner diameter of the capillary employed. This improvements should translate in lower LODs in thermooptical detection next to be undertaken in our laboratory.

ACKNOWLEDGMENT

This work was supported by the Commission pour L'encouragement de la Recherche Scientifique (Project 2156.1). We thank P. Nussbaum and H. P. Herzig (Institut de Microtechnique, Neuchâtel, Switzerland) for the construction of the HOEs, Profs. H. M. Widmer and R. Dändliker for supporting this study, and D. Raymond for correcting the manuscript.

Received for review August 31, 1993. Accepted October 12, 1993.®

® Abstract published in *Advance ACS Abstracts*, November 15, 1993.

Chapter 6 Hologram Based Thermo-Optical Absorbance Detection in Capillary Electrophoresis; Separation of Nucleosides and Nucleotides.

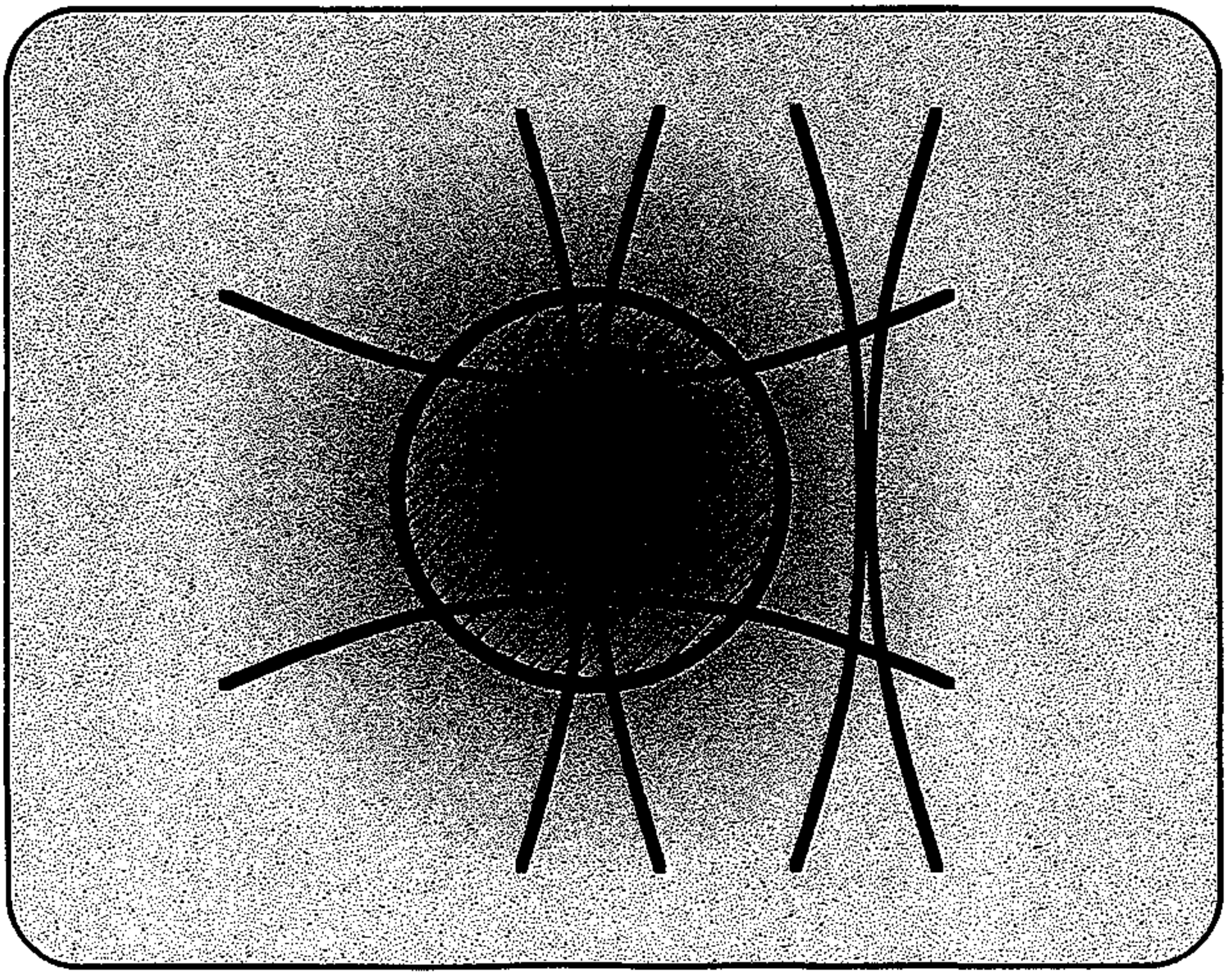

Hologram Based Thermo-Optical Absorbance Detection in Capillary Electrophoresis; Separation of Nucleosides and Nucleotides.

B. Krattiger, A. E. Bruno*, H. M. Widmer, R. Dändliker+
Ciba-Geigy Ltd., Corporate Analytical Research, 4002 Basle, Switzerland
+Institute of Microtechnology, University of Neuchâtel, 2000 Neuchâtel, Switzerland

Abstract

On-column thermo-optical absorbance (TOA) detection in capillary electrophoretic separations of various nucleoside and mono- and diphosphate nucleotide mixtures absorbing at 257 nm is demonstrated in the 20 μm i.d. capillaries. The analytes are optically *pumped* by a frequency doubled argon ion laser and *probed* by a laser diode or a HeNe laser beam guided to the detection volume by a holographic optical element. Absorption detection limits of 2.2 μAU using time constants of 0.3 s and 20 mW of UV power are obtained over a linear dynamic range covering three to four decades. As higher pumping power is required to enhance the thermo-optical sensitivity, photo-bleaching appears as a major problem in the quest for lower detection limits for some of the substances studied such as deoxyuridine and uridine. Concentration detection limits as low as 50 nM for adenosine monophosphate, corresponding to a mass detection limit of 0.4 fmole, and separation efficiencies up to 320 000 theoretical plates are measured. A theoretical model, which translates the obtained TOA signals into absorbances, is proposed and describes the TOA effect for smaller capillaries rather well.

---

* To whom correspondence should be addressed

INTRODUCTION

Various on-column optical detection methods have been devised for capillary electrophoresis (CE). When the sample of interest contains a fluorescent chromophore which coincides with a lasing line, laser induced fluorescence (LIF) is undoubtedly the best choice. Using this method concentration detection limits (LODs) as low as 10^{-10} M (0.2 am injected) for native bovine serum albumin (BSA) have been reported[1]. However, as the number of naturally fluorescent samples is small, and the laser emission wavelengths are limited, this case should be considered as an exception rather than the rule.

Concentration LODs in the 10^{-11} M range, or lower, are obtained in CE using pre-column labeling with fluorescent tags and LIF detection. However, direct derivatizations below the 10^{-7} M range have not been reported to date (the impressive LODs reported have been always obtained by analysis of samples which are first derivatized at high concentrations and then diluted to the low levels reported). Furthermore, derivatization procedures are not always available for the substance of interest or, are often rather tedious and, when available, might lead to quantification problems because the extent of derivatization is not always predictable. As the electrophoretic mobilities are often affected by the labels, different incorporation of the tags into the sample leads to additional peaks and decreased separation efficiency[1, 2].

The vast majority of substances of analytical interest absorb in the UV/vis range and therefore absorbance detection is the most popular detection method in CE. Due to the short absorbance paths the lower concentration LODs thus obtained are, in the most favorable cases, in the µM range. This disadvantage can be partially overcome by extending the optical path using flared capillaries, z-shaped cells[3, 4] or multi-reflection cells[5]. Non-linearities in the calibration curves, due to RI effects[6], are in these cases to be expected.

To obtain high sensitivity and accuracy, while avoiding derivatization procedures, the approach we follow is thermo-optical absorbance (TOA). In TOA detection[7-9] an intense laser pulse irradiates repeatedly the sample with a wavelength matching an absorption system in the sample. The amount of absorbed light, which is converted by radiationless transitions into heat, rises the solvent temperature in the illuminated region in a periodic fashion. As the refractive index (n) of a material is a function of the temperature (T), those periodic changes in T manifest in changes in the refractive index (Δn) which can be conveniently monitored by a laser based capillary RI detector[10-15] and easily decoded with a lock-in amplifier. Because the thus recovered Δn signal is dependent, among other parameters, on the extinction coefficient of the sample studied, the output can be calibrated to produce quantitative absorption measurements.

Based on the geometric configuration of the pump and probe beams two types of TOA schemes have been performed in conjunction with capillaries to date, thermal lensing (TL) and crossed beam thermo optical (CBTO) configurations. In TL, which has been used in high performance liquid chromatography (HPLC)[7, 8, 16-18], the pump and probe beams are collinear and the former induces a RI gradient across the probing path. In CBTO, first demonstrated by Yu and Dovichi in CE[19], the beams are "crossed" at 90° overlapping in the capillary lumen defining a small detection volume[20, 21]. This latter configuration (CBTO) is the one we use here, however, we prefer to use the general term TOA, instead of the specific CBTO term, to emphasize that the TOA effect is not related, at least in the present case, to the geometric arrangement of the beams. The unavoidable RI gradient is, in the case of small i.d. capillaries, not required to observe the TOA effect. Indeed, as argued in the theory section, it is the mean value of Δn across the detection lumen which is responsible for the TOA signal.

As a capillary RI detector for the TOA instrument we used the one based on a holographic optical element recently reported by us[12, 13]. The straightforward optical design and enhanced performance of this RI detector made its integration into a TOA device rather simple[15]. To evaluate the performance of the instrument and, considering the growing importance of DNA and RNA analysis, various CE separations of nucleosides and mono- and diphosphate nucleotides have been chosen for the study. Native proteins have also been studied by TOA and the results will be reported elsewhere.

THEORY

The principle of TOA detection in small capillaries, using the hologram based RI detector, is depicted in Fig. 1 and 2 and, the time evolution of the temperature for every pulse of light for two typical cases, is shown in Fig. 3. The heat produced during each pulse of the pump beam warms up rapidly the analyte and the surrounding fused silica (FS) of the capillary wall until the maximum temperature T_S is reached (see Figs. 2 and 3). The temperature difference, ΔT, induces a change in the locally persisting refractive index, Δn, which modifies the phase of the probe beam (with respect to the reference beam) which is detected interferometrically as explained in Ref. 12. Demodulation of the Δn signal with a lock-in amplifier constitutes, upon calibration, the TOA signal.

The radial distributions of ΔT and Δn, which are correlated through the (dn/dT) coefficients of the buffer and FS, are also displayed in Fig. 2 (bottom). The large discontinuity in the Δn at the buffer/FS interface is due to the fact that the (dn/dT) coefficient of the FS has opposite sign and, is eleven times smaller in magnitude than the corresponding coefficient of the aqueous buffer (the dn/dT coefficients are $-1.07\ 10^{-4}\ K^{-1}$ and $+9.5\ 10^{-6}\ K^{-1}$ for water and FS[22, 23] at room temperature, respectively). As the (dn/dT) of the FS is small as compared to that of the buffer and, as the two adjacent probe and reference beams sense almost the same temperature along their paths through the FS, the phase changes gathered in the path through the FS can be neglected.

Simple TOA Model: Dovichi[7] developed an elaborate mathematical formalism needed to compute the ΔT and Δn profiles within the analyte for larger cells under pure TL conditions where the heat generation is far from any wall. However, for small i.d. capillaries, the temperature drops mainly across the FS wall and not within the buffer. As the heat dissipates mainly through the wall (and not by mass flow), the temperature raise is mainly determined by the thermal resistance of the FS cell and not by the thermal properties of the buffer. For this reason Dovichi's model can not be used here and thus we present a simple model to predict ΔT and Δn inside small i.d. capillaries for the pure TOA case.

As the heat source can be considered point-like ($2\ w_0 \leq 20$ µm where $2\ w_0$ is the pump beam diameter) if compared to the outer capillary diameter (340 µm), and, as the heat dissipates isotropically, mostly through the FS wall, it is assumed that the cell geometry is spherical; i.e. two concentric spheres, the inner one filled with buffer and the outer one made of FS. The diameters of both spheres match those of inner and outer diameters of the capillary. As it can be seen in Fig. 3 the system reaches thermal equilibrium very rapidly (ca. 0.4 ms corresponding to 1/4 of the pulse width at the 314 Hz chopper frequency). The temperature profile is, at this point, assumed to be constant across the buffer and to drop across the FS wall as $1/r^2$.

The overall TOA instrumental response, R_{TOA}, of the present instrument is the signal voltage output from the lock-in amplifier (U_{TOA}) caused by a given absorbance, A, is

$$R_{TOA} = \frac{U_{TOA}}{A}, \qquad (1a)$$

or, in the differential form,

$$R_{TOA} = \frac{dU_{TOA}}{dA}, \qquad (1b)$$

where A is the product of pathlength (i.e. the i.d. of the capillary), concentration, c, and extinction coefficient, ε,

$$A = i.d.\ c\ \varepsilon. \qquad (2)$$

(dU_{TOA}/dA), Eq. 1b, can be mathematically decomposed as

$$\frac{dU_{TOA}}{dA} = \left(\frac{dU_{TOA}}{dU_{RI}}\right) \cdot \left(\frac{dU_{RI}}{dn}\right) \cdot \left(\frac{dn}{dT}\right) \cdot \left(\frac{dT}{dA}\right) \qquad (3)$$

where U_{RI} is the signal amplitude from the photodiode array (PDA) electronic conditioner (i.e. before the lock-in amplifier). The first two terms in Eq. 3 are related to the instrument. The third factor, (dn/dT), is the coefficient for the buffer (reported above for water), and the last two terms correspond to the actual TOA principle.

The first term in Eq. 3 is the lock-in amplification. It is the ratio of its efficiency, H, for a given signal shape (which has to be determined experimentally) to the sensitivity setting, S, (preset at 50 mV in most measurements)

$$\left(\frac{dU_{TOA}}{dU_{RI}}\right) = \frac{H}{S}\ . \qquad (4)$$

For a chopping frequency of 314 Hz and a non-bleaching sample (e.g. using 1 % acetone/water solution), H was measured to be 4 V.

An expression for the second bracket in Eq. 3, which corresponds to the instrumental response of the RI detector, was already given elsewhere (Eq. 18 in Ref. 12) and reads

$$\left(\frac{dU_{RI}}{dn}\right) = \frac{4\ C\ K\ i.d.}{\lambda_{Probe}}, \qquad (5)$$

where C = 0.9 is the fringe contrast, K = 10 V an amplification constant of the PDA conditioner and, λ_{Probe} = 633 nm the probe HeNe laser wavelength. Using these values, the RI response is (dU_{RI}/dn) = 1.14 mV/µRIU.

The last factor in Eq. 3, (dT/dA), represents the temperature change per absorbance, i.e. the TOA effect. Assuming that the temperature at the fluid/FS interface is the same as that of the fluid, the temperature excess ΔT across the FS sphere having a thermal resistance R and conducting a total heat flow P_{Heat} can be computed as

$$\Delta T = P_{Heat}\, R. \tag{6}$$

The power flow P_{Heat} in the assumed stationary state equals the absorbed light power, which is related to the absorbance A as

$$P_{Heat} = 2.303 \cdot A \cdot P_{UV} \tag{7}$$

and its substitution in Eq. 6 reveals

$$\Delta T = 2.303 \cdot R \cdot A \cdot P_{UV}\ . \tag{8}$$

The expression for (dT/dA) can be now obtained by taking the derivative of Eq. 8 with respect to A

$$\frac{dT}{dA} = 2.303 \cdot R \cdot P_{UV}. \tag{9}$$

The thermal resistance, R, entering in Eqs. 6, 8 and 9, can be computed by the integration of thermal resistance shells over the FS sphere as

$$R = \int_{r_i}^{r_o} \frac{dr}{4\pi\sigma r^2} = \frac{1}{4\pi\sigma}\left(\frac{1}{r_i} - \frac{1}{r_o}\right), \tag{10}$$

where $\sigma = 1.38$ W/K/m is the thermal conductivity of FS and, r_i (= i.d./2) and r_o (= o.d./2) are the inner and outer radii of the sphere (and capillary), respectively. According to Eq. 10, a sphere with i.d. = 20 µm and o.d. = 340 µm (present case), has a thermal resistance R = 5427 K/W. Using Eq. 8, 1 µW of absorbed light would raise the temperature inside the capillary by 5.4 mK.

The analytical expression for R_{TOA} can now be given by substituting Eq. 10 into Eq. 9 and then by substituting Eqs. 4, 5 and 9 into Eq. 3 rendering

$$R_{TOA} = \frac{4.606\ K\ H}{\pi\ S}\ \frac{C\ P_{UV}}{\lambda_{Probe}\ \sigma}\left(\frac{dn}{dT}\right)\left(1 - \frac{i.d.}{o.d.}\right). \qquad (11)$$

According to Eq. 11, for narrow bore capillaries, for which i.d./o.d. < 0.1, the TOA response is almost independent of both diameters (e.g. the last bracket contributes to less than 6 % to R_{TOA} in our case). We have measured R_{TOA} for capillaries having 10 and 20 µm i.d.s at 10 mW pumping power and, within the experimental accuracy, R_{TOA} remains constant as indicated by the present model.

The theoretical estimate for the R_{TOA} using Eq. 11, for a lock-in sensitivity of 50 mV and a pump power of 10 mW, gives R_{TOA} = 1.217 mV/µAU, whereas the measured values range from 1.0 to 1.4 mV/µAU for poor and good optical adjustment, respectively. Although there are many reasons which could explain this discrepancy (the most obvious could be that the model assumes a flat temperature profile in the analyte) we prefer not to speculate about it since the model described above is rather simple.

EXPERIMENTAL

TOA Detector: The experimental set-up of the TOA detector is shown in Fig. 4 and, the pumping scheme is shown in Fig. 1. It consists basically of a capillary RI detector, identical to the one we recently described[12] and, as a pump laser we used an intracavity frequency doubled Ar+ laser emitting at 257 nm (laser model 2025-5, doubler model 395 B, Spectra Physics, Mountain View, CA) as employed by Bruno et al.[20]. The frequency doubling system is stabilized by a feed back system (Mod. 295, Spectra Physics) to produce less than 0.5 % of intensity noise. The laser beam with a diameter of roughly 2 mm is focused by a FS lens f = 16 mm (#06 3010, Spindler & Hoyer, Göttingen, Germany), mounted on a 3-D translation stage (Microcontrole /Newport 3 MRN 03.5) to adjust the pump beam to the capillary cell (Fig. 1). The numerical aperture (NA) of the pump beam is therefore NA = 1/16 and the beam spot in the cell, 2 w_0, where the beam waist is $w_0 = \lambda/\pi NA$, is ca. 2.6 µm. The probe light source, either a HeNe laser (Mod. 106-1, Spectra Physics) connected via a polarization preserving single mode fiber (HB600, York Technology Inc., Chandlers Ford, Hampshire, GB) or, a laser diode (LD), first passes a collimator lens (f = 5 mm, diameter = 5 mm, plano-convex, Spindler & Hoyer) and then the HOE (as in Ref. 12). The TOA cell consists of a naked (i.e. polyimide removed) capillary (Polymicro Technologies, Phoenix, AZ) glued between two microscope slides with UV curing RI matching (RIM) glue (Norland Products Inc., New Brunswick, NJ) as shown in Fig. 1 (the pump beam entrance and exit surfaces of the capillary (Fig. 1) were kept free from RIM because the glue absorbs UV light and photo-degrades to dark spots). The capillary cell was glued onto a properly machined aluminum block for its temperature stabilization by means of a Peltier/thermistor system (Peltier element from Melcor, Trenton, NJ, controller from ILX Lightwave, Bozeman, MT).

The reference and probe beam positions of the RI detector were adjusted with respect to the capillary by monitoring the far field profile of the fringe pattern which, once optimized, illuminates an 8-element photodiode array (PDA) (KOM 2045, Siemens). The signal current from the PDA is analog conditioned by a circuit wired to render position sensitive detection (Model 301-DIV, UDT, Hawthorne, CA) and fed into a lock-in amplifier (SR 530, Stanford Research

Systems Inc.) operated at a time constant of 0.3 s and a sensitivity setting of 50 mV. The chopper (SR 540, Stanford Research Systems Inc.) for the pump beam also delivers the phase reference for the lock-in amplifier. The TOA signal output from the lock-in is acquired by a Macintosh IIfx computer using the LabVIEW hard- and software package (National Instruments, Austin, TX) and, the data was processed with the Igor program (WaveMetrix, Lake Oswego, OR).

Chemicals: The absorbance calibration solution consisted of 1 % (vol.) acetone in water. Its absorbance at 257 nm was determined (Uvikon 720 LC, Kontron, Switzerland) to be 1.265 AU/cm. The standard stock solutions of nucleosides and nucleotides were prepared in water (except adenosine and guanosine, which were dissolved in 0.1 M NaOH) and stored below -18 °C at a concentration of 5 mg/ml. Diluted samples were prepared each day in running buffer or in water. The filtered (0.22 µm) buffer solutions (all were obtained from Fluka) were vacuum degassed before use. The SDS buffer (pH 7.00) consisted of 20 mM sodium dihydrogen phosphate, 20 mM sodium tetra borate and 50 mM sodium lauryl sulfate and, the citrate buffer (pH 3.5) consisted of 20 mM sodium citrate. The nucleosides studied were adenosine (A), deoxyadenosine (dA), cytidine (C), guanosine (G), deoxyinosine (dI), deoxythymidine (dT), deoxyuridine (dU) and uridine (U). The 5'-mono- and diphosphate nucleotides studied were AMP, CMP, GMP, dTMP, ADP, CDP; GDP and dTDP. All these compounds were purchased from Fluka (Buchs, Switzerland). The extinction coefficients ε at 257 nm of both, nucleosides and nucleotides, are roughly $\varepsilon = 10^4\ \mathrm{l\ mol^{-1}\ cm^{-1}}$.

Capillary Electrophoresis: Capillaries were first rinsed with 0.1 M NaOH for some minutes and, before sample injection, with 0.1 M HCl, followed by water and buffer. CE was performed at room temperature applying hydrodynamic injection at a pressure of 25 mb for 30 s, by an automated injection system (Prince, Lauer Labs, Emmen, The Netherlands). Separations were performed in 20 µm i.d. capillaries having a total length of 75 cm and a length of 50 cm to the detection point. The separation voltage was 30 kV resulting in electrical currents of 6 µA for the SDS buffer and 3 µA for the citrate buffer. Conventional UV detection was performed with an absorbance detector (PHD 206, Linear Instruments, Reno, NV) using a time constant of 0.3 s under identical experimental CE conditions and capillary dimensions.

As nucleosides are uncharged in the pH region where they are stable, CE in hydrophilic buffers is not possible, they are commonly separated by micellar electrokinetic chromatography (MEKC)[24, 25]. The addition of surfactants to the background electrolyte, such as sodium dodecyl sulfate (SDS), above a critical concentration leads to micelles which allows separation of neutral species. Under these conditions neutral nucleosides are separated according to their different partitioning between the aqueous background electrolyte and the hydrophobic interior of the charged micelles[25]. Although nucleotides, containing charged phosphate groups, can be separated in hydrophilic buffers without the addition of SDS, we chose here the same buffer system to display both, the nucleosides and nucleotides species, in the same run.

RESULTS AND DISCUSSION

Noise Sources and Linear Dynamic Range: To investigate the contribution of the various sources to the total TOA noise the sources were, in as much as possible, isolated and, their individual contributions measured and determined according to the procedure suggested by Scott[26]. Considered were contributions to TOA noise from the lock-in amplifier, the PDA signal conditioner, the probe- and pump lasers and, from the data acquisition. The results are summarized in Table 1.

Fig. 5 shows the noise spectra measured at the PDA array for different probe lasers. All lasers investigated display the highest noise at the lower chopper frequencies. Schlieren effects due to air turbulences contribute to the low frequency noise. As the fringe position depends on the wavelength (Eq. 7b, Ref. 12), wavelength fluctuations translate into noise at higher chopping frequencies. For LDs the high frequency noise originates from wavelength shifts due to mode hopping which depends on the junction structure of the chip (gain guided, index guided) and, on the operating conditions (current, temperature, optical feed back)[27]. The index guided single mode LD model TOLD 9211 (Toshiba Inc.), requiring a careful adjustment of the operating temperature and current, manifests in lower noise than the gain guided multi mode LD model TOLD 9201, as can be seen in Fig. 5. HeNe lasers, having high intensity fluctuations of about 1%, display almost no wavelength noise. As the intensity fluctuations are referenced out by the divider in the PDA conditioning electronics[12], the HeNe laser rendered the lowest TOA noise and was therefore used in the CE separations reported. The chopper frequencies were chosen to be different from the harmonics of the 50 Hz line frequency to prevent aliasing effects. The lowest noise from within a series of 5 randomly selected chopper frequencies was obtained for the 314 Hz (Fig. 5) which therefore was selected for all subsequent TOA measurements. The lowest, almost flat, trace in Fig. 5 represents the noise due only to the electronics recorded by replacing the PDA by dummy resistors.

The TOA response is, according to Eq. 11, proportional to the pump power, but, it was noticed that increasing the pump power does not result in a linear increase in the S/N ratio. When using a transparent buffer system, a TOA measurement should be background free as in the case of LIF in the absence of scattered light. However, as it is here the case with the SDS buffer, small impurities, which display weak absorption around 257 nm, couple the noise of the pump beam into the final TOA baseline noise. In addition, buffer inhomogenities (e.g. bubbles, dust) lead to baseline spikes, with peak heights increasing with pump power.

High pumping powers are not always desirable, primarily because they might cause photo-bleaching, saturation, and cell degradation[21]. The optimum pumping power depends on the problem at hand. In the present case, the S/N ratio of the UV laser output was determined to be constant (at ca. 250) between 4 and 20 mW. Considering that the frequency doubling system is difficult to stabilize at powers higher than 20 mW over longer times, most measurements were performed at 10 mW.

Table 1 also contains empirical formulas to compute the different noise contributions. In the last column, the expected noise contributions for the separation shown in Fig. 6 are listed. The square root of the sum of the squares of the individual components yields the expected total noise of ≈ 3 mV which is to be compared with the measured baseline noise of 5 mV reported in the same table. The 2 mV discrepancy probably stems from buffer impurities absorbing at 257 nm or, turbulences in the cell due to Joule heat in CE which are not accounted in the evaluation.

TOA detection cells degrade by the high peak intensities of pulsed lasers[28] (e.g. 10 ns pulse widths) which are in the 0.2 GW/cm^2. The chopped cw laser used in our experiments delivers modest peak intensities of ca. 0.2 MW/cm^2 which are rather harmless to the FS cell. However, after a few days of operation, the FS of the capillaries display brown stains in the UV path which increasingly add noise due to increased background absorbance. For some buffer/sample combinations we also observed a dark coating growing at the inner capillary surface leading also to a monotonous increase of the baseline signal. These brown layers were easily removed by rinsing the capillary with HCl.

The linear dynamic range (LDR) in the present instrument, which expands to about 3-4 decades of TOA detection, is mainly given by the dynamic reserve of the lock-in amplifier and, also by the sinusoidal response of the RI detector (Eq.

16 in Ref. 12). Ignoring the limitations from the lock-in, the LDR would be close to 70 000 at 5 % deviation from linearity. This is based on the present RI detection limit of 0.1 µRIU and the 6.8 mRIU working range.

CE Separations: Fig. 6 displays the electropherogram of a mixture of four nucleosides, dU, U, dI and dA, (50 µg/ml each) separated in the SDS buffer in a 20 µm i.d. capillary. The electropherogram of the same mixture taken under identical experimental conditions, but recorded using conventional UV absorption, is shown in Fig. 7 for comparison purposes. The ca. 200 mV baseline offset in the TOA recorded electropherogram is due to the slight absorption of the SDS buffer and the capillary wall at 257 nm. Although the TOA detected electropherogram displays a better S/N ratio and no drift as compared to that recorded with the UV absorbance detector, the peak areas of the dU and U species do not represent their actual injected concentrations due to photo-bleaching. The relatively high UV intensities needed in the TOA measurements photo-degrade[21, 29-31] these species resulting in a lower peak height than those of the dI and dA species in spite of their similar extinction coefficients and concentrations.

A quick diagnostic regarding to the observed photo-bleaching effects can be obtained by looking at the time resolved traces shown in Fig. 3 for both significant cases; namely dU and dI. dU, which strongly photo-degrades, has an anomalous trace resulting in a smaller amplitude, whereas dI, which is photo-stable displays a standard TOA trace[20] with a larger amplitude. The anomalous shape of the dU trace indicates that the amount of dU in the illuminated region decreases with time, due to photo-dissociation decay, to a constant value. This constant value has contributions from the residual absorbance of the photo fragments and is also related to the flow rate which repopulates the irradiated region.

The degree of photo-bleaching, as a function of increasing power for the dU and dI species, continuously injected by pressure (5.7 bar), is depicted in Fig. 8. Although below 1 mW of UV power the TOA signals of dI and dU are comparable, as the power increases to 20 mW, the signal from dU is less than one third of that from dI.

Fig. 9 shows the MEKC electropherogram of four nucleosides A, C, G and dT and their monophosphate nucleotides (25 mM for all species diluted in water). The migration order of the GMP, dTMP, AMP and CMP is mainly determined by their charge. CMP, having a higher negative charge, and thus the fastest electrophoretic mobility against the electroosmotic flow, appears as the last peak in the electropherogram.

Diphosphates are not well separated in the SDS buffer because of their highly negative electrophoretic mobilities of comparable magnitude to that of the counteracting electroosmotic flow, lead to impractical long separation times. However, the CE separation of negatively charged diphosphate nucleotides was possible in a 20 mM sodium citrate buffer at pH = 3.5. The electropherogram of a mixture of diphosphate nucleotides (30 µg/ml ADP, 50 µg/ml GDP, 100 µg/ml CDP, and 200 µg/ml dTDP) is shown in Fig. 10. Due to the low pH the electroosmotic flow was small, the electric field was reversed and injection was performed at the cathode.

The performances of both, the TOA and conventional UV absorbance detectors, operated with 20 µm capillaries, were evaluated using a 1 % acetone/water solution. The TOA detector yielded a detection limit of about $6.7 \cdot 10^{-6}$ AU at 10 mW pump power and $2.2 \cdot 10^{-6}$ AU at 20 mW pump power. These values are to be compared with those obtained with the UV absorption instrument of $3 \cdot 10^{-4}$ AU (which is about 6 times higher than the typical noise obtained with 75 µm tubes). The poor performance of the UV detector is related to the fact[6, 32] that a great portion of the probing light propagates through the capillary wall without intercepting the 20 µm bore. The TOA absorbance noises are thus about 45 to 140 times smaller than those obtained by conventional absorbance when used in conjunction with 20 µm capillaries. The present TOA noise levels obtained in 20 µm capillaries are comparable with the value of $2.5 \cdot 10^{-6}$ AU reported by Waldron and Dovichi[21] in 50 µm-i.d. capillaries using CBTO.

The present TOA absorbance noise is somewhat lower than the values reported by Xue and Yeung[31] of 10^{-5} AU in a 75 µm capillary using a laser based absorbance detector equipped with a noise canceling electronics (corresponding to a concentration LOD 25 times lower than that obtained with a commercial CE system). The reported[31a] LOD for a dye with an extinction coefficient of $7.5 \cdot 10^{4}$ l mol^{-1} cm^{-1} is 20 nM which is lower than that reported for TOA in Table II for AMP of 50 nM. It must be noticed that the extinction coefficient of the dye used by Xue et al. is about 7.5 times higher than that of AMP, the i.d. of the capillary used by these authors[31a] is 3.2 times larger, our data is not post-run processed and, the definition[26] we used to compute the LODs is more conservative than the one used by Xue et al..

Electrophoretic efficiencies are not affected by photo-bleaching and, theoretical plates of more than 300 000 have been calculated from the dA and dI peaks. The corresponding concentration and mass LODs are listed in Table II. The LODs obtained with TOA are ca. 30 times lower for the photo-stable samples but only 2.4 times better for the photo-degrading samples. To determine the ultimate concentration LODs the injection volume was increased which resulted in additional band broadening degrading thus the separation efficiency. At the best LOD obtained (AMP, see above) the separation efficiency still was 130 000 theoretical plates.

CONCLUSIONS

For the CE separations performed in 20 μm capillaries using 10 mW pumping power, TOA is about 30 times more sensitive than standard UV absorbance. For the continuously injected samples (i.e. no electrical field) the enhancement was 45 times at 10 mW and 140 at 20 mW. For larger i.d. capillaries, these sensitivity enhancement factors will be smaller. This, because on one hand the capillary illumination in conventional absorbance is more efficient for larger i.d. capillaries while, on the other hand, the heat in the TOA detector is less efficiently removed.

To further improve TOA detection, beside e.g. enhancing the (dn/dT) coefficient of the buffer, various noise sources should be improved; the most important one being the background absorbance noise.

As we have shown here, the behavior of the TOA is similar to conventional absorbance with regards to pathlength dependence for non-bleaching substances (see APPENDIX), low mass LODs should be obtained with smaller-i.d. capillaries, whereas larger i.d.s will lead to reduced concentration LODs. A further improvement in the sensitivity of RI and TOA detectors could be certainly obtained using flared capillaries[14]. The use of flared capillaries should combine an improvement in both detection limits, mass and concentration, at the same time.

APPENDIX

It is to be noticed that by introducing Eq. 2 into Eq. 1a one obtains

$$U_{TOA} = R_{TOA}\ \text{i.d.}\ c\ \varepsilon, \qquad (12)$$

which indicates that, at least for capillaries having i.d. ≤ 20 μm where the R_{TOA} remains constant, U_{TOA} is proportional to the i.d. as in the case of conventional absorbance. For the small i.d. capillaries investigated, and at moderated pumping power (far from saturation), the TOA signal was experimentally found to be proportional to the capillary i.d. as predicted by Eq. 12.

The concentration LOD can be evaluated using

$$c_{LOD} = \frac{A_{LOD}}{\alpha \text{ i.d. } \varepsilon}, \tag{13}$$

where A_{LOD} is the peak-to-peak noise in absorbance units, α is the dilution of the sample due to peak broadening during the separation. The mass LODs are given by

$$m_{LOD} = c_{LOD} \frac{\pi \text{ i.d.}^2}{4} l_{inj}, \tag{14}$$

where l_{inj} is the injection plug length. The mass LOD can be given, in terms of c_{LOD}, by substituting Eq. 13 into 14 rendering

$$m_{LOD} = \frac{A_{LOD} \pi \text{ i.d. } l_{inj}}{4 \alpha \varepsilon}. \tag{15}$$

Considering that the A_{LOD} are independent of the i.d. dimensions, the lower concentration LODs are usually obtained with larger i.d.s whereas the lower mass LODs with smaller i.d. capillaries. This simplified analysis explains why the most impressive mass LODs are reported for CE (small i.d.) and, for HPLC (large i.d.), the lower concentration LODs.

ACKNOWLEDGMENTS

We thank E. S. Yeung (Iowa State University) and G. Bruin for providing critical comments and suggestions on this manuscript, U. Pieles for some of the samples and N. Burggraf for providing a data acquisition software. This project was supported by the Commission pour l 'Encouragement de la Recherche Scientifique (Switzerland, Project # 2156.1).

Table II. Detection Limits and Separation Efficiencies vs. Injection Parameters for various TOA and conventionally detected CE separations.

	Injection Parameters			Efficiency		Concentration LOD				Mass LOD			
Sample	Press [mb]	Plug [mm]	Vol [nl]	TOA $\times 10^3$	Abs $\times 10^3$	TOA [μM]	Abs [μM]	TOA [μg/ml]	Abs [μg/ml]	TOA [fmole]	Abs [fmole]	TOA [pg]	Abs [pg]
dA	25	1.3	0.39	310	346	1.1	28	0.26	7.2	0.41	11	0.10	2.8
dI	25	1.3	0.39	319	387	1.1	32	0.28	8.0	0.43	12	0.11	3.1
dU	25	1.3	0.39	281	388	14	32	3.2	7.4	5.5	13	1.3	2.9
U	25	1.3	0.39	93	98	24	60	5.8	15	9.3	24	2.3	5.8
A	50	2.5	0.79	91	-	0.39	-	0.11	-	0.31	-	0.09	-
C	50	2.5	0.79	59	-	2.0	-	0.49	-	1.6	-	0.39	-
G	50	2.5	0.79	91	-	0.51	-	0.15	-	0.41	-	0.11	-
dT	50	2.5	0.79	77	-	1.3	-	0.31	-	1.0	-	0.25	-
AMP	500	25	7.9	136	-	0.05	-	0.021	-	0.39	-	0.16	-
CMP	500	25	7.9	85	-	0.19	-	0.097	-	1.5	-	0.76	-
GMP	500	25	7.9	110	-	0.06	-	0.028	-	0.47	-	0.22	-
dTMP	500	25	7.9	83	-	0.20	-	0.092	-	1.6	-	0.72	-
ADP	25	1.3	0.39	158	-	1.1	-	0.50	-	0.42	-	0.20	-
CDP	25	1.3	0.39	158	-	6.8	-	3.4	-	2.7	-	1.3	-
GDP	25	1.3	0.39	209	-	1.0	-	0.51	-	0.40	-	0.20	-
dTDP	25	1.3	0.39	250	-	3.3	-	1.5	-	1.3	-	0.60	-

Press: pressure, Plug: injection plug length, Vol: injection volume, Abs: conventional absorbance detection, LOD: limit of detection.

Table I. Contribution of the individual noise sources to the total measured TOA noise.

Noise Source	Noise empirical relationships [mV]	Noise [e] [mV]
Pump Laser	0.4 % of Baseline Signal	1
HeNe Probe Laser	24 / S	0.5
Signal Conditioner	100 / S	2
Lock-In	1 [a] , 2 [b] , 4 [c]	2
DAQ System	0.2	0.2
Calculated Total Noise	[d]	3
Measured Noise in CE	-	5

The baseline signal and the sensitivity, S, are in mV units.

[a] between S =100 mV and S = 500 mV

[b] between S = 10 mV and S = 50 mV

[c] between S =1 mV and S = 5 mV

[d] $\sqrt{(0.004\times\text{Baseline Signal})^2+(24/S)^2+(100/S)^2+(1^{a},2^{b},4^{c})^2+0.2^2}$

[e] explicit values obtained from the empirical relationships using the experimental parameters from the separation shown in Fig. 6

REFERENCES

(1) Lee, T. T.; Yeung, E. S. *J. Chromatogr.* **1992**, *595*, 319-325.

(2) Swaile, D. F.; Sepaniak, M. J. *J. Liq. Chromatogr.* **1991**, *14*, 869-893.

(3) Chervet, J. P.; van Soest, R. E. J.; Ursem, M. *J. Chromatogr.* **1991**, *543*, 439-449.

(4) Moring, S. E.; Reel, R. T. *Anal. Chem.* **1993**, *65*, 3454-3459.

(5) Wang, T.; Aiken, J. H.; Huie, C. W.; Hartwick, R. A. *Anal. Chem.* **1991**, *63*, 1372-1376

(6) Bruno, A. E.; Gassmann, E.; Pericles, N.; Anton, K. *Anal. Chem.* **1989**, *61*, 876.

(7) Dovichi, N. J. *CRC Crit. Rev. Anal. Chem.* **1987**, *17*, 357-423.

(8) Yeung, E. S. In *Detectors for Liquid Chromatography*; John Wiley & Sons: NY, 1986.

(9a) Fang, L. H.; Swofford, R. L. In *Ultrasensitive Laser Spectroscopy* ; Ed.: Klinger, D. S.; Academic Press: NY, 1983.

(9b) Saz, J. M.; Díez-Masa, J. C. *J. Liq. Chromatogr.* **1994**, *17*, 499-520.

(10) Bruno, A. E.; Krattiger, B.; Maystre, F.; Widmer, H. M. *Anal. Chem.* **1991**, *63*, 2689-2697.

(11a) Krattiger, B.; Bruno, A. E.; Widmer, H. M.; Geiser, M.; Dändliker, R. *Appl. Opt.* **1993**, *32*, 956-965.

(11b) Zimmermann, E.; Souli, N.; Dändliker, R.; Krattiger, B. *Appl. Opt.*, submitted (1994).

(12) Krattiger, B.; Bruin, G. J. M.; Bruno, A. E. *Anal. Chem.* **1994**, *66*, 1.

(13) Bruno, A. E.; Krattiger, B. In *Carbohydrate Analysis*, El Rassi, Z., Ed.; Elsevier: New York, chapter 13 (in press).

(14) Saz, J. M.; Krattiger, B.; Bruno, A. E. *Anal. Methods Instrum.* (in press)

(15) Bruno, A. E.; Maystre, F.; Krattiger, B.; Nussbaum, P.; Gassmann, E. *Trends Anal. Chem.* **1994**, *13*, 190-198.

(16) Nolan, T. G.; Dovichi, N. J. *IEEE Circuits Devices Mag.* **1986**, *2*, 54-56.

(17) Nolan, T. G.; Bornhop, D. J.; Dovichi, N. J. *J. Chromatogr.* **1987**, *384*, 189-195.

(18) Rosenzweig, Z.; Yeung, E. S. *Appl. Spectrosc.* **1993**, *47*, 1175-1179

(19) Yu, M.; Dovichi, N. J. *Mikrochim. Acta* 1988, *111*, 27-40.

(20) Bruno, A. E.; Paulus, A.; Bornhop, D. J. *Appl. Spectrosc.* **1991**, *45*, 462.

(21) Waldron, K. C.; Dovichi, N. J. *Anal. Chem.* **1992**, *64*, 1396.

(22) Weast, R. C. In *CRC Handbook of Chemistry and Physics*; CRC Press, Inc.: Boca Raton, 1983-1984.

(23) Landhold, Börnstein In *Zahlenwerte und Funktionen aus Physik, Chemie, Astronomie, Geophysik, Technik*; II. Band, 8. Teil Optische Konstanten.

(24) Ohms, J. I.; Analysis of Nucleic Acid Derivatives and Analogs by P/ACE System 2 Using Capillary Electrophoresis. Application note. Beckman.

(25) Lecoq, A. F.; Montanarella, L. *J. Microcol. Sep.* **1993**, *5*, 105-118.

(26) Scott, R. P. W.; In *Liquid Chromatography Detectors*; Elsevier: NY, 1986

(27) Petermann, K. In *Laser Diode Modulation and Noise*; Kluwer Academic Press: Dordrecht, 1991.

(28) Kettler, C. N.; Sepaniak, M. J. *Anal. Chem.* **1987**, *59*, 1733.

(29) Jansson, M.; Roeraade, J.; Laurell, F. *Anal. Chem.* **1993**, *65*, 2766.

(30) Kuhr, W. G.; Yeung, E. S. *Anal. Chem.* **1988**, *60*, 2642-2646

(31a) Xue, Y.; Yeung, E. S. *Anal. Chem.* **1993**, *65*, 1988-1993.

(31b) Xue, Y.; Yeung, E. S. *Appl. Spectrosc.* **1994**, *48*, 502-506.

(32) Bruin, G. J. M.; Stegeman, G.; Asten, van A. C.; Xu, X.; Kraak, J. C.; Poppe, H. *J. Chromatogr.* **1991**, *559*, 163-181.

FIGURE CAPTIONS

Fig. 1: Detail of the TOA cell showing the optical arrangement of the pump, probe and reference beams. The probing and reference beam are separated by 14 μm. Notice that the RIM glue is not part of the propagation path of the pump beam.

Fig. 2: Steady state temperature and RI profiles across the cell during a pump pulse. The temperature excess, ΔT, is the temperature difference between sample T_S and room temperature T_R, i.e. $\Delta T = T_S - T_R$. The ΔT and Δn radial distributions are represented at the bottom of the figure.

Fig. 3: Time evolution of TOA signals corresponding to two nucleosides, dU and dI. Although both substances should display approximately the same absorbance, their corresponding TOA signals are rather different because dU photo-dissociates whereas dI is stable. High temperatures (top) correspond to low RI. The signal of the dU trace corresponds to a temperature raise of ca. 1.0 K. Concentration: 50 μg/ml each in SDS buffer, UV power: 20 mW, chopper frequency: 100 Hz. The spiky artifacts in the middle of the heating periods are from intensity transients from the mains rectifier of the pump laser power supply.

Fig. 4: Experimental set-up of the TOA detector. PDA: Photodiode array. HOE: Holographic optical element. KDP: Potassium dihydrogen phosphate frequency doubling crystal. MO: Microscope objective.

Fig. 5: Noise spectra for different probe light sources. The data was obtained from 5 selected chopping frequencies. TOLD 9201 and TOLD 9211 refer to the Toshiba LDs whereas the HeNe trace shows the spectra for a HeNe laser after a single mode fiber. The lowest trace displays the overall noise spectra due to the electronics.

Fig. 6: MEKC electropherogram of a mixture of nucleosides (dI, dU, U and dA) detected by TOA in a 20 μm i.d. capillary in SDS buffer at neutral pH. The hydrodynamically injected (25 mb, 30 s) sample mixture (50 μg/ml of each nucleoside) dissolved in buffer was separated at U = 30 kV resulting in 6 μA of current. The dI peak corresponds to a temperature raise of ca. 190 mK. Although the buffer was filtered and degassed, small bubbles are responsible for the small spikes in the baseline.

Fig. 7: Electropherogram of the same sample and separation as in Fig. 6 detected by a commercial UV/vis absorbance detector. The concentration LODs are ca. 2.4 to 30 times higher than those obtained with TOA detection shown in Fig. 6.

Fig. 8: TOA signal as a function of pumping power for two nucleosides, dU and dI. Because dU photo-dissociates it is associated to a non-linear behavior, whereas the stable dI gives a rather linear response to pumping power up to 20 mW (see their corresponding TOA signals in Fig. 3). Both sample solutions were pumped through the capillary by a pressure of 5.7 b. Concentration 50 µg/ml each in SDS buffer. The chopper frequency was 500 Hz.

Fig. 9: MEKC electropherogram of a mixture of nucleosides and their monophosphates nucleotides detected by TOA in a 20 µm i.d. capillary in SDS buffer at neutral pH. Sample: A, C, G, dT, AMP, CMP, GMP and dTMP. The sample is hydrodynamically injected (25 mb, 30 s) and the concentration is 25 mM for all species diluted in water. The species are separated at 30 kV rendering an electrical current of 6 µA.

Fig. 10: Capillary electropherogram of a mixture of nucleotide diphosphates separated in a 20 mM sodium citrate buffer at pH 3.5. The sample contained 30 µg/ml ADP, 50 µg/ml GDP, 100 µg/ml CDP and 200 µg/ml dTDP in water. The hydrodynamically injected (25 mb/30 s) sample was separated at 30 kV/3 µA, but the electric field was reversed (cathode at injection vial).

TOA paper version: 16 June 1994, 2:12 PM, page =

Fig.1

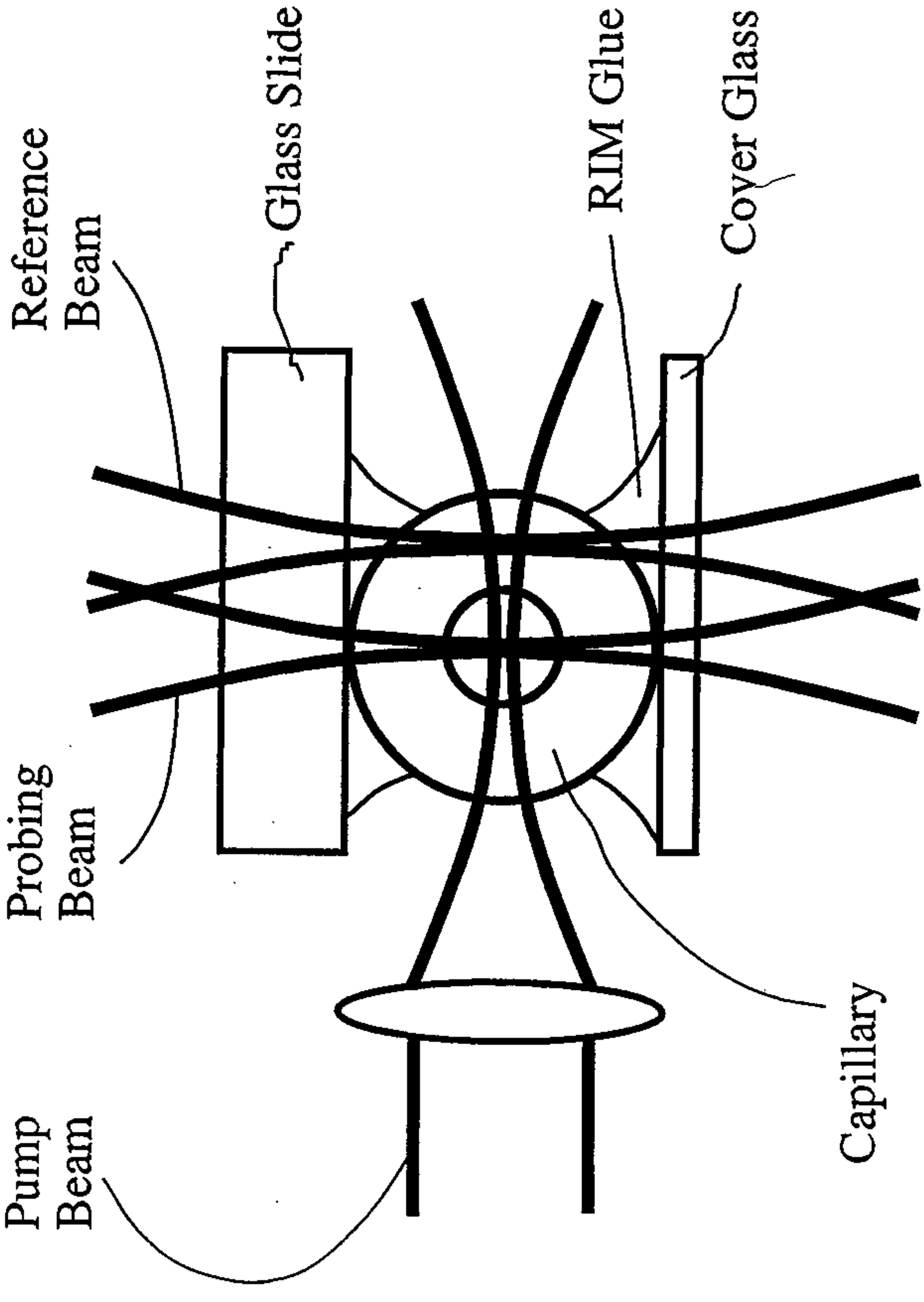
Reference Beam
Glass Slide
RIM Glue
Cover Glass
Probing Beam
Capillary
Pump Beam

Fig. 2

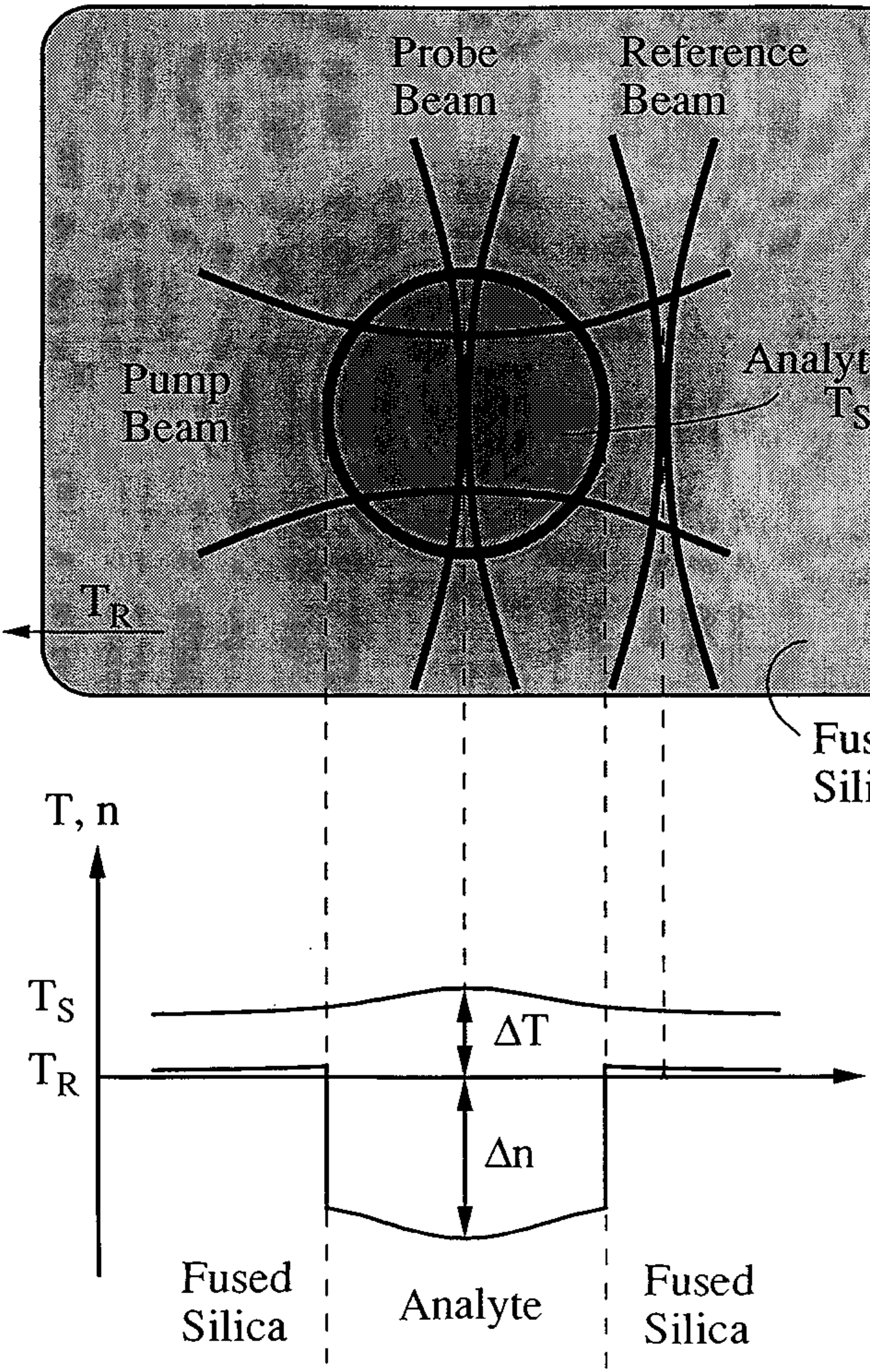

Probe Beam
Reference Beam
Pump Beam
Analyte T_S
T_R
Fused Silica
T, n
T_S
T_R
ΔT
Δn
Fused Silica
Analyte
Fused Silica

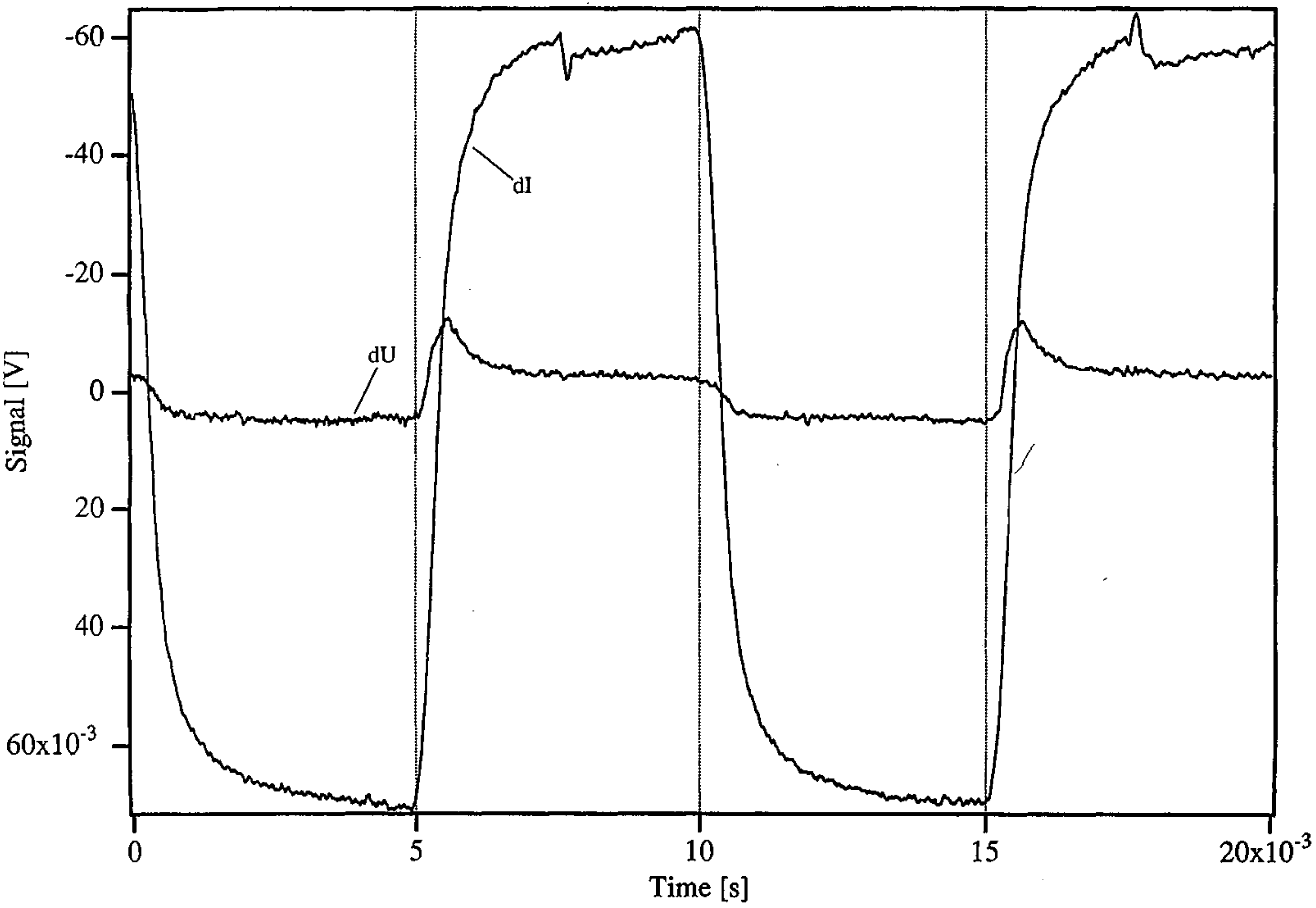

Fig3

Fig. 4

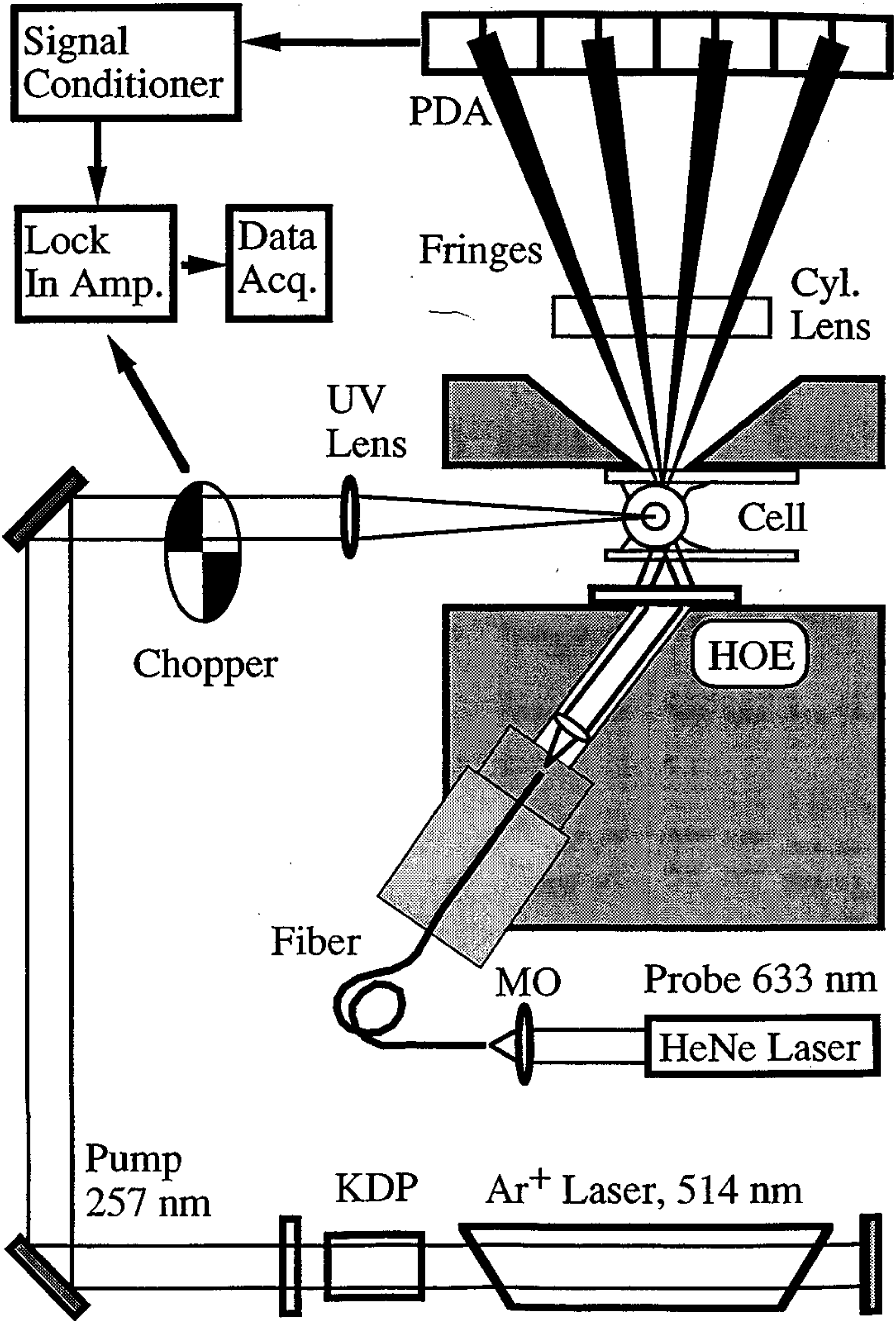
Signal Conditioner
PDA
Lock In Amp.
Data Acq.
Fringes
Cyl. Lens
UV Lens
Cell
Chopper
HOE
Fiber
MO
Probe 633 nm
HeNe Laser
Pump 257 nm
KDP
Ar+ Laser, 514 nm

Fig. 5

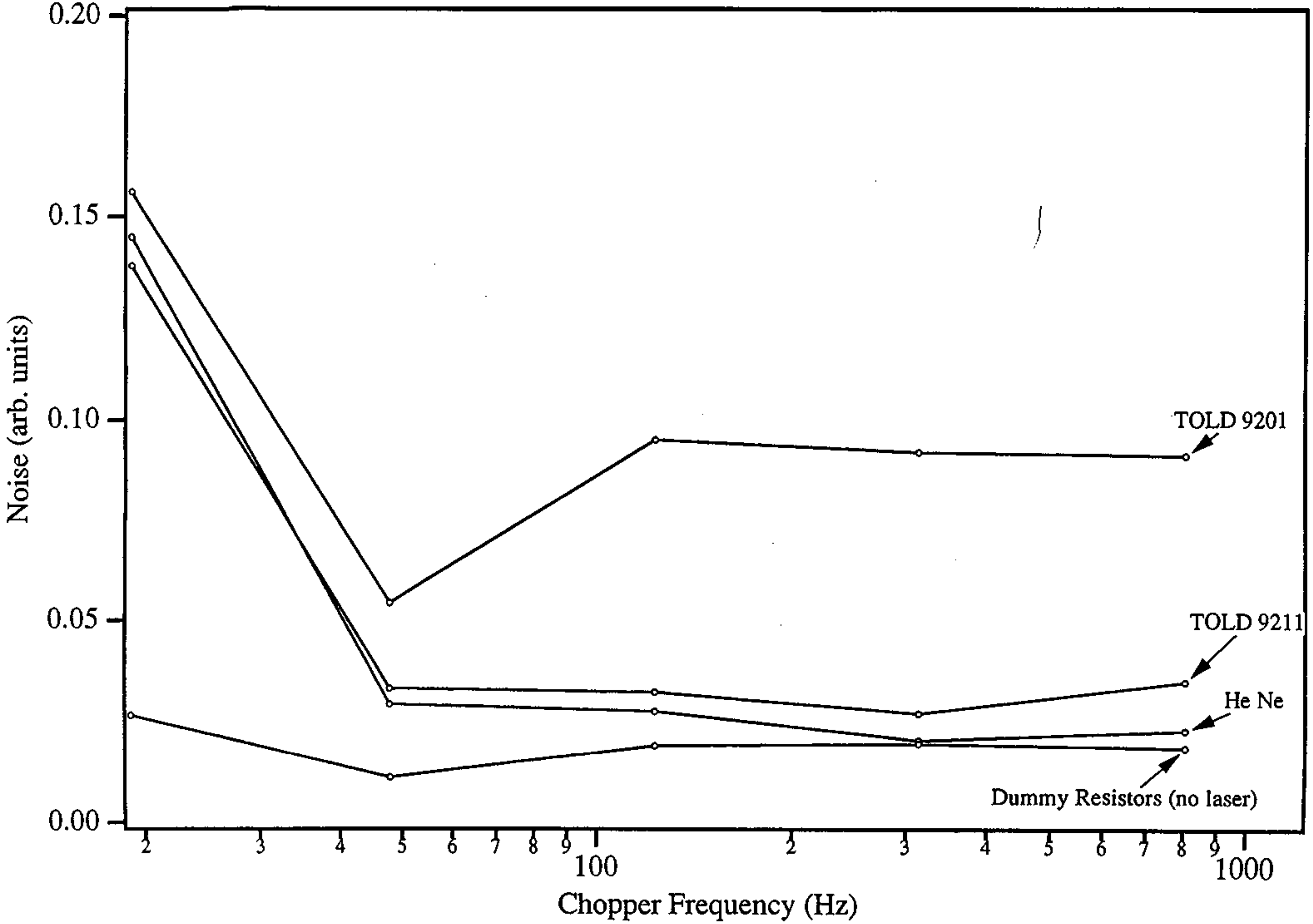
0.20
0.15
0.10
0.05
0.00
Noise (arb. units)
2
3
4
5
6
7
8
9
100
2
3
4
5
6
7
8
9
1000
Chopper Frequency (Hz)
TOLD 9201
TOLD 9211
He Ne
Dummy Resistors (no laser)

Fig.6

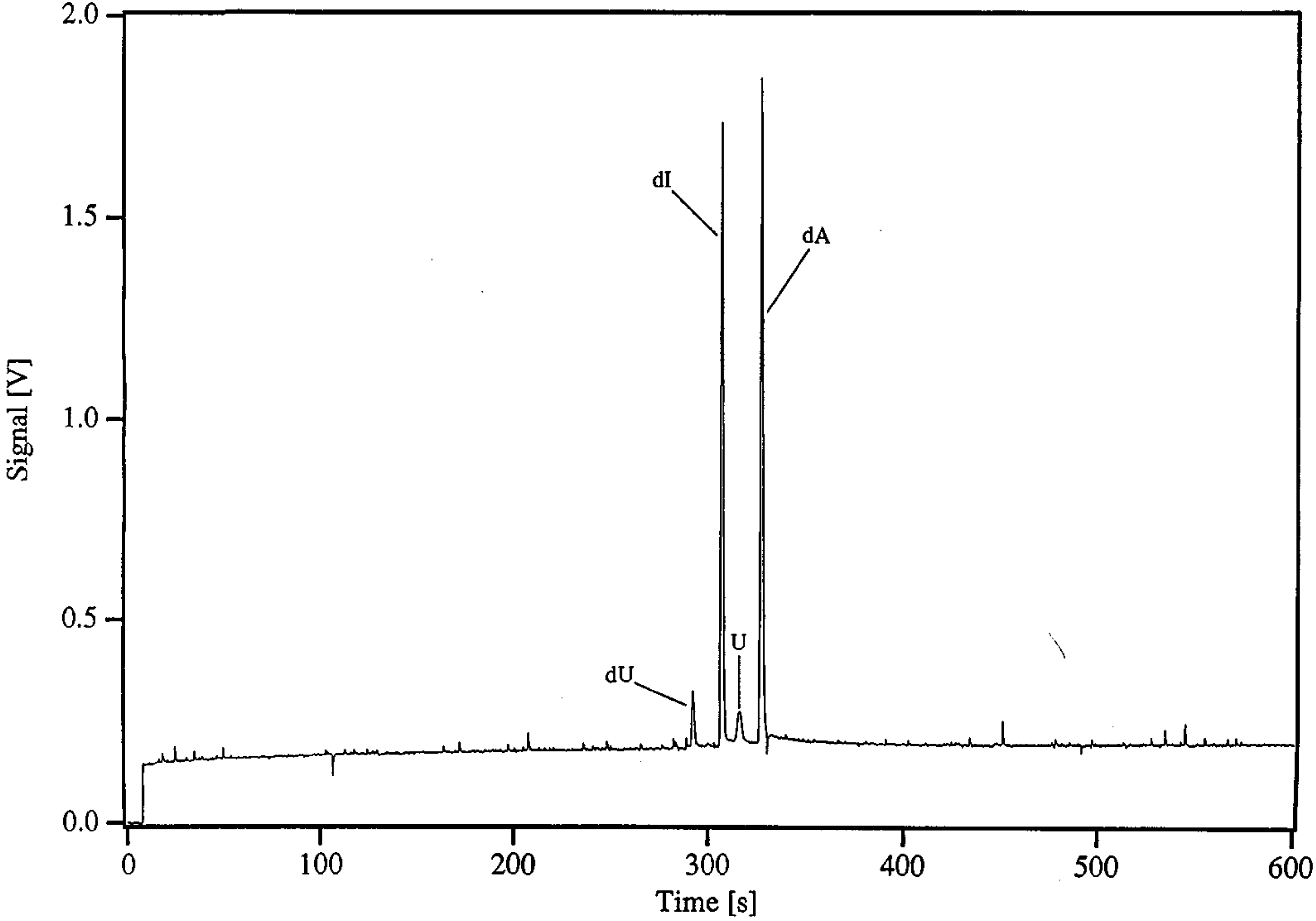

Fig. 7

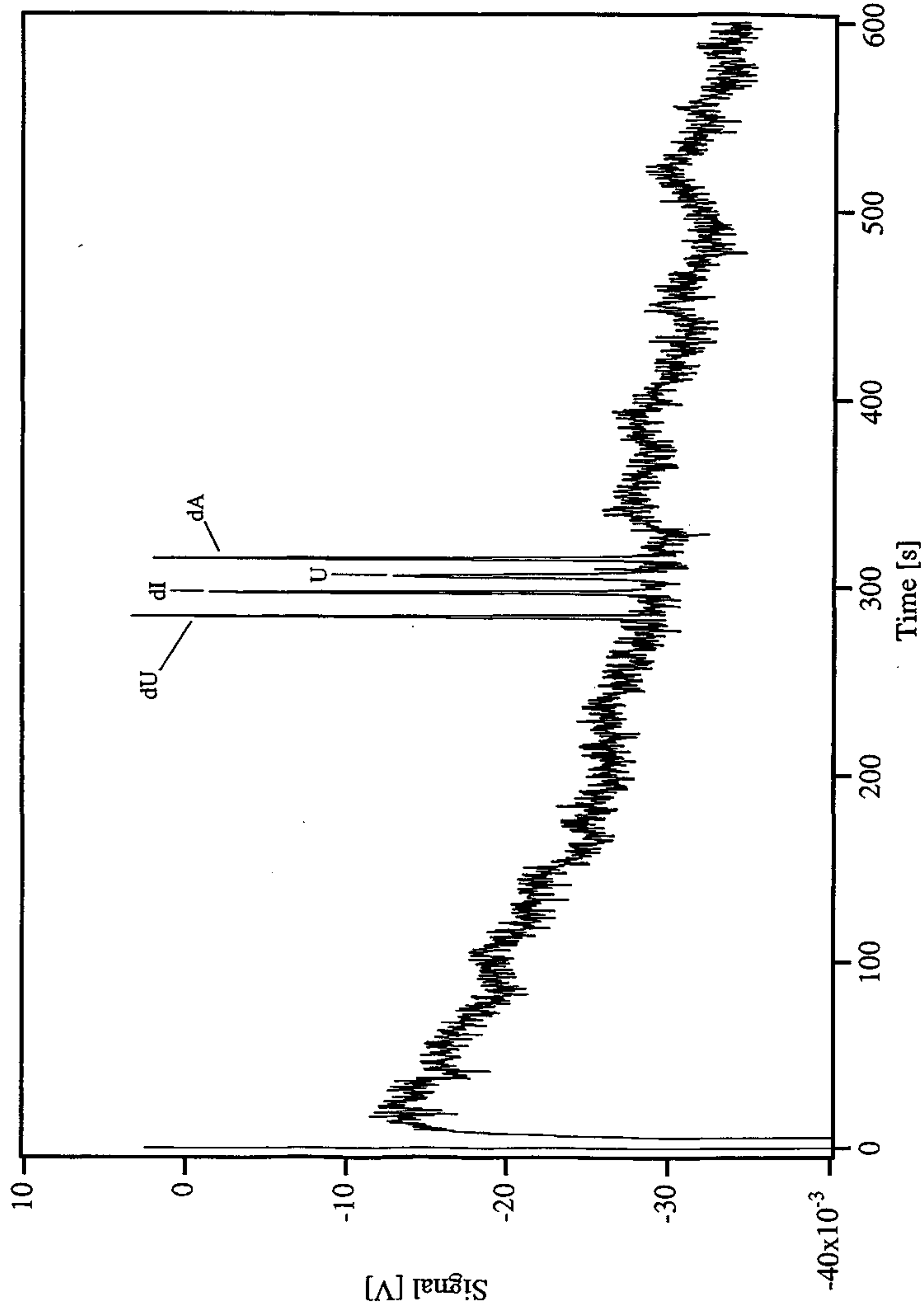
Signal [V]
10
0
-10
-20
-30
-40x10^{-3}
Time [s]
0
100
200
300
400
500
600
dU
dI
U
dA

Fig.8

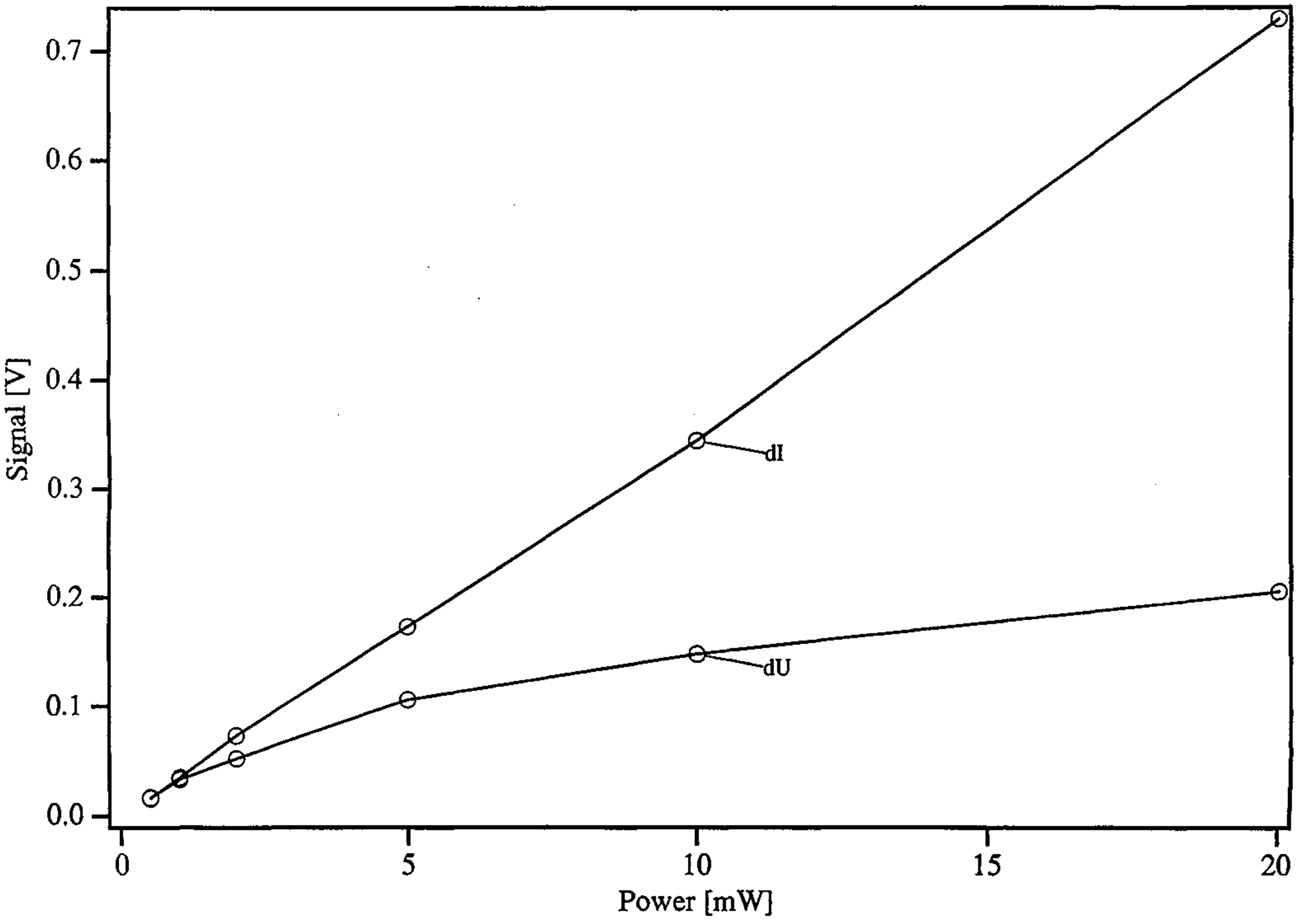

Fig. 9

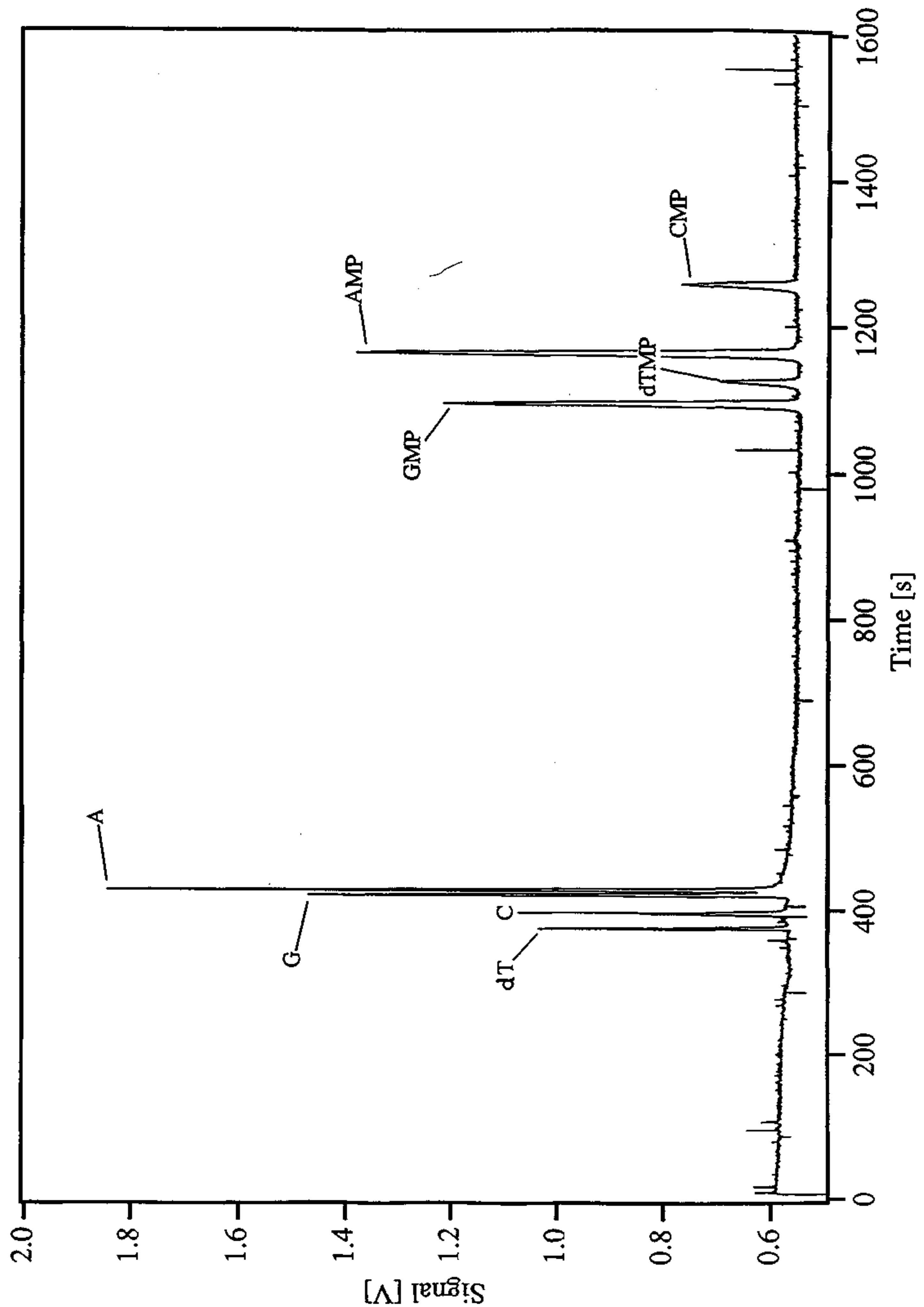

Signal [V]
2.0
1.8
1.6
1.4
1.2
1.0
0.8
0.6
Time [s]
0
200
400
600
800
1000
1200
1400
1600
A
G
C
dT
GMP
dTMP
AMP
CMP

Fig.10

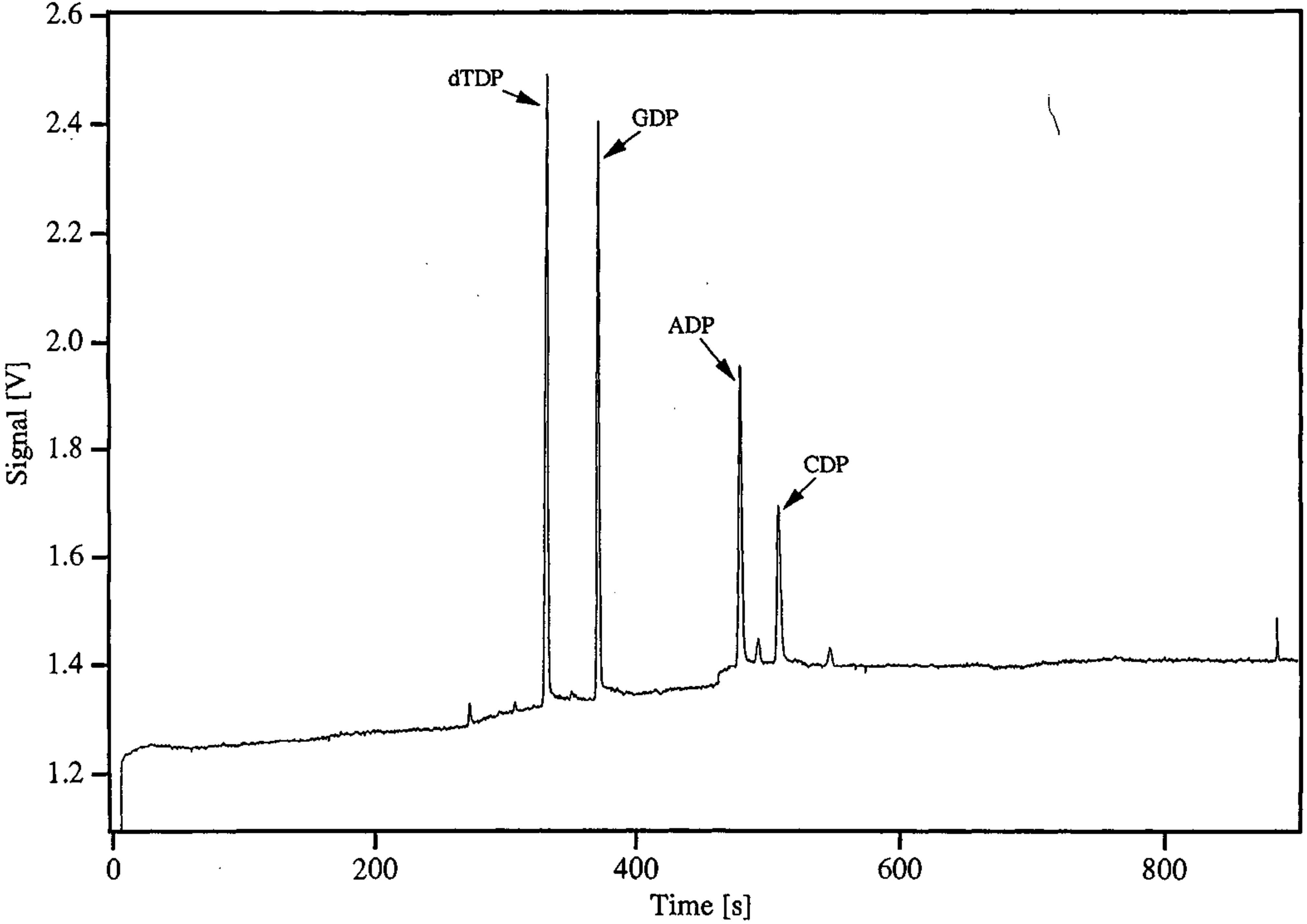
dTDP
GDP
ADP
CDP
2.6
2.4
2.2
2.0
1.8
1.6
1.4
1.2
Signal [V]
0
200
400
600
800
Time [s]

Chapter 7 The Pigtailing Approach to Optical Detection in Capillary Electrophoresis.

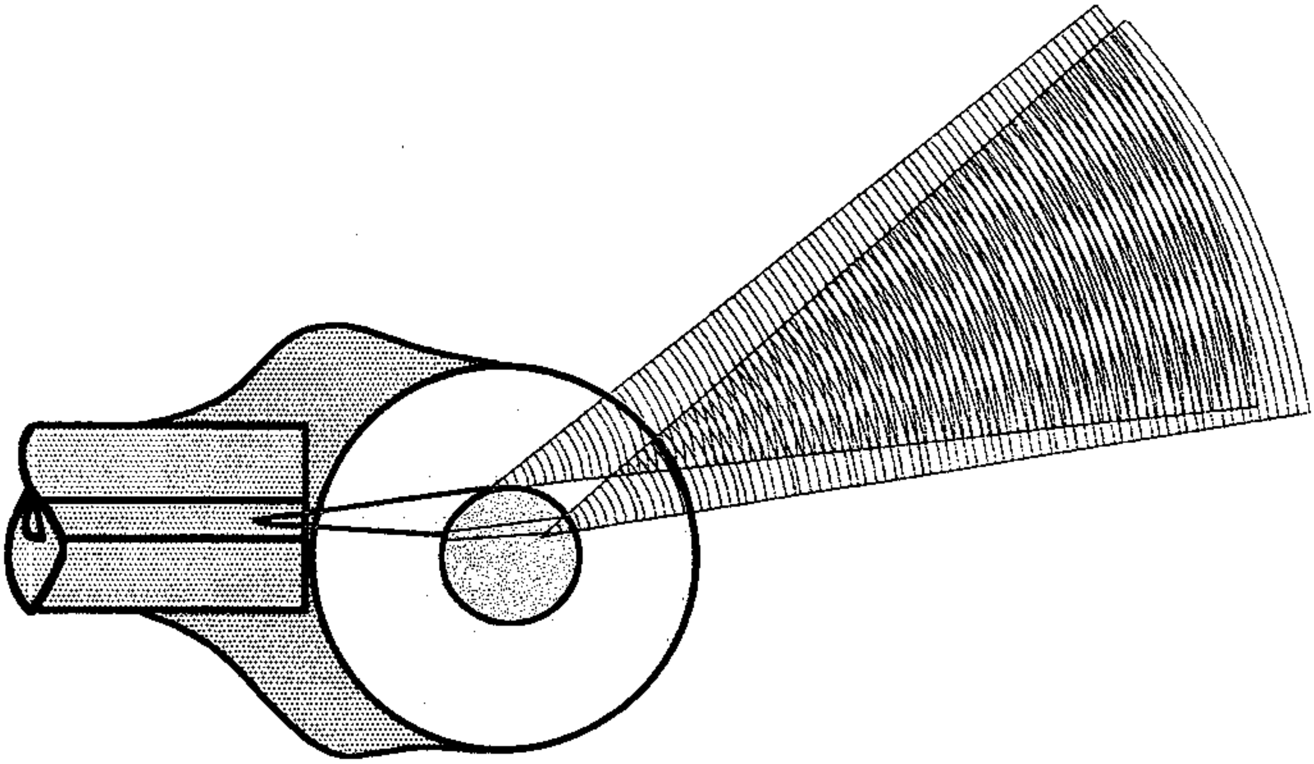

The pigtailing approach to optical detection in capillary electrophoresis

Alfredo E. Bruno*, François Maystre, Beat Krattiger, Philippe Nussbaum and Ernst Gassmann
Basel,Switzerland

A novel approach, called pigtailing, is presented for the construction of optical detectors for capillary electrophoresis. Optical components and procedures from other fields, mainly telecommunications, are incorporated into these devices to give miniaturized detection systems. Suitable light sources for the construction of pigtail absorbance, fluorescence, refractive index and thermo-optical detectors are light-emitting diodes (LEDs) and laser diodes. The best optical components are gradient-index lenses, optical fibers or diffractive optical elements. These components are joined to the capillary with refractive-index-matching materials to avoid refraction and reflections at the optical interfaces and to reduce mechanical vibrations. These joints also facilitate fast thermal equilibrium. The performance of absorption detectors depends mainly on the brightness of the selected LEDs. Two types of refractive-index capillary detectors are described: one features a single-mode polarization-preserving fiber whereas the second uses a customized holographic plate as the main optical element.

Introduction

The miniaturization of instrumental techniques for liquid-phase chemical separations usually provides many benefits, including more theoretical plates, faster analysis times, and lower reagent consumption. For these reasons, capillary electrophoresis (CE) represents an important trend in analytical chemistry [1]. Among the various instrumental features contributing to the overall performance of CE undoubtedly the most important one is detection, which is usually performed by optical methods. To preserve the spatial profile of the eluting substances only *on-column* detection is significant in CE [2]. Several arrangements suitable for *on-column* detection have been reported for absorption [2,3], fluorescence [4], and refractive index (RI) detection [5,6]. There is, however, a growing demand for improving the sensitivity of these detection systems, reducing their detection volume while retaining instrumental sensitivity [7], or devising completely new detectors based on novel principles and concepts.

In this article we present a general approach to detection which we refer to as pigtailing. Pigtailing takes advantage of the great amount of small optoelectronic hardware, developed primarily for communication purposes, such as gradient-index (GRIN) micro lenses, optical fibers, holographic optical elements (HOEs), laser diodes (LDs), light emitting diodes (LEDs), and refractive-index-matching (RIM) materials.

The pigtail concept

Most optical detectors make use of an optical bench on which their components, which are made of materials having rather different physical properties (*e.g.*, thermal expansions, indices of refraction, or elasticity) are mounted. The ultimate sensitivity delivered by these instruments is thus often limited by the noise and drift caused by thermal expansion of these materials, vibrations and schlieren effects in the light-propagation media. Furthermore, owing to these mechanical problems, the noise sources which preclude some de-

---

*To whom correspondence should be addressed.

0165-9936/94/$07.00

tectors from operating at their theoretical limits are generated at the various optical interfaces where reflection and refraction take place [3,5]. The noise at the interfaces is more pronounced when they are not flat, but have a curvature, as in the case of the lenses or capillaries [5] shown in Fig. 1. In addition, each interface is associated with Fresnel reflection losses which reduce the amount of light reaching the photodetector. As a result of all these effects, the more sophisticated and versatile the detector in question, the more noise can potentially reach the photodetector, as a consequence of the greater number of optical elements required.

The pigtailing approach is meant to address these problems. Accordingly, for those optical detectors whose performance is affected by the above-mentioned problems, one would expect maximum instrumental performance when the number of optical interfaces is reduced to the minimum of two. This situation would correspond to a detector in which the light, with the exception of unavoidable cell interfaces, is always propagated through a uniform medium which displays no discontinuities in the refractive index (*n*). This is most easily realized by choosing optical components having a common *n* value close to that of fused silica (n = 1.46) and connecting them by means of RIM materials or by glass soldering methods (not dealt with in this study) to eliminate the optical interfaces.

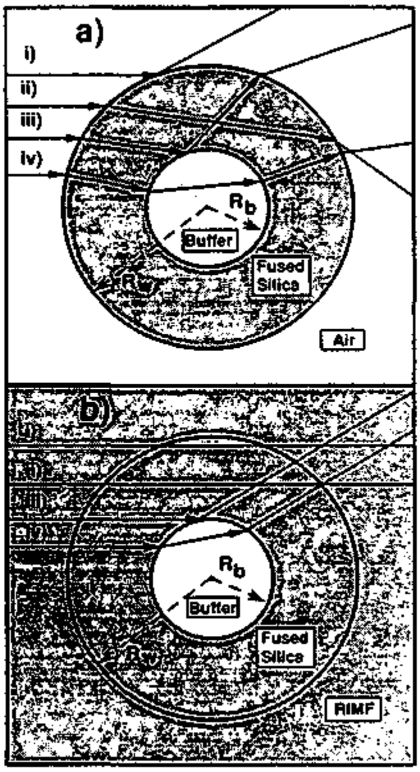

Fig. 1. Cross section of a side-illuminated capillary tube and corresponding ray-tracing of four significant cases for (a) a capillary surrounded with air and (b) a RIM fluid. Reflections and refractions at the different interfaces are indicated by arrows. The different *n* values of the various propagation media are: air (n = 1.0), aqueous buffer (n *ca.* 1.3), fused silica and RIM material with identical *n* (n = 1.46) (reprinted from ref. 5, with permission).

The use of RIM materials instead of air (n = 1) between two glass-like elements reduces the reflections roughly (from the Fresnel formulae) by

$$\beta = \left[\frac{(1.46 - n_i)}{(n_i - 1)}\right]^2 \qquad (1)$$

For a material having a refractive index of, *e.g.*, n_i = 1.50 this results already in a reduction by 156 times (*i.e.*, $\beta = 0.0064$) in the reflection effects.

The above-mentioned problems of an optical, mechanical and thermal nature, which might degrade the performance of the detectors in question, are simultaneously addressed are by pigtailing. Indeed, the glueing or soldering of components is always accompanied by a more efficient use of the illumination source and higher mechanical and thermal stability. A pigtail detector is thus one in which:

- light propagates with minimal refractions and reflections
- the optical components are arranged into the most rugged mechanical construction possible and
- the components are placed in direct contact to facilitate a fast thermal equilibrium.

The name, pigtail, is most commonly used for LEDs or LDs whose output is delivered by an optical fiber. In this regard, the word *pigtailing* is used here to refer to the coupling of optical fibers, GRIN lenses, capillary tubes, light sources, etc., using RIM materials.

Examples

LED-based capillary absorption detector

LEDs are miniature, extremely stable (*ca.* 10^{-5}), solid-state light sources with a very long lifetime, whose intensity can be modulated with a wave of any desired shape, and they require a low driving power. They are very attractive sources for small-volume absorption and fluorescence capillary detectors in the visible region. There are LEDs emitting in selective wavelengths from a wide range of the spectral region, ranging from the infrared (λ *ca.* 1000 nm) down to the blue (λ *ca.* 400 nm) with, in some cases, a fairly narrow bandwidth [8]. The light-power decreases very quickly as it approaches the blue region, and below λ = 430 nm they do not emit sufficiently to allow sensitive measurements. The emission cut-off is at λ = 400 nm (see Table 1 in ref. 8). This is perhaps the major drawback of LEDs, as compared with conventional sources. For comparison purposes we measured the output power of a typical red LED (Siemens hyper-rot, λ = 660 nm, LH 5424-QO) with a calibrated photodiode (PD). Driven by 10 mA it delivered 1.5 mW of light power (quoted to deliver 320 mcd). More light intensity can be obtained when the LEDs are operated by pulsed currents [8]. There are also LED crystals that emit at two different wavelengths. The color changes in these LEDs are obtained by changing the direction of the current. A recent publication [8] reviews the characteristics of LEDs suitable for optical detection.

LED-based absorption detectors for flow injection analysis and high-performance liquid chromatography using conventional cells have been reviewed in 1983 by Betteridge *et al.* [9], in 1988 by Trojanowicz *et al.* [10] and, most recently by Dasgupta *et al.* [8]. Some designs, such as these shown in Fig. 8 of ref. 8 and Fig. 1 of ref. 11, happen to conform to our definition of a pigtail detector.

Improvements over the past twenty years in the design of LED-based photometric devices have resulted in a reduction in the absorption noise levels (a.u.) by three orders of magnitude. Because, in most cases, these detectors are shot-noise limited, most of the improvements [8] are correlated with the higher throughputs of new LEDs and, to a lesser extent, the use of dual-beam configurations, better cell designs, quieter power supplies and more sophisticated processing electronics [12,13].

Previous LED-based absorption detectors, including those satisfying our pigtail definition, have not been used in conjunction with small capillaries. A diagram of the pigtail absorption detector using a 100 µm I.D. capillary that we have developed for CE is shown in Fig. 2. The first stage in the construction of LED-based absorption and fluorescence detectors is the pigtailing of a surface-emitting LED to a 1/2 pitch GRIN lens (we use SelFoc® GRINs from Nippon Sheet Glass, Japan). In this way, the crystal of the LED, having

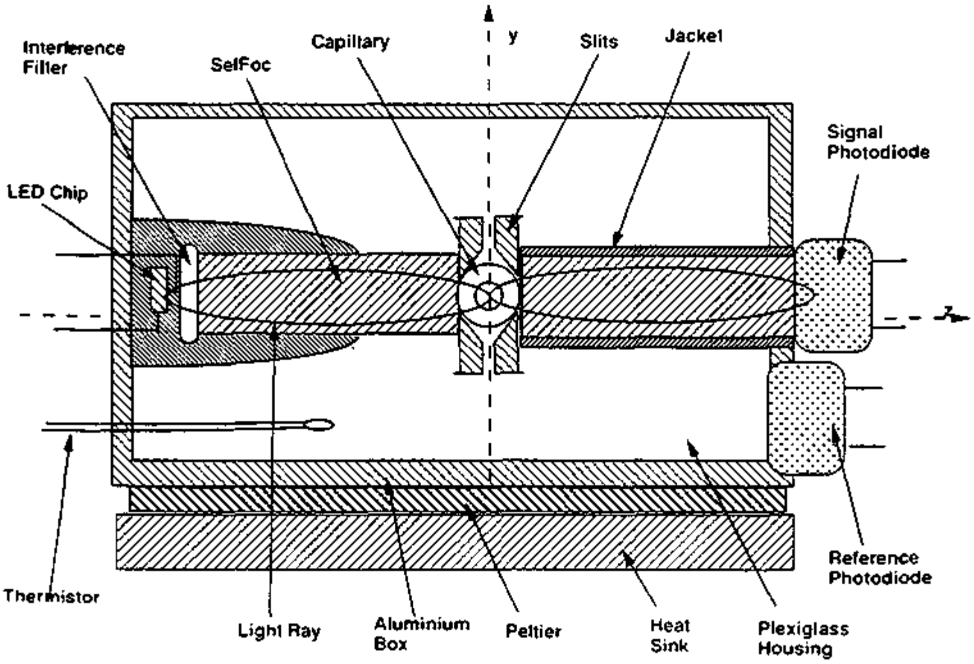

Fig. 2. Diagram of a capillary pigtail absorption detector. The naked capillary tube is masked by a set of steel slits and glued to a Plexiglas mounting piece using UV-curing RIM glues. The slit is 50×500 µm wide and has a large channel of *ca.* 400 µm to fit the capillary tube.

a typical area of about 280×280 µm, is imaged onto the capillary bore.

The pigtailing of the LED is achieved by first milling the Plexiglas body almost down to the emitting crystal and then glueing the GRIN lens with UV-curing RIM materials as indicated in Fig. 3. A GRIN lens is a cylindrical rod with a parabolic RI distribution, whose RI is higher at its optical axis and decreases toward its periphery; light rays thus propagate in a sinusoidal fashion through the rod. A GRIN lens performs the same optical functions as standard spherical lenses. However, what makes them unique for pigtailing purposes is that glueing does not disturb their lens properties. This is in contrast to conventional lenses whose focusing is based on refractions at both curved interfaces.

More than 1 µW of light is measured at the exit surface of the GRIN rod (first focal point) for a typical green LED used to illuminate the capillary tube. Then 50 µm wide slits select a portion of the LED chip image where the naked capillary tube is subsequently glued. A second GRIN lens, of 1/2 or 1/4 pitch, brings the light from the capillary to the probe PD. A PVC jacket round the second GRIN lens prevents scattered light reaching the probe PD. Scattered light propagated through the Plexiglas housing is collected by an array of PDs (Siemens KOM 2057-L). The set of GRIN lenses also separates the PDs from sources of heat which contribute to drift in the output signal – namely, the LED and, in CE, Joule heat. The analog electronic circuit is wired to produce absorbance as an output signal in a dual-beam arrangement. Zeroing is performed manually using a potentiometer.

The whole detector is glued to an aluminum plate and, when needed, thermostated using a small Peltier and calibrated thermistor driven by a thermo-electric system (ILX Lightwave model LDT-5412). The total size of the detector is only 3.2×2.0×1.5 cm which could be further reduced without compromising its performance. The fixing of all the components is carried out under the microscope by means of micro-manipulators, using UV-curing RIMs at every positioning step. To facilitate this process both Plexiglas bodies have a set of parallel holes which accept sliding glass rods of 3 mm diameter. The complete pigtail detectors, including the Peltier and the electronics, fit into a sealed 15×6×3 cm metal box.

With a green LED (Siemens HPG5066X) the short-term noise level is about $1 \cdot 10^{-5}$ a.u. for an integration time of 1 s and a feed-back resistance of the current-to-voltage amplifiers of 100 kΩ. With blue LEDs, which are less brilliant [13], the currents through the signal PD are less than 1 nA, requiring feed-back resistance as high as 5 MΩ, and the absorbance noise levels are somewhat

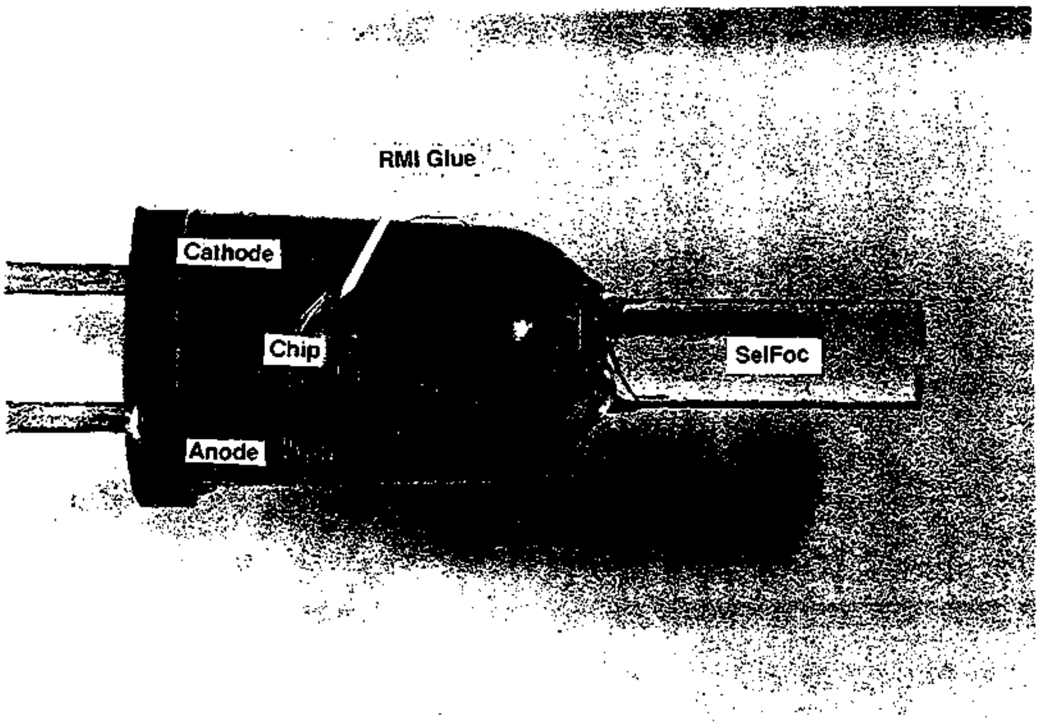

Fig. 3. Photograph of a GRIN lens pigtailed to an LED (type T 1-3/4, diameter 5 mm; the GRIN rod is seen distorted inside the LED due to the lens properties of the Plexiglas body).

higher (*ca.* 5·10^{-5} a.u.). Long-term drifts in the baseline are extremely low.

LED-based capillary fluorescence detector

Laser induced fluorescence (LIF) is, to date, the most sensitive detection method available for CE [1]. Many researchers are shifting from gas to solid-state [14] lasers. There is an increasing tendency to use blue [15] excitation, using the second-harmonic (415 nm) from near-infrared LDs and, in the infrared of the spectrum [16], using the fundamental emission from LDs. The secrets for high sensitivity when employing LIF in conjunction with capillary tubes are to use microscope objectives with high numerical apertures, spatial masks to restrict the field of view, to carefully select the interference filters, to use high quantum-yield PMTs with low dark currents, and optimize the excitation-laser power to account for photobleaching and saturation. The most difficult problem, once the above-mentioned aspects have been taken care of, is the scattering of light from the capillary walls. Fluorescence detectors which operate without scattering light are known as background-free detectors, and the baseline noise is dominated by the dark current of the PMT. Background-free detectors are not uncommon for gas-phase detection but they are more difficult to realize in the liquid phase, and it is even more difficult in the presence of liquid-filled narrow-bore capillary tubes. This is mainly because scattered light is produced at the four unavoidable optical interfaces in the measuring zone (see Fig. 1).

A few solutions have been proposed to minimize the amount of scattered light. The most successful approach consists of the elimination of all optical interfaces around the measuring zone in a "windowless cell" design known as a sheath flow cuvette [7] at the end of the capillary. Unfortunately, the method is not particularly easy to implement and not all optical detectors can be constructed in such a way. However, the same principles can be partially applied to at least eliminate the outer capillary interface by immersing the capillary in RIM materials. This approach has been taken by Kurosu *et al.* [17] and Bruno *et al.* [5,18]. Another approach, using optical fibers, is due to de Bokx *et al.* [19]. In this case the excitation and emission fibers were tapered into the capillary in a design that is fully consistent with the pigtailing concept formulated here.

LEDs, instead of lasers or conventional arc lamps, have been used to induce fluorescence in various devices [20] which give impressive sensitivities. The high stability of LEDs translates into very low noise, even in the presence of scattered light, and thus to high signal-to-noise ratios.

None of these devices [20] has been used in conjunction with small capillaries suitable for CE. Using the same arrangement as in the absorption detector (Figs. 2 and 3) for excitation, and multimode optical fibers to collect emission, we constructed the pigtail capillary LED-based fluorescence detector whose design is shown in Fig. 4. To further minimize scattering light arising from the inner silica–buffer interface, the collecting fibers are conveniently placed at the back and at an angle close to 45° with respect to both the optical excitation axis and the capillary axis as indicated in Fig. 4a. We employed a compact device (Hamamatsu, HC120 series) as a PMT which included the high voltage supply and the output amplifier in the same unit and is driven by a 12 V power supply. The electropherogram of 10^{-4} M rhodamine B in a 100 µm I.D. capillary is shown Fig. 5. The limit of detection, as determined from the figure, is 10^{-7} M (S/N *ca.* 2000).

LD-based capillary RI detectors

The major issue in the quest for maximum sensitivity in the construction of capillary RI detectors is thermal and mechanical stability [5]. Pigtailing thus appears to be a tantalizing construction option. The first pigtail RI detector, based on schlieren effects, is due to Pawliszin [21]. This detector features a LED as the light source pigtailed to a multimode fiber; a second fiber, placed off-axis, was used for collection. The windows of the cells are, as in the capillary fluorescence cell design from de Bokx *et al.* [19], the ends of both optical fibers. This RI detector is, however, not suitable for CE.

We have demonstrated two types of capillary RI pigtail detectors [22] suitable for CE based on interferometry [5,18]; one model features a single-mode fiber whereas the second uses a holographic element as the main optical element [6]. Both RI capillary detectors are also suitable for thermo-optical (TO) absorption [7,23].

"Off-axis" RI detector

In this design [5,18], shown in Fig. 6, the capillary acts as a beam splitter, a strongly divergent lens, and a phase shifter leading to a broad fan of

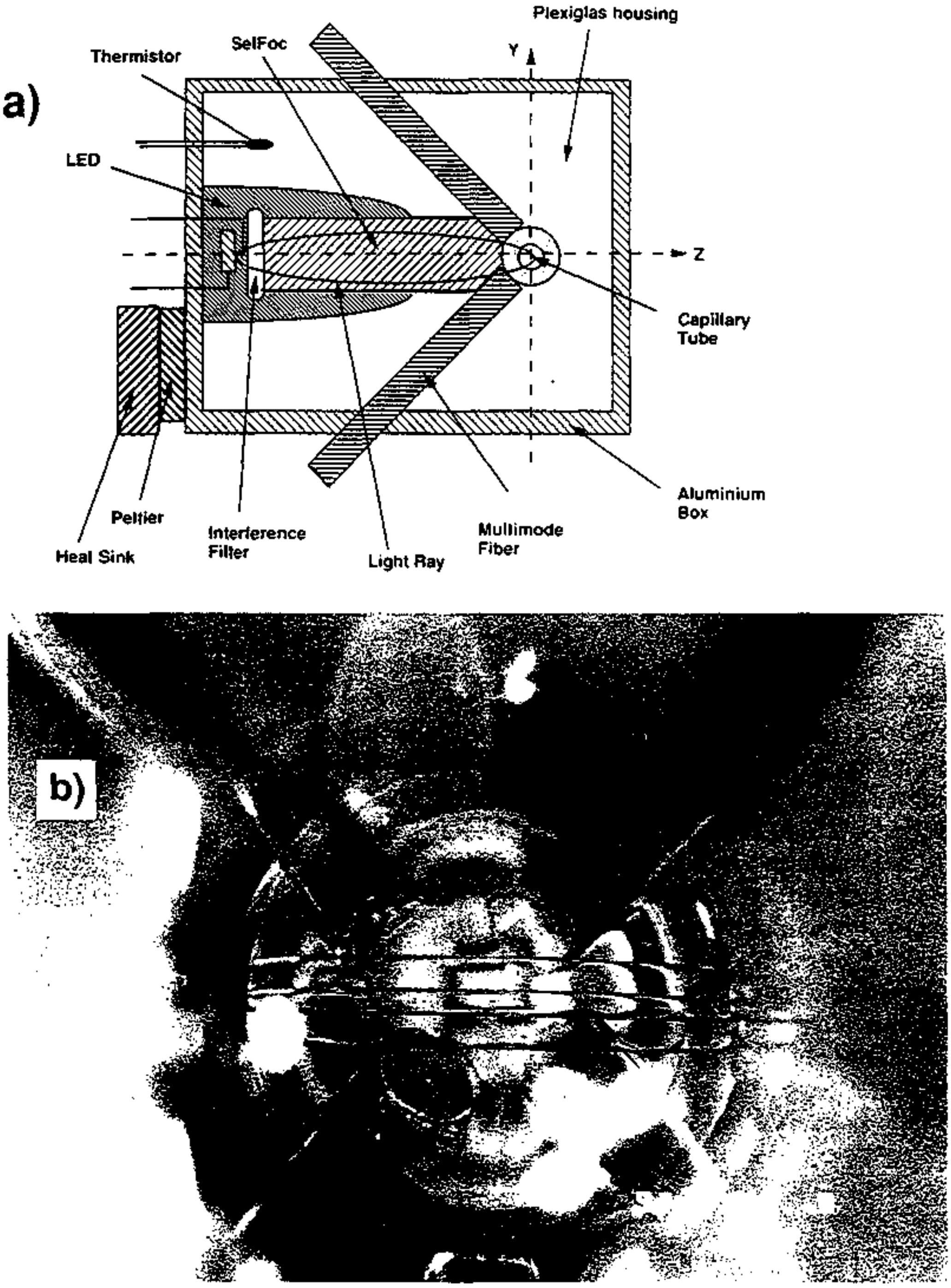

Fig. 4. Cross-sectional side view (a), of the LED-based pigtail capillary fluorescence detector; the four collecting fibers are placed at an angle of ca. 45° with respect to the capillary and optical axis, as shown in the picture. (b) The picture shows a top view before filling all cavities with RIM materials.

fringes on the other side of the capillary. These fringes shift with a change in the RI in the capillary medium. Their lateral displacements are monitored by a position-sensitive diode (PSD), which after calibration, constitutes the output signal.

The main propagation medium is a single-mode polarization-preserving fiber pigtailed at both ends; *i.e.* to the LD and capillary. Proper "off-axis" illumination of the capillary is achieved by first positioning the fiber end (from a commercially pigtailed LD) with respect to the capillary and then glueing it with fast UV-curing RIM glues. The optimum offset of the fiber with respect to the capillary is one in which the fringes display maximum contrast and high intensity [18]. Because the beam width at the capillary orifice depends on the

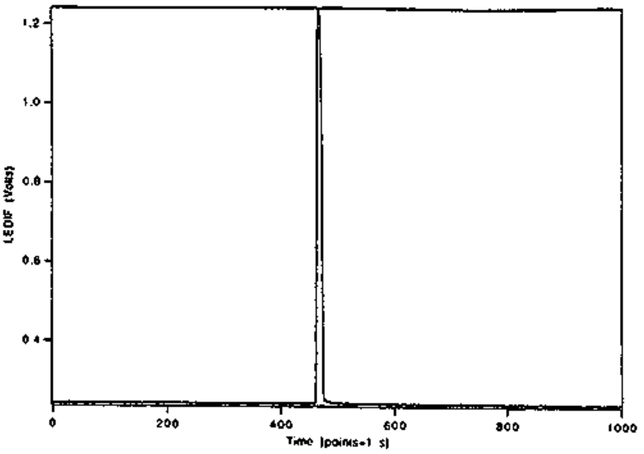

Fig. 5. Electropherogram of $2 \cdot 10^{-4}$ *M* rhodamine B in a 100 μm capillary, recorded with a pigtail fluorescence detector featuring a green LED ($\lambda_{max.}$ = 560 nm).

thickness of the capillary wall it is preferable to use thin-wall capillaries. As in any interferometric measurement, wavelength fluctuations translate into signal noise, and therefore the LD and capillary cell are temperature-stabilized by Peltier control units and quiet power supplies.

The noise obtained with this detector under static conditions is about 2 μRIU in a 25 μm capillary. This sensitivity degrades under electrophoretic conditions because of Joule heat effects. The linear dynamic range extends over about three decades. The "off-axis" RI method can be used with capillaries having I.D. ≥15 μm; diffraction effects starts to dominate the interference pattern in smaller I.D. capillaries [18].

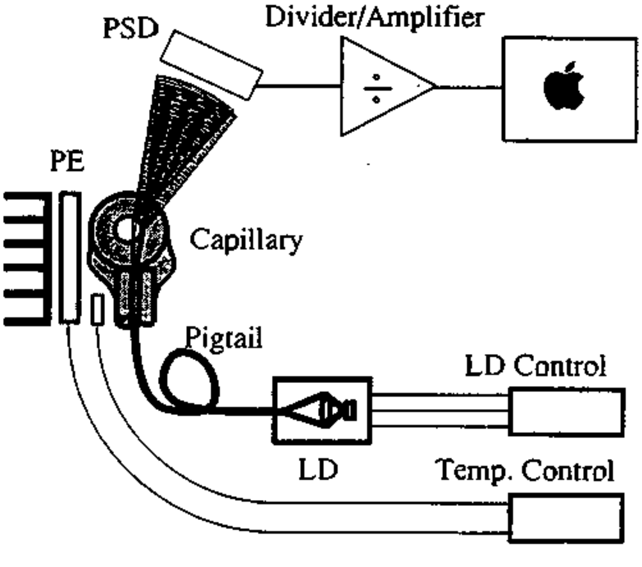

Fig. 6. Diagram of the pigtail "off-axis" RI detector. PE = Peltier element.

Holographic RI detector

HOEs are components used in optics to deflect and to shape light beams. What makes HOEs attractive for optical detection in small volumes is that complex operations, which are difficult to realize with conventional optical elements, are readily incorporated into a single HOE. HOEs are being refined and find application in various optoelectronic devices such as laser writers, FAX machines, and CD players, and in analytical chemistry [24]. We demonstrated the use of customized HOEs in the design of a RI capillary detector [6].

The geometric arrangement of the HOE-based RI detector is shown in Fig. 7. The optical functions, played by the capillary in the off-axis version, are basically transferred to the HOE. The HOE, placed before the capillary, acts as a superposition of two lenses displaced by a predetermined distance and thus transforms the incoming single beam into two focussed spots with beam waists of *ca.* 1 μm. As in the off-axis RI detector, the capillary is surrounded by RIM material to eliminate the reflections and refractions at the outer capillary wall. In the HOE version, in contrast to the off-axis version, the observed fringes are equally spaced, allowing the use of diode arrays for their detection (see Fig. 7). The probing arm of the interferometer crosses the capillary

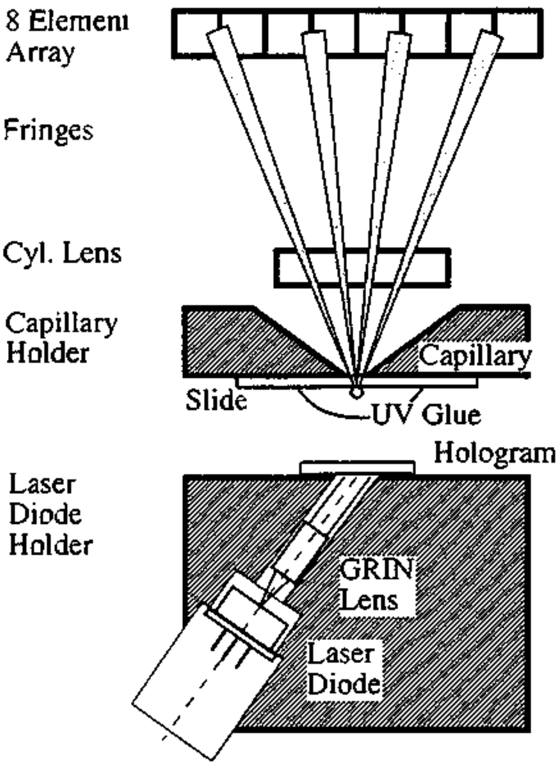

Fig. 7. Diagram of the holographic refractive index detector.

through the center where the optical path, and thus phase changes, are larger.

This detector was demonstrated by Krattiger *et al.* [6] for the CE separation of small cations in a 10 µm I.D. tube. The electropherogram of a mixture of underivatized saccharides recorded with the holographic RI detector in a 25 µm I.D. capillary is shown in Fig. 8. The detection limits and linear dynamic range rendered by this RI detector are comparable to those delivered by the off-axis version. However, the HOE version is more suitable than the off-axis design for capillaries having I.D.s ≤20 µm.

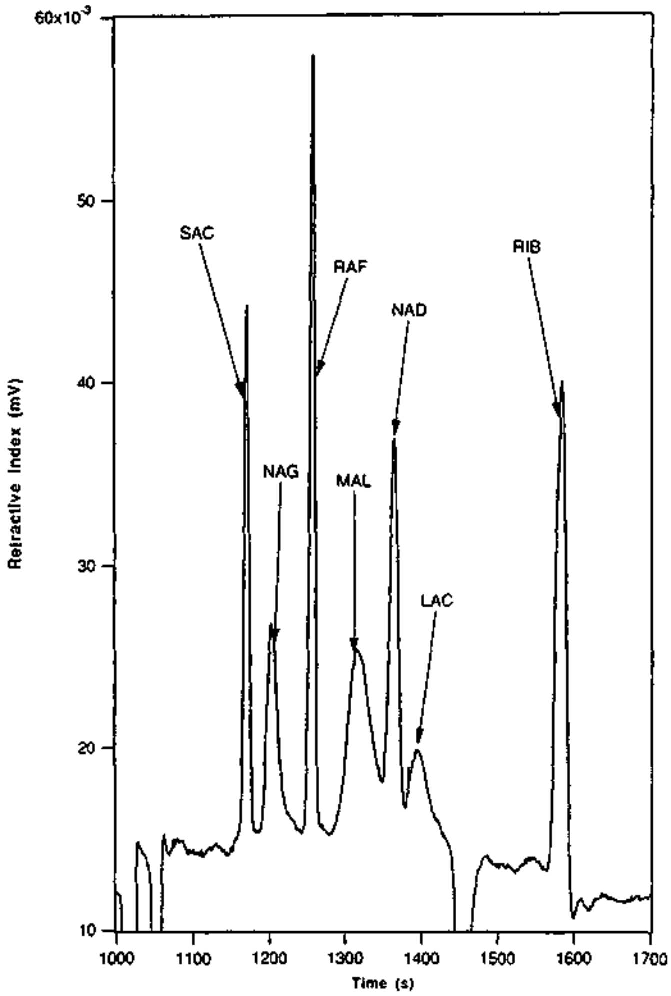

Fig. 8. Electropherogram of a mixture of seven underivatized saccharides recorded with the hologram RI detector. The peaks correspond to sucrose (SAC), N-acetyl-D-glucosamine (NAG), raffinose (RAF), maltose (MAL), N-acetyl-D-galactosamine (NAD), lactose (LAC) and ribose (RIB). Each 7.3 m*M* except for sucrose and raffinose which are 3.6 m*M*. The buffer employed in this separation consists of 50 m*M* borate with cyclohexylamino-propanesulfonic acid (CAPS) at pH = 9.4. The capillary length is 70 cm, 50 to detector; I.D. = 25 µm; electrical field = 170 V/cm (12 kV); current = 7.7 µA; hydrodynamic injection 100 mbar during 6 s (*i.e.*, injection plug *ca.* 1 mm). The first two negative peaks are due to the two buffers and the negative peak at 1450 s is due to an impurity.

Conclusions

The analogy between the pigtail approach to optical detection and other technologies such as electronics and digital computation is rather obvious. In all cases, in order to achieve lower noise, faster responses, smaller drifts, etc., the rule is to simplify the architecture of the device in question. The associated disadvantage is that in the process one ends up by compromising instrumental versatility for specificity.

Because radiance is more important than the total light-output power for the illumination of small surfaces, the use of edge-emitting, instead of surface-emitting LEDs with a directional radiation pattern, would be better suited for the construction of pigtail absorbance and fluorescence detectors. However such LEDs are only available for wavelengths above 700 nm. Two-wavelength absorption and fluorescence pigtail detectors could be constructed with single LEDs emitting at two wavelengths. A more general possibility, for constructing multi-wavelength absorption pigtail detectors, would be to use multi-element LED arrays emitting at selected wavelengths which would correlate with a photodiode array at the other side of the capillary, in an architecture similar to the one shown in Fig. 2.

Further developments of pigtail detectors will follow advances in the development of LEDs and LDs, mainly in a shortening of their emission wavelengths and an increase in their power output.

References

1 S.F.Y. Li, *Capillary Electrophoresis*, Elsevier, Amsterdam, 1992.
2 F. Foret, M. Deml, V. Kahle and P. Boček, *Electrophoresis*, 7 (1986) 430.
3 A.E. Bruno, E. Gassmann, N. Pericles and K. Anton, *Anal. Chem.*, 61 (1989) 876.
4 L.N. Amankwa, M. Albin and W. Kuhr, *Trends Anal. Chem.*, 11 (1992) 114.
5 A.E. Bruno, B. Krattiger, F. Maystre and H.M. Widmer, *Anal. Chem.*, 63 (1991) 2689.

6 B. Krattiger, G. Bruin and A.E. Bruno, *Anal. Chem.*, 66 (1994) 1.

7 N.J. Dovichi, *Rev. Sci. Instrum.*, 61 (1990) 3653.

8 P.K. Dasgupta, H.S. Bellamy, H. Liu, J. Lopez, E.L. Loree, K. Morris, K. Petersen and K.A. Mir, *Talanta*, 40 (1993) 53.

9 D. Betteridge, W.C. Cheng, E.L. Dagless, P. Davis, T.B. Goad, D.R. Deans, D.A. Newton and T.B. Pierce, *Analyst* (*London*), 108 (1983) 1.

10 M. Trojanowicz, P.J. Worsfold and J.R. Clinch, *Trends Anal. Chem.*, 7 (1988) 301.

11 F.I. Ormaza-Gonzaléz and P.J. Statham, *Anal. Chim. Acta*, 244 (1991) 63.

12 H. Liu, P.K. Dasgupta and H.J. Zheng, *Talanta*, 40 (1993) 1331.

13 P.C. Hauser and D.W.L. Chiang, *Talanta*, 40 (1993) 1193.

14 A.P. Larson, H. Ahlberg and S. Folestad, *Appl. Opt.*, 32 (1993) 794.

15 T. Imasaka, K. Nishitani and N. Ishibashi, *Analyst* (*London*), 116 (1991) 1407.

16 A.J.G. Mank, H. Lingeman and C. Gooijier, *Trend Anal. Chem.*, 11 (1992) 210.

17 Y. Kurosu, T. Sasaki and M. Saito, *J. High Resolut. Chromatogr.*, 14 (1991) 86.

18 B. Krattiger, A.E. Bruno, H.M. Widmer, M. Geiser and R. Dändliker. *Appl. Opt.*, 32 (1993) 856.

19 P.K. de Bokx, E.E.A. Gillisen, P. van de Weijer, M.H.L. Bekkers, C.H.M. van Bommel and H.G. Janseen, *J. Chromatogr.*, 598 (1992) 115.

20 O.S. Wolfbeis (Editor), *Fluorescence Spectroscopy*, Springer, New York, 1993.

21 J. Pawliszin, *Anal. Chem.*, 58 (1986) 3207.

22 A.E. Bruno and B. Krattiger, in Z. El Rassi (Editor), *Carbohydrate Analysis*, Elsevier, Amsterdam, in press.

23 A.E. Bruno, A. Paulus and D.J. Bornhop, *Appl. Spectrosc.*, 45 (1991) 462.

24 J.M. Tedesco, H. Owe, D.M. Pallister and M.D. Morris. *Anal. Chem.*, 65 (1993) 441A.

A.E. Bruno, F. Maystre, B. Krattiger, P. Nussbaum and E. Gassmann are at the Corporate Analytical Research Division of Ciba-Geigy Ltd., 4002 Basel, Switzerland.

Chapter 8 Conclusions

Σ

Chapter 8. CONCLUSIONS

Summary: In *Chapter 2* a RI detector based on the design originally proposed by Bornhop and Dovichi[1] is described. In this instrument, refractive index matching fluids (RIMF) and position sensitive detectors (PSDs) are introduced in conjunction with thermoelectric stabilization, integrated into a compact, highly symmetric cell design. A detailed analysis of the noise sources is made with emphasis in shot noise and the noise due to thermal fluctuations, and used to improve the detector. Considering their importance in biochemistry, food science, etc. underivatized sugar mixtures were chosen to demonstrate the new detection method in a CE separation.

Chapter 2 extended the use of RI detection to the CE domain. The detector performance is based on the advantage of immersing the capillaries in RIMF, which greatly simplified the complex scattering patterns known from previously reported experiments. The fringe intensities associated with naked capillaries were low and, the behavior of the pattern was not predictable. With the new set-up, fringe detection was easier because the fringes are wider and carry higher intensities. The RIMF showed also effective removal from the Joule heat produced during CE. The novelties related to this chapter lead to a patent application[2].

In *Chapter 3* a model is presented to predict the fringe patterns of "off-axis" illuminated capillaries. The theory is based on ray tracing and considers phases and intensities.

The calculated patterns are compared to measured intensity distributions and matching was found over a large angular range. The model mimics well the interference patterns for capillaries having i.d.s in the range from 20 to 250 µm. The results are used to improve "off-axis" RI detectors. It was noticed that these RI detectors are path length dependent and larger i.d.-tubes can produce higher sensitivities.

In *Chapter 4* a capillary RI detector based on a Wollaston prism is reported. This detector is demonstrated in CE separations of sugars with a flared as well as with a standard capillary. The S/N ratio of the two cases are compared.

The bubble in the flared capillary showed greater potential in improving the *S/N* ratio than expected, because two beneficial effects are multiplied: First, the larger i.d. leads to a longer probing path increasing the signal, and second, the locally increased cross section at the detection site reduces Joule heat generation and hence noise.

Chapter 5 demonstrates the use of holographic optical elements (HOE) in an "on-axis" capillary RI detectors. The fringe pattern is theoretically explained as well as the relation between its shift and the RI change in the analyte.

The combination of holographic optics with LDs on the instrumental side and the elegant FASI injection with displacement detection on the analytical side allowed the RI detection in capillaries with i.d.s as small as 5 µm. To explain the negative RI peaks, it is suggested that the buffer ions, which display a large difference in the molar refractivity with respect to that of the sample within the zone, are depleted by the sample. The novelties related to this chapter lead to a patent application[3].

Thermo-optical absorbance (TOA) detection based on the hologram RI detector was presented in *Chapter 6*. It is the first demonstration of a TOA detection of underivatized sample in CE. The operating principle is explained and a simple model is introduced to predict the detector performance. Stepwise noise analysis was performed for each component of the TOA detection system. The detector is compared to conventional absorbance. The power dependence of photo bleaching of the sample was investigated.

The presented TOA detector operates under a different principle than the previous thermal lensing set-ups. Therefore different properties are obtained. The present detector shows enhanced sensitivity with capillary i.d. whereas the sensitivity of thermal lensing detectors are reported to be rather independent with path length.

Chapter 7 introduces a general concept of detector design. The pigtailing concept claims that the detector properties can sometimes be improved by gluing the optical components with refractive index matching (RIM) glue and by reducing the number the optical interfaces to a minimum. Among the various detectors built according to this concept, there is also a capillary RI detector. This "pigtail" RI detector is constructed by gluing an optical fiber on the capillary. As the hologram RI detector is also a "pigtail" detector, it is sketched along with CE application. Other "pigtail" detectors were presented such as light emitting diode (LED) based fluorescence and absorbance detectors.

The pigtailing construction principle is often applied in optical engineering, it can even be found in nature in the human eye. In this chapter this principle is applied to detection in analytical chemistry. As it combines the highest stability and the simplest construction, it will be the ideal way for mass production of cheap disposable analysis devices. The novelties related to this chapter lead to a patent application[4].

Suggestions for Further Instrumental Improvements: At the end of a work one knows about the things which one could have done better. Suggestions for improvements can only be omitted for a perfect work and, as this is not the case, some suggestions are presented here.

Although the major contribution to noise originated often from buffer impurities and Joule heat, it is challenging to further improve the detection systems to be prepared for enhanced buffers. Because the intrinsic detector noise (without noise due to separation) has often many important contributing sources, improvements have to be done at various points simultaneously.

Improvements of the capillary RI detectors are expected if the optical path lengths of the probe and reference beams are identical. In this case the fringe pattern would be independent of the wavelength and therefore no noise is expected to come from wavelength fluctuations associated to laser diodes, which are preferred because of their small size and good intensity stability. This "white light" interferometer approach could be achieved by adjusting the Wollaston prism in Chapter 4 or by choosing the optimum position of the photo detector array (PDA) in the hologram detector described in Chapter 5.

Improvements would also be possible at the detection of the fringe pattern. The PDA detection for the fringe shifts was applied because these devices simplified the experimental set-up. Although the maximum amount of light is collected here, which can help to reduce the noise, the signal is not maximized with fringe shift. This could be achieved by detecting only the slopes of the fringes. This effect has been seen but not studied in detail.

The pigtailing concept was only partially applied for the fiber based and the hologram detector because between the cell and the position sensitive detector air was still the propagation medium. This space, being about 10 cm long, has to be filled with a transparent solid in order to completely fulfill the concept.

Acceptance of Capillary RI Detection: There are various reasons which explain why RI detectors are not commercially available for CE. The first reason is a dilemma of interdependence. On one hand, the number of known applications is important for commercial success when selling capillary RI detectors. On the other hand, method development depends on the availability of equipment. A second reason for the absence of capillary RI detectors on the market lies probably in the bad reputation of RI detection per se, which is claimed to be about 1-2 orders of magnitude less sensitive than absorbance detection. In this context it seems completely weird to apply an "insensitive" detection principle to CE, which already suffers from its bad detection limits due to the short optical probing paths. This bad reputation of the RI however, turns into a wrong prejudice if one thinks of transparent samples. In this work we focused on the instrumental side and, although the new detectors are always accompanied with analytical applications, one application per detector is not enough. Other optimized applications should be demonstrated in order to get out of this dilemma and to defeat the prejudice. Another reason is that the construction of capillary RI detectors is not as easy as of absorbance or fluorescence detectors. This problem, however, should mainly be eliminated now by the present work.

Suggestions for other Studies: In CE method development, normally a separation has to be optimized to yield high efficiency, sensitivity, or speed. To avoid time consuming experiments, in the case of absorbance, computer simulations are carried out and the whole electropherogram, including peak heights and elution times, are predicted. Such an approach should be adapted for RI detection in CE separations in order to screen for good buffers for optimized detection limits.

Using the off-axis principle it is possible to choose the position of the probing ray by choosing the monitoring fringe. Observing a fringe at high scattering angles returns the refractive index in the zone close to the inner capillary surface while a fringe close to the optical axis reveals mainly the bulk RI in the capillary lumen. Therefore, it is possible to detect simultaneously along different paths when observing more than one fringe. This principle will be most suitable to study temperature distributions across the capillary during CE or the effect of coatings on the local sample concentration.

Previously, all capillary RI detectors are primarily used in conjunction with liquid buffers in separations. Maystre et al.[5] used a RI sensor in the RI equalizer set-up designed to cancel RI fluctuations to enhance polarimetric detection in HPLC. However, such devices can be generally used as RI sensors for various applications. One example One example would be to use them with a gas inside, instead of a liquid, to measure its RI changes. As the RI of a gas depends on its density, pressure and temperature, these capillary RI detectors are suitable for remote sensing of any of these properties. To measure the pressure, one capillary end has to be inserted to the measuring site, while the other end has to be blocked. Assuming a resolution of 0.1 µRIU (150 µm-i.d. capillary) a resolution in pressure of 0.3 mb would be obtained when working with air at normal conditions. This corresponds to a resolution in density of 0.5 g/m^3. Sensitive remote temperature sensing is possible via gas pressure.

References

(1) Bornhop, D. J.; Dovichi, N. J. *Anal. Chem.* **1986**, *58*, 504.

(2) Bruno, A. E.: "Interferometric Measuring Arrangement for Refractive Index Measurements in Capillary Tubes" United States Patent 5,251,009.

(3) Geiser, M.; Herzig, H. P.; Bruno, A. E.; Kratöger, B.: "Interferometric Apparatus for Monitoring Changes of the Refractive Index of Fluid Samples in Capillary Tubes" Patent Application, Dec. 1993.

(4) Bruno, A. E.; Krattiger, B.; Effenhauser, C. S.; Maystre, F.; Nussbaum, P.: "Optical Detection Arrangement for Small Volume Chemical Analysis of Fluid Samples" Patent Application, Mar. 5, 1993.

(5) Maystre, F.; Bruno, A. E.; Kühner, Ch. *Anal. Chem.* (in press).

Reprinted from

TrAC

ELSEVIER

The pigtailing approach to optical detection in capillary electrophoresis

Alfredo E. Bruno*, François Maystre, Beat Krattiger, Philippe Nussbaum and Ernst Gassmann
Basel,Switzerland

A novel approach, called pigtailing, is presented for the construction of optical detectors for capillary electrophoresis. Optical components and procedures from other fields, mainly telecommunications, are incorporated into these devices to give miniaturized detection systems. Suitable light sources for the construction of pigtail absorbance, fluorescence, refractive index and thermo-optical detectors are light-emitting diodes (LEDs) and laser diodes. The best optical components are gradient-index lenses, optical fibers or diffractive optical elements. These components are joined to the capillary with refractiva-index-matching materials to avoid refraction and reflections at the optical interfaces and to reduce mechanical vibrationa. These joints also facilitate fast thermal equilibrium. The performance of absorption detectors depends mainly on the brightness of the selected LEDs. Two types of refractive-index capillary detectors are described: one features a single-mode polarization-preserving fiber whereas the second uses a customized holographic plate as the main optical element.

Introduction

The miniaturization of instrumental techniques for liquid-phase chemical separations usually provides many benefits, including more theoretical plates, faster analysis times, and lower reagent consumption. For these reasons, capillary electrophoresis (CE) represents an important trend in analytical chemistry [1]. Among the various instrumental features contributing to the overall performance of CE undoubtedly the most important one is detection, which is usually performed by optical methods. To preserve the spatial profile of the eluting substances only *on-column* detection is significant in CE [2]. Several arrangements suitable for *on-column* detection have been reported for absorption [2,3], fluorescence [4], and refractive index (RI) detection [5,6]. There is, however, a growing demand for improving the sensitivity of these detection systems, reducing their detection volume while retaining instrumental sensitivity [7], or devising completely new detectors based on novel principles and concepts.

In this article we present a general approach to detection which we refer to as pigtailing. Pigtailing takes advantage of the great amount of small optoelectronic hardware, developed primarily for communication purposes, such as gradient-index (GRIN) micro lenses, optical fibers, holographic optical elements (HOEs), laser diodes (LDs), light emitting diodes (LEDs), and refractive-index-matching (RIM) materials.

The pigtail concept

Most optical detectors make use of an optical bench on which their components, which are made of materials having rather different physical properties (*e.g.*, thermal expansions, indices of refraction, or elasticity) are mounted. The ultimate sensitivity delivered by these instruments is thus often limited by the noise and drift caused by thermal expansion of these materials, vibrations and schlieren effects in the light-propagation media. Furthermore, owing to these mechanical problems, the noise sources which preclude some de-

---

*To whom correspondence should be addressed.

0165-9936/94/$07.00

tectors from operating at their theoretical limits are generated at the various optical interfaces where reflection and refraction take place [3,5]. The noise at the interfaces is more pronounced when they are not flat, but have a curvature, as in the case of the lenses or capillaries [5] shown in Fig. 1. In addition, each interface is associated with Fresnel reflection losses which reduce the amount of light reaching the photodetector. As a result of all these effects, the more sophisticated and versatile the detector in question, the more noise can potentially reach the photodetector, as a consequence of the greater number of optical elements required.

The pigtailing approach is meant to address these problems. Accordingly, for those optical detectors whose performance is affected by the above-mentioned problems, one would expect maximum instrumental performance when the number of optical interfaces is reduced to the minimum of two. This situation would correspond to a detector in which the light, with the exception of unavoidable cell interfaces, is always propagated through a uniform medium which displays no discontinuities in the refractive index (n). This is most easily realized by choosing optical components having a common n value close to that of fused silica (n = 1.46) and connecting them by means of RIM materials or by glass soldering methods (not dealt with in this study) to eliminate the optical interfaces.

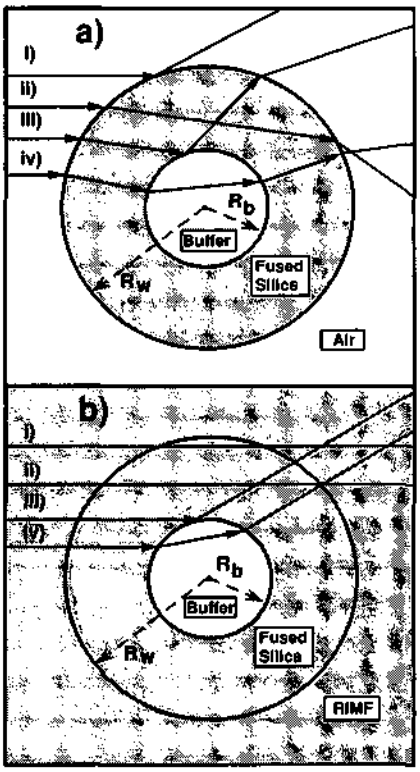

Fig. 1. Cross section of a side-illuminated capillary tube and corresponding ray-tracing of four significant cases for (a) a capillary surrounded with air and (b) a RIM fluid. Reflections and refractions at the different interfaces are indicated by arrows. The different n values of the various propagation media are: air (n = 1.0), aqueous buffer (n *ca.* 1.3), fused silica and RIM material with identical n (n = 1.46) (reprinted from ref. 5, with permission).

The use of RIM materials instead of air (n = 1) between two glass-like elements reduces the reflections roughly (from the Fresnel formulae) by

$$\beta = \left[\frac{(1.46 - n_i)}{(n_i - 1)} \right]^2 \tag{1}$$

For a material having a refractive index of, *e.g.*, n_i = 1.50 this results already in a reduction by 156 times (*i.e.*, β = 0.0064) in the reflection effects.

The above-mentioned problems of an optical, mechanical and thermal nature, which might degrade the performance of the detectors in question, are simultaneously addressed are by pigtailing. Indeed, the glueing or soldering of components is always accompanied by a more efficient use of the illumination source and higher mechanical and thermal stability. A pigtail detector is thus one in which:

- light propagates with minimal refractions and reflections
- the optical components are arranged into the most rugged mechanical construction possible and
- the components are placed in direct contact to facilitate a fast thermal equilibrium.

The name, pigtail, is most commonly used for LEDs or LDs whose output is delivered by an optical fiber. In this regard, the word *pigtailing* is used here to refer to the coupling of optical fibers, GRIN lenses, capillary tubes, light sources, etc., using RIM materials.

Examples

LED-based capillary absorption detector

LEDs are miniature, extremely stable (*ca.* 10^{-5}), solid-state light sources with a very long lifetime, whose intensity can be modulated with a wave of any desired shape, and they require a low driving power. They are very attractive sources for small-volume absorption and fluorescence capillary detectors in the visible region. There are LEDs emitting in selective wavelengths from a wide range of the spectral region, ranging from the infrared (λ *ca.* 1000 nm) down to the blue (λ *ca.* 400 nm) with, in some cases, a fairly narrow bandwidth [8]. The light-power decreases very quickly as it approaches the blue region, and below λ = 430 nm they do not emit sufficiently to allow sensitive measurements. The emission cut-off is at λ = 400 nm (see Table 1 in ref. 8). This is perhaps the major drawback of LEDs, as compared with conventional sources. For comparison purposes we measured the output power of a typical red LED (Siemens hyper-rot, λ = 660 nm, LH 5424-QO) with a calibrated photodiode (PD). Driven by 10 mA it delivered 1.5 mW of light power (quoted to deliver 320 mcd). More light intensity can be obtained when the LEDs are operated by pulsed currents [8]. There are also LED crystals that emit at two different wavelengths. The color changes in these LEDs are obtained by changing the direction of the current. A recent publication [8] reviews the characteristics of LEDs suitable for optical detection.

LED-based absorption detectors for flow injection analysis and high-performance liquid chromatography using conventional cells have been reviewed in 1983 by Betteridge *et al.* [9], in 1988 by Trojanowicz *et al.* [10] and, most recently by Dasgupta *et al.* [8]. Some designs, such as these shown in Fig. 8 of ref. 8 and Fig. 1 of ref. 11, happen to conform to our definition of a pigtail detector.

Improvements over the past twenty years in the design of LED-based photometric devices have resulted in a reduction in the absorption noise levels (a.u.) by three orders of magnitude. Because, in most cases, these detectors are shot-noise limited, most of the improvements [8] are correlated with the higher throughputs of new LEDs and, to a lesser extent, the use of dual-beam configurations, better cell designs, quieter power supplies and more sophisticated processing electronics [12,13].

Previous LED-based absorption detectors, including those satisfying our pigtail definition, have not been used in conjunction with small capillaries. A diagram of the pigtail absorption detector using a 100 µm I.D. capillary that we have developed for CE is shown in Fig. 2. The first stage in the construction of LED-based absorption and fluorescence detectors is the pigtailing of a surface-emitting LED to a 1/2 pitch GRIN lens (we use SelFoc® GRINs from Nippon Sheet Glass, Japan). In this way, the crystal of the LED, having

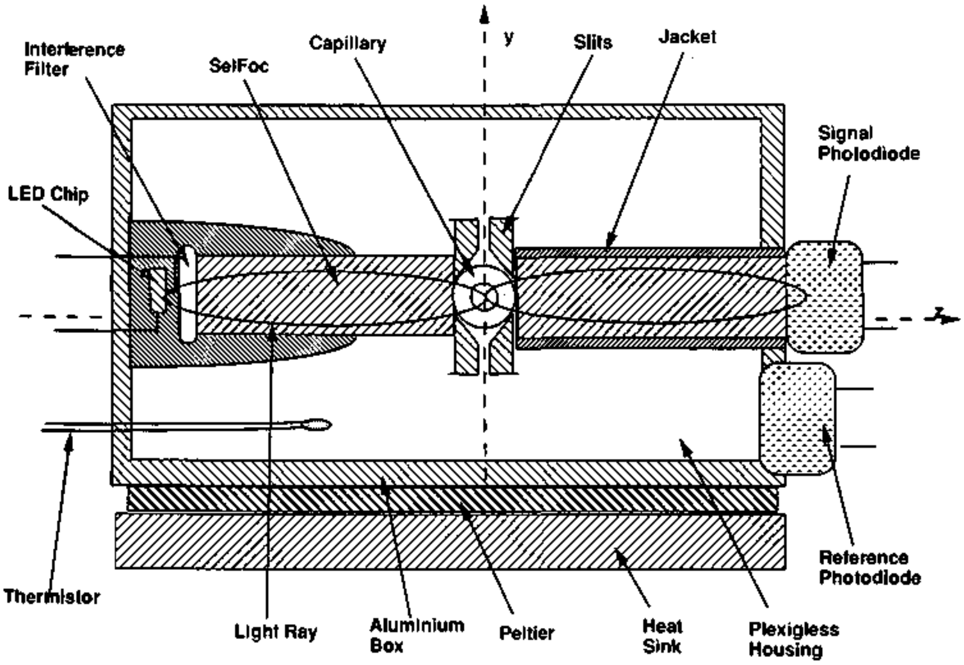

Fig. 2. Diagram of a capillary pigtail absorption detector. The naked capillary tube is masked by a set of steel slits and glued to a Plexiglas mounting piece using UV-curing RIM glues. The slit is 50×500 µm wide and has a large channel of *ca.* 400 µm to fit the capillary tube.

a typical area of about 280×280 μm, is imaged onto the capillary bore.

The pigtailing of the LED is achieved by first milling the Plexiglas body almost down to the emitting crystal and then glueing the GRIN lens with UV-curing RIM materials as indicated in Fig. 3. A GRIN lens is a cylindrical rod with a parabolic RI distribution, whose RI is higher at its optical axis and decreases toward its periphery; light rays thus propagate in a sinusoidal fashion through the rod. A GRIN lens performs the same optical functions as standard spherical lenses. However, what makes them unique for pigtailing purposes is that glueing does not disturb their lens properties. This is in contrast to conventional lenses whose focusing is based on refractions at both curved interfaces.

More than 1 μW of light is measured at the exit surface of the GRIN rod (first focal point) for a typical green LED used to illuminate the capillary tube. Then 50 μm wide slits select a portion of the LED chip image where the naked capillary tube is subsequently glued. A second GRIN lens, of 1/2 or 1/4 pitch, brings the light from the capillary to the probe PD. A PVC jacket round the second GRIN lens prevents scattered light reaching the probe PD. Scattered light propagated through the Plexiglas housing is collected by an array of PDs (Siemens KOM 2057-L). The set of GRIN lenses also separates the PDs from sources of heat which contribute to drift in the output signal – namely, the LED and, in CE, Joule heat. The analog electronic circuit is wired to produce absorbance as an output signal in a dual-beam arrangement. Zeroing is performed manually using a potentiometer.

The whole detector is glued to an aluminum plate and, when needed, thermostated using a small Peltier and calibrated thermistor driven by a thermo-electric system (ILX Lightwave model LDT-5412). The total size of the detector is only 3.2×2.0×1.5 cm which could be further reduced without compromising its performance. The fixing of all the components is carried out under the microscope by means of micro-manipulators, using UV-curing RIMs at every positioning step. To facilitate this process both Plexiglas bodies have a set of parallel holes which accept sliding glass rods of 3 mm diameter. The complete pigtail detectors, including the Peltier and the electronics, fit into a sealed 15×6×3 cm metal box.

With a green LED (Siemens HPG5066X) the short-term noise level is about $1 \cdot 10^{-5}$ a.u. for an integration time of 1 s and a feed-back resistance of the current-to-voltage amplifiers of 100 kΩ. With blue LEDs, which are less brilliant [13], the currents through the signal PD are less than 1 nA, requiring feed-back resistance as high as 5 MΩ, and the absorbance noise levels are somewhat

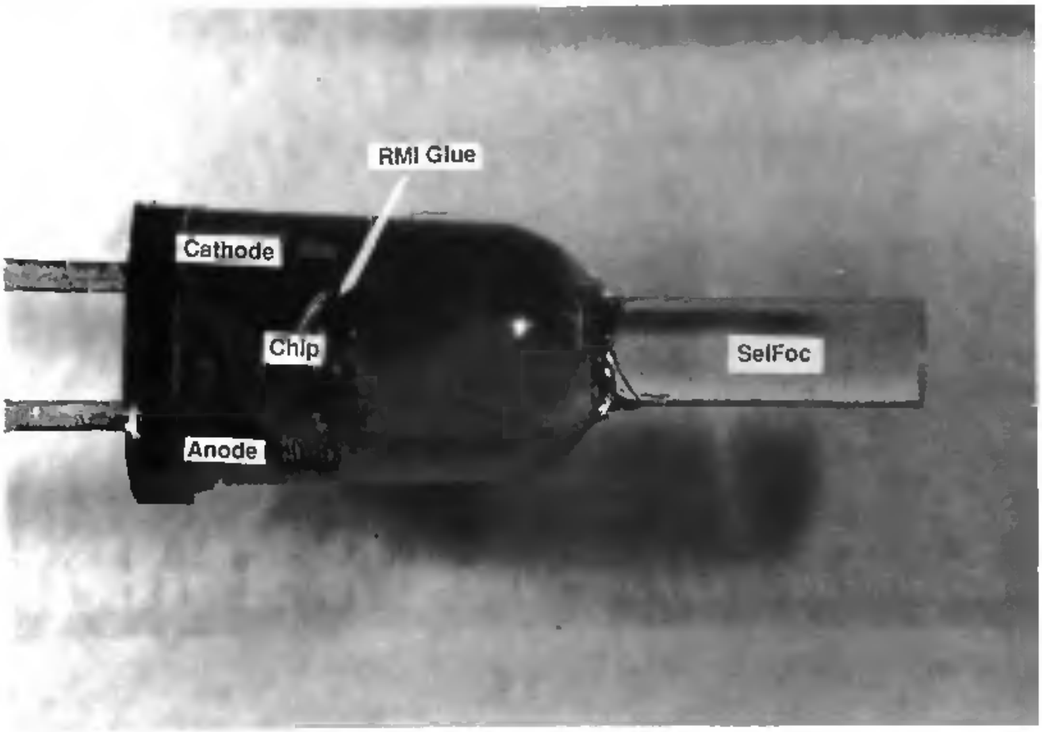

Fig. 3. Photograph of a GRIN lens pigtailed to an LED (type T 1-3/4, diameter 5 mm; the GRIN rod is seen distorted inside the LED due to the lens properties of the Plexiglas body).

higher (*ca.* $5\cdot10^{-5}$ a.u.). Long-term drifts in the baseline are extremely low.

LED-based capillary fluorescence detector

Laser induced fluorescence (LIF) is, to date, the most sensitive detection method available for CE [1]. Many researchers are shifting from gas to solid-state [14] lasers. There is an increasing tendency to use blue [15] excitation, using the second-harmonic (415 nm) from near-infrared LDs and, in the infrared of the spectrum [16], using the fundamental emission from LDs. The secrets for high sensitivity when employing LIF in conjunction with capillary tubes are to use microscope objectives with high numerical apertures, spatial masks to restrict the field of view, to carefully select the interference filters, to use high quantum-yield PMTs with low dark currents, and optimize the excitation-laser power to account for photobleaching and saturation. The most difficult problem, once the above-mentioned aspects have been taken care of, is the scattering of light from the capillary walls. Fluorescence detectors which operate without scattering light are known as background-free detectors, and the baseline noise is dominated by the dark current of the PMT. Background-free detectors are not uncommon for gas-phase detection but they are more difficult to realize in the liquid phase, and it is even more difficult in the presence of liquid-filled narrow-bore capillary tubes. This is mainly because scattered light is produced at the four unavoidable optical interfaces in the measuring zone (see Fig. 1).

A few solutions have been proposed to minimize the amount of scattered light. The most successful approach consists of the elimination of all optical interfaces around the measuring zone in a "windowless cell" design known as a sheath flow cuvette [7] at the end of the capillary. Unfortunately, the method is not particularly easy to implement and not all optical detectors can be constructed in such a way. However, the same principles can be partially applied to at least eliminate the outer capillary interface by immersing the capillary in RIM materials. This approach has been taken by Kurosu *et al.* [17] and Bruno *et al.* [5,18]. Another approach, using optical fibers, is due to de Bokx *et al.* [19]. In this case the excitation and emission fibers were tapered into the capillary in a design that is fully consistent with the pigtailing concept formulated here.

LEDs, instead of lasers or conventional arc lamps, have been used to induce fluorescence in various devices [20] which give impressive sensitivities. The high stability of LEDs translates into very low noise, even in the presence of scattered light, and thus to high signal-to-noise ratios.

None of these devices [20] has been used in conjunction with small capillaries suitable for CE. Using the same arrangement as in the absorption detector (Figs. 2 and 3) for excitation, and multimode optical fibers to collect emission, we constructed the pigtail capillary LED-based fluorescence detector whose design is shown in Fig. 4. To further minimize scattering light arising from the inner silica–buffer interface, the collecting fibers are conveniently placed at the back and at an angle close to 45° with respect to both the optical excitation axis and the capillary axis as indicated in Fig. 4a. We employed a compact device (Hamamatsu, HC120 series) as a PMT which included the high voltage supply and the output amplifier in the same unit and is driven by a 12 V power supply. The electropherogram of 10^{-4} *M* rhodamine B in a 100 µm I.D. capillary is shown Fig. 5. The limit of detection, as determined from the figure, is 10^{-7} *M* (S/N *ca.* 2000).

LD-based capillary RI detectors

The major issue in the quest for maximum sensitivity in the construction of capillary RI detectors is thermal and mechanical stability [5]. Pigtailing thus appears to be a tantalizing construction option. The first pigtail RI detector, based on schlieren effects, is due to Pawliszin [21]. This detector features a LED as the light source pigtailed to a multimode fiber; a second fiber, placed off-axis, was used for collection. The windows of the cells are, as in the capillary fluorescence cell design from de Bokx *et al.* [19], the ends of both optical fibers. This RI detector is, however, not suitable for CE.

We have demonstrated two types of capillary RI pigtail detectors [22] suitable for CE based on interferometry [5,18]; one model features a single-mode fiber whereas the second uses a holographic element as the main optical element [6]. Both RI capillary detectors are also suitable for thermo-optical (TO) absorption [7,23].

"Off-axis" RI detector

In this design [5,18], shown in Fig. 6, the capillary acts as a beam splitter, a strongly divergent lens, and a phase shifter leading to a broad fan of

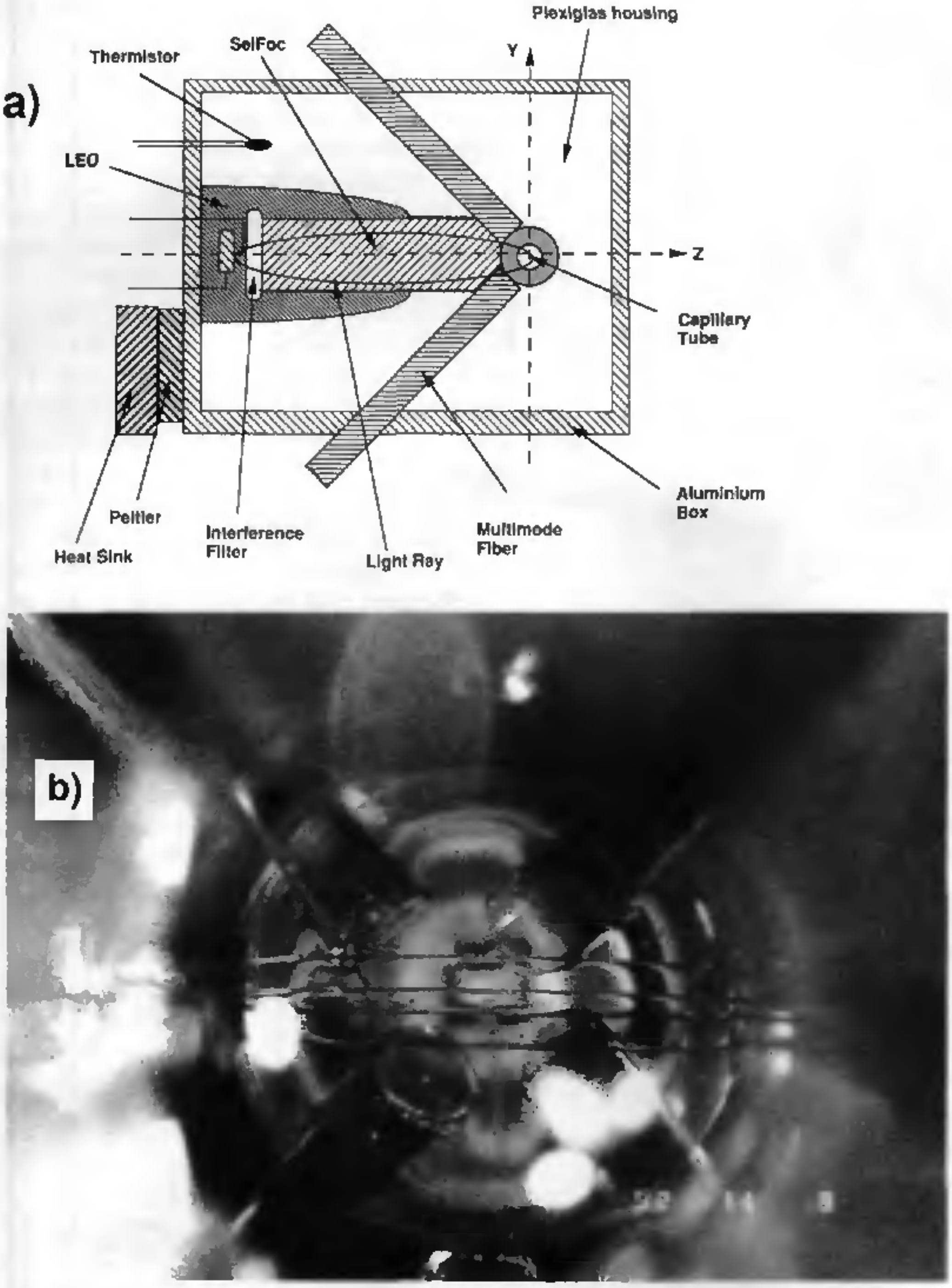

Fig. 4. Cross-sectional side view (a), of the LED-based pigtail capillary fluorescence detector; the four collecting fibers are placed at an angle of *ca.* 45° with respect to the capillary and optical axis, as shown in the picture. (b) The picture shows a top view before filling all cavities with RIM materials.

fringes on the other side of the capillary. These fringes shift with a change in the RI in the capillary medium. Their lateral displacements are monitored by a position-sensitive diode (PSD), which after calibration, constitutes the output signal.

The main propagation medium is a single-mode polarization-preserving fiber pigtailed at both ends; *i.e.* to the LD and capillary. Proper "off-axis" illumination of the capillary is achieved by first positioning the fiber end (from a commercially pigtailed LD) with respect to the capillary and then glueing it with fast UV-curing RIM glues. The optimum offset of the fiber with respect to the capillary is one in which the fringes display maximum contrast and high intensity [18]. Because the beam width at the capillary orifice depends on the

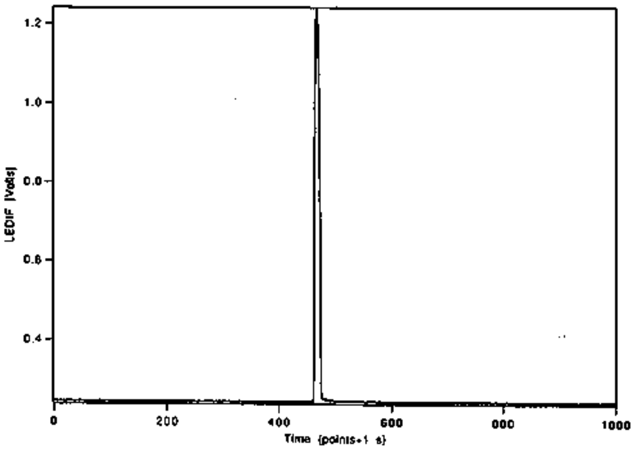

Fig. 5. Electropherogram of $2 \cdot 10^{-4}$ *M* thodamine B in a 100 µm capillary, recorded with a pigtail fluorescence detector featuring a green LED ($\lambda_{max.}$ = 560 nm).

thickness of the capillary wall it is preferable to use thin-wall capillaries. As in any interferometric measurement, wavelength fluctuations translate into signal noise, and therefore the LD and capillary cell are temperature-stabilized by Peltier control units and quiet power supplies.

The noise obtained with this detector under static conditions is about 2 µRIU in a 25 µm capillary. This sensitivity degrades under electrophoretic conditions because of Joule heat effects. The linear dynamic range extends over about three decades. The "off-axis" RI method can be used with capillaries having I.D. ≥15 µm; diffraction effects starts to dominate the interference pattern in smaller I.D. capillaries [18].

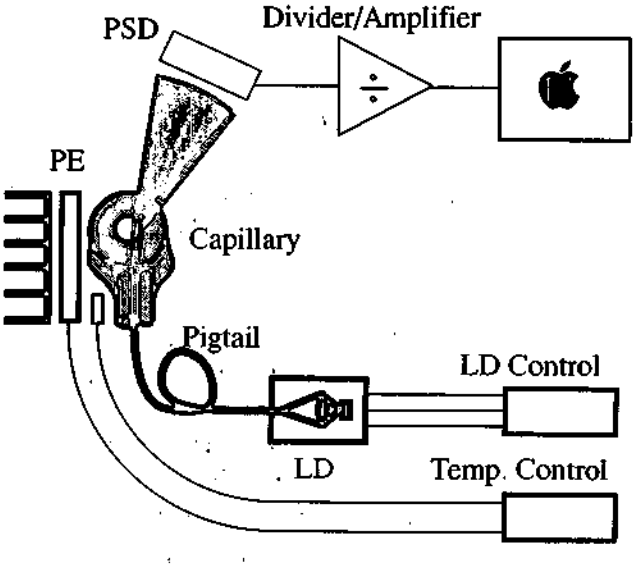

Fig. 6. Diagram of the pigtail "off-axis" RI detector. PE = Peltier element.

Holographic RI detector

HOEs are components used in optics to deflect and to shape light beams. What makes HOEs attractive for optical detection in small volumes is that complex operations, which are difficult to realize with conventional optical elements, are readily incorporated into a single HOE. HOEs are being refined and find application in various optoelectronic devices such as laser writers, FAX machines, and CD players, and in analytical chemistry [24]. We demonstrated the use of customized HOEs in the design of a RI capillary detector [6].

The geometric arrangement of the HOE-based RI detector is shown in Fig. 7. The optical functions, played by the capillary in the off-axis version, are basically transferred to the HOE. The HOE, placed before the capillary, acts as a superposition of two lenses displaced by a predetermined distance and thus transforms the incoming single beam into two focussed spots with beam waists of *ca.* 1 µm. As in the off-axis RI detector, the capillary is surrounded by RIM material to eliminate the reflections and refractions at the outer capillary wall. In the HOE version, in contrast to the off-axis version, the observed fringes are equally spaced, allowing the use of diode arrays for their detection (see Fig. 7). The probing arm of the interferometer crosses the capillary

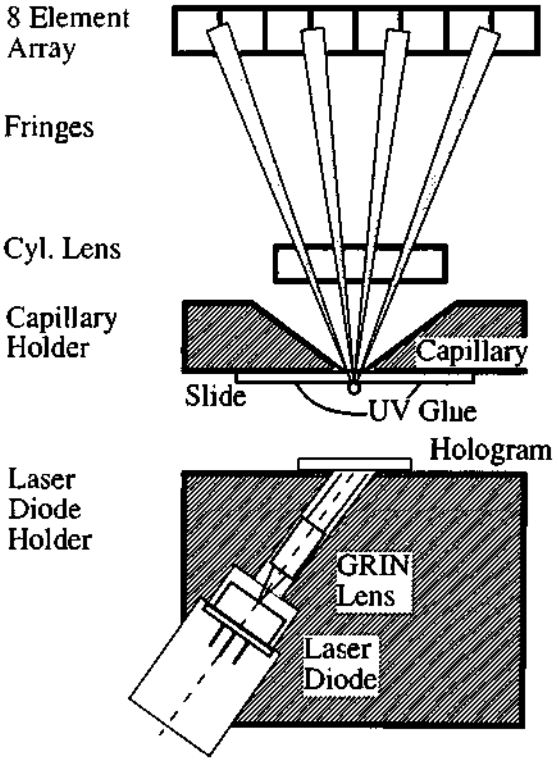

Fig. 7. Diagram of the holographic refractive index detector.

through the center where the optical path, and thus phase changes, are larger.

This detector was demonstrated by Krattiger *et al.* [6] for the CE separation of small cations in a 10 μm I.D. tube. The electropherogram of a mixture of underivatized saccharides recorded with the holographic RI detector in a 25 μm I.D. capillary is shown in Fig. 8. The detection limits and linear dynamic range rendered by this RI detector are comparable to those delivered by the off-axis version. However, the HOE version is more suitable than the off-axis design for capillaries having I.D.s ≤20 μm.

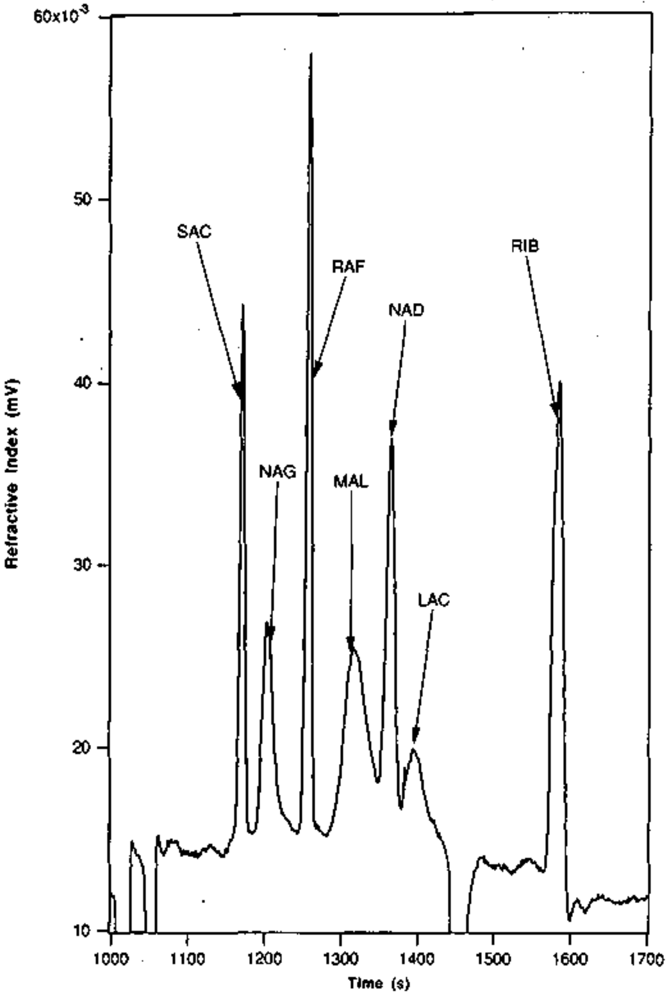

Fig. 8. Electropherogram of a mixture of seven underivatized saccharides recorded with the hologram RI detector. The peaks correspond to sucrose (SAC), N-acetyl-D-glucosamine (NAG), raffinose (RAF), maltose (MAL), N-acetyl-D-galactosamine (NAD), lactose (LAC) and ribose (RIB). Each 7.3 m*M* except for sucrose and raffinose which are 3.6 m*M*. The buffer employed in this separation consists of 50 m*M* borate with cyclohexylamino-propanesulfonic acid (CAPS) at pH = 9.4. The capillary length is 70 cm, 50 to detector; I.D. = 25 μm; electrical field = 170 V/cm (12 kV); current = 7.7 μA; hydrodynamic injection 100 mbar during 6 s (*i.e.*, injection plug *ca.* 1 mm). The first two negative peaks are due to the two buffers and the negative peak at 1450 s is due to an impurity.

Conclusions

The analogy between the pigtail approach to optical detection and other technologies such as electronics and digital computation is rather obvious. In all cases, in order to achieve lower noise, faster responses, smaller drifts, etc., the rule is to simplify the architecture of the device in question. The associated disadvantage is that in the process one ends up by compromising instrumental versatility for specificity.

Because radiance is more important than the total light-output power for the illumination of small surfaces, the use of edge-emitting, instead of surface-emitting LEDs with a directional radiation pattern, would be better suited for the construction of pigtail absorbance and fluorescence detectors. However such LEDs are only available for wavelengths above 700 nm. Two-wavelength absorption and fluorescence pigtail detectors could be constructed with single LEDs emitting at two wavelengths. A more general possibility, for constructing multi-wavelength absorption pigtail detectors, would be to use multi-element LED arrays emitting at selected wavelengths which would correlate with a photodiode array at the other side of the capillary, in an architecture similar to the one shown in Fig. 2.

Further developments of pigtail detectors will follow advances in the development of LEDs and LDs, mainly in a shortening of their emission wavelengths and an increase in their power output.

References

1 S.F.Y. Li, *Capillary Electrophoresis*, Elsevier, Amsterdam, 1992.
2 F. Foret, M. Deml, V. Kahle and P. Boček, *Electrophoresis*, 7 (1986) 430.
3 A.E. Bruno, E. Gassmann, N. Pericles and K. Anton, *Anal. Chem.*, 61 (1989) 876.
4 L.N. Amankwa, M. Albin and W. Kuhr, *Trends Anal. Chem.*, 11 (1992) 114.
5 A.E. Bruno, B. Krattiger, F. Maystre and H.M. Widmer, *Anal. Chem.*, 63 (1991) 2689.

6 B. Krattiger, G. Bruin and A.E. Bruno, *Anal. Chem.*, 66 (1994) 1.

7 N.J. Dovichi, *Rev. Sci. Instrum.*, 61 (1990) 3653.

8 P.K. Dasgupta, H.S. Bellamy, H. Liu, J. Lopez, E.L. Loree, K. Morris, K. Petersen and K.A. Mir, *Talanta*, 40 (1993) 53.

9 D. Betteridge, W.C. Cheng, E.L. Dagless, P. Davis, T.B. Goad, D.R. Deans, D.A. Newton and T.B. Pierce, *Analyst (London)*, 108 (1983) 1.

10 M. Trojanowicz, P.J. Worsfold and J.R. Clinch, *Trends Anal. Chem.*, 7 (1988) 301.

11 F.I. Ormaza-Gonzaléz and P.J. Statham, *Anal. Chim. Acta*, 244 (1991) 63.

12 H. Liu, P.K. Dasgupta and H.J. Zheng, *Talanta*, 40 (1993) 1331.

13 P.C. Hauser and D.W.L. Chiang, *Talanta*, 40 (1993) 1193.

14 A.P. Larson, H. Ahlberg and S. Folestad, *Appl. Opt.*, 32 (1993) 794.

15 T. Imasaka, K. Nishitani and N. Ishibashi, *Analyst (London)*, 116 (1991) 1407.

16 A.J.G. Mank, H. Lingeman and C. Gooijier, *Trend Anal. Chem.*, 11 (1992) 210.

17 Y. Kurosu, T. Sasaki and M. Saito, *J. High Resolut. Chromatogr.*, 14 (1991) 86.

18 B. Krattiger, A.E. Bruno, H.M. Widmer, M. Geiser and R. Dändliker. *Appl. Opt.*, 32 (1993) 856.

19 P.K. de Bokx, E.E.A. Gillisen, P. van de Weijer, M.H.L. Bekkers, C.H.M. van Bommel and H.G. Janseen, *J. Chromatogr.*, 598 (1992) 115.

20 O.S. Wolfbeis (Editor), *Fluorescence Spectroscopy*, Springer, New York, 1993.

21 J. Pawliszin, *Anal. Chem.*, 58 (1986) 3207.

22 A.E. Bruno and B. Krattiger, in Z. El Rassi (Editor), *Carbohydrate Analysis*, Elsevier, Amsterdam, in press.

23 A.E. Bruno, A. Paulus and D.J. Bornhop, *Appl. Spectrosc.*, 45 (1991) 462.

24 J.M. Tedesco, H. Owe, D.M. Pallister and M.D. Morris. *Anal. Chem.*, 65 (1993) 441A.

A.E. Bruno, F. Maystre, B. Krattiger, P. Nussbaum and E. Gassmann are at the Corporate Analytical Research Division of Ciba-Geigy Ltd., 4002 Basel, Switzerland.

Reprinted from Analytical Chemistry, 1995, *34*.

Hologram-Based Thermooptical Absorbance Detection in Capillary Electrophoresis: Separation of Nucleosides and Nucleotides

Beat Krattiger, Alfredo E. Bruno,* H. Michael Widmer, and René Dändliker[†]

Corporate Analytical Research, Ciba-Geigy Ltd., 4002 Basle, Switzerland

On-column thermooptical absorbance (TOA) detection in capillary electrophoretic separations of various nucleoside and mono- and diphosphate nucleotide mixtures absorbing at 257 nm is demonstrated in 20 μm i.d. capillaries. The analytes are optically *pumped* by a frequency-doubled argon ion laser and *probed* by a laser diode or by a He/Ne laser beam guided to the detection volume by a holographic optical element. Absorption detection limits of 2.2 μAU using time constants of 0.3 s and 20 mW of UV power are obtained over a linear dynamic range covering three to four decades. As higher pumping power is required to enhance the thermooptical sensitivity, photobleaching appears as a major problem in the quest for lower detection limits for some of the substances studied such as deoxyuridine and uridine. Concentration detection limits as low as 50 nM for adenosine monophosphate, corresponding to a mass detection limit of 0.4 fmol, and separation efficiencies up to 320 000 theoretical plates are measured. A theoretical model, which translates the obtained TOA signals into absorbances, is proposed and describes the TOA effect for smaller capillaries rather well.

Various on-column optical detection methods have been devised for capillary electrophoresis (CE). When the sample of interest contains a fluorescent chromophore that coincides with a lasing line, laser-induced fluorescence (LIF) is undoubtedly the best choice. Using this method, concentration detection limits (LODs) as low as 10^{-10} M (0.2 am injected) for native bovine serum albumin (BSA) have been reported.[1] However, as the number of naturally fluorescent samples is small, and the laser emission wavelengths are limited, this case should be considered as an exception rather than the rule.

Concentration LODs in the 10^{-11} M range, or lower, are obtained in CE using precolumn labeling with fluorescent tags and LIF detection. However, direct derivatizations (samples are first derivatized at high concentrations and then diluted to the impressive low levels reported) below the 10^{-7} M range have not been reported to date. Furthermore, derivatization procedures are not always available for the substance of interest or are often rather tedious and, when available, often lead to quantification problems because the extent of derivatization is not always predictable. As the electrophoretic mobilities are often affected by the labels, different incorporation of the tags into the sample leads to additional peaks and decreased separation efficiency.[1,2]

The vast majority of substances of analytical interest absorb in the UV/visible range, and therefore, absorbance detection is the most popular detection method in CE. Due to the short absorbance paths, the lower concentration LODs thus obtained are, in the most favorable cases, in the micromolar range. This disadvantage can be partially overcome by extending the optical path by use of flared capillaries, z-shaped cells,[3,4] or multireflection cells.[5] Nonlinearities in the calibration curves, due to RI effects,[6] are to be expected.

To obtain high sensitivity and accuracy, while avoiding derivatization procedures, the approach we follow is thermooptical absorbance (TOA). In TOA detection,[7–9] an intense laser pulse irradiates repeatedly the sample with a wavelength matching an absorption system in the sample. The amount of absorbed light, which is converted by radiationless transitions into heat, rises the solvent temperature in the illuminated region in a periodic fashion. As the refractive index (n) of a material is a function of the temperature (T), those periodic changes in T manifest in changes in the refractive index (Δn) which are conveniently monitored by a capillary RI detector[10–15] and easily decoded with a lock-in amplifier. Because Δn signal is dependent, among other parameters, on the extinction coefficient of the sample studied, the

---

[†] Institute of Microtechnology, University of Neuchâtel, 2000 Neuchâtel, Switzerland.

(1) Lee, T. T.; Yeung, E. S. *J. Chromatogr.* **1992**, *595*, 319–325.

(2) Swaile, D. F.; Sepaniak, M. J. *J. Liq. Chromatogr.* **1991**, *14*, 869–893.

(3) Chervet, J. P.; van Soest, R. E. J.; Ursem, M. *J. Chromatogr.* **1991**, *543*, 439–449.

(4) Moring, S. E.; Reel, R. T. *Anal. Chem.* **1993**, *65*, 3454–3459.

(5) Wang, T.; Aiken, J. H.; Huie, C. W.; Hartwick, R. A. *Anal. Chem.* **1991**, *63*, 1372–1376

(6) Bruno, A. E.; Gassmann, E.; Pericles, N.; Anton, K. *Anal. Chem.* **1989**, *61*, 876.

(7) Dovichi, N. J. *CRC Crit. Rev. Anal. Chem.* **1987**, *17*, 357–423.

(8) Yeung, E. S. *Detectors for Liquid Chromatography*; John Wiley & Sons: New York, 1986.

(9) (a) Fang, L. H.; Swofford, R. L. In *Ultrasensitive Laser Spectroscopy*; Klinger, D. S., Ed.; Academic Press: New York, 1983. (b) Saz, J. M.; Díez-Masa, J. C. *J. Liq. Chromatogr.* **1994**, *17*, 499–520. (c) Wu, J.; Odake, T.; Kitamori, T.; Sawada, T. J. C. *Anal. Chem.* **1991**, *63*, 2216–2218.

(10) Bruno, A. E.; Krattiger, B.; Maystre, F.; Widmer, H. M. *Anal. Chem.* **1991**, *63*, 2689–2697.

(11) (a) Krattiger, B.; Bruno, A. E.; Widmer, H. M.; Geiser, M.; Dändliker, R. *Appl. Opt.* **1993**, *32*, 956–965. (b) Zimmermann, E.; Dändliker, R.; Krattiger, B.; Souli, N., submitted for publication in *J. Opt. Soc. A*.

(12) Krattiger, B.; Bruin, G. J. M.; Bruno, A. E. *Anal. Chem.* **1994**, *66*, 1.

(13) Bruno, A. E.; Krattiger, B. In *Carbohydrate Analysis, High Performance Liquid Chromatography and Capillary Electrophoresis*; El Rassi, Z., Ed.; Elsevier: New York, 1994; Chapter 11, p 431.

(14) Saz, J. M.; Krattiger, B.; Bruno, A. E. *Anal. Methods Instrum.*, in press.

(15) Bruno, A. E.; Maystre, F.; Krattiger, B.; Nussbaum, P.; Gassmann, E. *Trends Anal. Chem.* **1994**, *13*, 190–198.

0003-2700/95/0367-0124$9.00/0

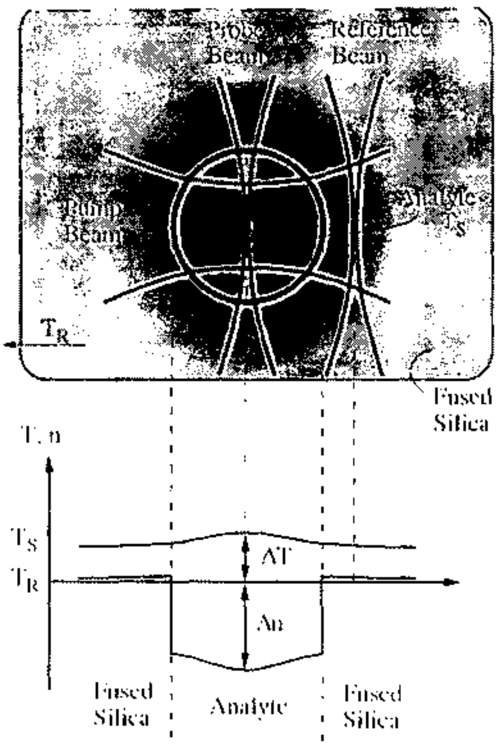

Figure 1. Detail of the TOA cell showing the optical arrangement of the pump, probe, and reference beams (top) and steady-state temperature and RI radial profiles across the cell during a pump pulse (bottom). The temperature excess, ΔT, is the temperature difference between sample T_S and room temperature T_R. The probing and reference beam are separated by 14 μm.

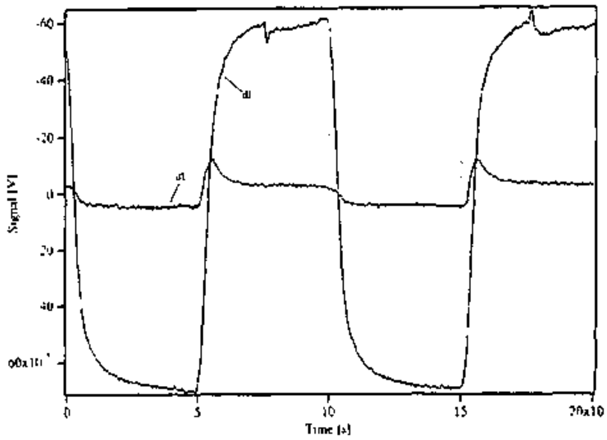

Figure 2. Time evolution of TOA signals for dU and dI. dU photodissociates whereas dI is stable. The signal of the dU trace corresponds to a temperature rise of ~1.0 K: concentration 50 μg/mL each in SDS buffer, UV power 20 mW, and chopper frequency 100 Hz.

output can be calibrated to produce quantitative absorption measurements.

Based on the geometric configuration of the pump and probe beams, mainly three types of TOA schemes have been performed in conjunction with capillaries to date: capillary vibration method (CVL), thermal lensing (TL), and crossed-beam thermooptical (CBTO) configurations. The CVL method exploits the vibrations of the capillary induced by the absorption of an intense pulsed laser.[9] In TL, which has been used[7,8,16-18] in HPLC, the pump and probe beams are collinear where the former induces a RI gradient across the probing path. In CBTO, demonstrated by Yu and Dovichi in CE,[19] the beams are "crossed" at 90° overlapping in the capillary lumen defining a small detection volume.[20,21] This latter configuration (CBTO) is the one we use here; however, we prefer to use the general term TOA, instead of the specific CBTO term, to emphasize that the TOA effect is not related, at least in the present case, to the geometric arrangement of the beams. The unavoidable RI gradient is, in the case of small inner diameter capillaries, not required to observe the TOA effect. Indeed, as argued in the Theory section, it is the mean value of Δn across the detection lumen that is responsible for the TOA signal.

As a capillary RI detector for the TOA instrument we used the one based on a holographic optical element.[12,13] The straightforward optical design and enhanced performance of this RI detector made its integration[15] into a TOA device rather simple. To evaluate the performance of the instrument, and considering the growing importance of DNA and RNA analysis, various CE separations of nucleosides and mono- and diphosphate nucleotides have been chosen for the study. Native proteins have also been studied by TOA, and the results will be reported elsewhere.

THEORY

The principle of TOA detection in small capillaries is depicted in Figure 1, and the time evolution of the temperature during and after a pulse of light for two typical cases is shown in Figure 2. The heat produced during each pulse of the pump beam rapidly warms the analyte and the surrounding fused silica (FS) of the capillary wall until the maximum temperature T_S is reached (see Figures 1 and 2). The heat-induced changes in the refractive index, Δn, modifies the phase of the probe beam and is interferometrically detected.[12] Demodulation of the Δn signal constitutes, upon calibration, the TOA signal.

The steady-state radial distributions of ΔT and Δn of the buffer and FS are also displayed in Figure 1 (bottom). The large discontinuity in the Δn at the buffer/FS interface is due to the signs of the dn/dT coefficient of the FS, which has opposite sign and is 11 times smaller in magnitude than the corresponding coefficient of the aqueous buffer (i.e., -1.07×10^{-4} and $+9.5 \times 10^{-6}$ K^{-1} for H_2O and FS[22,23] at 20 °C, respectively). As the dn/dT of FS is small as compared to that of the buffer, and as both beams propagate only 14 μm apart, they sense similar temperatures along their paths through the FS; the phase changes gathered in the path through the FS are referenced.

TOA Model. Dovichi[7] developed a mathematical formalism needed to compute the ΔT and Δn profiles within the analyte for larger cells under pure TL conditions where the heat generation is far from the FS wall. However, for small inner diameter capillaries, the temperature drops mainly across the FS wall and not within the buffer; the temperature rise is mainly determined by the thermal resistance of the FS cell and not by the thermal

---

(16) Nolan, T. G.; Dovichi, N. J. *IEEE Circuits Devices Mag.* **1986**, *2*, 54–56.
(17) Nolan, T. G.; Bornhop, D. J.; Dovichi, N. J. *J. Chromatogr.* **1987**, *384*, 189–195.
(18) Rosenzweig, Z.; Yeung, E. S. *Appl. Spectrosc.* **1993**, *47*, 1175–1179.
(19) Yu, M.; Dovichi, N. J. *Mikrochim. Acta* **1988**, *111*, 27–40.
(20) Bruno, A. E.; Paulus, A.; Bornhop, D. J. *Appl. Spectrosc.* **1991**, *45*, 462.
(21) Waldron, K. C.; Dovichi, N. J. *Anal. Chem.* **1992**, *64*, 1396.
(22) Weast, R. C., Ed. *CRC Handbook of Chemistry and Physics*; CRC Press, Inc.: Boca Raton, FL, 1983–1984.
(23) Landholt-Börnstein *Zahlenwerte und Funktionen aus Physik, Chemie, Astronomie, Geophysik, Technik*; Springer Verlag: Berlin, 1976; II. Band, 8.

properties of the buffer. For this reason, Dovichi's model cannot be used here and we present a simple model to predict ΔT and Δn inside small inner diameter capillaries for the TOA case.

As the heat source can be considered pointlike ($2w_0 \leq 20$ μm where $2w_0$ is the pump beam diameter) if compared to the outer capillary diameter (340 μm), and as the heat dissipates isotropically, it is assumed that the cell geometry is spherical, i.e., two concentric spheres, the inner one filled with buffer and the outer one made of FS. The diameters of both spheres match those of inner and outer diameters of the capillary. As it can be seen in Figure 2, the system reaches thermal equilibrium very rapidly (~0.4 ms, corresponding to one-fourth of the pulse width at the 314 Hz chopper frequency). The temperature profile is, during a pulse, constant across the buffer and drops across the FS wall as $1/r^2$.

The overall TOA instrumental response, R_{TOA}, of the present instrument is the signal voltage output from the lock-in amplifier (U_{TOA}) caused by a given absorbance (A) and is, in differential form,

$$R_{\mathrm{TOA}} = \mathrm{d}U_{\mathrm{TOA}}/\mathrm{d}A \tag{1}$$

where A is the product of path length, concentration, c, and extinction coefficient, ϵ,

$$A = \mathrm{i.d.}c\epsilon \tag{2}$$

($\mathrm{d}U_{\mathrm{TOA}}/\mathrm{d}A$) can be mathematically decomposed as

$$\frac{\mathrm{d}U_{\mathrm{TOA}}}{\mathrm{d}A} = \left(\frac{\mathrm{d}U_{\mathrm{TOA}}}{\mathrm{d}U_{\mathrm{RI}}}\right)\left(\frac{\mathrm{d}U_{\mathrm{RI}}}{\mathrm{d}n}\right)\left(\frac{\mathrm{d}n}{\mathrm{d}T}\right)\left(\frac{\mathrm{d}T}{\mathrm{d}A}\right) \tag{3}$$

where U_{RI} is the signal amplitude from the photodiode array (PDA) electronic conditioner. The first two terms in eq 3 are instrumental whereas the last two terms describe the actual TOA principle (one is the $\mathrm{d}n/\mathrm{d}T$ coefficient for the buffer above mentioned).

The first term in eq 3 corresponds to the lock-in amplification. It is the ratio of its efficiency, H, for a given signal shape to the sensitivity setting, S, which was set to 50 mV in most measurements and

$$\mathrm{d}U_{\mathrm{TOA}}/\mathrm{d}U_{\mathrm{RI}} = H/S \tag{4}$$

For a chopping frequency of 314 Hz, H was measured to be 4 V using a 1% acetone/water solution.

An expression for the second parentheses in eq 3, which corresponds to the instrumental response of the RI detector, was given elsewhere[12] and reads

$$\mathrm{d}U_{\mathrm{RI}}/\mathrm{d}n = 4CK\mathrm{i.d.}/\lambda_{\mathrm{probe}} \tag{5}$$

where $C = 0.9$ is the fringe contrast, $K = 10$ V is an amplification constant of the PDA conditioner, and $\lambda_{\mathrm{probe}} = 633$ nm is the probe He/Ne laser wavelength. Using these values, the RI response is $\mathrm{d}U_{\mathrm{RI}}/\mathrm{d}n = 1.14$ mV/μRIU.

The last factor in eq 3 ($\mathrm{d}T/\mathrm{d}A$) represents the temperature change per absorbance, i.e., the TOA effect. Assuming that the temperature at the fluid/FS interface is the same than that of the fluid, the ΔT across the FS sphere having a thermal resistance R and conducting a total heat flow P_{heat} can be computed as

$$\Delta T = P_{\mathrm{heat}}R \tag{6}$$

The power flow P_{heat} in the assumed stationary state equals the absorbed light power, which is related to the absorbance A as

$$P_{\mathrm{heat}} = 2.303AP_{\mathrm{UV}} \tag{7}$$

and its substitution in eq 6 reveals

$$\Delta T = 2.303RAP_{\mathrm{UV}} \tag{8}$$

The expression for $\mathrm{d}T/\mathrm{d}A$ can be now obtained by taking the derivative of eq 8 with respect to A

$$\mathrm{d}T/\mathrm{d}A = 2.303RP_{\mathrm{UV}} \tag{9}$$

The thermal resistance, R, entering in eqs 6, 8, and 9, can be computed by the integration of the thermal resistance shells as

$$R = \int_{r_i}^{r_o} \frac{\mathrm{d}r}{4\pi\sigma r^2} = \frac{1}{4\pi\sigma}\left(\frac{1}{r_i} - \frac{1}{r_o}\right) \tag{10}$$

where $\sigma = 1.38$ W/(K·m) is the thermal conductivity of FS and r_i (= i.d./2) and r_o (= o.d./2) are the inner and outer radii of the sphere, respectively. According to eq 10, a sphere with i.d. = 20 μm and o.d. = 340 μm (present case) has a thermal resistance R = 5427 K/W. Using eq 8, 1 μW of absorbed light would raise the temperature inside the capillary by 5.4 mK.

The analytical expression for R_{TOA} can now be given by substituting eq 10 into eq 9 and then by substituting eqs 4, 5, and 9 into eq 3 rendering

$$R_{\mathrm{TOA}} = \frac{4.606KH}{\pi S}\,\frac{CP_{\mathrm{UV}}}{\lambda_{\mathrm{probe}}\sigma}\left(\frac{\mathrm{d}n}{\mathrm{d}T}\right)\left(1 - \frac{\mathrm{i.d.}}{\mathrm{o.d.}}\right) \tag{11}$$

According to eq 11, for narrow-bore capillaries, for which i.d./o.d. < 0.1, the TOA response is almost independent of both diameters (e.g., the last parenthesis contributes to less than 6% to R_{TOA} in our case). We measured R_{TOA} for capillaries having inner diameters of 10 and 20 μm at 10 mW pumping power, and within the experimental accuracy, R_{TOA} remains constant as predicted by the present model.

The theoretical estimate for the R_{TOA}, for a lock-in sensitivity of 50 mV and a UV power of 10 mW, is $R_{\mathrm{TOA}} = 1.217$ mV/μAU, whereas the measured values range from 1.0 to 1.4 mV/μAU depending on the degree of optical overlap.

EXPERIMENTAL SECTION

TOA Detector. The experimental setup of the TOA detector which realizes the pumping scheme shown in Figure 1 consists basically of a hologram-based capillary RI detector[12] and a pump source, which is a frequency-doubled Ar$^+$ laser emitting at 257 nm[20] (laser Model 2025-5/395 B, Spectra Physics, Mountain View, CA). The frequency-doubling system is stabilized by a feedback system to produce less than 0.5% intensity noise. The 2 mm wide UV beam is focused by a FS lens $f = 16$ mm mounted on a 3-D translation stage (Microcontrole 3 MRN 03.5). The numerical aperture (NA) of the pump beam is therefore NA = $^1/_{16}$ and the beam spot in the cell ($2w_0 = 2\lambda/\pi\mathrm{NA}$) is ~2.6 μm. The probe light, provided by either a He/Ne laser (Model 106-1, Spectra Physics) connected via a polarization preserving single-mode fiber (HB600, York Technology Inc., Chandlers Ford, Hampshire, GB) or a laser diode (LD), propagates through a collimator lens (f = 5 mm, diameter 5 mm; Spindler & Hoyer) and a HOE.[12] The TOA cell consists of a naked capillary (Polymicro Technologies, Phoenix, AZ) glued between two microscope slides with UV-curing RI matching (RIM) glue (Norland Products Inc., New Brunswick, NJ) as shown in Figure **1b** of ref 12 (the pump beam entrance and exit surfaces of the capillary were kept free from RIM glue). The capillary cell was glued onto a machined aluminum block for its temperature stabilization provided by a Peltier/thermistor system (ILX Lightwave, Bozeman, MT).

The far-field profile of the fringe pattern is monitored by an eight-element PDA (KOM 2045, Siemens), which is analog-conditioned by a position-sensitive circuit (Model 301-DIV, UDT, Hawthorne, CA) and fed into a lock-in amplifier (SR 530, Stanford Research Systems Inc.) operated at a time constant of 0.3 s and a sensitivity of 50 mV. The chopper (SR 540) for the pump beam also provides the phase reference for the lock-in amplifier. The TOA signal from the lock-in is acquired by a Macintosh IIfx computer using the LabVIEW package (National Instruments, Austin, TX), and the data were processed with the Igor program (WaveMetrix, Lake Oswego, OR).

Chemicals. The standard stock solutions of nucleosides and nucleotides were prepared in water (except adenosine and guanosine, which were dissolved in 0.1 M NaOH) and stored below −18 °C at a concentration of 5 mg/mL. Diluted samples were prepared each day in running buffer or in water. The filtered (0.22 μm) buffer solutions (all from Fluka) were vacuum degassed before use. The sodium dodecyl sulfate (SDS) buffer (pH 7.00) consisted of 20 mM sodium dihydrogen phosphate, 20 mM sodium tetraborate, and 50 mM sodium lauryl sulfate, and the citrate buffer (pH 3.5) consisted of 20 mM sodium citrate. The nucleosides studied were adenosine (A), deoxyadenosine (dA), cytidine (C), guanosine (G), deoxyinosine (dI), deoxythymidine (dT), deoxyuridine (dU), and uridine (U). The 5′-mono- and diphosphate nucleotides studied were AMP, CMP, GMP, dTMP, ADP, CDP, GDP, and dTDP (from Fluka). The extinction coefficients ϵ at 257 nm of nucleosides and nucleotides, are $\epsilon = \sim 10^4$ L mol^{-1} cm^{-1}.

Capillary Electrophoresis. CE was performed at room temperature by applying hydrodynamic injection at a pressure of 25 mbar for 30 s by means of an automated injection system (Prince, Lauer Labs, Emmen, The Netherlands). Separations were performed in 20 μm i.d. capillaries having a total length of 75 cm and a length of 50 cm to the detection point. The separation voltage was 30 kV, resulting in electrical currents of 6 μA for the SDS buffer and 3 μA for the citrate buffer. Conventional UV detection was performed with an absorbance detector (PHD 206, Linear Instruments, Reno, NV) under identical experimental conditions.

As nucleosides are uncharged in the pH region where they are stable, CE in hydrophilic buffers is not possible; they are separated by micellar electrokinetic chromatography (MEKC).[24,25] The addition of surfactants to the background electrolyte, such as SDS, above a critical concentration leads to micelles, which allows separation of neutral species. Under these conditions, neutral nucleosides are separated according to their different partitioning between the aqueous background electrolyte and the hydrophobic interior of the charged micelles.[25] Although nucleotides, containing charged phosphate groups, can be separated in hydrophilic buffers without the addition of SDS, we chose here the same buffer system to display both, the nucleoside and nucleotide species, within the same run.

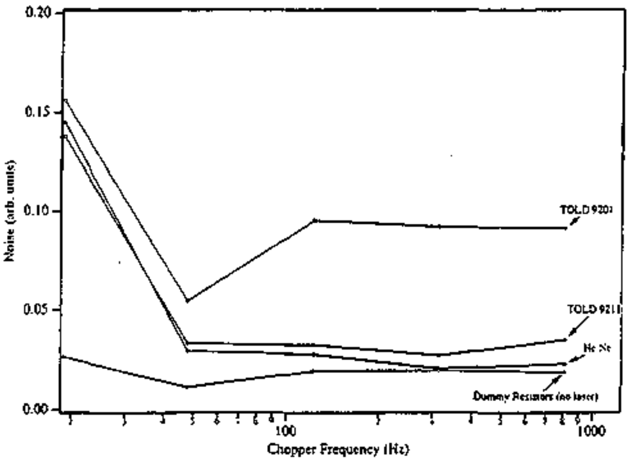

Figure 3. Noise spectra for different probe light sources. The data were obtained from five chopping frequencies. TOLD 9201 and TOLD 9211 are (Toshiba) LDs. The lowest trace displays the noise due to the electronics (the POA is replaced with dummy resistors).

RESULTS AND DISCUSSION

Noise Sources and Linear Dynamic Range. To investigate the contribution of the various sources to the total TOA noise the sources were, in as much as possible, isolated, and their individual contributions were measured and determined according to the procedure suggested by Scott.[26] Considered were contributions to TOA noise from the lock-in amplifier, the PDA signal conditioner, the probe and pump lasers, and the A/D converter.

Figure 3 displays the noise spectra measured at the PDA array for different probe lasers. All lasers investigated display the highest noise at the lower chopper frequencies. Schlieren effects contribute to the low-frequency noise while the high-frequency noise originates from wavelength shifts (eq 7b, ref 12) in the LDs due to mode hopping and operating conditions.[27] The index-guided single-mode LD Model TOLD 9211 (Toshiba Inc.) renders lower noise than the gain-guided multimode LD Model TOLD 9201, as can be seen in Figure 3. He/Ne lasers, having higher intensity fluctuations, display small wavelength jitter. As the intensity fluctuations are referenced in the PDA conditioning electronics,[12] a He/Ne laser rendered the lowest TOA noise and was therefore used in the CE separations reported here. The lowest noise was obtained near 314 Hz (Figure 3), which was selected for all measurements. The lowest, almost flat, trace corresponds to the noise due to the electronics.

The TOA response is proportional to the pump power (eq 11), but it was noted that increasing the pump power does not result in a linear increase in the S/N ratio. When a transparent buffer system is used, a TOA measurement should be background free (as in LIF in the absence of scattered light). However, with the SDS buffer, small impurities, which display weak absorption around 257 nm, couple the noise of the pump beam into the final TOA noise. High pumping powers might cause photobleaching, saturation, and cell degradation.[21] The best S/N ratios were observed between 4 and 20 mW, and most measurements were performed at 10 mW.

The different noise contributions and empirical formulas used to compute them are given in Table 1. The square root of the

---

(24) Ohms, J. I. Analysis of Nucleic Acid Derivatives and Analogs by P/ACE System 2000 Using CE. Beckman application note DS-73PA. 1990.

(25) Lecoq, A. F.; Montanarella, L. *J. Microcolumn Sep.* **1993**, *5*, 105–118.

(26) Scott, R. P. W. *Liquid Chromatography Detectors*; Elsevier: New York, 1986.

(27) Petermann, K. *Laser Diode Modulation and Noise*; Kluwer Academic Press: Dordrecht, The Netherlands, 1991.

Table 1. Contribution of the Individual Noise Sources to the Total Measured TOA Noise[a]

noise source	noise empirical relationships (mV)	noise[b] (mV)
pump laser	0.4% of baseline signal	1
He/Ne probe laser	$24/S$	0.5
signal conditioner	$100/S$	2
lock-in	1,[c] 2,[d] 4[e]	2
DAQ system	0.2	0.2
calcd total noise	[f]	3
measd noise in CE		5

[a] The baseline signal and the sensitivity, S, are in millivolt units. [b] Explicit values obtained from the empirical relationships using the experimental parameters from the separation shown in Figure 4. [c] Between $S = 100$ and 500 mV. [d] Between $S = 10$ and 50 mV. [e] Between $S = 1$ and 5 mV. [f] $[(0.004 \times \text{baseline signal})^2 + (24/S)^2 + (100/S)^2 + (1,^c 2,^d 4^e)^2 + 0.2^2]^{1/2}$.

sum of the squares of the individual components yields the expected total noise of ~3 mV, which is to be compared with the measured baseline noise of 5 mV reported in the same table. The 2 mV discrepancy probably stems from buffer impurities absorbing at 257 nm or turbulences due to Joule heat in CE, which are not accounted for in the evaluation.

TOA detection cells degrade by the high peak intensities of pulsed lasers[28] delivering powers in the order of 0.2 GW/cm^2 or higher. The chopped cw laser used in our experiments delivers modest peak intensities of ~0.2 MW/cm^2, which are rather harmless to the FS cell. However, after a few days of operation, and for some buffer/sample combinations, we observed a dark coating (which was removed by HCl) growing at the inner capillary surface leading also to a monotonous increase of the baseline TOA signal.

The linear dynamic range (LDR) in the present instrument is mainly given by the dynamic reserve of the lock-in amplifier and also by the sinusoidal response of the RI detector (eq 16 in ref 12). It covers about three or four decades of TOA signal (~70 000 at 5% deviation from linearity for a detection limit of 0.1 μRIU and 6.8 mRIU working range).

CE Separations. Figure 4 displays the electropherogram of a mixture of four nucleosides, dU, U, dI, and dA (50 μg/mL each), separated in the SDS buffer in a 20 μm i.d. capillary. The electropherogram of the same mixture taken under identical experimental conditions, but recorded using conventional UV absorption, is shown in Figure 5 for comparison purposes. The ~200 mV baseline offset in the TOA recorded electropherogram is due to the slight absorption of the SDS buffer. Although the TOA-detected electropherogram displays a better S/N ratio and practically no drift as compared to that recorded with the UV absorbance detector, the peak areas of the dU and U species do not represent their actual concentrations due to photobleaching. The relatively high UV intensities needed in the TOA, as compared to conventional absorbance measurements, photodegrade[21,29-31] these species, resulting in a lower peak height than those of the dI and dA species in spite of their similar extinction coefficients and concentrations.

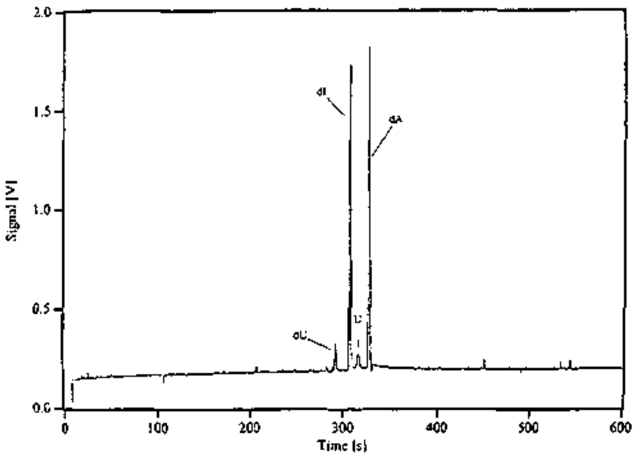

Figure 4. MEKC electropherogram of a mixture of nucleosides (dI, dU, U, dA) detected by TOA in a 20 μm i.d. capillary in SDS buffer at neutral pH. The hydrodynamically injected (25 mbar during 30 s) sample mixture (50 μg/mL of each nucleoside) was dissolved in buffer and was separated at $U = 30$ kV resulting in 6 μA of current. The dI peak corresponds to a temperature rise of ~190 mK.

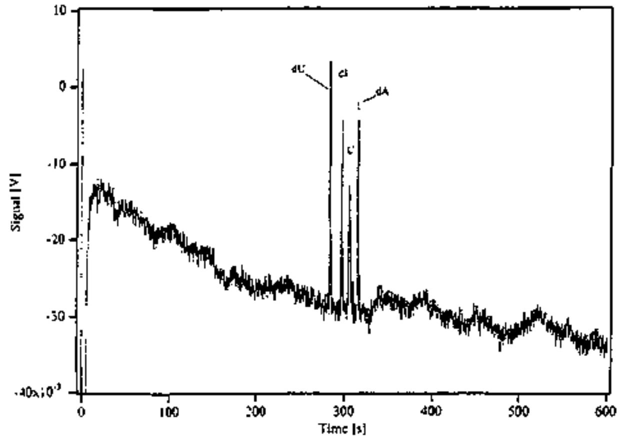

Figure 5. Electropherogram of the same sample and separation as in Figure 4 detected by a commercial UV/visible absorbance detector. The concentration LODs are ~2.4–30 times higher than those obtained with TOA detection.

A quick diagnostic regarding to the observed photobleaching effects can be obtained by looking at the time-resolved traces shown in Figure 2 for both significant cases; namely, dU and dI. dU, which strongly photodegrades, has an anomalous trace resulting in a smaller amplitude, whereas dI, which is photostable, displays a standard TOA trace[20] with a larger amplitude. The anomalous shape of the dU trace indicates that the amount of dU in the illuminated region decreases with time, due to photodissociation decay, to a constant value. This constant value has contributions from the residual absorbance of the photofragments, and its magnitude depends also on the flow rate, which repopulates the irradiated region. The degree of photobleaching, as a function of increasing power for the dU and dI species, continuously injected by pressure (5.7 bar), is depicted in Figure 6. Although below 1 mW of UV power, the TOA signals of dI and dU are comparable; as the power increases to 20 mW, the signal from dU is about one-third that from dI.

Figure 7 shows the MEKC electropherogram of four nucleosides, A, C, G, and dT, and their monophosphate nucleotides (25 mM for all species diluted in water). The migration order of the GMP, dTMP, AMP, and CMP is mainly determined by their

---

(28) Kettler, C. N.; Sepaniak, M. J. *Anal. Chem.* **1987**, *59*, 1733.
(29) Jansson, M.; Roeraade, J.; Laurell, F. *Anal. Chem.* **1993**, *65*, 2766.
(30) Kuhr, W. G.; Yeung, E. S. *Anal. Chem.* **1988**, *60*, 2642–2646.
(31) (a) Xue, Y.; Yeung, E. S. *Anal. Chem.* **1993**, *65*, 1988–1993. (b) Xue, Y.; Yeung, E. S. *Appl. Spectrosc.* **1994**, *48*, 502–506.

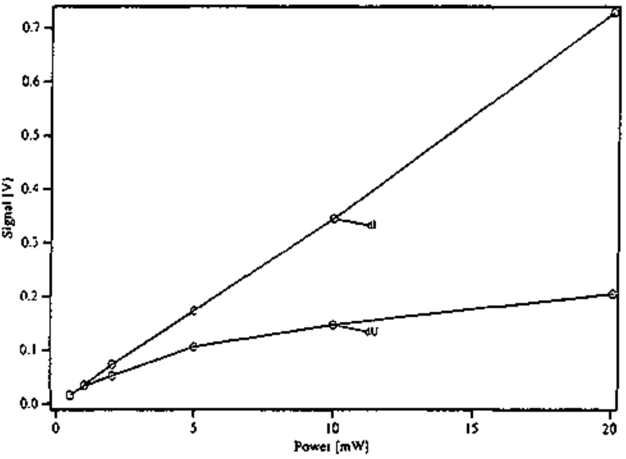

Figure 6. TOA signal as a function of pumping power for two nucleosides, dU and dI. Because dU photodissociates it is associated with a nonlinear behavior, whereas the stable dI gives a rather linear response to pumping power up to 20 mW (see their corresponding TOA signals in Figure 2). Solutions were 50 μg/mL each in SDS buffer and were pumped by a pressure of 5.7 bar. The chopper frequency was 500 Hz.

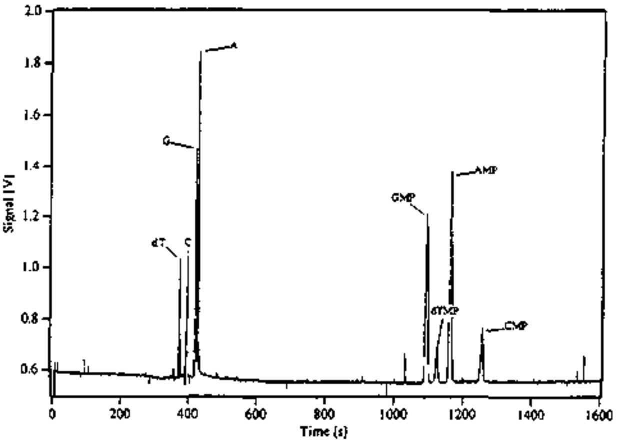

Figure 7. MEKC electropherogram of a mixture of nucleosides and their monophosphate nucleotides detected by TOA in a 20 μm i.d. capillary in SDS buffer at neutral pH. The sample is hydrodynamically injected (25 mbar during 30 s), and the concentration is 25 mM for all species in water. The species are separated at 30 kV, rendering an electrical current of 6 μA.

charge. CMP, having a higher negative charge, and thus the fastest electrophoretic mobility against the electroosmotic flow, appears as the last peak in the electropherogram.

Diphosphates are not well separated in the SDS buffer because of their highly negative electrophoretic mobilities, of magnitude comparable to that of the counteracting electroosmotic flow, leading to impractical long separation times. However, the CE separation of negatively charged diphosphate nucleotides was possible in a 20 mM sodium citrate buffer at pH 3.5. The electropherogram of a mixture of diphosphate nucleotides (30 μg/mL ADP, 50 μg/mL GDP, 100 μg/mL CDP, 200 μg/mL dTDP) is shown in Figure 8. Due to the low pH, the electroosmotic flow was small, the electric field was reversed, and injection was performed at the cathode.

The performances of both, the TOA and conventional UV absorbance detectors, operated with 20 μm capillaries, were evaluated using a 1% acetone/water calibration solution which at 257 nm displays an absorbance of 1.265 AU/cm. The TOA detector yielded a detection limit of ~6.7 × 10^{-6} AU at 10 mW pump power and 2.2 × 10^{-6} AU at 20 mW pump power. These values are to be compared with those obtained with the UV absorption instrument of 3 × 10^{-4} AU (which is ~6 times higher than the typical noise obtained with 75 μm tubes). A great portion of the probing light propagates through the capillary wall without intercepting the 20 μm bore,[6,32] resulting in a rather poor performance in the case of the UV detector. The TOA absorbance noises are thus ~45–140 times smaller than those obtained by conventional absorbance when used in conjunction with 20 μm capillaries. The present TOA noise levels obtained in 20 μm capillaries are comparable with the value of 2.5 × 10^{-6} AU reported by Waldron and Dovichi[21] in 50 μm i.d. capillaries using CBTO.

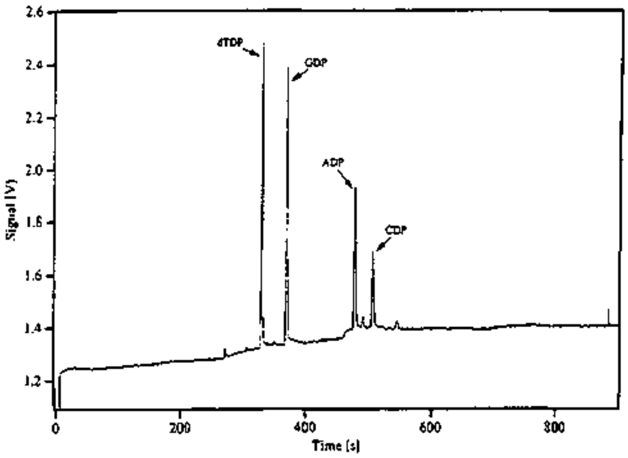

Figure 8. Capillary electropherogram of a mixture of nucleotide diphosphates separated in a 20 mM sodium citrate buffer at pH 3.5. The sample contained 30 μg/mL ADP, 50 μg/mL GDP, 100 μg/mL CDP, and 200 μg/mL dTDP in water. The hydrodynamically injected (25 mbar during 30 s) sample was separated at U = 30 kV, rendering a current of 3 μA. The electric field was reversed, i.e., cathode at injection vial.

The present TOA absorbance noise is somewhat lower than the values reported by Xue and Yeung[31] of 10^{-5} AU in a 75 μm capillary using a laser-based absorbance detector equipped with noise-canceling electronics (corresponding to a concentration LOD 25 times lower than that obtained with a commercial CE system). The reported[31a] LOD for a dye with ϵ = 7.5 × 10^4 L mol^{-1} cm^{-1} is 20 nM, which is lower than that reported for TOA for AMP of 50 nM. It must be noted that the extinction coefficient of the dye used by Xue et al. is ~7.5 times higher than that of AMP, the inner diameter of the capillary used by these authors[31a] is 3.2 times larger, our data is not postrun processed, and the definition[26] we used to compute the LODs is somewhat more conservative than the one used by Xue et al.

For the CE separations performed in 20 μm capillaries using 10 mW pumping power, TOA is ~30 times more sensitive than standard UV absorbance. For the continuously injected samples (i.e., no electrical field), the enhancement was 45 times at 10 mW and 140 times at 20 mW. For larger inner diameter capillaries, these sensitivity enhancement factors will be smaller. This, because on one hand the capillary illumination in conventional absorbance is more efficient for larger inner diameter capillaries, while on the other hand, the heat in the TOA detector is less efficiently removed.

Electrophoretic efficiencies are not affected by photobleaching, and theoretical plates of more than 300 000 have been calculated

---

(32) Bruin, G. J. M.; Stegeman, G.; Asten, van A. C.; Xu, X.; Kraak, J. C.; Poppe, H. *J. Chromatogr.* **1991**, *559*, 163–181.

from the dA and dI peaks using moderate injections and 130 000 plates were reached at the best LODs. The LODs obtained with TOA are ~30 times lower for the photostable samples but only 2.4 times better for the photodegrading samples.

Although the wavelength and power output provided by a frequency-doubled Ar^+ laser system are convenient to perform sensitive TOA measurements of biological substances, its size, cost, and operation complexity do not match the inexpensive, easy to align, and highly miniaturized hologram-based RI detector employed.[12] A solid-state laser system (e.g., a frequency-quadrupled LD-pumped Nd/YAG laser) would have been more compatible with the integrated RI detector used.

ACKNOWLEDGMENT

We thank E. S. Yeung (Iowa State University) and G. Bruin for reviewing the manuscript and providing critical comments and suggestions and U. Pieles for some of the samples. This project was supported by the Commission pour l'Encouragement de la Recherche Scientifique (Switzerland, Project 2156.1).

Received for review June 27, 1994. Accepted October 4, 1994.[⊗]

AC940635E

[⊗] Abstract published in *Advance ACS Abstracts,* November 1, 1994.

Enhanced Refractive Index Detection for Capillary Electrophoresis Using Flared Capillaries

Joaè Maria Saz,† Beat Krattiger,
Alfredo E. Bruno,* François Mayare,
H. Michaal Widmar

Abstract: A novel on-column refractive index detector suitable for capillary electrophoresis, whose optical arrangement is based on a known interferometric principle, is described. In the present version the holographic element is replaced by two conventional optical elements, a Wollaston prism and a microscope objective. When using refractive index detection in capillary electrophoresis the noise is dominated by Joule heat effects, so we have introduced the use of flared capillaries to minimize this effect. Typical flared capillaries have a diameter three times larger at the bubble, where optical detection is performed, than at the separation section resulting in a large enhancement in the instrumental sensitivity. The usefulness of the detector has been demonstrated in the capillary electrophoretic separation of a mixture of underivatized sugars resulting in detection limits in the high μM range.

Keywords: refractive index, interferometry, capillary electrophoresis, flared capillary, Wollaston prism, underivatized sugars

1. Introduction

Recent instrumental improvements[1–4] in refractive index (RI) detectors for capillary electrophoresis (CE) are bringing this rather insensitive technique closer to the useful realm. The most recent improvement was given by Krattiger et al.[1] who introduced the use of holographic optical elements in optical detection for CE in a compact and highly sensitive RI detector which was used with capillaries having inner diameters (i.d.s) as small as 5 μm. The holographic element, in this 'on-axis' interferometric design[3], divides the initial beam into two focusing beams. One beam probes the capillary bore through the middle whereas the second beam, propagating through the capillary wall and refractive index matching (RIM) material, acts as the reference beam in this double-slit Young interferometer[5]. Because in this arrangement the probing beam propagates through the middle of the core the fully available optical path length is used; as compared to, e.g. the 'off-axis' designs[2,6], larger shifts of equally spaced fringes detected by a photo-diode array (PDA) result in a higher instrumental response.

Electrical currents produce Joule heat[7] which is known to degrade separation efficiency in CE due to band broadening and, when using RI detection, it is the dominant source of noise due to schlieren effects in the buffer[2]. Considering that these thermal effects are proportional to the cross section of the capillary and also that small i.d. tubes offer a higher surface to volume ratio which facilitates heat dissipation through the capillary wall, the use of smaller i.d. capillaries is preferred from the separation point of view. However, as the decrease in optical path length is correlated with a reduction in the sensitivity, the optimum capillary diameter is the result of a compromise between detection and separation arguments.

The RI detector presented here uses an optical arrangement identical to that recently reported[1]. However, the core of the interferometer, given by the holographic element in the previous design[1], is realized here by means of a set of conventional optical elements. The main novelty in the present arrangement is the use of flared capillaries (Figure 1) to enhance the instrumental sensitivity. Flared capillaries, presently in use in conjunction with UV/vis detectors, allow an increase in optical path lengths without compromising the benefits observed in the separation efficiency associated with thinner capillaries. The performance of this detector is evaluated using a synthetic mixture of underivatized sugars as a test sample.

2. Theory

2.1. Principle of operation

The optical configuration of this detector is identical to that of the hologram-based RI detector already

---

**Author for correspondence:*
Dr A.E. Bruno
Corporate Analytical Research
Ciba-Geigy Ltd.
CH-4002 Basel (Switzerland)

†Department of Analytical Chemistry
Faculty of Science
University of Alcalá de Henares
28871 Alcalá de Henares
Madrid (Spain)

Acknowledgments: The authors would like to thank P. Nussbaum and R. Dändliker (Institut de Microtechnique, Neuchâtel, Switzerland) for lending us the Wollaston prism and for providing technical support. One of us (J.M.S.) would like to thank J.C. Diez-Masa (Instituto de Quimica Orgánica del CSIC) for making the three month visit to the Ciba-Geigy laboratories possible and, to the Universidad de Alcalá de Henares and Comunidad Autonoma de Madrid, for the financial support.

CCC 1063-5246/93/040203-05

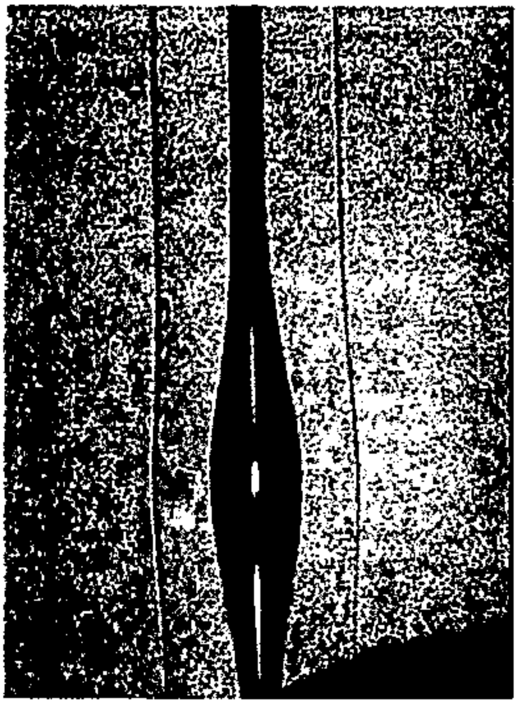

Figure 1. Picture of the bubble of the flared capillary employed. The i.d. at separation part and bubble are 50 μm and 150 μm and the o.d. are 310 μm and 340 μm, respectively.

described[1]. In the present version the holographic element is replaced by two conventional optical elements, a Wollaston prism[3] and a microscope objective (MO), arranged as shown in Figure 2. The diverging beam of a laser diode (LD), which is first collimated by a lens within the laser module, is divided by the Wollaston prism into two orthogonally polarized beams diverging by an angle α. The MO, placed at its focal distance f from the Wollaston prism, makes both beams parallel and focuses them. The capillary is also placed at a distance f from MO (i.e., the Wollaston prism and capillary are placed symmetrically with respect to the MO) in such a way that its bubble intercepts the probe beam. The remaining beam, the reference beam, propagates undisturbed by its side. Both beams, the probing and reference beam, can, after passing through a polarizer, recombine and mix in the far field and, because they originate from the same coherent source, they build up a regularly spaced interference pattern, as shown in Figure 2.

Changes in the refractive index (Δn) in the bubble part of the capillary modify the optical phase of the probing beam resulting in a lateral shift of the interference pattern. These shifts are monitored by a PDA wired to produce a position sensitive output signal[1,2] which, upon calibration, becomes the output signal of the RI detector. The polarizer at 45°, placed before the PDA (Figure 2), ensures maximum contrast of the fringes. The capillary bubble is surrounded with RIM material ($n = 1.46$) to eliminate unwanted reflection and refraction at the optical interfaces[2] as well as to allow an efficient removal of the Joule heat produced in CE which is known[2] to contribute to the overall noise due to schlieren effects in the buffer.

2.2. Beam diagnostic

The beam waists (twice the spot size, $2w_0$) of both beams, at the focal point of the ten times MO employed ($f = 17\,\mathrm{mm}$), is estimated by

$$w_0 = \frac{2\lambda f}{\pi d}, \tag{1}$$

where d are the original beam diameters. The spot size is fifty times smaller than the i.d. at the bubble (i.d. = 150 μm) implying that the entire probing beam propagates through the capillary flare.

The beams after the MO are separated by a distance D which is given approximately by

$$D \approx f\alpha, \tag{2}$$

where α is the diverging angle of the Wollaston prism employed. In the present case $\alpha = 0.5°$ and thus $D \approx 150\,\mu\mathrm{m}$ which is about half the external diameter of the capillary (o.d. = 340 μm). The reference beam thus propagates through the capillary wall without intercepting the core.

2.3. Instrument response

As in the hologram based RI detector[1], the instrumental response is given by

$$\frac{\mathrm{d}U}{\mathrm{d}n} = \frac{4C\,\mathrm{i.d.}\,K}{\lambda} \tag{3}$$

where $\mathrm{d}U/\mathrm{d}n$ is the change in the voltage output per RI unit (RIU) change, K the amplification of the electronic circuit (10 V in our case) and C the fringe contrast given by[5]

$$C = \frac{I_{\max} - I_{\min}}{I_{\max} + I_{\min}}. \tag{4}$$

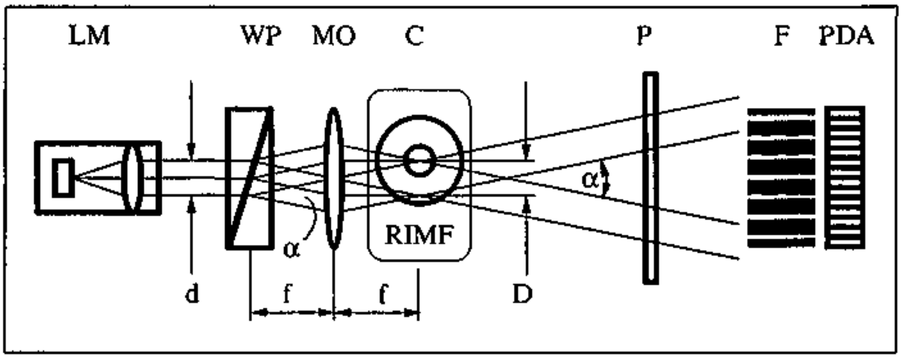

Figure 2. Diagram of the detector experimental set-up. LM: laser module, WP: Wollaston prism, MO: microscope objective, C: capillary cell, P: polarizer, F: fringe pattern, PDA: photo-detector array.

In equation (4), $I_{\max}$ and $I_{\min}$ refer to the maximum and minimum intensity observed in the fringe pattern, respectively. In practice C is most easily determined by noticing that

$$C = \frac{U_{\max}\pi}{2K} \qquad (5)$$

[derived from equation (13) of ref. [1]) and by measuring the highest signal voltage, $U_{\max}$, as the PDA is scanned through the fringe pattern. The maximum signal measured in our instrument was 6 V leading to a contrast of $C = 0.94$ which is very close to the maximum ($C_{\max} = 1$) to be observed when $I_{\min}$ is zero, equation (4). The instrumental response of our instrument is, as calculated using equation (3), $\mathrm{d}U/\mathrm{d}n = 8.4\,\mathrm{mV}\,\mu\mathrm{RIU}^{-1}$.

3. Experimental

3.1. RI detector

The RI detector (Figure 2) was assembled almost entirely with commercially available components (Spindler & Hoyer, Germany). The multimode LD, the driving electronics and the collimating lens are contained in the laser module (LDM 135, Imatronic Inc., Batavia, IL). The LD lases at 672 nm and delivers 1 mW of output power. Precautions are taken to adjust the LD chip parallel with respect to the capillary to minimize the effects of aberration. The Wollaston prism (PWQ30.10, Bernhard Halle Nachfl. GmbH & Co., Berlin, Germany), MO (Spindler & Hoyer, Germany) and polarizer are adjusted to produce the best fringe contrast.

The flared part of the capillary is introduced in a heavy wall fused silica tube (i.d. ≈ 1 mm, o.d. ≈ 6 mm) and the empty space is filled with RIM material (#19569 and 19571, R.P. Cargille Laboratories Inc., Cedar Grove, NJ, USA) to form the 'detection cell'. One side of the heavy wall tube was polished flat to form the 'entrance window' and it was mounted in an aluminum body.

Only 14 of the 46 elements PDA (S4111 series, Hamamatsu) are used to detect seven adjacent fringes. The odd and even numbered elements are wired together (as shown in Figure 4 of ref. [1]) and both channels are fed into a position sensitive amplifier (Model 301-DIV, UDT, Hawthorne, CA) delivering a signal proportional to the fringe shift which is rather insensitive to light intensity fluctuations[2]. The LM and the detection cell are thermostated by temperature controllers (Model LDT-5412, ILX Lightwave, Bozeman, MT) using Peltier elements (Melcor, Trenton, NJ). The LabView (National Instruments, Austin, TX) and IGOR (WaveMetrics, Lake Oswego, OR) software packages, running on a Macintosh IIfx, were used for data acquisition and analysis.

3.2. Capillary electrophoresis

The flared capillary (Hewlett Packard, #G 1600-61-231) employed had an i.d. of 50 µm at the separation part and 150 µm at the bubble (Figure 1) and a length of 60 cm (50 cm to the detector). The standard 50 µm i.d. capillary (Polymicro, Phoenix, AZ, USA), used for comparison purposes, had a length of 75 cm (50 cm to detector). CE is performed at 8 kV and 10 kV with the flared and standard capillary, respectively. Injection, in both cases, was hydrodynamically performed with a Prince CE system (Lauer Labs, Emmen, The Netherlands). Chemicals were purchased from Merck (Darmstadt, Germany) and Fluka (Buchs, Switzerland).

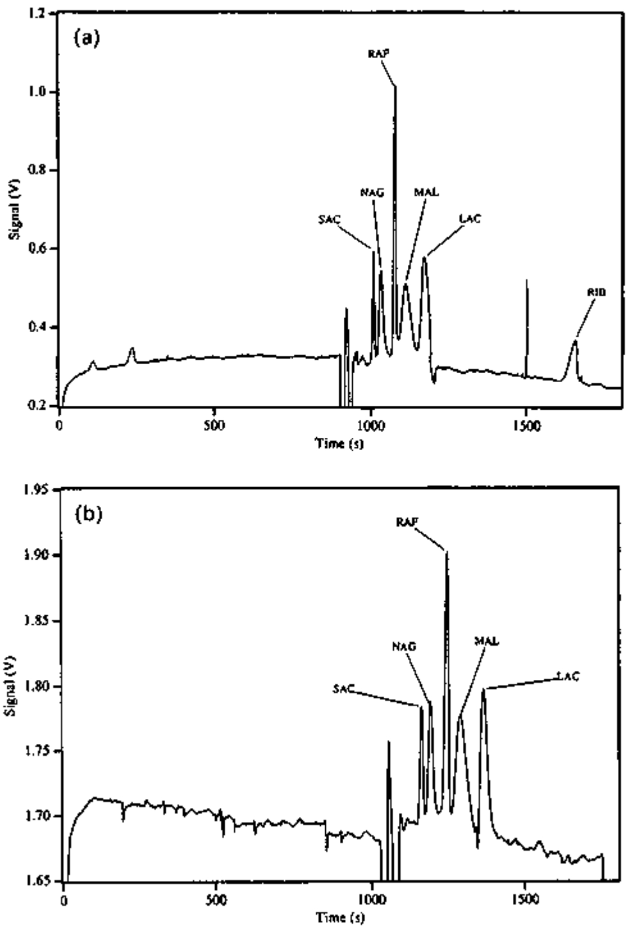

Figure 3. Electropherograms of a mixture of sugars obtained with the RI detector operated in conjunction with (a) the bubble and (b) the standard capillaries. The peaks are identified as: SAC: saccharose, NAG: N-acetyl-D-glucosamine, RAF: raffinose, MAL: maltose, LAC: lactose, RIB: ribose. Electrical field of 10 kV and a current of 19 µA. The concentration of each sugar is 8.3 mM and the electrophoretic conditions and buffer employed are reported in the Experimental section.

4. Results and discussion

The present RI detector is demonstrated with both a flared and a standard capillary in the CE separation of a mixture of six underivatized sugars. The corresponding electropherograms are shown in Figures 3(a) and 3(b). Most sugars are neutral species and therefore not eligible for CE (see ref. [9] for the pK and ref. [10] for the mobilities of sugars). This difficulty is overcome using borate buffers[4,9–11]. Borate complexes sugars into various types of negatively charged species. The magnitude of the charge, and thus their electroosmotic mobility, depends mainly on the concentration of borate. Six forms of sugars coexist in aqueous solutions, α- and

Table 1. Signal, noise and limits of detection obtained with the standard and flared capillary. Peak height data from the raffinose peak in Figures 3(a) and 3(b).

	Standard capillary	Flared capillary	Flared/standard
Signal/mV	221	706	3.2
Noise/mV	11.5	6.75	1.7
S/N	19	105	5.4
LOD/μM	860	160	0.19

Table 2. Electrophoretic mobilities obtained with the standard and flared capillaries obtained for various sugars in the borate/CAPS buffer employed.

	Standard (10^{-5} cm^2 V^{-1} s^{-1})	Flared (10^{-5} cm^2 V^{-1} s^{-1})
SAC	3.65	3.56
NAG	4.54	4.46
RAF	6.09	6.01
MAL	7.14	6.99
LAC	8.86	8.73
RIB	—	18.10

β-pyranoses and furanose forms, as well as the open-chain and hydrated forms multiplying the complexation possibilities. Saccharose and raffinose complex into a single species and therefore appear as the sharpest peaks in the electropherograms. The broadening observed in the other peaks is due to the various complexes associated with each type of sugar having similar mobilities (rather than to column overloading). Optimal results were obtained with a 33 mM borate/13.3 mM CAPS buffer (3-cyclohexylamino-1-propanesulfonic acid) at pH 9.4 where the current decreased by a factor of about four with respect to a 100 mM borate buffer previously used[2] while efficiency is maintained.

Table 1 summarizes the S/N and the limits of detection (LOD) obtained with the normal and flared capillary with the present RI detector from the raffinose peak in the electropherograms shown in Figs. 3(a) and 3(b). The theoretical plate numbers, determined from the raffinose peak, are 60000 and 130000 for the standard and flared capillary, respectively. The electrophoretic mobilities of the investigated sugars in the buffer employed are reported in Table 2.

The increase in the capillary i.d. at the detection zone, offered by flared capillaries when using RI detection, results in a decrease in the overall noise and an increase in the signal, leading to a five-fold enhancement in the S/N. Although the observed three-fold increase in the signal is easily explained using equation (3), dealing with the instrumental response, a quantitative analysis to explain the observed decrease in the noise is not straightforward.

There are various sources contributing to the overall noise. A schlieren effect in the detection path caused by Joule heat is, in the present case, the dominant source[2] while the electronics, particles or bubbles in the buffer and wavelength jitter contribute to a lesser extent to the overall noise. With regard to Joule heat there are a few factors that play a role in dissipating heat in the presence of flared capillaries. Considering that FS has good heat conducting property, and air a poor one, the rate of heat dissipation for naked capillaries is mainly determined by the o.d. and the inner volume-to-surface ratio which increases for smaller capillaries. In the case of capillaries having their outer wall in contact with RIM materials the o.d. can be considered as infinite and the volume-to-surface plays a smaller role in determining the rate of heat dissipation. It has to be noticed that the total electrical current (I) remains constant along the capillary including the bubble. However, at the bubble, the cross section is nine times higher, therefore the associated electrical resistance (R) is nine times smaller than in the rest of the capillary and, the electric field (E) should also decrease by the same amount (i.e., $E \approx RI$). Because Joule heat, and its associated schlieren effects, are caused by the electrical field, they should also decrease explaining the observed reduction in the noise.

The separation efficiencies obtained from the electropherograms displayed in Figures 3(a) and 3(b) are rather similar. Although the bubble introduces a small dead volume in the capillary, the smooth change in cross section (see Figure 1) should not alter the laminar flow, and peak broadening is not expected. The small differences in the electrophoretic mobilities reported in Table 2 are within the experimental error.

5. Conclusions

The 'on-axis' illumination configuration for the construction of capillary RI detectors, based on commercially available optical elements proposed here provides more flexibility and is certainly easier to realize than the configuration based on holographic plates. One advantage offered by the present arrangement is that light losses are very small at the Wollaston prism as compared to those associated with a hologram, demonstrated by the diffraction efficiencies which are in the 10–30% range. However, using multi-element photodetectors, light intensity is no longer an issue in the quest for higher sensitivity. The major issue in this regard is thermal and mechanical stability[3] which is better achieved using miniature optical components such as holographic plates. Therefore, we believe that the best capillary RI detector would be one based on 'on-axis' illumination using a holographic element and featuring a flared capillary. The LODs reported in Table 1 are better than those reported in ref. [2] and comparable with those obtained by other methods provided that the sugars are not derivatized[4,10].

References

[1] B. Krattiger, G.J.M. Bruin, A.E. Bruno: *Anal. Chem. 66* (1994) 1.

[2] A.E. Bruno, F. Maystre, B. Krattiger, H.M. Widmer: *Anal. Chem. 63* (1991) 2689.

[3] A.E. Bruno, B. Krattiger, F. Maystre, P. Nussbaum, E. Gassmann: *Trends in Anal. Chem. 13* (1994) 190.

[4] A.E. Bruno, B. Krattiger: in E. Rassi, (Ed.): *Carbohydrate Analysis*, Elsevier, New York, Ch. 11 (in press).

[5] M. Born, E. Wolf: *Principles of Optics*, Pergamon, New York (1989).
[6] B. Krattiger, A.E. Bruno, H.M. Widmer, M. Geiser, R. Dändliker: *Appl. Opt. 32* (1993) 956.
[7] S.F.Y. Li: in *Capillary Electrophoresis*, Elsevier, New York (1992).
[8] E. Hecht, A. Zajac: *Optics*, Addison-Wesley, Reading (1979).
[9] J.A. Rendle: in H.S. Isbell (Ed.): *Carbohydrates in Solution*, ACS, Washington DC (1973), p. 54.
[10] S. Hoffstetter-Kuhn, A. Paulus, E. Gassmann, H.M. Widmer: *Anal. Chem. 63* (1991) 1541.
[11] S. Honda, S. Iwase, A. Makino, S. Fujiwara: *Anal. Biochem. 176* (1989) 72.

Received 8 February 1994
Accepted 19 April 1994

Anal. Chem. 1991, *63*, 2689–2697

On-Column Laser-Based Refractive Index Detector for Capillary Electrophoresis

Alfredo E. Bruno,* Beat Krattiger, François Maystre, and H. Michael Widmer

CIBA-GEIGY Ltd., Analytical Research, CH-4002 Basel, Switzerland

The interference pattern from side-illuminated capillary tubes has been exploited to develop a sensitive universal refractive index (RI) detector suitable for nanoliter on-column capillary separation techniques. A 2-fold benefit is obtained by surrounding the capillary tube with a RI-matching fluid: the fringe pattern is simplified, and thermal noise is reduced. The key to RI detection in CE, provided that the instrument delivers sufficient sensitivity, has been found to be thermal stability. A thermal stability of $\Delta T = 2.0 \times 10^{-4}$ °C is achieved in a Peltier cooled RI cell having a highly symmetric design aimed to ensure fast thermal response from the thermoelectric system. The linear dynamic range extends to more than 3 orders of magnitude with a typical RMS noise level of 3×10^{-8} RIU and baseline drifts of 2×10^{-8} RIU h^{-1} at 1 Hz. This is about 1 order of magnitude above the calculated shot noise limit for these tube dimensions. These noise levels correspond to an angular deflection of the selected fringe of 100 nrad, which has been obtained by using a large position-sensitive photodiode. The optical geometric arrangement of the photodiode, with respect to the fringe width, has been optimized theoretically. A detailed description of the instrument and its noise sources is presented, and the technique is demonstrated in CE in the analysis of underivatized carbohydrates using a 50-μm tube.

INTRODUCTION

Capillary electrophoresis (CE) in undoubtedly *the trend* in liquid-phase chemical analysis. Several features including speed of analysis, high resolution, and efficiency account for the present acceleration in the acceptance of this technique. High electric fields are used in CE to force ionic solutes to migrate through a buffer- or gel-filled capillary. The species, injected in minute amounts, are separated along the tube on the basis of charge, size, or both (*1, 2*) and are subsequently detected near the capillary end. The various forms of this technique, capillary zone electrophoresis (CZE), isothachophoresis (ITP), micellar electroosmotic chromatography (MECC), and capillary gel electrophoresis (CGE), have been successfully demonstrated in the analysis of pharmaceuticals, peptides, proteins, carbohydrates, oligonucleotides, subcellular structures, and even whole cells (*3–10*).

Various instrumental aspects contribute to the overall performance in CE. Detection, being perhaps the most important one, is most conveniently carried out using optical methods. The benefits observed when the inner diameter of the capillary is reduced are compromised in the detection stage when path length dependent optical schemes are used (*11, 12*). There is therefore a growing demand to improve the sensitivity of known detection systems or to develop alternative ones. Primarily because of their spatial coherence, lasers have led to the development of a series of novel capillary detectors featuring impressive detection limits (*13*).

In order to preserve the spatial profile of the eluting substances achieved in high-performance separations, only on-column detection (*11*) is meaningful in CE. The most popular detection scheme used in CE is UV/vis absorption (*14–16*). It is accomplished by modifying a conventional absorbance photometer using optical fibers or masking the optical path with a pair of slits (*11*). However, nonlinear responses for absorbance vs concentration curves are not uncommon (*11*). These are due to stray light and/or changes in the refractive index (RI) of the mobile phase due to solute concentration, pressure gradients, etc., which alter the optical path and lead to unwanted dynamic effects. For absorption measurements in narrow-bore capillaries, crossed-beam thermooptical (CBTO) absorption techniques (*17*) offer definite advantages. An interesting feature of CBTO is that as the capillary's diameter is reduced, the pumped heat is more efficiently quenched at the walls and high electric fields can be applied along the tube for faster separations (*12*).

Laser-induced fluorescence (*15*) (LIF) is the most sensitive detection method devised to date. However, because only a few molecules of interest fluoresce at available laser lines, rather complicated precolumn derivatizations (*16*) are required.

Much stricter conditions than those required for example in liquid chromatography (HPLC), are to be met when designing a detector for CE. Therefore, not all detection schemes of standard use have been made available to CE. Bulk RI detection, unavoidable when the substances of interest neither absorb nor fluoresce, is a typical example. Joule heat poses the major challenge in the development of a RI detector suitable for CE. Since most applications require a sensitivity below $\Delta n = 10^{-6}$ RIU (RI units, n is the RI of the mobile phase) and the change in RI with the temperature (dn/dT) for most solvents is of the order of 10^{-4} RIU/K at room temperature, thermal stability becomes the limiting factor in the quest for lower detection limits.

A RI detector, whose operational principle is based on the interference pattern arising from side-illuminated fused-silica capillaries, demonstrated in HPLC by Bornhop and Dovichi (*18–20*), has shown promising results. An insightful theoretical analysis was later given by Synovec (*21*), and various refinements, aimed to adapt the technique to CE, was subsequently published (*22–24*).

The approach given by Chen et al. (*22*), to overcome thermal fluctuations inside the capillary in CE, was to partially modulate the electric fields in a so-called analyte velocity modulation method. The sensitivity of this detector appears to be comparable to those attained with other methods (*23, 24*), but much instrumental work and applications are awaited to fully appreciate the benefits of this technique.

Pawliszyn (*23, 24*) proposed a concentration gradient differential detector based on Schlieren optics which is rather insensitive to thermal fluctuations inside the capillary suitable for ITP. However, as, in this method, one obtains the first derivative of the signal, it is necessary to integrate the output signal to reconstruct the electropherogram, and the optical arrangement needs to be optimized for each separation system.

---

* To whom correspondence should be addressed.

0003-2700/91/0363-2689$02.50/0

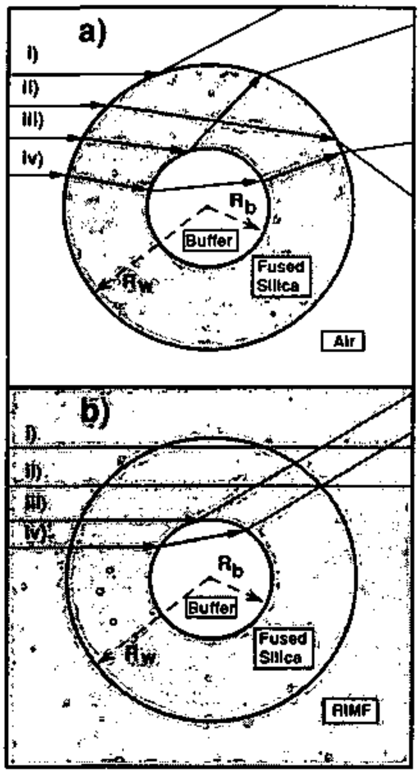

Figure 1. Capillary tube cross section and corresponding ray-tracing diagram for four significant rays: (a) capillary surrounded with air. (b) capillary surrounded with RIMF. Reflections and refractions at the different interfaces are indicated as arrows. The different n values of the propagating media are represented by the density of the pattern; e.g. air [n = 1.00] has no associated pattern, water (n = 1.333) has a lighter dotted pattern, and fused silica (n = 1.467) and RIMF (n = 1.467) are represented by identical darker patterns.

In this contribution we describe a RI detector based on the design originally proposed by Bornhop et al. (*18–20*). In the present instrument we introduce the use of index-matching fluids (RIMFs) and position-sensitive photodiodes (PSDs), in conjuction with thermoelectric stabilization, integrated into a compact, highly symmetric RI cell design. A detailed analysis of the noise sources, with emphasis in the shot noise and the noise due to thermal fluctuations, is made and used to improve the detector. In addition, we present a model to study the interference pattern produced by the capillary. The improvements obtained in the overall detector performance are demonstrated in the CE separation of synthetic underivatized saccharide mixtures. Considering their importance in biochemistry, food science, etc., sugar mixtures were chosen to demonstrate the new technique. Also, it has been recently shown (*16, 25–28*) that CE represents an alternative to other traditional (*29*) and electrophoretic methods (*30–32*) used in the analysis of sugars.

THEORY

Index-Matched Capillary Walls. The present detection method takes advantage of the light interferences, typical of side-illumination of liquid-filled capillary tubes by laser light (*18–20*), to measure changes in the RI (Δn) of the effluents. As in the case of optical fibers (*33*), when coherent light strikes a capillary transversaly, the light is scattered over 360° in the plane perpendicular to the capillary axis. The resulting fringe pattern is characteristic of the capillary dimensions, RI of the propagating media (i.e. capillary wall and orifice), focusing properties of the beam, and light polarization. As shown in Figure 1, depending on their incident position and angle, the light rays either (i) are reflected at the outer capillary surface, (ii) enter the capillary, propagate through its wall, and emerge without intercepting the inner bore, (iii) are reflected at the inner capillary wall/liquid interface, or (iv) propagate through both the capillary wall and bore. Hence, the interference pattern is produced by four types of scattered rays, and therefore is rather complex, as shown in Figure 2 (top). Some of the fringes change their position as a consequence of changes in the RI of the effluent. The angular shift of the fringes, due to refractions and changes in the optical path of the rays (*34*), are used to measure the effluent's Δn. Without index-matching fluid around the capillary, it is difficult to select a sensitive fringe which also has a high contrast. In addition, only a very small fraction of the total optical power is available in every fringe and sharp fringes led to a narrow dynamic range of the detector in question. It is thus desirable to simplify the fring pattern in order to select the fringe which shifts the most for a given Δn and to direct the optical power into these fringes.

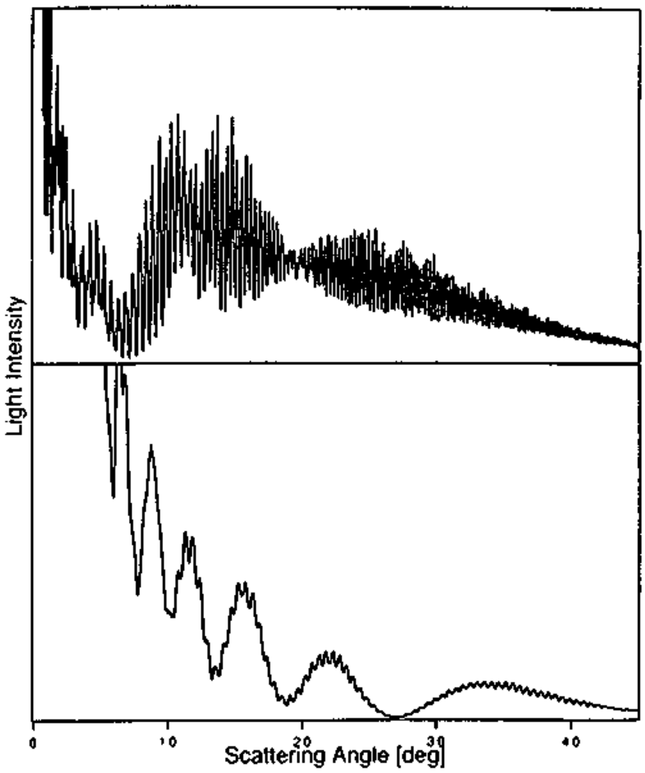

Figure 2. (Top) forward scattering fringe pattern of a water-filled silica capillary having i.d. = 50 μm and o.d. = 365 μm side-illuminated with a He–Ne laser beam. (Bottom) fringe pattern for the same capillary immersed in RIMF. The scattering angle ϕ = 0° corresponds to the optical axis. The residual high-frequency intensity modulation in the bottom figure is most likely due to a slight mismatch of the RIMF caused by temperature differences.

Simplification of the fringe pattern is achieved here by immersing the fused-silica (FS) capillary in a transparent liquid (RIMF) having the same index of refraction as the capillary wall (i.e n = 1.4587 at T = 25 °C for λ = 632.8 nm). This technique is routinely used to measure the core dimensions of optical fibers (*33*). In this way, the reflections and refractions at the external capillary wall (i.e. type i rays) are eliminated according to basic optical principles (*34*). The overall pattern is dominated by interferences between the rays of type iii and iv, as illustrated in Figure 1b. The total number of refractions and reflections, indicated by arrows in the figure, is dramatically reduced from 10 to 3, resulting in a much simpler interference pattern, as shown in Figure 2 (bottom).

Modeling of the Interference Pattern. Computer simulations have been used to predict the fringe shifts per Δn and thus to maximize the sensitivity of the instrument. The profile of the whole interference pattern, for the simplified case in which the capillary is immersed in RIMF and has an i.d. greater than 30 μm, can be quantitatively described by

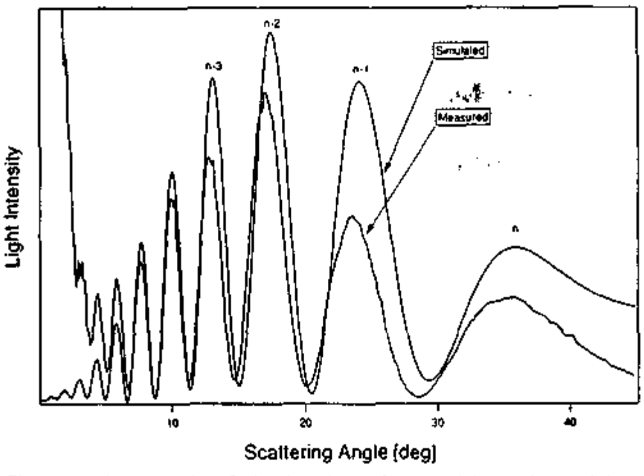

Figure 3. Measured and simulated interference fringes for an i.d. = 50 μm capillary immersed in RIMF. Fringes are arbitrarily labeled starting with n, which is the last well-defined and easily identified fringe from the optical axis.

Table I. Shot Noise Limits for Different Fringes of the Scattering Pattern[a]

fringe no.	$n - 1$	$n - 2$	$n - 3$	
position	24	16	12	deg
ang shift	−223	−200	−172	deg/Δn
4σ	7.7	5.3	3.2	deg
P_{opt}	25*	25*	10*	μW
δ_{sn}	3.4×10^{-8}	2.3×10^{-8}	2.2×10^{-8}	rad
Δn_{sn}	8.7×10^{-9}	6.6×10^{-9}	7.3×10^{-9}	

[a] These values are typical for an i.d. = 50 μm i.d. capillary filled with water and illuminated by a 2-mW He–Ne laser (λ = 633 nm). The detection bandwith is assumed to be B = 1 Hz. The values quoted with an asterisk are measured data.

a ray-tracing model which does not take into account diffraction effects.

In the present optical configuration the capillary behaves as a pseudo Mach–Zehnder interferometer and the fringes are thus the result of interactions between two rays. The *reference* beam (ray iii in Figure 1b) strikes the wall/buffer interface at an angle greater than critical (α_{crit} = 66°) and is totally reflected. The *sampling* beam (ray iv in Figure 1b) propagates through the capillary bore where it is refracted twice at the wall/buffer interfaces (Figure 1). Both rays propagate through different optical paths, and as they recombine in the far field, they form the observed interferences. Depending on whether the optical path difference between the reference and sampling ray is an integer multiple or an integer multiple plus one half of the wavelength, constructive and destructive interferences occur (*33, 34*).

A computer program based on classical optics (*34*) has been developed and was used to select a priori the most sensitive fringe to Δn, for a given capillary diameter, known polarization, and intensity distribution of the incoming beam, for each ray. For each scattering direction the algorithm computes the associated trajectories of both rays and therefore their intensities and relative phase differences. The far-field distribution is computed by making use of coherent superposition of rays, assuming that the incident beam is a bundle of parallel rays with a Gaussian intensity profile. A typical result of the measured and computed interference patterns for a 50-μm capillary is shown in Figure 3, and significant results are summarized in the upper part of Table I.

Thermal Analysis. Once the problems associated with the selection of a monitoring fringe have been solved, the thermal instability in the capillary is the limiting factor in the quest for maximum detection sensitivity, at least in CE. In this regard, an additional benefit is observed when surrounding the capillary with RIMFs, i.e. the possibility to further stabilize the temperature inside the capillary in the detection region. Because the thermal conductivity coefficients of liquids are about 20 times larger than that of air, the surrounding RIMF acts as an efficient heat sink.

Table II. Definitions (Reproduced from Reference 38) and Values of Dimensionless Variables for a Fused-Silica Capillary (i.d. = 50 μm and o.d. = 365 μm) Cooled by Naturally Convecting Air and by a Surrounded Liquid (RIMF) in Contact with a Thermoelectric Cooling System

		convecting air	RIMF
$\theta = (T - T_0)/\Delta T_{ref}$	dimensionless temp	1.102^a 0.843^b	40.20^a 39.66^b
$\eta = r/R_B$	dimensionless radial coordinate	$r/25$	$r/25$
$\Delta T_{ref} = \kappa_0 E^2 R^2{}_B/k$	characteristic temp rise	0.64^c	0.64^c
$\lambda = \sqrt{\kappa_1 \Delta T_{ref}}$	autothermal param	0.172^d	0.172^d
$\mathrm{Bi}_{0A} = h_{0A}R_B/k$	overall biot no.	0.055^e	1.22^f
$f(\lambda)$		0.457^g	0.968^f

[a] Computed with eq A-1, at r = 0 μm. [b] Computed with eq A-1, at $r = R_b$ = 25 μm. [c] κ_0 = 1 S/m, $k_{|H_2O|}$ = 0.61 W m^{-1} K^{-1}, E = 250 V cm^{-1}. [d] κ_1 = 0.046 K^{-1}, from ref 38. [e] Typical value, taken from ref 38. [g] Computed using eq A-2.

The support buffer in the capillary, which has an associated electrical resistance of $R = U/I$ dissipates a considerable amount of heat, up to P = 1.3 W in the present case, resulting in various negative side effects in CE. The thermal Joule effect associated with CE and its consequences to column efficiency have been thoroughly studied (*35–40*). Of relevance to this study are a detailed knowledge of the temperature profile in the capillary bore as a function of radial position and the total difference in temperature between the center of the capillary (hottest region) and its surrounding at the detection part of the tube.

In the absence of the polyimide coating, which was removed in the detection region and under the assumption that the only heat source is the electrical current circulating in the buffer (e.g. there is no absorption of the laser light in the detection volume), the total temperature change from the center of the capillary to the surrounding thermal bath ΔT_{total} can be subdivided into

$$\Delta T_{total} = \Delta T_b + \Delta T_w + \Delta T_{sur} \qquad (1)$$

where ΔT_b is the temperature drop in the bore, ΔT_w in the wall, and ΔT_{sur} in the surrounding bath.

The temperature distribution $T(r)$ is known (*35*) to be approximately parabolic across the bore and logarithmic across the silica wall and in the immersion bath. According to the theory of Grushka et al. (*36, 37*), the temperature profile $T(r)$ within the capillary satisfies

$$k\frac{1}{r}\frac{d}{dr}r\frac{dT}{dr} = -E^2\kappa \qquad (2)$$

where E is the applied electric field, k is the thermal conductivity of the buffer, and κ is its electrical conductivity.

Exact solutions to eq 2 in the capillary bore have most recently been proposed in terms of the dimensionless variables θ, ΔT_{ref}, λ, η, Bi_{0A}, and ΔT_b, defined and computed in Table II, by Gobie and Ivory (*38*). In this formalism, ΔT_b can be obtained by integrating eq 2 with the appropriate boundary conditions in the capillary bore (i.e. from $r = 0$ to $r = R_b$, in Figure 1) and reads

$$\Delta T_b = \theta \Delta T_{ref} \qquad (3)$$

Details on the evaluation of the dimensionless temperature θ and on the characteristic temperature raise, ΔT_{ref}, are given

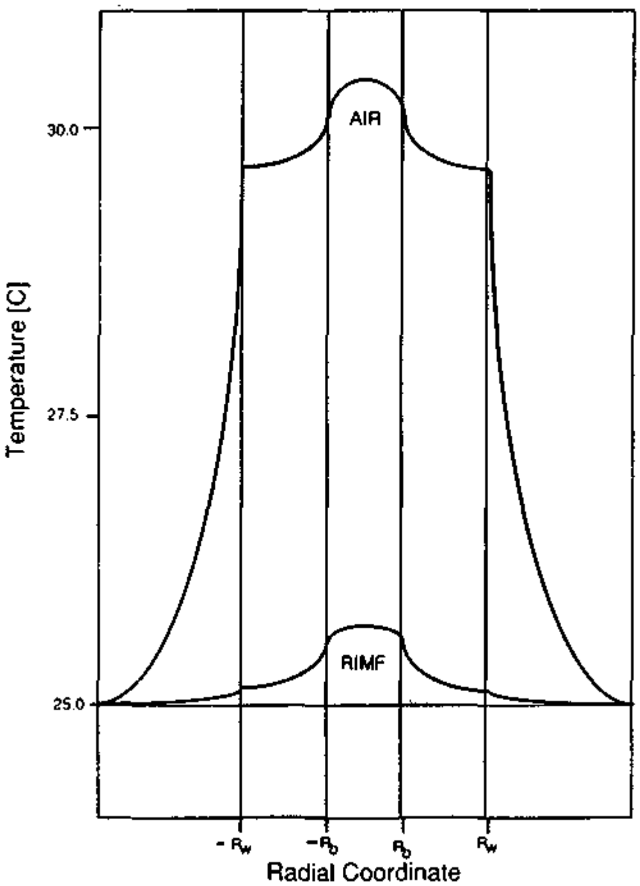

Figure 4. Temperature profile as a function of the radial coordinate in the capillary bore and fused-silica wall (i.d. = 50 μm, o.d. = 365 μm) and surrounding media for a capillary filled with an aqueous solution and immersed in RIMF (lower trace) and cooled by naturally convecting air (upper trace). Both profiles have been computed as explained in the text.

in the Appendix, and the results are reported in Table II. It is found that $\Delta T_b = 0.350$ °C when the capillary is surrounded by air and $\Delta T_b = 0.165$ °C when the capillary is surrounded by RIMF.

The temperature drop in the capillary wall ΔT_w can be computed with

$$\Delta T_w = \frac{EI}{2\pi}\left[\frac{1}{k_w}\ln\frac{R_w}{R_b}\right] \tag{4}$$

where I is the electrical current and k_w is the thermal conductivity of the capillary wall. Equation 4 has been derived from eq 3 in ref 37, by ommiting the term representing the temperature drop in the polyimide coating. Setting $R_w/R_b = 7.5$ as well as the other experimental values (see Experimental Section) in eq 4, it is found that $\Delta T_w = 0.305$ °C for both cases considered—air- and RIMF-cooled capillaries.

Finally, to compute the temperature drop in the RIMF bath, we follow the approach used by Nelson et al. (*40*) to tackle a similar problem. Accordingly (*40*), ΔT_{sur} is given by

$$\Delta T_{sur} = EI/2\pi h R_{sur} \tag{5}$$

where R_{sur} is the radius of the surrounding bath. Using the values (*40*) of $h = 2600$ W m^{-2} K^{-1} for RIMF, $h = 70$ W m^{-2} K^{-1} for air and taking $R_{sur} = 1$ mm, one obtains $\Delta T_{sur} = 0.125$ °C in the RIMF and $\Delta T_{sur} = 4.63$ °C in air.

ΔT_{total} (eq 2) is computed using the values above for ΔT_b, ΔT_w, and ΔT_{sur}. Finally, the total temperature drop from the center of the capillary to the surrounding media is, for the RIMF-thermocooled case, $\Delta T_{total} = 0.60$ °C and, for the naturally convecting air case, is $\Delta T_{total} = 5.29$ °C. Adding to these values the temperature at which the thermocooler operates (i.e. typically 25 °C), one obtains the value of the temperature at the center of the bore. For the RIMF-cooling case it is found that at the center of the bore $T(r = 0) = 25.60$ °C and for the naturally convecting air-cooled case $T(r = 0) = 30.28$ °C. A summary of the temperature calculations is presented in Table III. Temperature gradients and thus thermal noise are localized in the neighborhood of the inner and outer capillary wall interfaces (Figure 4).

Table III. Temperature Variations (°C) across a Capillary Tube Cooled by Naturally Convecting Air and by a Surrounded Liquid (RIMF) in Contact with a Thermoelectric Cooling System[a]

	ΔT_b	ΔT_w	ΔT_{sur}	ΔT_{total}	$T(r = 0)$
air	0.350	0.305	4.631	5.286	30.28
RIMF	0.165	0.305	0.125	0.595	25.60

[a] Capillary dimensions i.d. = 50 μm and o.d. = 365 μm, applied electric field E = 25– V cm^{-1}, current = 57 μA.

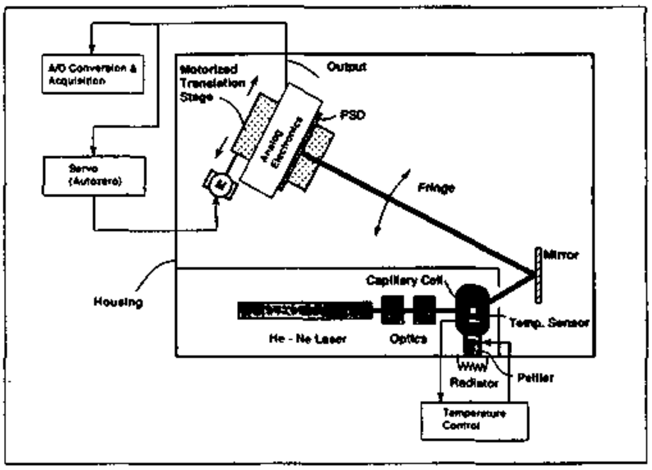

Figure 5. Instrumental optomechanical arrangement of the capillary refractive index detector.

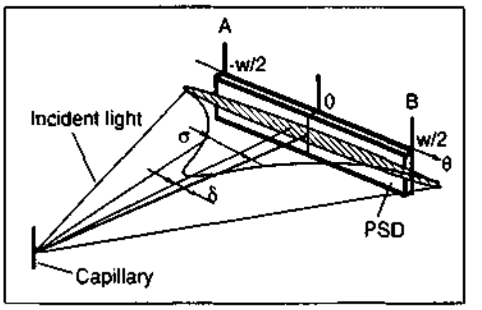

Figure 6. PSD geometric arrangement used to measure the fringe deflection angle δ. The width of the PSD is *w* and the fringe angular spread (spot size) is σ. A null signal is produced when the center of gravity of the fringe is centered on the PSD.

Position-Sensitive Diode (PSD). A Δn in the capillary bore results in an angular displacement of the scattering fringes. The shift of a selected fringe is measured with a PSD which, upon calibration, gives an electrical signal proportional to Δn. Although most high-resolution position sensors are built with dual photodiodes (*23, 24*), for this experiment, PSDs were found to be quieter, especially at frequencies below 1 Hz; most certainly due to the fact that PSDs are made of a single silicon chip and therefore their characteristics are constant over the whole device (*41–43*). Moreover, state of the art PSDs are known to have good linearity and low dark current properties which make them attractive for applications requiring very high resolution (*44*).

The optical arrangement which has been used to measure fringe shifts is shown in Figure 5. The light from one fringe is directed to the detector and forms an elliptical spot whose center of gravity is centered on the detector (Figure 6). As the spot moves across the active area, output currents I_A and I_B are generated which are proportional to the distance between the location of the center of the spot and the end contacts of the detector (*44*). To produce a signal with zero output for a centered spot, which in addition cancels the intensity fluctuations of the light (e.g. due to laser noise), the complementary outputs currents of the detector are wired to yield

$$V(\delta) = \frac{I_A - I_B}{I_A + I_B} \tag{6}$$

The angular resolution of the detection scheme depends on the width of the selected fringe as well as on the ratio of the PSD width to the spot size. This ratio is given by the distance from the capillary to the actual PSD location. In order to determine the geometric configuration which would render the highest sensitivity and to calculate the value of the shot noise limited angular shift, the following analysis is made.

For a narrow light spot at a distance δ away from the center of the detector (Figure 6), the difference between the two photocurrents, as obtained after the substraction in the PSD circuit, is (*43, 44*)

$$I_A - I_B = I(\delta) = sP_{opt}\frac{2}{w}\delta \tag{7}$$

where w is the PSD width, P_{opt} is the total optical power within the spot, and s is the spectral sensitivity of the detector (i.e. $s = 0.35$ A W^{-1} at $\lambda = 633$ nm for the Hamamatsu S1352 employed (*41*)). If the light intensity is distributed over the whole surface of the detector rather than on a point (Figure 6), the detector response can be calculated by adding the contributions of each point (*44*). For a normalized Gaussian distribution having a width σ and with the center of gravity at position δ, it can be shown that

$$I(\delta) = sP_{opt} \int_{-w/2}^{w/2} \frac{2\theta}{w} \frac{1}{\sigma\sqrt{2\pi}} \exp\left[-\frac{1}{2}\left(\frac{\theta - \delta}{\sigma}\right)^2\right] d\theta \tag{8}$$

Furthermore, it can be verified that for small angular displacements (i.e. $\delta \ll w$) around $\delta = 0$, the sensitivity can be expressed as

$$\frac{dI}{d\delta} \cong G(a,\sigma) = sP_{opt}\frac{1}{\sigma\sqrt{2\pi}}\left[\int_{-2\sigma/a}^{2\sigma/a} \frac{a}{2\sigma} \exp\left[-\frac{1}{2}\left(\frac{\theta}{\sigma}\right)^2\right] d\theta - \exp\left[-\frac{1}{2}\left(\frac{2}{a}\right)^2\right]\right] \tag{9}$$

where $a = 4\sigma/w$ is the *aspect ratio* of the spot size to the detector width. Figure 7 shows that the behavior of the sensitivity G and of the relative sensitivity σG vary according to eq 9. The curve for the relative sensitivity displays an almost linear increase near zero followed by an exponential decay for large values of the *aspect ratio*. These results indicate that in order to obtain the best performance, the PSD must be operated at a distance from the capillary where the selected fringe and the detector width leads to an aspect ratio of $a \cong 0.9$.

Shot Noise. Among all the phenomena which limit the smallest measurable angular shift, shot noise sets an ultimate limit which is given by the nature of light itself. The shot noise limit therefore constitutes a valuable benchmark and allows the determination of the margin left for the improvement of the optical detector.

To calculate the shot noise limit for the present optical configuration, it is assumed that the angular position of the selected fringe moves sinusoidally about the center position with an amplitude δ and at a frequency Ω. The expression for the output detector signal can be derived from eq 9 as

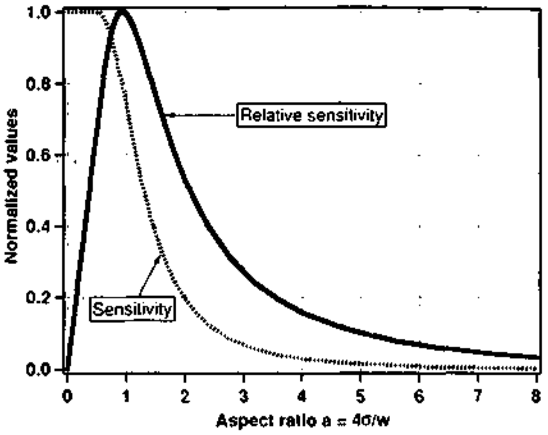

Figure 7. Theoretical sensitivity of a PSD detector for a Gaussian spot as a function of finite width.

$$I(t) = sP_{opt}0.37\frac{1}{\sigma}\delta \sin(\Omega t) \tag{10}$$

where the factor 0.37 arises from the evaluation of the maximum sensitivity (in eq 9). The corresponding signal power is therefore

$$\langle I^2(t)\rangle = \frac{1}{2}\left(0.37sP_{opt}\frac{1}{\sigma}\right)^2\delta^2 \tag{11}$$

The power spectrum of the shot noise is known to be white (i.e. flat) and its density $\langle I_{sn}^2\rangle$ is proportional to the optical power reaching the detector (*45*). To take into account that both the $(I_A - I_B)$ and $(I_A + I_B)$ outputs generate independent noise contributions to the useful signal (eq 10), the total shot noise power becomes

$$\langle I_{sn}^2\rangle = 4BesP_{opt} \tag{12}$$

where B is the detection bandwidth and e is the elementary charge. Shot noise limited detection is reached when the signal power (eq 11) equals the shot noise power (eq 12), i.e.

$$\left(\frac{\delta}{\sigma}\right)_{sn} = 2\sqrt{Be2\frac{1}{s}\frac{1}{P_{opt}}7.11} \tag{13}$$

Substituting in eq 13 typical values for this experiment (e.g. $B = 1$ Hz, $s = 0.35$, and $P_{opt} = 25$ μW), one obtains $(\delta/\sigma)_{sn} = 1 \times 10^{-6}$. Furthermore, eq 13 is used to compute the shot noise limits associated with various fringes employed in the present measurements (Table I). It is found that shot noise limits are very similar for the last three fringes ($n - 1$, $n - 2$, and $n - 3$) with associated values which are only 1 order of magnitude smaller than the measured noise value of $\Delta n = 2.5 \times 10^{-8}$ (see Results). For optical powers below about 10 μW, the thermal noise level of the electronics becomes comparable to the shot noise, and therefore would set new detection limits.

EXPERIMENTAL SECTION

RI Cell. The best thermal stability in the cell is achieved when the thermocooler system is set at a temperature slightly higher than ambient. The resulting ca. 1 °C temperature gradient is localized near the cell windows and is directly correlated to a n gradient in the RIMF and fused silica according to their dn/dT thermal coefficients. Small fluctuations in the temperature around the exit air/window/RIMF interface, in contact with the environment, introduce an additional source of noise if a flat exit window is employed.

In a cell constructed with two plane parallel windows, the incoming laser beam crosses the entrance air/window/RIMF interface at 90°, and the n gradient does not alter the light-propagating path (i.e. no refraction). However, at the exit window,

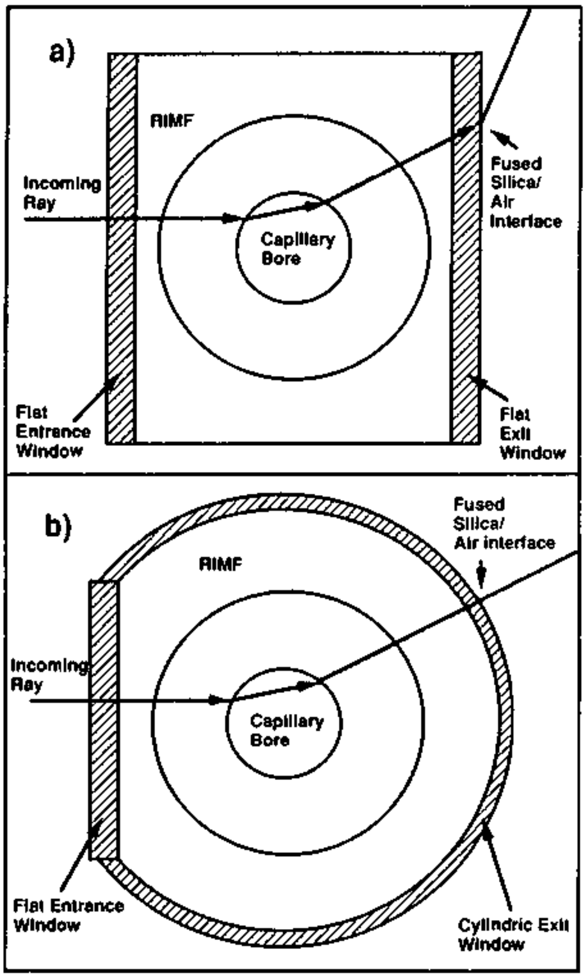

Figure 8. Ray path of a significant ray crossing a RI cell fitted with two flat windows (a) and crossing a cell having a flat antrance window but a cylindric exit window coaxially placed to the capillary axis (b). Refractions are indicated as arrows.

the rays are scattered at all angles and the propagating ray is refracted as it crosses this last interface, as illustrated in Figure 8a. Small fluctuations in the temperature around this interface, which is in contact with the environment, cause the rays to change their paths and introduce additional noise.

This source of noise was eliminated by replacing the flat exit window with a cylindrical one, placed coaxially with respect to the capillary tube, as indicated in Figure 8b. In this optical arrangement the scattered rays cross the exit window perpendicularly, independent of their scattering angles, thus avoiding refraction.

The design of the cell takes into account the effects discussed above. The capillary tube and the flat entrance window are mounted and sealed with a pair of "O" rings and screws whereas the cylindrical exit window is epoxied to the cell body. The capillary is coiled into a groove around the external part of the aluminum block before it enters the chamber filled with RIMF after crossing a region in contact with the Peltier element. The Peltier element (Melcor, FC 06.6605L) is in contact with the capillary tube 5 mm before it enters the chamber filled with RIMF. A calibrated thermistor (ILX Lightwave DL 890884) is placed on the opposite side of the thermocooler, in close contact with the capillary tube in a small hole in the aluminum block. Both elements are driven by a thermoelectric system (ILX Lightwave Model LDT-5412). When no electrical current flows through the buffer, the short-term thermal stability (τ = 1 s) of the system is better than 2×10^{-4} °C and has a typical drift of less than 1×10^{-2} °C h^{-1}.

A good RIMF should have a refractive index as close as possible to the value of the FS, have a small dn/dT coefficient, not be photodegrade, and have a good transmittance. We employed a commercial RIMF oil (Nos. 19569 and 19571, R. P. Cargille Laboratories Inc., Cedar Grove, NJ) having $n = 1.4571$ and $dn/dT = 3.86 \times 10^{-4}$ RIU K^{-1} at 25 °C.

RI Detector. A diagram of the experimental setup is shown in Figure 5 and has been constructed using commercial parts (Spindler & Hoyer, Germany).

A very important aspect to be considered in the overall design of the instrument is that the RI detector measures Δn originated not only at the capillary bore but at any point of the optical path from the laser output coupler to the PSD. The laser (Uniphase No. 1103P), optical isolator (constructed with a polarizing filter and a $\lambda/4$ plate, Dr. Steeg & Reuter, Germany, Nos. 011110 and 042005, respectively), focusing optics, and cell are therefore mounted on four sliding stainless steel rods (S & H No. 061216) in contact with each other to prevent air flows in the beam path. The laser beam has a diameter of 600 μm and is focused into the capillary bore with a $f = 40$ cylindrical lens producing a beam waist of ca. 23 × 600 μm in the capillary bore. The cell volume, defined by the capillary i.d. and the beam waist, for a 50 μm i.d. tube is 1.2 nL. The fringe selected for the measurement is directed onto the PSD (S1352, 2.5 × 34 mm, Hamamatsu, Japan) using a mirror. An autozero for the instrument is constructed by feeding the output of the PSD into a servo system (No. MMC-QR-030024-02LD-00A, Maxon Motor, Switzerland) which drives the PSD to the desired position by means of a DC motor (No. 2230F0112S, Faulhaber, Germany).

Capillary Electrophoresis. The Ce results reported here have been performed in an i.d. = 50 μm, o.d. = 365 μm fused-silica capillary (Polymicro Technologies, Phoenix, AZ) where 5 mm of the polyimide coating were removed for detection. The home-built CE apparatus has been previously described (*10, 12*). Data acquisition was performed with the Nelson software package (Perkin-Elmer, Switzerland) on an IBM AT computer.

The chemicals needed for the preparation of the electrolyte solutions were purchased from Merck (Darmstadt, Germany) and the carbohydrates from Fluka (Buchs, Switzerland).

RESULTS

The overall sensitivity of the RI detector depends mainly on the size of the capillary tube employed and to a less extent on the fringe selected for the measurement. For the 50-μm capillaries and a time constant of τ = 1 s (B = 1 Hz) the short-term RMS noise (i.e. "grass") is 2.5×10^{-8} RIU corresponding to a thermal stability of 2.5×10^{-4} °C computed with the Nelson software (Figure 9). With only the inherent time constant of the PSD amplifiers (i.e. τ < 1 ms), the noise level rises to 1.8×10^{-7} RIU. In both cases, the baseline drifts are about 2×10^{-6} RIU h^{-1}. These performances were obtained using the RI detector in a flow injection analysis mode (FIA) under constant, pressure-induced flow conditions using the fringes labeled ($n - 1$) and ($n - 2$) in Figure 3 appearing at 24 and 16° from the optical axis. These fringes shift 210 ± 10°/RIU (Table I). Combining this information with the noise levels, it is found that the fringe deflection stability of the apparatus is 100 *n*-radians (6 μ-deg).

For the typical widths of the selected fringes, the optimum working distance from the capillary for the PSD is approximately 28 cm (see Position-Sensitive Diode subsection). In this position the minimum measured angular deflection of 100 nrad corresponds to a position resolution capability of 3×10^{-2} μm or 1 order of magnitude better than the manufactured specification (*41, 42*), which is 1 μm.

Unfortunately, in CE one cannot make full use of the above reported sensitivities because of the heat produced by Joule effect. The degrading effect that voltage and current have in terms of baseline drift can be seen in Figure 10. Although the short-term noise does not significantly degrade with increasing E and I, the baseline medium term drift (i.e. τ = 1 min) degrades at a rapid pace and, at currents higher than 60 μA, the noise reaches a level unacceptable for CE experiments.

The linear dynamic range of the apparatus extends from the achieved sensitivity up to 10^{-3} RIU, which corresponds to 4 orders of magnitude in the present case. This has been

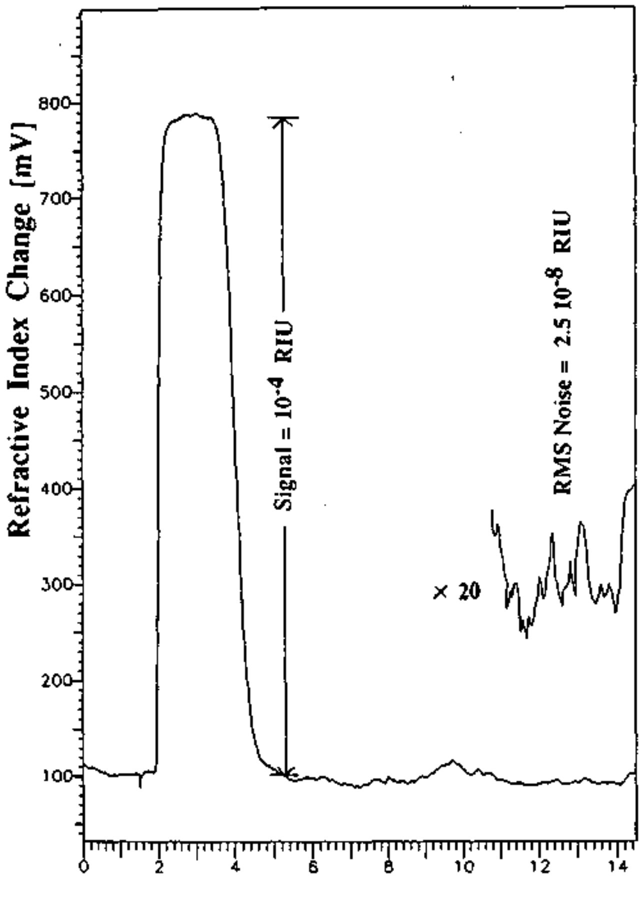

Figure 9. Sensitivity performance of the RI detector operator in the FIA mode with an i.d. = 50 μm capillary. The peak corresponds to an injection of 0.5 μL of saccharose aqueous solution calibrated to produce a Δn = 1.0 × 10^{-4} RIU.

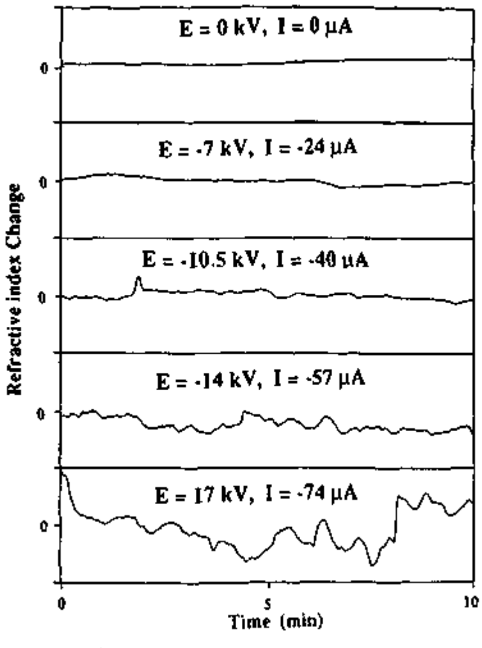

Figure 10. Degradation of the baseline of the RI detector in the CE mode with increasing voltage (E) and current (I).

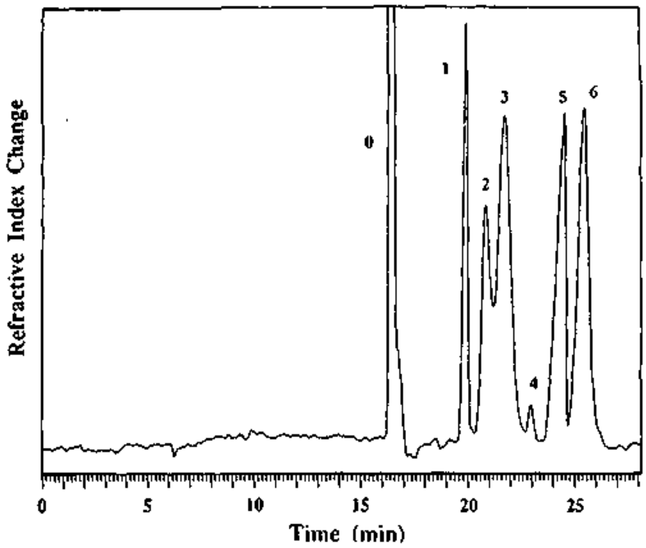

Figure 11. Electropherogram of a mixture of five underivatized saccharides. The peaks are identified as buffer (0), saccharosa (1), N-acetylglucosamine (2), cellubiosa (3), impurity (4), N-acetylgalactosamine (5), and lactose (6). Conditions: each 1% except for saccharose, 0.5%; buffer 100 mM tetraborate, pH 9.; capillary length 70 cm, 55 to detector; i.d. = 50 μm; CE voltage, 14 kV; current, 50 μA; injection time 7 s at 12 kV; thermocooler temperature 27 °C; interference fringe, n – 2.

determined from a double logarithmic plot of output signal vs RI constructed using saccharose solutions having concentrations ranging from 58 μM to 150 mM (2 × 10^{-3}% to 5% w/v) operating the instrument in the FIA mode (R = 1.000). The lowest measured detection limit for saccharose at S/N = 2 is 10 μM. At $\Delta n > 10^{-3}$ RIU, the fringe selected for the measurement "walk away" from the PSD and strong deviations from linearity are observed.

An electropherogram of a mixture of five underivatized saccharides is shown in Figure 11. The first peak (0), appearing at t = 16 min, results from the difference in the n values of the buffer and the sample and serves as an electroosmotic flow rate marker. The remaining peaks correspond to saccharose (1), N-acetylglucosamine (2), cellobiose (3), N-acetylgalactosamine (5), and lactose (6); peak (4) is an impurity. The injected volume is 6.6 nL corresponding to 33 ng of saccharose and similar amounts for the other species.

Most sugars are neutral species and therefore not eligible for CE. This difficulty can be overcome in borate buffers (*25*). Borate complexes sugars (*44*, *48*) into two types of single negatively charged species. The magnitude of the charge and thus their electroosmotic mobility depend mainly on the concentration of borate—higher concentrations leading to more stable complexes (*25*). Borate solutions (100 mM) were employed as support buffers to ensure stable complexations resulting in electrophoretic currents atypically high for an i.d. = 50 μm tube.

Six forms of sugar coexist in aqueous solutions, α- and β-pyranoses and -furanoses, as well as the open-chain and hydrated forms (see Figure 1 of ref 25), multiplying the complexation possibilities. Only saccharose does not form complexes and therefore appears as the sharpest peak in the electropherogram (Figure 11). The broadening observed in the remaining peaks is due to the complexation effects rather than to column overloading. For this reason saccharose was chosen to determine the separation efficiency of the system (*47*). The best theoretical plate number, N, was obtained by electrokinetically injecting 6 mM saccharose solutions for t = 2 s at E = −11 kV (saccharose has an electrophoretic mobility (*25*) of $\mu_{total} = 3.3 \times 10^{-4}$ cm^2 V^{-1} s^{-1}), resulting in N = 1.6 × 10^5.

Under identical FIA experimental conditions, a higher RI sensitivity is obtained with a 100-μm capillary than with the 50-μm capillary employed here. However, in CE the electric current is proportional to the area of the capillary cross section and therefore to the square of its radius (i.e. area = πR_b^2 and $I \propto R_b^2$). The current is expected to increase 4 times for a capillary twice the diameter, for identical voltages across the capillary and under stable CE conditions. In the electropherogram shown in Figure 11 the current derived with a 50-μm tube is 57 μA. For an i.d. = 100 μm tube under identical electric field the current would be 228 μA, a value at which the buffer would have already boiled even before this current value was reached (*40*). The choice of the capillary diameter for the present experiments was thus the result of a compromise between these two opposite factors.

DISCUSSION

A smooth temperature gradient inside the capillary bore leads to a smaller temperature fluctuations in the buffer (see Thermal Analysis subsection). This, in turn, corresponds to small $\Delta T_{\mathrm{total}}$ and ΔT_b values as desired, and vice versa. Thermal fluctuations are responsible for the observed noise in the baseline, thus precluding the instrument to operate at the expected shot noise limit. Larger turbulences in the optical path, associated with large temperature gradients, are located near the buffer/capillary wall and capillary wall/RIMF or air interfaces as shown in Figure 4. In order to retain sufficient sensitivity to be able to perform CE using RI detection, the use of a very efficient and stabilized thermal bath at the measuring region is imperative. Furthermore, it is apparent from inspection of eq 4 that ΔT_w decreases with smaller R_w/R_b ratios for both cases studied, indicating that faster heat dissipation is obtained when thick-wall capillaries are employed (*40*).

Angular deflections slightly better than the here obtained 100 nrad have been achieved (*24*) through the use of quiet electronics and using a very stable LED light source in a test bench with a bicell as PSD. However it will be very difficult to realize these 2-fold improvements in a real system subject to material expansions and mechanical vibrations and employing much noisier laser light.

A comparison between the present results (Figure 11), obtained without the use of RIMF, PSD, and thermocooling (e.g. with an instrument as that proposed by Dovichi et al. (*18–20*), would have been interesting. However, no such information exists in the literature and, from our experience, the *S/N* ratios obtained under CE conditions with such an experimental setup were much worse than those shown in the bottom trace of Figure 10 as a consequence of inefficient heat dissipation, precluding the experiment to succeed. This most likely explains the absence of this information in the literature.

The approach to achieve higher stability of the sugar complexes given by Hoffstetter-Kuhn et al. (25) was to increase column temperature using moderate concentrations of borate (as compared to those here used, e.g. 60 mM) obtaining similar separation efficiencies. Absorption detection at 190 nm was possible in this case because borate was found to induce a red shift in the quartz UV absorption profile of the studied saccharides. To increase the temperature while retaining high buffer concentration and thus to profit from both complexation mechanisms, our experimental setup would have to be modified. Separation and detection, with the present integrated cell design, can only be carried out at identical temperatures. To realize different temperatures the separation part of the capillary should be separated from detection as usually done in other separation techniques.

Admittedly, the chemical system selected to demonstrate the instrumental capability was not the most suitable if one considers that high buffer concentrations were required. For a chemical system such as peptides or small ions, requiring lower buffer concentrations in the separations or for hyphenation of this RI instrument to conventional and micro HPLC (i.e. small or no Joule effects, respectively), the use of larger i.d. capillaries (e.g. 75 or 100 μm) would be more appropriate.

CONCLUSIONS

The present work extends the scope of RI detection to the CE domain. The performance delivered by the described instrument is comparable to or better than, in terms of sensitivity and linearity, that offered by alternative universal methods such as electric field modulation (*22*), differential methods (*24*), or indirect absorption or fluorescence techniques (*49*) which were the goals of the present investigation.

The ultimate detection limits for this instrument, given by the shot noise, have not been reached. Instrumental improvements and intensive application work aiming to approach the theoretical limits are now being undertaken.

It must be noted that the use of RIMFs to improve instrumental performance is not restricted to RI detection. It has been proposed (*50*) that the use of RIMFs should also benefit absorbance and fluorescence detectors employing capillaries. Indeed, it has been just demonstrated that RIMF is a very effective means to improve the sensitivity of fluorescence detection in CE (*51*).

ACKNOWLEDGMENT

We thank S. Hoffstetter-Kuhn for her advice in the CE results and E. Gassmann, M. Moriseau, and T. Olefirowicz for the critical reading of this manuscript as well as the corrections they proposed. We thank P. E. Jordi for the CAD design and mechanical work and A. Wüthrich for his advice in the electronics.

APPENDIX

Dimensionless Parameters. In terms of J_i (for $i = 0, 1$), the Bessel functions of the first kind, θ is given by (*38*)

$$\theta = \frac{1}{\lambda^2}\,\frac{J_0(\lambda\eta) - J_0(\lambda) + \dfrac{2\lambda}{\mathrm{Bi}_{\mathrm{oA}}}J_1(\lambda)}{\mathrm{f}(\lambda)} \qquad \text{(A-1)}$$

where the function f(λ), representing the *autothermal* effect (*38*), is given by

$$\mathrm{f}(\lambda) = J_0(\lambda) - \frac{2\lambda}{\mathrm{Bi}_{\mathrm{oA}}}J_1(\lambda) \qquad \text{(A-2)}$$

The $\mathrm{Bi}_{\mathrm{oA}}$ parameter appearing in the denominator of eq A-2 is the overall biot number defined in Table II where, in addition, the computed values of θ, f(λ), and $\mathrm{Bi}_{\mathrm{oA}}$ are reported.

The *heat-transfer* coefficient, h_{oA}, for a bare capillary (i.e. without the polyimide coating) can be evaluated using (*35*)

$$h_{\mathrm{oA}} = \frac{1}{R_{\mathrm{L}}}\left\{\left[\frac{\ln\left(\dfrac{R_w}{R_b}\right)}{k_w}\right] + \left[\frac{1}{R_{\mathrm{P}}h_s}\right]\right\}^{-1} \qquad \text{(A-3)}$$

where k_w is the thermal conductivity of the wall and h_s is the *surface heat transfer* coefficient (h) and $k_w = 1.5$ W m^{-1} K^{-1}. For liquid-cooled capillaries h_s is so large that the last term in the denominator can be neglected (*35*) and $h_{\mathrm{oA}} = 3.0 \times 10^4$ W m^{-2} K.

LITERATURE CITED

(1) Jorgenson, J. W.; DeArman Lukacs, K. D. *Science* 1983, *222*, 266.
(2) Mikkers, R. E. P.; Evaeraerts, F. M.; Verhaeegaen, Th. P. *J. Chromatogr.* 1979, *169*, 11.
(3) Gordon, M. J.; Huang, X.; Pentoney, S. L.; Zare, R. N. *Science* 1988, *242*, 224.
(4) Grossman, P. D.; Colburn, J. C.; Lauer, H. H.; Nielson, R. M.; Riggin, R. G.; Sittapalmam, G. S.; Rickard, E. C. *Anal. Chem.* 1989, *61*, 1186.
(5) Ewing, A. G.; Wallingford, R. A.; Olefirowicz, T. M. *Anal. Chem.* 1989, *61*, 292A.
(6) Lauer, H. H.; McManigill, D. *Anal. Chem.* 1986, *58*, 166.
(7) Nielsen, R. G.; Sittampalam, G. S.; Rickard, E. C. *Anal. Biochem.* 1989, *177*, 20.
(8) Tsuda, T.; Takagi, K.; Watanabe, T.; Satake, T. *HRC & CC, J. High Resolut. Chromatogr. Chromatogr.* 1988, *11*, 72.

(9) Cohen, A. S.; Paulus, A.; Karger, B. L. *Chromatographia* **1987**, *24*, 15.
(10) Paulus, A.; Gassmann, E.; Field, M. J. *Electrophoresis* **1990**, *11*, 702.
(11) Yang, F. *HRC & CC, Commun.* **1981**, *4*, 83.
(12) Bruno, A. E.; Paulus, A.; Bornhop, D. *J. Appl. Spectrosc.* **1991**, *45*, 462.
(13) Dovichi, N. J. *Rev. Sci. Instrum.* **1990**, *61* (12), 653.
(14) Bruno, A. E.; Gassmann, E.; Pericles, N.; Anton, K. *Anal. Chem.* **1989**, *61*, 876.
(15) Gassmann, E.; Kuo, J. E.; Zare, R. N. *Science* **1985**, *230*, 813.
(16) Liu, J.; Shirota, O.; Novotny, M. *Anal. Chem.* **1991**, *63*, 413.
(17) Dovichi, N. *CRC Crit. Rev. Anal. Chem.* **1987**, *17*, 357.
(18) Bornhop, D. J.; Dovichi, N. J. *Anal. Chem.* **1986**, *58*, 504.
(19) Bornhop, D. J.; Dovichi, N. J. *Anal. Chem.* **1987**, *59*, 1632.
(20) Bornhop, D. J.; Nolan, T. G. Dovichi, N. J. *J. Chromatogr.* **1987**, *384*, 181.
(21) Synovec, R. E. *Anal. Chem.* **1987**, *59*, 2877.
(22) Chen, C. Y.; Demane, T.; Huang, S. D.; Morris, M. D. *Anal. Chem.* **1989**, *61*, 1590.
(23) Pawliszyn, J. *Anal. Chem.* **1988**, *60*, 2796.
(24) Pawliszyn, J. *Spectrochim. Acta Rev.* **1990**, *13*, 354.
(25) Hoffstetter-Kuhn, S.; Paulus, A.; Gassmann, E.; Widmer, H. M. *Anal. Chem.* **1991**, *63*, 1541.
(26) Honda, S.; Iwase, S.; Makino, A.; Fujiwara, S. *Anal. Biochem.* **1989**, *176*, 72.
(27) Garner, T. W.; Yeung, E. S. *J. Chromatogr.* **1990**, *515*, 639.
(28) Nardi, A.; Fanali, S.; Foret, F. *Electrophoresis* **1990**, *11*, 774.
(29) Churms, S. C. *J. Chromatogr.* **1990**, *500*, 555.
(30) Bettler, B.; Amado, R.; Neukom, H. *J. Chromatogr.* **1990**, *498*, 213.
(31) Scher, H. *Electrophoresis* 1990, *11*, 18.
(32) Al-Hakim, A.; Linhardt, R. *Electrophoresis* **1990**, *11*, 23.
(33) Marcuse, D. In *Principles of Optical Fiber Measurements*; Academic Press: New York, 1981.
(34) Born, M.; Wolf, E. In *Principles of Optics*; Pergamon Press: New York, 1989.
(35) Knox, J. H. *Chromatographia* **1988**, *26*, 329.
(36) Jones, E. J.; Grushka, E. *J. Chromatogr.* **1989**, *466*, 219.
(37) Grushka, E.; McCormick, R. M.; Kirkland, J. J. *Anal. Chem.* **1989**, *61*, 241.
(38) Goble, W. A.; Ivory, C. F. *J. Chromatogr.* **1990**, *516*, 191.
(39) Vinther, A.; Sieberg, H. *J. Chromatogr.* **1991**, *559*, 27–42.
(40) Nelson, R. J.; Paulus, A.; Cohen, A. S.; Guttman, A.; Karger, B. L. *J. Chromatogr.* **1989**, *480*, 111.
(41) Hamamatsu. Technical note TN-102, 1982.
(42) United Detector Technology. Technical note The guide to position sensing. 1988.
(43) Siebert, H. P. *Sensoren 1*; *Elektronik* **1988**; *241*, 34.
(44) Renn, C. N.; Synovec, R. E. *Anal. Chem.* **1988**, *60*, 1188.
(45) Yariv, A. In *Optical Electronics*, 3rd ed.; CDS College Publishing: New York, 1985.
(46) Demtröder, W. In *Laser Spectroscopy*, Springer-Verlag: Berlin, 1982.
(47) Huang, X.; Gordon, M. J.; Zare, R. M. *Anal. Chem.* **1988**, *60*, 375.
(48) Consden, T. W.; Stanier, W. M. *Nature* **1952**, *169*, 783.
(49) Garner, T. W.; Yeung, E. S. *J. Chromatogr.* **1990**, *515*, 639.
(50) Bruno, A. E. Eur. Pat. Appl. No. 67-17928, 1990.
(51) Kurosu, Y.; Sasaki, T.; Saito, M. *J. High Resolut. Chromatogr.* **1991**, *14*, 86.

RECEIVED for review July 1, 1991. Accepted September 12, 1991.

a reprint from Applied Optics

Laser-based refractive-index detection for capillary electrophoresis: ray-tracing interference theory

Beat Krattiger, Alfredo E. Bruno, H. Michael Widmer, Martial Geiser, and René Dändliker

The fringe pattern observed in a far field after a laser beam illuminates a fused silica capillary immersed in a refractive-index matching material and filled with an analyte fluid is exploited to develop a sensitive optical detector for capillary chemical analysis. The inner capillary interface splits the laser beam into a reflected beam fan and a refracted beam fan, which, on overlapping in the far field, lead to interferences. The intensity and the position of the fringes for capillaries with 250 μm $\geq$ i.d. (inner diameter) $\geq$ 25 μm are well reproduced by the presented model. The calculation predicts the fringe pattern for various beam/i.d. geometric configurations and is used to optimize the performance of the nanoliter–picoliter refractive-index on-column detection studied. It is found that the best contrast corresponds to a capillary that is illuminated with a beam waist of $w_0 \sim$ i.d./12, which is off-center focused with an offset of $s \sim$ i.d./2. For a given interference pattern, the fringes that are found to be more sensitive to Δn are those that appear near the optical axis but still retain high intensity and contrast. The sensitivity increases approximately linearly with the fringe number, and the maximal fringe number increases proportionally with the i.d.

1. Introduction

The development of nanoliter–picoliter optical detectors for capillary separation techniques, such as capillary electrophoresis (CE), is gaining considerable importance in chemical analysis. Indeed, CE represents the trend in fluid-phase chemical separation sciences.[1] Several aspects, including speed of analysis, high resolution, and efficiency account for the acceptance of this technique.[2] High electrical fields across the capillary ends force the ionic species to migrate through a buffer-filled capillary. The different species travel at different speeds according to their charge, size, or both. However, the high resolution delivered by CE is often lost at the detection stage, which is most conveniently done by optical methods,[3] as a result of hyphenation with relatively insensitive detectors.

Because the separation performance increases with a reduction of the inner diameter (i.d.) of the capillary tube employed in CE separations, there is a growing demand to upgrade low-volume detectors used in high-performance liquid chromatography[4] (HPLC) or to develop new detectors that are specifically suitable for CE.[3] Refractive-index universal detection (i.e., detection that responds to virtually all compounds), which is the third most important detection choice in HPLC after absorbance and fluorescence, has not been made available to CE until recently and then only in research laboratories (i.e., no commercial refractive-index detector exists to date for CE).

An issue in the quest to develop nanoliter or picoliter detectors for capillary techniques is that sensitivity is compromised when the i.d. of the tube is reduced. Primarily because of their spatial coherence, lasers have led to the development of a series of novel optical detectors that feature impressive detection limits. Dovichi[5] and Bruno *et al.*[6] have succeeded in developing an on-column laser-based refractive-index detector as well as various related thermo-optical detectors that display sensitivities that are not linear with respect to path length, as is the case in absorption or fluorescence.

Further instrumental developments in the original design[7,8] of the refractive-index detector of Dovichi *et al.* demonstrated in HPLC and flow injection analysis (FIA) were made in our laboratory.[9] We demonstrated the use of refractive-index capillary detection

---

B. Krattiger, A. E. Bruno, and H. M. Widmer are with Analytical Research, Ciba-Geigy, 4002 Basel, Switzerland. M. Geiser and R. Dändliker are with the Institut de Microtechnique, Université de Neuchâtel, 2000 Neuchâtel, Switzerland.

Received 14 May 1992.
0003-6935/93/060956-10$05.00/0.

in CE for the analysis of underivatized saccharides in i.d. = 50-μm tubes. This instrument featured refractive-index matching fluids (RIMF's) and position-sensitive photodiodes.

A far-field interference pattern is observed[9-11] whenever a coherent light beam strikes a transparent cylindrical object such as an optical fiber[10] or a capillary tube. The angular fringe displacement that is due to changes in the refractive index in the core of the capillary, Δn_i, corresponds to phase shifts between the two recombining rays, the TIR (total internally reflected) ray and the TP (transmitted probing) ray (Fig. 1) and constitutes the output signal of the refractive-index detector. In a previous paper[9] we demonstrated that, as in the case of step-index fibers,[10] the complex light-scattering pattern of freestanding capillaries is greatly simplified after their immersion in a matching material, which results in a geometric configuration such as that shown in Fig. 1. This translates into manifold benefits for the performance of the CE detector. The number of fringes is reduced and the light intensity in the remaining fringes is larger than it would be otherwise. In addition, the RIMF acts as a heat sink that reduces the thermal noise associated with Joule heat in CE.

Here we present a theoretical model based on geometric optics (ray tracing) that accurately reproduces recorded fringe patterns of capillaries with 250 μm ≥ i.d. ≥ 25 μm. (Although CE is performed with capillaries with i.d. < 100 μm we extended the analysis to larger i.d.'s for those interested in using the refractive-index detector for HPLC.) The model is used to calculate the fringe shift as a function of the refractive-index change Δn_i for a given capillary i.d. and beam waist. The path-length dependence of the fringe sensitivity as a function of i.d. and fringe number is investigated to find geometric configurations that should render higher instrumental performance.

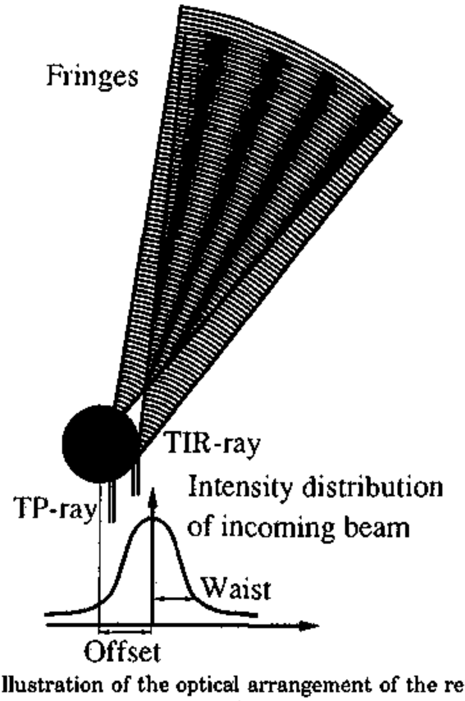

Fig. 1. Illustration of the optical arrangement of the refractive-index detector for CE, which resembles a Young double-slit interferometric arrangement. The fringes, which are formed by the coherent addition of the exiting TP and TIR rays, are represented as moiré structures in the figure.

2. Theoretical Model

A. Introduction to Theory

As indicated by Watkins,[11] because the capillary dimensions considered here are much larger than the illuminating wavelength, ray-tracing methods are adequate to describe the optical problems encountered. These ray-tracing methods are simpler and easier to implement than those based on wave theory. Because the capillary is immersed in an RIMF the outer capillary wall is optically dissolved, as illustrated in Fig. 1 of Ref. 9; the total number of reflections and refractions is thus reduced from 10 to 3 as the number of interfering fans is reduced from 4 to 2. The optical device under investigation consists of only a cylindrical string represented by the fluid-filled capillary bore embedded in a large surrounding media with the refractive index of fused silica. The illumination consists of a set of parallel rays that interact with the fluid string in the capillary bore, in which the following effects are considered (Figs. 1 and 2):

(1) Snell's refraction law is used to relate the ray impact height x_{TP} to the ray output angle α.

(2) Reflection law determines the dependency between the ray impact height x_{TIR} and emerging angle α.

(3) Depending on the impact height x_{TP}, the TP ray undergoes a phase change that is due to the refractive index in the fluid string.

(4) The TIR ray undergoes a phase shift at the reflection, depending on its angle of incidence, its polarization, and on the refractive indices n_i and n_e.

(5) Because of the divergence lens and the mirror effect of the capillary, both rays suffer an intensity decrease, depending on their impact height and distance to the detector.

(6) The intensity of the TP ray is further decreased because of reflections of parts of the ray at the

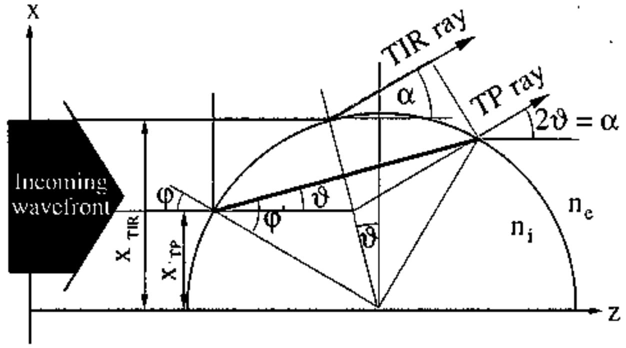

Fig. 2. Geometric parameters used to describe the paths of the TIR and the TP rays.

two fluid string–fused silica interfaces. This intensity decrease also depends on the polarization, the angle of incidence, and on the refractive indices n_i and n_e.

(7) The illuminating beam has an intensity profile (i.e., Gaussian) that defines the initial impact intensities for both rays.

The final aim is to calculate the interference pattern in the far field $I(\alpha)$ as a function of the scattering angle α while taking into account effects (1)–(7). To simplify the formalism, we derive all equations as functions of $H_{\mathrm{TP}} = x_{\mathrm{TP}}/R$, which is the reduced height with respect to the capillary radius R. It should be noted that, unlike that of Watkins,[11] the present model now includes effects (4)–(7).

B. Ray Tracing and Phases

Only the realistic case in which the refractive index n_i in the core is smaller than n_e of the capillary wall and the surrounding propagation media is considered here (e.g., the use of aqueous buffers with $n_i = 1.332$ and fused silica capillaries with $n_e = 1.457$). The laser beam, propagating in the z direction, strikes the capillary from one side perpendicularly to the capillary (the y axis); i.e. the discussion is restricted to a two-dimensional system.

Depending on the entrance height, the capillary core splits the incoming beam into a TP ray and a TIR ray. As their original phases are altered, both rays interfere subsequently in the far field. In other words, the capillary acts (1) as a beam splitter, (2) as a dephaser for the incoming rays, (3) as a diverging mirror for the TIR ray, and (4) as a diverging lens for the TP ray (see Figs. 1 and 5). The overall system thus performs like a Young double-slit arrangement.

To simplify the analysis it is convenient to introduce three reduced variables:

$$N = \frac{n_i}{n_e} \leq 1, \tag{1a}$$

$$H_{\mathrm{TP}} = \frac{x_{\mathrm{TP}}}{R}, \qquad 0 \leq H_{\mathrm{TP}} \leq H_{\mathrm{max}}, \tag{1b}$$

$$H_{\mathrm{TIR}} = \frac{x_{\mathrm{TIR}}}{R}, \qquad H_{\mathrm{max}} \leq H_{\mathrm{TIR}} \leq 1, \tag{1c}$$

where R is the capillary internal radius (i.e., R = i.d./2), N is the reduced refractive index, H_{TP} is the reduced impact height of the TP ray, and x_{TP} is the impact for the incoming TP ray (see Fig. 2).

The necessary condition for the two beams TP and TIR to interfere in the far field is that they be parallel, i.e., that they emerge in the same direction α (Fig. 2.). In this case the entrance height H_{TIR} of the TIR ray is related to the entrance height H_{TP} of the TP ray by

$$H_{\mathrm{TIR}} = \frac{1}{N}[(N^2 - H_{\mathrm{TP}}^2)^{1/2}(1 - H_{\mathrm{TP}}^2)^{1/2} + H_{\mathrm{TP}}^2]. \tag{2}$$

Using definitions (1a), (1b), and Snell's law, we find that the refraction angle $\alpha = 2\vartheta$ (Fig. 2) is given by

$$\alpha(H_{\mathrm{TP}}) = 2[\arcsin(H_{\mathrm{TP}}/N) - \arcsin(H_{\mathrm{TP}})]. \tag{3}$$

From geometric considerations (Fig. 2) it can be shown that the optical path lengths OP (i.e., the geometric path multiplied by the refractive index of the propagating media) for the TIR and TP rays are given by

$$\mathrm{OP}_{\mathrm{TIR}}(N, H_{\mathrm{TP}}) = \frac{2Rn_e}{N}[(N - H_{\mathrm{TP}})(1 - H_{\mathrm{TP}}^2)^{1/2} + H_{\mathrm{TP}}(N^2 - H_{\mathrm{TP}}^2)^{1/2}], \tag{4a}$$

$$\mathrm{OP}_{\mathrm{TP}}(N, H_{\mathrm{TP}}) = 2Rn_e(N^2 - H_{\mathrm{TP}}^2)^{1/2}. \tag{4b}$$

According to the Fresnel equations for TIR,[12] the TIR ray undergoes a phase shift $\Phi_{p,s}$ as a function of the angle of incidence, namely,

$$\Phi_p = -2\arctan\left(\frac{1}{N^2}\left\{\frac{N^2(1-N^2)}{H_{\mathrm{TP}}^2[(1-N^2)^{1/2} - (N^2 - H_{\mathrm{TP}}^2)^{1/2}]^2} - 1\right\}^{1/2}\right), \tag{5a}$$

$$\Phi_s = -2\arctan\left(\left\{\frac{N^2(1-N^2)}{H_{\mathrm{TP}}^2[(1-N^2)^{1/2} - (N^2 - H_{\mathrm{TP}}^2)^{1/2}]^2} - 1\right\}^{1/2}\right), \tag{5b}$$

where the subscripts p and s refer to parallel and perpendicular polarizations, respectively.

Introducing these additional phase shifts $\Phi_{p,s}$ that are due to the TIR, we find that the total phase difference between the interfering rays is given by

$$\Psi(H_{\mathrm{TP}}, N) = \frac{2\pi}{\lambda}(\mathrm{OP}_{\mathrm{TP}} - \mathrm{OP}_{\mathrm{TIR}}) - \Phi_{p,s}, \tag{6a}$$

which, by using Eqs. (4), becomes

$$\Psi(H_{\mathrm{TP}}, N) = \frac{4\pi R n_e}{\lambda}\frac{H_{\mathrm{TP}} - N}{N} \times [(1 - H_{\mathrm{TP}}^2)^{1/2} - (N^2 - H_{\mathrm{TP}}^2)^{1/2}] - \Phi_{p,s}. \tag{6b}$$

C. Fringes and Sensitivity

Assuming that the amplitudes of the two emerging rays are the same (constant for all scattering angles), the far-field light intensity is simply proportional to $1 + \cos(\Psi)$ (Fig. 3). The fringes are conveniently labeled by the fringe order

$$m = \frac{\Psi}{2\pi}, \tag{7}$$

where $m = 0$ corresponds to the outermost fringe $(\alpha = \alpha_{\max})$ for which the phase difference is 0. The magnitude of m increases toward the optical axis $(H_{\mathrm{TP}} = 0)$ where the fringe labeled $m_{\max}$ appears (note that m is negative and the subscript max refers to its magnitude only).

The phase difference [Eq. (6b)] reaches its maximum value for emerging rays propagating along the optical axis (i.e., $H_{\mathrm{TP}} = 0, \alpha = 0$) and its minimum for rays striking at the critical angles where reflection and refraction coincide (i.e., $H_{\mathrm{TP}} = H_{\max}$), which, from Snell's law and Eq. (1b) (Fig. 2) occurs at

$$H_{\max} = N. \tag{8}$$

At $m = 0$, the TIR and TP rays overlap at the capillary interface and the distinction between the TIR and the TP ray is no longer meaningful. The geometric path difference and also the phase shift Φ [Eqs. (5) and (6b)] vanish at this point.

The maximum fringe number $m_{\max}$ occurs at $\Psi_{\max}$. Taking into account that the phase shift $\Phi = -\pi$ [Eqs. (5)] and using Eq. (6a), we find that

$$m_{\max} = \frac{\Psi_{\max}}{2\pi} = \frac{2R(n_i - n_e) + 0.5\lambda}{\lambda}. \tag{9}$$

For illumination with $\lambda = 0.633\ \mu\mathrm{m}$ (He–Ne laser) and for a 25-μm-i.d. capillary with $\Delta n = n_e - n_i = 0.125$ (water-filled fused silica capillary), one gets $m_{\max} = -4$, which indicates that a total of 5 fringes are expected to occur, with $m = 0, -1, -2, -3$, and -4.

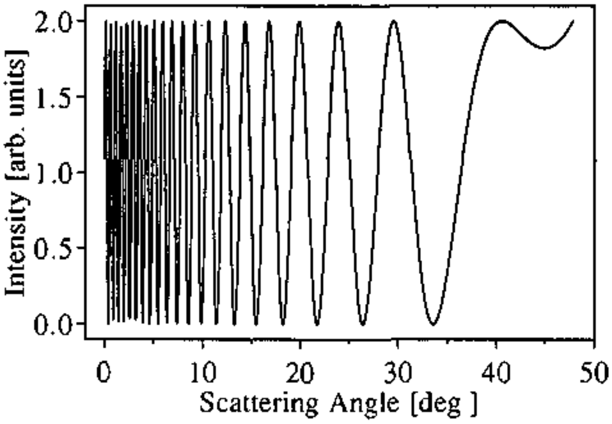

Fig. 3. Ideal fringe pattern (equal intensities of interfering rays) versus scattering angle α for a water-filled capillary with i.d. = 100 μm and $N = 0.914$.

As the current interferometric setup corresponds to a device that is used for the measurement of refractive-index changes, it is convenient to define an instrumental sensitivity S, which is considered as the differential change of the phase with refractive index and normalized to the fringe width $(\Delta\Psi = \pi)$, that is,

$$S = \frac{1}{\pi}\frac{\partial\Psi}{\partial n_i} = \frac{1}{\pi n_e}\frac{\partial\Psi}{\partial N}. \tag{10}$$

Neglecting the phase shift $\Phi_{s,p}$ that is due to the TIR, we derive the sensitivity S from Eq. (6b) as

$$S = \frac{4R}{\lambda}\left\{\frac{H_{\mathrm{TP}}}{N^2}\left[(N^2 - H_{\mathrm{TP}}{}^2)^{1/2} - (1 - H_{\mathrm{TP}}{}^2)^{1/2}\right] + \frac{(N - H_{\mathrm{TP}})}{(N^2 - H_{\mathrm{TP}}{}^2)^{1/2}}\right\}. \tag{11a}$$

Equation (11a) indicates that as H_{TP} increases $\partial\Psi/\partial N$ decreases. The largest phase change for a given ΔN (or Δn_i) would then be observed for the fringe appearing on the optical axis, as seen in Fig. 4, which shows the dependence of S on the scattering angle α. In Fig. 4 the maximum value of S is then

$$S_{\max} = \frac{4R}{\lambda}, \tag{11b}$$

which indicates that, in the absence of a phase shift that is due to the total reflection, the maximal sensitivity to the capillary size increases linearly with the capillary dimensions.

D. Ray Amplitudes

If the intensities of all interfering rays were the same, the best monitoring fringe (the one used to track the fringe shifts) for refractive-index detection would be the one appearing near the optical axis. However, fringe patterns reveal low fringe contrast in this

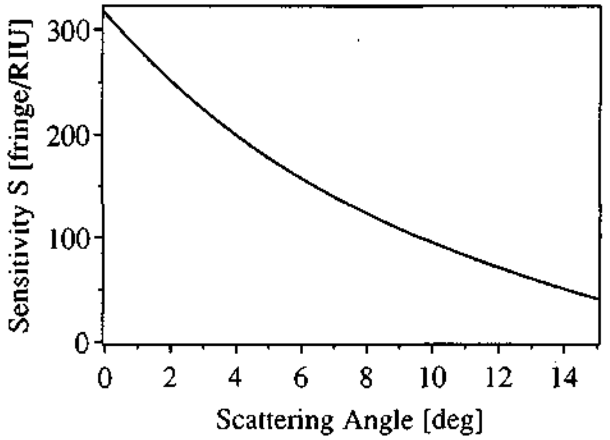

Fig. 4. Sensitivity S as a function of scattering angle α for a 100-μm-i.d. water-filled capillary. S is maximum for axial rays, where the longest possible optical path through the sample occurs. RIU, refractive-index unit.

region because the TIR ray carries low intensity compared with the TP ray.

The TIR ray does not suffer amplitude losses because of Fresnel's formulas[12] at the capillary interface, but the TP ray is partially reflected at both interfaces as it twice crosses the fused silica–fluid string interface [effect 6]. The total amplitude transmissions for both polarizations T_p and T_s can be computed by multiplication of the individual amplitude transmission coefficients given by the Fresnel formulas[12] as

$$T_p(H_{\mathrm{TP}}) = \frac{4N^2(N^2 - H_{\mathrm{TP}}^2)^{1/2}(1 - H_{\mathrm{TP}}^2)^{1/2}}{[(N^2 - H_{\mathrm{TP}}^2)^{1/2} + N^2(1 - H_{\mathrm{TP}}^2)^{1/2}]^2}, \tag{12a}$$

$$T_s(H_{\mathrm{TP}}) = \frac{4(N^2 - H_{\mathrm{TP}}^2)^{1/2}(1 - H_{\mathrm{TP}}^2)^{1/2}}{[(N^2 - H_{\mathrm{TP}}^2)^{1/2} + (1 - H_{\mathrm{TP}}^2)^{1/2}]^2}. \tag{12b}$$

In addition, the radius of curvature of the capillary wall introduces a divergence effect in the (x, z) plane, which also contributes to the attenuation of the intensities for both rays. This effect can be accounted for by invoking power conservation in the beam before and after the capillary, i.e., $P_{\mathrm{out}} = P_{\mathrm{in}}$, where P is the total optical power over the whole cross section. The geometric beam cross sections before and after the capillary (see Fig. 5) are $\Delta x \Delta y$ and $(\Delta \alpha u)\Delta y$, respectively, and power conservation thus yields

$$I_{\mathrm{in}} \Delta x \Delta y = I_{\mathrm{out}}(\Delta \alpha u)\Delta y. \tag{13}$$

The intensity attenuation D^2 for the rays in the far field at a distance u from the capillary axis, if we take into account the spreading of the rays, is given by

$$D_{\mathrm{TP}}^2(H_{\mathrm{TP}}) = \frac{I_{\mathrm{out}}}{I_{\mathrm{in}}} = \left| \frac{1}{u} \frac{\partial x_{\mathrm{TP}}}{\partial \alpha} \right|, \tag{14a}$$

$$D_{\mathrm{TIR}}^2(H_{\mathrm{TP}}) = \frac{I_{\mathrm{out}}}{I_{\mathrm{in}}} = \left| \frac{1}{u} \frac{\partial x_{\mathrm{TIR}}}{\partial \alpha} \right|. \tag{14b}$$

The corresponding factor for the amplitude attenuation is D. Because D_{TIR}^2 can be only positive and $\partial x_{\mathrm{TIR}}/\partial \alpha$ is negative, only the absolute values are to be considered. It can be shown that they can be written as

$$D_{\mathrm{TP}}^2(H_{\mathrm{TP}}) = \frac{R}{2u} \frac{(1 - H_{\mathrm{TP}}^2)^{1/2}(N^2 - H_{\mathrm{TP}}^2)^{1/2}}{(1 - H_{\mathrm{TP}}^2)^{1/2} - (N^2 - H_{\mathrm{TP}}^2)^{1/2}}, \tag{15a}$$

$$D_{\mathrm{TIR}}^2(H_{\mathrm{TP}}) = \frac{(1 - H_{\mathrm{TP}}^2)^{1/2}}{u}. \tag{15b}$$

Finally, the complex amplitudes A associated with both rays, in terms of H_{TP}, OP, T, and D, are given by

$$A_{\mathrm{TP}} = T(H_{\mathrm{TP}})D_{\mathrm{TP}}(H_{\mathrm{TP}})\exp[i\mathrm{OP}_{\mathrm{TP}}(H_{\mathrm{TP}})], \tag{16a}$$

$$A_{\mathrm{TIR}} = D_{\mathrm{TIR}}(H_{\mathrm{TP}})\exp[i\mathrm{OP}_{\mathrm{TIR}}(H_{\mathrm{TP}})]. \tag{16b}$$

The far-field light intensity I that is obtained by the superposition of the two rays is given by[12]

$$I(N, H_{\mathrm{TP}}) = |A_{\mathrm{TP}} + A_{\mathrm{TIR}}|^2 = (A_{\mathrm{TP}})^2 + (A_{\mathrm{TIR}})^2 + 2A_{\mathrm{TP}}A_{\mathrm{TIR}}\cos\Psi(N, H_{\mathrm{TP}}), \tag{17}$$

where the relative phase Ψ of the two rays is given by Eq. (6b).

The weight of the two attenuation factors D and T is different. D_{TP} and D_{TIR} strongly dominate over the whole fringe pattern, whereas the influence of T is small and visible only for scattering angles greater than $\alpha = 40°$. For this reason T can be omitted in the calculation unless the zero-order fringe ($m = 0$) is investigated.

Typical fringe patterns, as the one shown in Fig. 6 for a 100-μm-i.d. capillary, have been calculated as a function of the scattered angle α [Eq. (3)] by using Eq. (17). In the figure, the intensities associated with both individual rays [the square of Eqs. (16)] are also

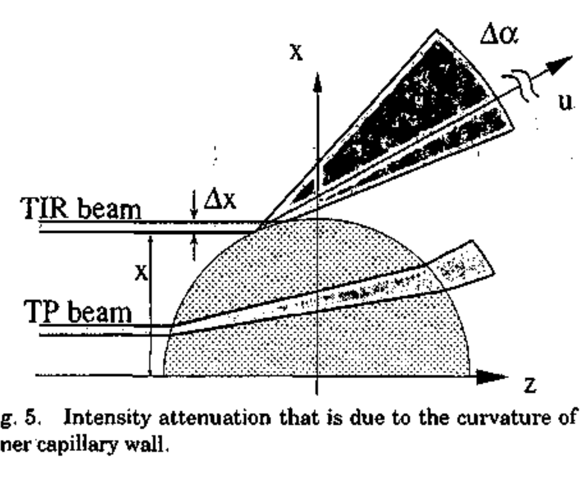

Fig. 5. Intensity attenuation that is due to the curvature of the inner capillary wall.

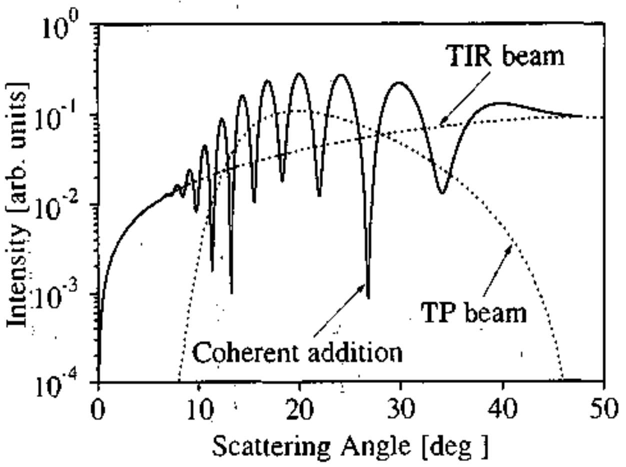

Fig. 6. Fringe pattern simulation for a 100-μm-i.d. fused silica capillary filled with water, illuminated by a beam with a waist of $w_0 = 8.4$ μm and an offset of $s = 48$ μm. The individual intensity contributions of the TIR and TP rays are given as dotted curves. Maximum fringe contrast is observed for equal intensities at $\alpha = 12°$ and $\alpha = 28°$.

displayed. Highest contrast is observed when the individual intensities are identical, i.e., $|A_{\mathrm{TP}}|^2 = |A_{\mathrm{TIR}}|^2$, which occurs, in this case, at approximately $\alpha = 12°$ and $\alpha = 28°$.

E. Gaussian Beams

Until now, the incoming rays were considered to have uniform intensity. If the illumination is provided by a laser, the intensity distribution in the beam cross section is essentially Gaussian. For a Gaussian incoming beam the initial ray amplitude A_G of the ray is given by[13]

$$A_G(H) = A_0 \exp\left[-\left(\frac{HR - s}{w_0}\right)^2\right], \qquad (18)$$

where s is an incoming offset parameter in the x direction (see Fig. 1) and w_0 is the waist of the incoming beam.

It is interesting to observe how the interference pattern changes as the incoming beam waist w_0 or the offset s varies ($s = 0$ corresponds to on-center illumination and $s \neq 0$ corresponds to off-axis illumination). In this way it is possible to make an *a priori* prediction regarding which geometric configuration would render the highest fringe contrast. This is shown in Fig. 7, where the fringe pattern for a 100-μm-i.d. capillary and a beam waist of $w_0 = 8.4$ μm for seven different configurations, with offsets ranging from $s = 0$ μm to $s = 60$ μm, are simulated. For $s \leq 30$ μm the whole beam cross section transverses the capillary without suffering reflection losses. The lens effect of the fluid string translates the beam offsets into an angular deflection of the spot, whose Gaussian beam profile is, although distorted, conserved. If the beam offsets are further increased, a substantial part of the light is also reflected and interference fringes are visible, as shown for $s = 40$ μm. An additional increase in the offset increases the fringe contrast, because balance in the intensities of the two outgoing rays is approached. In this case it is apparent that an off-axis illumination of $s = \mathrm{i.d.}/2 = 50$ μm gives the best illumination condition (i.e., the highest fringe contrast) for the current purpose. If the beam offset is further increased, the contrast fades because only the faint intensity of the slope of the Gaussian beam profile now transverses the center of the fluid string, which reduces the TP intensity with respect to the TIR intensity. Furthermore, the overall intensity decreases rapidly because the mirror effect at the fluid string surface disperses the beam strongly. The Gaussian beam profile is reproduced again, this time by the mirror effect, as shown in the curved base line for $s = 60$ μm in Fig. 7.

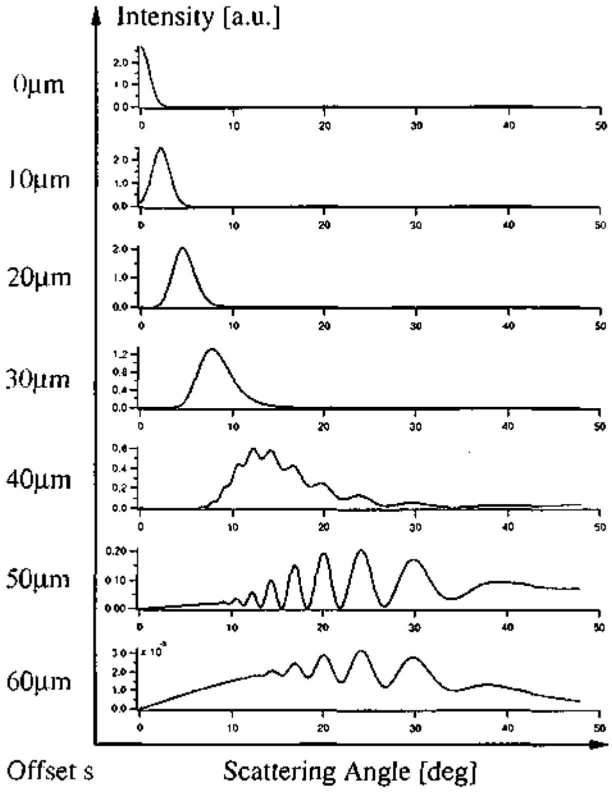

Fig. 7. Fringe pattern simulations for 100-μm-i.d. capillary illuminated by a beam with a waist $w_0 = 8.4$ μm for various beam offsets ranging from $s = 0$ μm to $s = 60$ μm.

3. Experimental Results

A. Experimental Setup

The experimental setup consists basically of a goniometer with a photodetector attached to the rotating arm (see Fig. 8) driven by a computer (a Macintosh IIfx with the LabView package for data acquisition and Igor software for calculations). The light source is a linearly polarized He–Ne laser with 2-mW output power (Uniphase 1103P). An optical isolator, placed immediately after the output coupler, is used to decouple the laser resonator from retroreflections. Spatial filtering was not necessary. The incoming laser beam is focused by a 5× microscope objective onto the capillary, resulting in a spot size of $2w_0 = 16.8$ μm. The fused silica capillaries investigated ($n_e = 1.457$ at $T = 25$°C for $\lambda = 632.8$ nm) had an outer diameter of ~330 μm and inner diameters ranging from 5 to 250 μm (Polymicro Technologies).

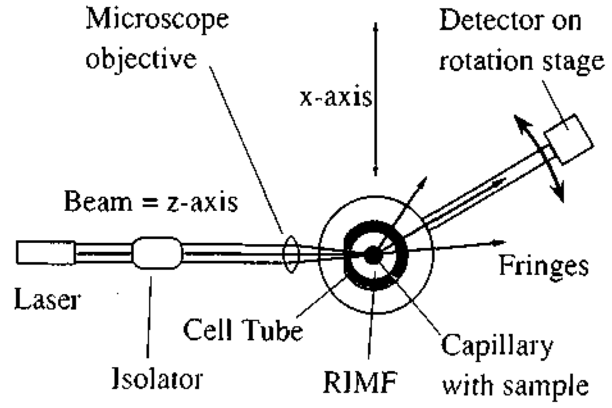

Fig. 8. Experimental setup used to record the fringe patterns. The capillary, which is immersed in RIMF, is concentric to the cell tube and the x-axis translation corresponds to the beam offset s.

In all cases the protective polyimide coatings were removed. The capillary is immersed in a cell filled with RIMF[9] (e.g., Ciba-Geigy transparent index matching epoxy V.P. XW 396/397) and is mounted on a two-dimensional translation stage. To allow a 360° observing angle we made the cell from a glass tube (9-mm diameter) with a flat polished entrance window (4.4 mm × whole tube length) to prevent cylindrical aberrations on the beam waist (see Fig. 8 of Ref. 9). The concentric arrangement of the capillary within the cell tube permits all rays originating from the capillary to cross the cell tube perpendicularly, which, in turn, preserves the original direction of the rays when returning to the air, where the detection is performed. To guarantee perfect centering of the capillary with respect to the cell tube, the fringe patterns corresponding to two on-axis illuminations from two perpendicular directions were recorded. If both patterns are symmetric around the zero deflection angle, the capillary is assumed to be centered.

The angular distribution of the light intensity is measured by a standard Si p-i-n photodiode (BPW 34) at a distance of 10 cm away from the capillary (far field). A set of slits is located in front of the photodiode, so as to produce a view field of 1.1° and to prevent perturbations that are due to background light from the environment.

B. Results

The measured fringe patterns are the same as those employed in the refractive-index detector described in Ref. 9. A comparison between the calculated and the measured fringe patterns is provided in Fig. 9, in which the fringe pattern of a 100-μm-i.d. capillary as well as the corresponding simulation are plotted as functions of the scattering angle. For the calculations we employed values given in the literature for the refractive indices and measured values for the beam waists. The beam offsets and i.d.'s were varied (e.g., to account for the tolerance in the i.d. dimensions) in order to obtain their best fit. The calculated and the recorded fringe patterns for capillaries with i.d. = 50 μm down to 5 μm are shown in Fig. 10. Although the recording has not been done with the same accurary as the one displayed in Fig. 9, it is apparent that the quality of the fit degrades with smaller i.d.'s (see discussion Section 4).

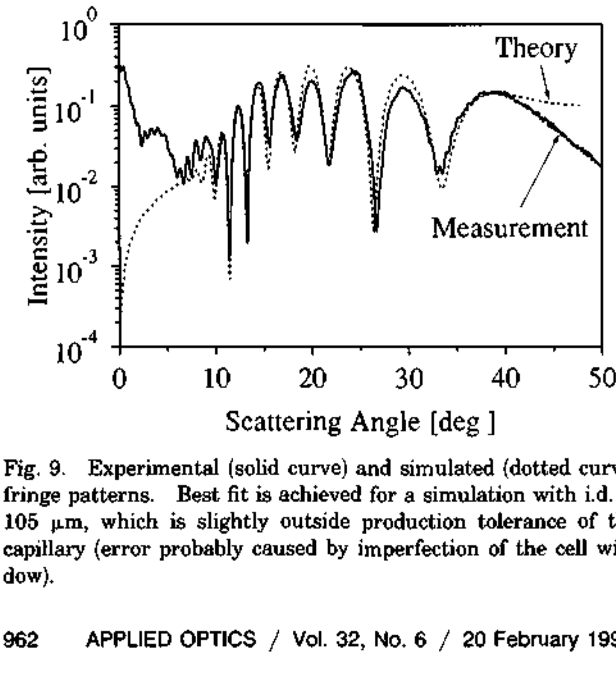

Fig. 9. Experimental (solid curve) and simulated (dotted curve) fringe patterns. Best fit is achieved for a simulation with i.d. = 105 μm, which is slightly outside production tolerance of the capillary (error probably caused by imperfection of the cell window).

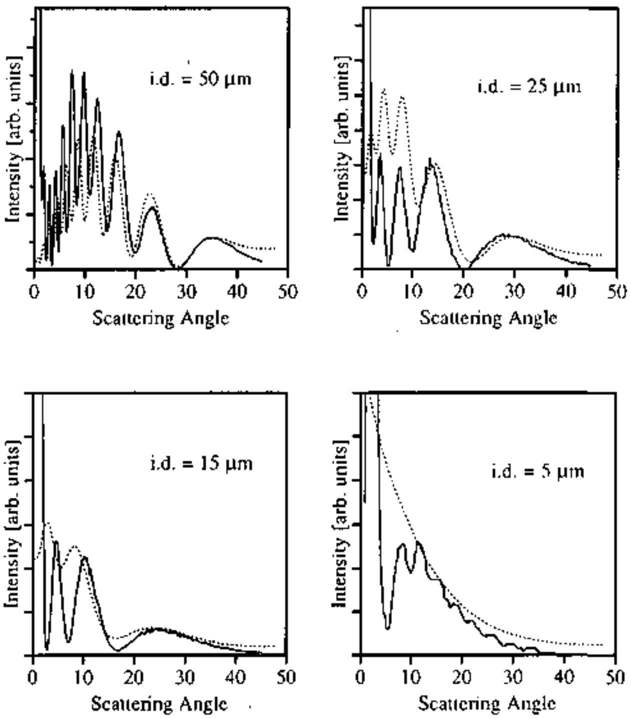

Fig. 10. Recorded and simulated fringe patterns for capillaries with i.d. = 50, 25, 15, and 5 μm illuminated by a besm with a waist of w_0 = 22 μm and beam offsets of s = 36, 21, 19, and 0 μm, respectively.

4. Discussion

Ignoring interference effects, Synovec[14] developed a pure deflection ray-tracing model to predict the sensitivity associated with a (TP) ray [see Eqs. (28)–(32) in Ref. 14]. The presented model and the experimental results indicate, at least for capillaries witb i.d. ≤ 250 μm, that the dominant effect is interference, not deflection as previously proposed.[3,6,14]

The simulated fringe pattern shown in Fig. 9 for a 100-μm-i.d. tube mimics the recorded fringes over the scattering region of interest ($5° < \alpha < 40°$) within experimental accuracy. As mentioned by Watkins,[11] for angles $\alpha < 5°$ the detector (shown in Fig. 8) is too close to the optical axis, and interference configurations other than those shown in Fig. 1 arise and lead to discrepancies between theory and measurement (e.g., diffraction of incoming rays grazing to the capillary bore). The intensity behavior on the opposite side of the fringe pattern is dominated by the intensity of TIR rays (Fig. 6). In this region, the discrepancy between measurement and calculation observed in the fringe with m = 0 (Fig. 9) could be related to deviations from the ideal TIR that is due to

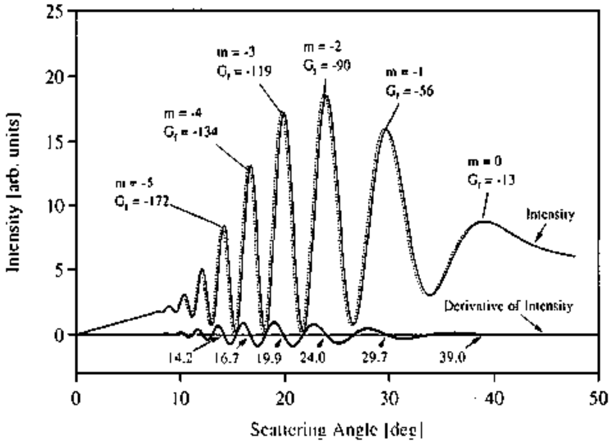

Fig. 11. Sensitivity calculation performed with two fringe patterns for a 100-μm-i.d. tube illuminated by a beam with $w_0 = 8.4$ μm for $\Delta n_i = 1.0 \times 10^{-3}$ refractive-index units. The first derivative of the fringe pattern simulation is used to determine the points of maximum intensity, and is shown in the lower trace.

surface effects (surface roughness leads to reflection loss) or to diffraction effects (the TP ray crosses the bore close to the interface and the optical path differences have dimensions that are comparable to those of λ).

As predicted in Section 2 it is observed that the best fringe contrast corresponds to off-center illumination with a beam offset of $s \sim$ i.d./2 = R. The beam waist should be smaller than the bore radius of the capillary, or more precisely, it should be in the range of $(x_{TIR} - x_{TP})$, e.g., $w_0 \sim$ i.d./12. This permits a greater degree of freedom when choosing the distribution of initial intensity for the two competitive rays by variation of the offset parameter s. The initial intensity distribution should be such that the exiting rays, after suffering all losses, have equal intensity. This is the condition that is required for enhancing the contrast and thus the instrumental sensitivity of capillary refractive-index detection.

The model fails to simulate the fringe pattern of capillaries with i.d.'s that are smaller than 25 μm, as shown in Fig. 10. This was expected, considering that the current model is based entirely in geometric optics and does not include diffraction effects. As the dimensions of the i.d. approach those of λ, it is imperative to account for these effects. This kind of correction to the current model would be necessary to study interference patterns for small i.d. capillaries used in thermo-optical absorption measurements.[6]

Taking into account that beam deflections are measured[9] with a position sensitive detector, the most significant parameter to judge instrumental performance is the fringe sensitivity G_f, which is conveniently defined as the fringe angular displacement Δα per refractive index change Δn_i normalized to the angular fringe width σ:

$$G_f = \frac{\Delta\alpha}{\Delta n_i \sigma}. \tag{19}$$

For the ideal situation in which paraxial fringes with maximum contrast are considered and the fringe width σ is taken at half-maximum intensity (FWHM), the fringe sensitivity reaches the theoretical value of

$$G_f = -\mathrm{S}. \tag{20}$$

If the contrast is not maximum, the resulting fringe width σ is larger, which reduces the magnitude of G_f. The magnitude of G_f has been determined numerically from the angular shift between two fringe pattern simulations for two values of n_i that differ by a small amount, e.g., $\Delta n_i = 1.0 \times 10^{-3}$ refractive-index units, as shown in Fig. 11. For the most usual case, in which the solvent has a refractive index smaller than that of the fused silica (i.e., $n_i < n_e$), a positive change in Δn in the bore (which is due to a substance, to be detected, that is dissolved in the solvent) translates into an angular shift toward the optical axis and G_f is negative (dotted curve in Fig. 11). The fringe positions and their angular shifts Δα are more accurately determined from the zeros of the derivative of the fringe pattern (also displayed in Fig. 11), whereas their associated FWHM σ are obtained graphically by drawing tangents to the slopes and then measuring their separation. This procedure

Table 1. Computed Fringe Sensitivities G_f As Defined in Eq. (19) for the Most Important Fringes for Capillaries with 25 μm ≤ i.d. ≤ 250 μm

	25 μm[a]		50 μm		75 μm		100 μm		250 μm	
m	Angle	G_f	Angle	G_f	Angle	G_f	Angle	G_f	Angle	G_f
−0	29.7	−16 lc	35.5	−18 lc	37.8	−17 lc	39.0	−13 lc	42.0	−17 lc
−1	14.4	−31	22.8	−48	27.1	−55	29.7	−56	36.3	−61
−2	8.1	−34	16.0	−67	20.8	−81	24.0	−90	32.3	−108
−3	4.4	−34 lc	11.8	−81	16.5	−106	19.9	−119	29.3	−141
−4	1.8	? li, lc	8.7	−102	13.3	−122	16.7	−134	26.8	−188
−5	*b*	*b*	*c*	*c*	10.9	−155	14.2	−172	*c*	*c*

[a] lc, Low-contrast fringe; li, low-intensity fringe.
[b] Value does not exist.
[c] Not evaluated.

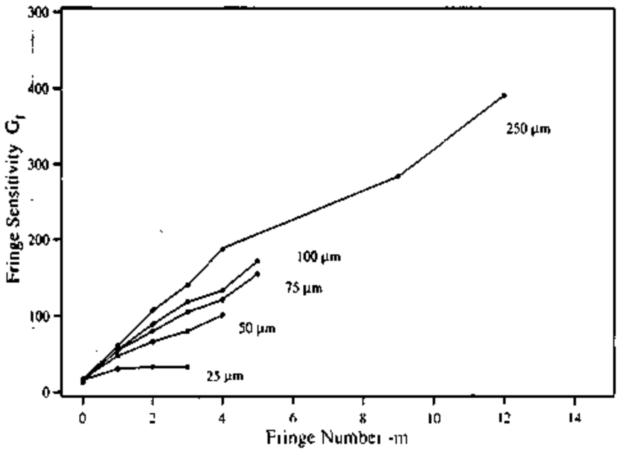

Fig. 12. Fringe sensitivity G_f as a function of fringe number m for various capillaries (data from Table 1). The larger capillaries display more fringes and, for equivalent fringes, higher sensitivities. The fringe number dependence can also be interpreted as the path-length dependence of G_f.

was repeated for all the capillaries studied and the results are summarized in Table 1.

The dependence of G_f on the fringe number and on the capillary i.d. is displayed in Fig. 12. It is noted that the sensitivity increases as a function of the fringe number. With an increasing fringe number the fringes approach the optical axis, which corresponds to longer TP paths through the fluid string and thus collects larger phase difference changes for a given variation of n_i. The fringe number dependence of G_f can, therefore, also be interpreted as its path-length dependence.

The relative insensitive behavior (e.g., constant G_f for a large angular region) for the 25-µm-i.d. capillary is due to the low contrast associated with higher-order fringes. Equivalent fringes for capillaries of different sizes are generated from rays that strike the wall interface at different angles, which explains the observed behavior in the fringe sensitivities G_f of the various capillaries studied.

In the described refractive-index detector, the fringe displacement Δn is measured with a position-sensitive photodiode whose resolving power is a function of G_f and the fringe intensity (see the shot noise and position-sensitive photodiode sections in Ref. 9). The selection of the most suitable fringe to be used in the refractive-index detector (which is called the monitoring fringe in Ref. 9) is not trivial. In addition to G_f, it requires the inspection of the power associated with each fringe. This is important to be able to determine the expected instrumental noise and thus predict the ultimate detection limit.

Furthermore, according to Eq. (11a), the maximum value of $\partial\Psi/\partial n_i$ corresponds to the fringe that appears closest to the optical axis. This fringe, however, is narrow for large capillaries and must be widened by a lens or by a long path through free air to reach the position-sensitive photodiode under optimal geometric conditions.[9] This widening introduces additional noise by temperature variations in air (e.g., schlieren effects) and refraction at the lens surfaces. However, paraxial fringes carry only a fraction of the light power compared with lower-order fringes. As a consequence of these counteracting effects a recipe for the choice of the monitoring (best) fringe cannot be easily formulated. As only a rule of thumb, one should try to use the fringes that appear as close as possible to the optical axis, provided they carry sufficient intensity and display higb contrast.

Equation (19) is also useful to predict the instrumental angular resolution required in a refractive-index detector with detection limits (i.e., noise level) in the $\Delta n_i = 10^{-8}$ refractive-index unit range (which is tbe typical value of a good commercial refractive-index detector for HPLC with a cell path length of 1 cm and a cell volume of 10 µL). For a 100-µm-i.d. capillary the corresponding fringe width (data from Fig. 11) is $\sigma = 1.8°$ and $G_f = -119$ when the fringe order $m = -3$ is used, which indicates that the position-sensitive photodetector should be able to resolve angular spot shifts as small as $\Delta\alpha = 2 \times 10^{-6°}$. Commercial position-sensitive photodetectors are quoted as delivering a resolution of $10^{-6°}$ and, by using specific electronics, it is possible to improve the quoted spot detection by almost 1 order of magnitude,[9,15] which indicates that the construction of a refractive-index detector suitable for on-column detection with a noise level of Δn_i (noise) $= 10^{-9}$ refractive-index units is a realistic proposition, provided that one selects the proper monitoring fringe, a much higher illuminating power, such as the one used in Ref. 9 (to avoid operating at shot noise limit), and a thermal stability of $\Delta T \sim 10^{-4}$°C within a detection bandwidth of $B = 1$ Hz.

This work was supported by the CERS (Commission pour L'encouragement de la Recherche Scientifique), project 2156.1. We also thank P. Jordi for fruitful discussions and mechanical help from his workshop. Electronic help was provided by A. Wüthrich. For scientific discussion we thank F. Maystre and H. P. Herzig. This paper was presented at the OSA Laser Applications to Chemical Analysis Meeting, Salt Lake City, Utah, 1992.[16]

References

1. T. Braun and S. Nagydiosi-Rozsa, "Capillary electrophoresis: prospects for growth," Trends Anal. Chem. **10**, 266–268 (1991).
2. A. G. Ewing, R. A. Wallingford, and T. M. Olefirowicz, "Capillary electrophoresis," Anal. Chem. **61**, 292A–303A (1989).
3. N. J. Dovichi, "Laser-based microchemical analysis," Rev. Sci. Instrum. **61**, 3653–3666 (1990).
4. E. S. Yeung, *Detectors for Liquid Chromatography* (Wiley, New York, 1986), Chap. 1.
5. N. J. Dovichi, "Thermo-optical spectrometries in analytical chemistry," Crit. Rev. Anal. Chem. **17**, 357–423 (1987).
6. A. E. Bruno, A. Paulus, and D. J. Bornhop, "Thermo-optical absorption detection in 25-µm-i.d. capillaries: capillary electrophoresis of dansylamino acids mixtures," Appl. Spectrosc. **45**, 462–467 (1991).

7. D. J. Bornhop and N. J. Dovichi, "Simple nanoliter refractive index detector," Anal. Chem. **58**, 504–505 (1986).
8. D. J. Bornhop and N. J. Dovichi, "Simultaneous laser-based refractive index and absorbance determinations within microliter diameter capillary tubes," Anal. Chem. **59**, 1632–1636 (1987).
9. A. E. Bruno, B. Krattiger, F. Maystre, and H. M. Widmer, "On-column laser-based refractive index detector for capillary electrophoresis," Anal. Chem. **63**, 2689–2697 (1991).
10. D. Marcuse, *Principles of Optical Fibre Measurements,* 1st ed. (Academic, New York, 1981), Chap. 4.5, p. 153.
11. L. S. Watkins, "Scattering from side-illuminated clad glass fibers for determination of fiber parameters," J. Opt. Soc. Am. **64**, 767–772 (1974).
12. M. Born and E. Wolf, *Principles of Optics* (Pergamon, New York, 1980), Chap. 1.5, p. 36.
13. A. Yariv, *Optical Electronics* (Holt, Rinehart & Winston, New York, 1985), Chap. 2.5, p. 28.
14. R. E. Synovec, "Refractive index effects in cylindric detector cell designs for microbore high-performance liquid chromatography," Anal. Chem. **59**, 2877–2884 (1987).
15. J. Pawliszin, M. F. Weber, and M. J. Dignam, "Dual-beam laser deflection sensor," Rev. Sci. Instrum. **56**, 1740–1743 (1985).
16. A. E. Bruno, "Laser based refractive index detection in capillary tubes," in *Laser Applications to Chemical Analysis,* Vol. 2 of 1992 OSA Technical Digest Series (Optical Society of America, Washington, D.C., 1992), p. 165.